A matter of life and death: the formation and destruction of planetary bodies

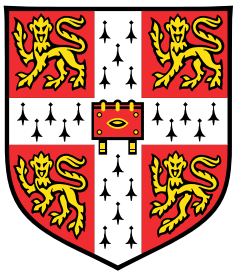

Marc Gabriël Brouwers

Advisor: Dr. Amy Bonsor &
Prof. Mark Wyatt

Institute of Astronomy
University of Cambridge

This dissertation is submitted for the degree of
Doctor of Philosophy

St Edmund's College

March 2023

To my parents and to Marieke, for providing two loving homes.

Declaration

I hereby declare that this thesis is the result of my own work and includes nothing which is the outcome of work done in collaboration except as declared in the text. This dissertation is not substantially the same as any that I have submitted, or, is being concurrently submitted for a degree, diploma or other qualification at the University of Cambridge or any other University or similar institution except as declared in the Preface and specified in the text. I further state that no substantial part of my dissertation has already been submitted, or, is being concurrently submitted for any such degree, diploma or other qualification at the University of Cambridge or any other University of similar institution except as declared in the Preface and specified in the text.

- Chapter 2 is based on the published work: *Prograde spin-up during gravitational collapse* by R. G. Visser, M. G. Brouwers (co-first authors), *Astronomy and Astrophysics*, volume 663, July 2022. Much of the text and figures also appears in the PhD thesis: *From Pebble to Super Earth* by Rico Visser. This work was done in close collaboration with Rico Visser, and the general theory was developed together. I have performed the analytical derivations and written the text that appears in the paper and in this thesis. Rico Visser has performed the *Rebound* simulations and created the figures.

- Chapter 3 is based on the published work: *How planets grow by pebble accretion IV. Envelope opacity trends from sedimenting dust and pebbles* by M. G. Brouwers, C. Ormel, A. Bonsor, A. Vazan, *Astronomy and Astrophysics*, volume 653, September 2021. I have written the text for this work and made the figures.

- Chapter 4 is based on the published work: *A road-map to white dwarf pollution: Tidal disruption, eccentric grind-down, and dust accretion* by M. G. Brouwers, A. Bonsor, U. Malamud, *Monthly Notices of the Royal Astronomical Society*, volume 509, October 2021. I have written the text for this work and made the figures. It also features some parts of the published work: *Circularization of tidal debris around white dwarfs: implications for gas production and dust variability* by U. Malamud, E. Grishin, M. G.

Brouwers, *Monthly Notices of the Royal Astronomical Society*, volume 501, December 2020. Any work led by U. Malamud is credited explicitly in the chapter text.

- Chapter 5 is based on the published work: *Asynchronous accretion can mimic diverse white dwarf pollutants I: core and mantle fragments* by M. G. Brouwers, A. Bonsor, U. Malamud, *Monthly Notices of the Royal Astronomical Society*, volume 519, February 2023. I have written the text for this work and made the figures.

- Chapter 6 is based on the published work: *Asynchronous accretion can mimic diverse white dwarf pollutants II: water content* by M. G. Brouwers, A. M. Buchan, A. Bonsor, U. Malamud, E. Lynch, L. Rogers, D. Koester, *Monthly Notices of the Royal Astronomical Society*, volume 519, February 2023. I have written the text for this work and made the figures. One of the accompanying derivations, shown in appendix C.3, was largely developed by Elliot Lynch.

This thesis does not exceed the prescribed limit of 60,000 words.

Marc Gabriël Brouwers
March 2023

Acknowledgements

Firstly, I would like to thank my supervisor Amy Bonsor for her guidance throughout my PhD, for being endlessly encouraging about new ideas, and for sending chocolates when the pandemic got me stranded during Christmas. I would like to thank Andy Buchan and Laura Rogers for our shared time of doing a PhD together, and for their involvement in my work. I would also like to thank Uri Malamud for always being ready to discuss science, and Rico Visser for his passion for unorthodox ideas. I also thank Elliot Lynch for his never-ending supply of brilliant suggestions - seemingly regardless of topic. I will always be grateful to Allona Vazan and Chris Ormel for introducing me to research at the University of Amsterdam, and for their continued encouragement and inspiration afterwards. Additionally, I would like to thank Carsten Dominik for his support and mentorship throughout my academic journey. Finally, I thank my office mates Alex Hackett, Erik Rosenberg, Andy Buchan (again), Hannah Petrovic and Frances Rigby for their sanity and support, and for notifying me of the events in the institute which I surely would have missed without them.

Secondly, I deeply appreciate my friends at St Edmund's College and elsewhere in Cambridge, who have made my time here so special. I must especially thank my brother Rakesh Chand and his amazing wife Samiksha Sen, who are my Nepali family. I would also like to thank Samuel Hartman for being crazy enough to visit me in a car from 1951, and for going winter camping with me in the Scottish hills and in the far polar North of Sweden. An important caveat to this statement is that I have not yet made it back from this final trip at the time of writing.

Finally, I would like to express my gratitude to my family and my partner in Amsterdam, who welcomed me back during the pandemic and during regular visits. I thank my parents for endless love and encouragement, and my father additionally for generous donations to my museum. I am also grateful to my two brothers, for running simulations on their computers earlier in my career, and for running more slowly than me during a police chase. I would like to end by thanking Marieke, for listening tirelessly to countless hours of practice talks, and for supporting me through so many days and nights of research.

Abstract

Since the discovery of the first exoplanets in the 1990s, our knowledge of planets has expanded far beyond the Solar System, and surveys like *Kepler* and *Tess* have revealed a huge diversity of other worlds. In response to this new information, a novel field of planetary astronomy has sprung up to deal with the major questions, including: How do planets form out of proto-planetary discs? What are the bulk and atmospheric compositions of planets, and what are their building blocks? In this thesis, I contribute to the literature around both of these questions, by studying accretion processes across the lifetime of planetary bodies. My thesis is organized chronologically, starting with the birth of planetary building blocks, and ending with the destruction of fully-formed planets. Besides the shared topic of planetary astronomy, a second unifying theme in this thesis is the use of simple analytical methods to pursue novel research ideas.

The first strand of my research (Chapter 2) deals with the formation of planetesimals - a plausible starting point for planet formation. I develop a new theory that relates the formation of these planetesimals to the spinning motion around their own axis. Specifically, I show that a general mechanism exists, whereby objects that gravitationally collapse next to an external potential naturally acquire spin angular momentum that is aligned with their orbital angular momentum (prograde). Planetesimals in the Solar System have a strong prograde bias, and prograde spin-up, therefore, provides new evidence for the popular hypothesis that they formed via gravitational collapse.

The second strand of my research (Chapter 3) deals with the formation of the planets themselves, which likely grow via the accretion of large planetesimals, as well as smaller particles called *pebbles*. In this work, I study how the accretion of pebbles changes the opacity of planetary envelopes during their formation, which crucially determines how quickly accretion heat is lost, and how much hydrogen and helium the planet can bind. I show that relatively low opacities are predicted from this process, unless the pebble accretion rate crosses a certain threshold. The implication of this work is that the accretion of nebular gas during planet formation might be more efficient than previously thought, especially during periods of slow pebble accretion.

The final strand of my research (Chapters 4, 5, and 6) takes us to the end of a planet's lifetime, when its host star has left the main sequence and has shed its outer layers to become a white dwarf star. Many of these white dwarfs show metal absorption lines in their spectra, indicative of *pollution* with accreted planetary material. From the analysis of such spectra, the composition of exoplanetary material can be recovered. In this work, I explore how planetary material could have accreted onto these stars, and try to link this process to observable features, such as the accretion rate and infrared excess. I also explore the possibility that different components of a pollutant could accrete onto these stars *asynchronously*, over different periods of time, which is a crucial process to understand for the pollutant composition to be correctly interpreted based on the measured stellar abundances.

Table of contents

List of figures **7**

List of tables **21**

1 Introduction **23**
1.1 The early stages of star and planet formation 25
1.1.1 Proto-planetary discs 25
1.1.2 Dynamics and growth of solid particles 26
1.1.3 Planetesimal formation via gravitational collapse 27
1.1.4 Rotation of planetesimals and binaries 28
1.2 From planetesimals to planets 28
1.2.1 Collisional growth and traditional models 28
1.2.2 Planetary growth via pebble accretion 29
1.2.3 Gas accretion & giant planet formation 30
1.3 The observed exoplanet population 31
1.3.1 Low-mass planets 32
1.3.2 Giant planets 32
1.4 White dwarf pollution 33
1.4.1 Post-main sequence planetary survival 33
1.4.2 Compositional analysis of polluted white dwarfs 34
1.4.3 Accretion onto white dwarfs 35
1.5 Thesis layout 36

2 Prograde spin-up during gravitational collapse **39**
2.1 Introduction 39
2.2 Analytical evaluation of prograde spin-up 43
2.2.1 Position and velocity of shearing radial arcs 44
2.2.2 Trajectory of the cloud's centre-of-mass 44

2.2.3 Transfer of orbital angular momentum to rotation 47
2.3 Numerical evaluation of cloud collapse in orbit 50
2.3.1 Comparison with analytical formulation 50
2.3.2 Visualization of the prograde spin-up mechanism 51
2.4 Application: Formation of planetesimals 53
2.4.1 Binary formation criterion 55
2.4.2 Dependence of spin-up on initial conditions 56
2.5 Discussion 57
2.5.1 Comparison to hydrodynamic simulations of binary formation in the Kuiper belt 58
2.5.2 Relevance of prograde spin-up during planet formation 59
2.5.3 Potential application to molecular clouds and stars 60
2.6 Conclusions 61

3 Envelope opacity generated by pebble accretion 63
3.1 Introduction 63
3.2 Model description 66
3.2.1 Two-population approach 66
3.2.2 Sedimentation of solids 67
3.2.3 Dust-pebble collisions 69
3.2.4 Pebble-pebble collisions 71
3.3 Analytical opacity expressions 74
3.3.1 Pebble opacity expression 75
3.3.2 Steady state between dust replenishment and sweep-up. 76
3.3.3 Dust opacity in steady state 77
3.4 Envelope opacity trends 77
3.4.1 Envelope structure 78
3.4.2 Trend with planet mass 79
3.4.3 Trend with orbital separation 80
3.4.4 Trend with pebble accretion rate 83
3.4.5 Description of three opacity regimes 84
3.5 Implications for giant planet formation 86
3.5.1 Trends in the critical metal mass 87
3.5.2 Implications for the formation of Uranus and Neptune 89
3.6 Discussion 90
3.6.1 Comparison with contemporary works 90
3.6.2 Pebble versus planetesimal accretion 91

3.6.3 Model caveats and improvements 92
3.7 Summary and conclusions 92

4 A road-map to white dwarf pollution: tidal disruption, eccentric grind-down, and dust accretion 95
4.1 Introduction 95
4.2 Stage I: from asteroid to tidal debris disc 97
4.2.1 The tidal disruption criterion 97
4.2.2 Tidal disc morphology 99
4.2.3 Debris size distribution 102
4.3 Intermezzo: collision-less evolution via PR drag 105
4.3.1 PR contraction timescale and accretion rate 105
4.3.2 Peak accretion rates by collision-less PR drag 108
4.4 Stage IIa: collisions induced by orbital perturbations 109
4.4.1 Differential geodetic precession 109
4.4.2 Gravitational perturbations by a planet 112
4.4.3 Drag-assisted circularization via pre-existing material 114
4.4.4 Orbital changes due to the Yarkovski effect 115
4.5 Stage IIb: calculation of eccentric collisional grind-down 115
4.5.1 Numerical setup 115
4.5.2 General trends in eccentric grind-down rates 118
4.5.3 Event lifetimes and peak accretion rates 120
4.6 Stage III: infrared emission from accreting fragments or dust 122
4.6.1 Infrared emission from a collision-less tidal disc 122
4.6.2 Emission from collisional dust production 126
4.6.3 Radial optical depth of the tidal debris disc 129
4.7 Discussion 130
4.7.1 Fork (1): direct asteroid impact, ejection or tidal debris disc formation 131
4.7.2 Fork (2): sublimation, continued scattering by a planet or orbital perturbations and collisions 133
4.7.3 Fork (3): outcome of continued scattering by a planet 133
4.7.4 Fork (4): rapid circularization or collisional grind-down 134
4.7.5 Fork (5): the link between dust circularization and infrared excess . 135
4.7.6 Main road: model caveats and improvements 136
4.8 Summary and conclusions 137

5 Asynchronous accretion can mimic diverse white dwarf pollutants I: core and mantle fragments 139
5.1 Introduction . . . 139
5.2 Disruption of differentiated asteroids . . . 141
5.2.1 Geometry of core and mantle fragments in tidal discs . . . 142
5.2.2 Ejection bias of mantle and crustal fragments . . . 143
5.3 Asynchronous accretion of core and mantle fragments . . . 145
5.3.1 Scenario I: differential precession and collisional grind-down . . . 145
5.3.2 Scenario II: scattering of core fragments by a planet . . . 147
5.4 Test of preferential mantle ejection . . . 150
5.4.1 White dwarf sample with Fe/Mg or Fe/Ca abundance ratios . . . 151
5.4.2 Evidence for a core bias in the total accreted material . . . 151
5.5 Discussion . . . 154
5.5.1 Interpretation of photospheric abundances . . . 154
5.5.2 Observational tests for asynchronous core-mantle accretion . . . 155
5.5.3 Asynchronous accretion in alternative models . . . 155
5.6 Summary and conclusions . . . 157

6 Asynchronous accretion can mimic diverse white dwarf pollutants II: water content 159
6.1 Introduction . . . 160
6.2 Timescale of sublimative erosion . . . 162
6.2.1 Very slow sublimation of refractory minerals . . . 164
6.3 Implied water content during accretion . . . 166
6.4 Observational tests of asynchronous ice-refractory accretion . . . 170
6.4.1 Description of white dwarf sample . . . 171
6.4.2 Calculation of oxygen excess with `PyllutedWD` . . . 171
6.4.3 Prediction I: oxygen excess and stellar temperature . . . 172
6.4.4 Prediction II: rare instances of near-pure ice accretion . . . 173
6.4.5 Comparison with previous estimates of oxygen excesses . . . 175
6.5 Discussion . . . 176
6.5.1 Interpretation of dry/wet photospheric abundances . . . 176
6.5.2 Observational tests for asynchronous volatile-refractory accretion . . . 176
6.5.3 Uncertainties in volatile/refractory accretion timescales . . . 178
6.5.4 Challenges in accurately constraining the accretion state . . . 180
6.6 Summary and conclusions . . . 180

7 Conclusions **183**
7.1 Formation of planetesimals and their spins 183
7.1.1 Future work 184
7.2 Planetary growth and opacity due to pebble accretion 185
7.2.1 Future work 186
7.3 Accretion of planetary material onto white dwarfs 187
7.3.1 Future work 188

Appendix A Prograde spin-up appendices **191**
A.1 Rebound settings and convergence 191
A.2 Angular momentum transformation between local rotating and inertial frames 193
A.3 Initial rotational condition of spherical clouds 194
A.4 Collapse of a spherical cloud in a co-moving frame 195

Appendix B Opacity appendices **197**
B.1 Expression of the critical metal mass with a non-isothermal radiative layer . 197
B.2 Variation of the limiting velocity 198

Appendix C White dwarf appendices **201**
C.1 Neglection of asteroid rotation on tidal disc geometry 201
C.2 Filling timescale of a tidal disc 202
C.3 Neglection of heat diffusion during fragment sublimation 204
C.4 Radiation pressure around SDSS J0914+1914 206
C.5 Posterior distributions of accretion state and excess oxygen 209
C.6 White dwarf sample used in chapter 5 212
C.7 White dwarf sample used in chapter 6 218

References **221**

List of figures

2.1 Schematic setup of our analytical calculation (Sect. 2.2). We consider a two-dimensional cloud of mass $M_{\rm cl}$ in a stationary frame, whose origin lies on the central mass $M_{\rm C} \gg M_{\rm cl}$ (where the dotted lines cross). The initial shape of the cloud is that of a partial annulus, bounded by inner and outer circles with radii $r_0 \pm R_{\rm cl}$ and radial lines at angles $\pm\theta_0$. We follow the position $(\bar{x}_{\rm cl}, \bar{y}_{\rm cl})$ and velocity $(\bar{v}_{\rm x,cl}, \bar{v}_{\rm y,cl})$ of the cloud's centre-of-mass over time and calculate the specific rotational angular momentum of cloud particles (in direction $\hat{z}$) relative to this point as $l_{\rm rot} = (xv_{\rm y} - yv_{\rm x}) - (\bar{x}_{\rm cl}\bar{v}_{\rm y,cl} - \bar{y}_{\rm cl}\bar{v}_{\rm x,cl})$, shown in the colour plot at $t = 0$. The initial velocities of the cloud particles correspond to circular, Keplerian motion. Particles that start on the x-axis initially contribute retrograde rotation due to shear, whereas particles on the y-axis contribute prograde rotation due to curvature. The integrated result is a net initial prograde rotational angular momentum that increases over time if the cloud orbits freely (see Eq. 2.14b). 40

2.2 Illustration of the inward centre-of-mass shift in our analytical example. The particles follow circular orbits around a central mass without mutual interactions. As the particles shear out over time, the ensemble deforms into an increasingly extended single arc, shifting the centre-of-mass position (open circular dot) closer to the orbital midpoint. 45

2.3 The amount of spin-up over time for clouds shaped as partial annuli and spheres. Top: Simulated prograde spin-up of clouds in the shape of partial annuli that orbit around a central mass with (blue, SG) and without (red, NSG, Eq. 2.14) self-gravity enabled. When self-gravity and collisions are included, the prograde spin-up levels off around the free-fall timescale (plotted here for an equivalent sphere), when cloud shear comes to a halt. Bottom: Same calculation, computed with spherical clouds and varying initial densities. Their initial rotation scales as $L_0 \propto (R_{\rm cl}/R_{\rm H})^2$, whereas the prograde spin-up during their collapse scales as $L_{\rm rot} \propto (R_{\rm cl}/R_{\rm H})^5$ (see Sect. 2.2.3). As a result, sparse clouds with $R_{\rm cl} \simeq R_{\rm H}$ accumulate most of their rotation during their collapse, whereas the rotation of denser clouds remains largely unchanged. . 48

2.4 Orbital evolution of two non-interacting particles and their centre-of-mass, initiated without rotation. Over time, both the interior (magenta arrow) and the exterior (orange arrow) particles start to revolve around their mutual centre-of-mass (black arrow) in a prograde fashion, as shown by the angular displacement that develops relative to the horizontal dashed line. The quadratic prograde spin-up over time is additionally shown in the inserted panel, with the rotation at the different snapshots depicted by the black dots. 51

2.5 Overview of the collapse of a uniform cloud in orbit around a central mass, shown in a stationary frame. The spherical cloud is initiated with size $R_{\rm H}$ and without any rotation. The snapshots from t = 0 to $t = 0.8\ \omega_0^{-1}$ are enlarged in scale for clarity. We highlight the positions and directions of two particles; one that is initiated closest to the central mass (magenta arrow) and one that starts the furthest away from the central mass (orange arrow). We also indicate the position and direction of the cloud's centre-of-mass (black edged arrow) and plot its initial distance (dark red semicircle). At the end of the collapse, the centre-of-mass has shifted slightly inward toward the central mass, and the two particles have performed half a prograde revolution, confirming the prograde rotation of the object that is formed. 53

2.6 Possible binary configurations for a given rotational angular momentum budget ($L_{\mathrm{rot,binary}}$) at two distances from the central star (40 au, solid; 1 au, dashed), assuming that the components themselves spin at near-breakup rates with density $\rho_{\mathrm{p}} = 1$. When $L_{\mathrm{rot,binary}} < 0.06\,L_{\mathrm{H}}$, only single planetesimals are formed at 1 au as the break-up spin exceeds the angular momentum budget, whereas this critical value lies between 0.02-0.03 L_{H} at 40 au. Large amounts of rotational angular momentum $\gtrsim 0.1 L_{\mathrm{H}}$ can only be contained in binaries with increasingly wide mutual orbits and increasingly similar masses, especially in the outer disc. 54

2.7 Prograde spin-up in the collapse, visualized for a wide range of orbital separations, asteroid sizes and initial conditions. The dashed horizontal lines tangent to the circles represent the rotation prior to collapse, while the arrows indicate the magnitude of prograde spin-up. The ringed circles represent the size of the asteroid that forms, and their colours show the total centre-of-mass displacement during the collapse δa. The systems within the dark red lines represent cases where there is insufficient rotational angular momentum to form binaries ($\omega_{\mathrm{spin}} < \omega_{\mathrm{crit}}$). The systems above and below the red lines show the formation of prograde and retrograde binaries, respectively. The preference for prograde binary formation is clearly visible, especially in the outer disc. 57

3.1 Schematic diagram of our two-population opacity model. Depending on the velocities of sedimenting pebbles, they can experience growth (coalescence), fragmentation, or erosion. In the growth-limited regime, the pebble size in the interior is regulated by the collision and sedimentation timescales ($R_{\mathrm{peb}} = R_{\mathrm{coal}}$). In the velocity-limited regime, fragmentation and/or erosion restrict the pebble size below the growth potential ($R_{\mathrm{peb}} = R_{\mathrm{vlim}} < R_{\mathrm{coal}}$). In our model, dust grains of constant size are produced in collisions between pebbles or in high-velocity pebble-dust encounters (erosion), while they are lost by sticking encounters with slow-moving pebbles (dust sweep-up), leading to a local steady state in their abundance. 66

3.2 Erosive mass loss of pebbles that enter the envelope of a growing planet at its Bondi radius ($r_{\rm B}$). The parameters of the planet are shown in Table 3.1. The three lines correspond to initial pebble entry sizes of 0.1 cm (dotted), 1 cm (dashed) and 10 cm (solid). Due to the positive feedback of erosive mass-loss on the dust abundance, the pebbles rapidly converge to the size $R_{\rm erosion}$ (Eq. 3.7) where collisions with dust grains switch from causing mass loss via erosion to sticking (sweep-up). 70

3.3 Characteristic pebble size limits at the Bondi radius, plotted with the parameters of Table 3.1. The colours indicate the pebble size where $v_{\rm fall,peb} = v_{\rm lim} = 2.4$ m/s, the common limit set via erosion with micron-sized grains and fragmentation. The white dashed line separates the Stokes and Epstein regimes, while the dotted line indicates the regions where either growth rate or erosion/fragmentation limits the local pebble size. The plus sign marks the default planet mass (5 $M_\oplus$) and distance (5 AU). 74

3.4 Pebble growth tracks (a), their resulting pebble opacity (b), and produced dust opacity (c) for a standard set of model runs at 5 AU (see Table 3.1). The different lines indicate a range of planet masses, with the arrow indicating a logarithmic progression from $0.5 - 20$ $M_\oplus$. The triangles indicate the location of the RCB, while the stars indicate the depth where the ambient temperature exceeds the sublimation temperature (2500 K) and the opacity from solids vanishes. The colours in the top panel show the ratio of the pebble size in the model relative to $R_{\rm vlim}$ (Eq. 3.14). The colours in the two lower panels show the relative value of the indicated opacity to the total opacity. 81

3.5 Pebble growth tracks (a), their resulting pebble opacity (b), and produced dust opacity (c) for a standard set of model runs at 5 AU (see Table 3.1). This figure is the same as Fig. 3.4, but now the mass is fixed at the default 5 $M_\oplus$ and the planet's distances from the star are varied logarithmically from $0.1 - 30$ AU. 82

3.6 Pebble growth tracks (a), their resulting pebble opacity (b), and produced dust opacity (c) for a standard set of model runs at 5 AU (see Table 3.1). This figure is the same as Fig. 3.4, but now the mass is fixed at the default 5 $M_\oplus$ and the pebble accretion rates are varied logarithmically from $10^{-7} - 10^{-4}$ $M_\oplus$/yr. 84

3.7 Compilation grid of 10^6 runs, where the colours indicate the opacity at the RCB as a function of the planet's semi-major axis and mass at four different pebble accretion rates. The white dashed lines divide the zones where different opacity contributions dominate. The red dotted lines mark the parameter space where the entire envelope is convective due to high opacities in the velocity-limited regime. 86

3.8 Trends in the critical metal mass as a function of distance. The different lines correspond to a variation in solids accretion rates: 10^{-7} $M_\oplus$/yr (dotted), 10^{-6} $M_\oplus$/yr (dashed), 10^{-5} $M_\oplus$/yr (solid), with proportional gas accretion $\dot{M}_{\rm xy}/\dot{M}_{\rm peb} = 5$ and the remaining parameters set by Table 3.1. Planets with grain-free envelopes (gray lines) exhibit a downward trend with orbital separation because the molecular opacity scales positively with temperature. The opacity generated by pebbles and dust (black lines) increases the critical mass significantly in the outer disc, especially at higher accretion rates. . . 88

4.1 Schematic diagram of the main road to white dwarf pollution examined in this work. In the precursor to its pollution, the star sheds its outer layers during post-main sequence evolution (dashed border). This widens and destabilizes the orbits of surrounding bodies and causes some asteroids to be scattered towards the star through interactions with nearby planets. In the first stage of accretion, asteroids that cross the Roche radius tidally disrupt and form eccentric structures with an orbital spread, which we refer to as (eccentric) *tidal discs*. The orbits of the surviving fragments are perturbed via various processes, including differential precession, causing high-velocity collisions and grind-down within the eccentric tidal disc (stage II). The resulting dust then circularizes and accretes onto the star via various drag forces (stage III). 96

4.2 The maximum sizes of objects that are safe from tidal disruption at a distance r from a 0.6 $M_\odot$ white dwarf, plotted for three different tensile strengths. Large asteroids (>100 km) always disrupt close to the Roche radius of the star, whereas smaller fragments ($\ll$ km) can survive deep pericentre passages ($r \ll r_{\rm Roche}$) due to their material strength. 99

4.3 Orbital width (δa) that contains 90 % of the bound fragments around a 0.6 $M_\odot$ white dwarf. Small asteroids on tight orbits experience non-dispersive breakup and form a non-dispersive stream. The width of the tidal disc increases with the progenitor size and its orbital separation. Very large objects like planets with $R \gg R_{\rm crit}$ experience bimodal breakup with half of their mass being ejected from the system. 101

4.4 Post-breakup orbits after a strengthless asteroid tidally disrupts near a 0.6 $M_{\odot}$ white dwarf. Panel (a) indicates the tidal disc that forms when a small (1 km from 3 AU) asteroid disrupts, yielding a thin orbital spread. Panel (b) corresponds to a 50 km asteroid from 3 AU, which produces a wider – but still completely bound disc. When both the asteroid size and semi-major axis increase to 500 km and 30 AU (c), the outcome is a bimodal disruption event, with nearly half of the material becoming unbound from the white dwarf. . 103

4.5 The smallest dust grains ($R_{\rm blow}$) that interact with the stellar light ($< Q >= 1$) and can remain bound despite the star's radiation pressure. The figure assumes the disruption of a strengthless asteroid at the Roche radius of a 0.6 $M_{\odot}$ white dwarf (from Eq. 4.10). The three lines correspond to different asteroid semi-major axes, and the tidal disruption is assumed to occur at the orbit's pericentre. 105

4.6 Collision-less mass accretion rates of asteroid fragments via PR drag onto a 0.6 $M_{\odot}$ white dwarf. The top panel (a) shows how the accretion rate varies with the size distribution (different colours) and orbital separation (line style). The lower panel (b) indicates what fragments reach the star via PR drag after a certain time ($t_{\rm acc}$). Accretion starts with the smallest bound fragments $R_{\rm blow}$, as bigger fragments take longer to circularize. The curves flatten over time due to the declining luminosity of the cooling star (Eq. 4.14), meaning that fragments larger than $1-10$ cm cannot be accreted via PR drag alone. 107

4.7 Peak collision-less accretion rates via PR drag onto a warm (10^4 K) 0.6 $M_{\odot}$ white dwarf as a function of asteroid radius and fragment size distribution. The solid and (dashed) lines correspond to asteroid semi-major axes of 3 and (10 AU). Explaining observed implied accretion rates beyond 10^9 g/s (Farihi et al., 2012) by PR drag alone requires large asteroids ($R_{\rm ast} > 500$ km) to break up into a steep fragment size distribution ($\alpha > 3.6$). 108

4.8 Differential apsidal precession of fragment orbits from a 100 km asteroid originating from 3 AU. The orbits do not cross at $t = 0$ (panel a) but angular differences increase as a function of time, and at 0.1 Myr (panel b) the orbits cross at both pericentre and apocentre. At 1 Myr (panel c), both the relative angles and collision velocities have grown further, and the collision locations are spread out over a wider range in space. 111

4.9 Continued scattering of fragments that cross the chaotic zone of a planet ($M_{\rm pl} = 10\ {\rm M}_{\oplus}$) that resides at the apocentre of a scattered asteroid. This figure depicts the eccentric tidal disc, dividing the fragments between those that are likely to be directly re-scattered by the planet (red) and those that now lie outside the planet's chaotic zone (green). The top panel (a) shows that most fragments from a 50 km asteroid from 3 AU are susceptible to scattering (fraction $f_{\rm cross}$). Fragments from a larger 500 km asteroid that originates from 30 AU (panel b) are spread bimodally (see Sect. 4.2) and are mostly safe from further scattering. 113

4.10 Time evolution of the collision rate ($\dot{M}_{\rm col}$) from our model of eccentric collisional grind-down induced by differential apsidal precession (see text for details). In the top panel (a), we take asteroids from 10 AU and vary their size between 50-500 km. In the bottom panel (b), we take 100 km asteroids and vary their initial semi-major axis between 3-30 AU. The open and filled dots indicate the points where a total of 50% and 90% of the fragment mass has catastrophically collided, respectively. Larger asteroids on tighter orbits disrupt to form tidal discs whose fragments collide within the shortest period of time. 116

4.11 Timescales for the collisional grind-down of fragments in eccentric tidal discs ($t_{\rm col}$), calculated with our numerical model based on differential apsidal precession (see text for details). The grind-down timescale is defined as the time required for half of the mass to catastrophically collide. Fragments within tidal discs that form from large asteroid progenitors on tight orbits grind down within the shortest period of time. 119

4.12 Cumulative time when the rate of dust production from collisional grind-down lies above a certain rate $t(\dot{M}_{\rm col} > \dot{M}_{\rm x})$. The values correspond to calculations with our collisional model (see text for details). Larger asteroids produce more fragments, leading to more rapid grind-down and higher peak collision rates. Asteroids that originate from the inner zone of planetary systems (solid lines, 3 AU) generate higher peak collision rates compared to those on wider orbits (dashed lines, 10 AU) but they spend less time accreting at more moderate rates, making their pollution less likely to be observed if the subsequent accretion of small dust is sufficiently rapid. 121

4.13 Simulated emission per unit surface area at 10 μm from fragments accreting onto G29-38 (0.59 $M_\odot$, 11240 K, 17.5 pc) via collision-less PR drag, computed assuming optically thin properties (See Sect. 4.3.1 and Sect. 4.6.2 for details on PR drag and this emission). The three panels correspond to snapshots at different times after the tidal disruption event of an asteroid from 3 AU, and the colours are normalized individually per panel. Just after the tidal disruption event (a), the fragments are still highly eccentric, and their emission is minimal. The smallest fragments accrete just after 1900 yr (b), when their more contracted orbits begin to generate far more emission. The final panel corresponds to 10^5 yr, when all fragments smaller than 100 μm have already reached the star. The disc contains an elliptical inner gap because fragments are not yet fully circularized when they enter the sublimation distance (white dashed circle). The Roche radius is indicated with a red dotted circle, just outside the sublimation zone. 123

4.14 Simulated emission spectra from a 750 km asteroid disruption around G29-38 computed by our model (see text), followed by collision-less and optically thin orbital contraction via PR drag. The dotted line indicates the contribution from the star, with the dash-dotted ($t = 0$), dashed ($t = 1900$ yr) and solid ($t = 10^5$ yr) lines including the emission from the fragments at different times. The points indicate the emission from the system as observed in several surveys (largely compiled by Farihi et al. (2014), original references in the text). 124

4.15 Simulated emission per unit surface area at 10 μm from constant dust production and accretion at a rate of 10^7 g/s via PR drag, computed assuming optically thin properties. The top panel (a) shows the resulting emission without apsidal precession, and the bottom panel (b) shows the axisymmetrically averaged emission. The disc contains an elliptical inner gap because fragments are not yet fully circularized when they enter the sublimation zone (white dashed circle). The Roche radius is indicated with a red dotted circle, just outside the sublimation zone. Axisymmetrically averaged, the structure becomes visible as a ring-like structure mostly contained within the Roche radius. 127

4.16 Simulated emission spectra of G29-38, with dust accretion via PR drag at three different rates. The dotted line indicates the contribution from the star, with the dash-dotted (10^7 g/s), dashed (10^8 g/s) and solid (10^9 g/s) lines including the emission from circularizing dust at different accretion rates. The points indicate the observed emission from the system in several surveys (largely compiled by Farihi et al. (2014), original references in the text). . . 128

4.17 Road-map outlining potential routes for planetary material to arrive in the atmospheres of white dwarfs. Our suggested main route (red arrows and boxes) begins with the injection of an asteroid into the stellar Roche radius, followed by a tidal disruption event, orbital perturbations, collisional grind-down, and finally dust accretion. Alternative accretion channels are shown in purple, with physical selection criteria at five numbered points. The detectable characteristics of these different accretion channels are listed in green, provided that they are sufficiently well-constrained. 132

5.1 Schematic overview of how the asynchronous accretion of a differentiated asteroid onto a white dwarf can mimic the photospheric signature of either a core- or mantle-rich object. In this simplified scenario, a differentiated asteroid tidally disrupts into fragments composed of core or mantle material. Mantle fragments are preferentially ejected out of the system in greater proportions, and bound core and mantle fragments occupy distinct orbital zones in the tidal disc (Section 5.2). Core fragments collide or scatter sooner on average, leading to a core-rich early accretion phase, followed by a mantle-rich late accretion phase (Section 5.3). The form of this figure was inspired by the conceptually similar Fig. 1 of Buchan et al. (2022). An accompanying version of this figure that details asynchronous ice-refractory accretion is presented in chapter 6. 140

5.2 Distribution of core and mantle fragments after the tidal disruption of a differentiated asteroid from 10 AU around a white dwarf. The top panels provide a top-down view of the tidal disc, and show that core (black) and mantle (brown) fragments are spread to distinct, but partially overlapping orbital ranges. The histogram plots in the lower panels show the distribution of material in more detail. The solid red line indicates the core mass fraction (CMF) at a given orbit, which can be compared to the 30% CMF of the asteroid progenitor (red dotted line). The innermost orbits of the tidal disc always contain exclusively mantle material, while the outer orbits are enhanced in core material if the asteroid was large (right panels), and depleted otherwise (left and middle panels). 141

5.3 Enhancement in bound core mass fraction ($\delta CMF_{\rm disc} = (CMF_{\rm disc} - CMF_{\rm ast})\,/CMF_{\rm ast}$, colours) of tidal discs compared to their asteroid progenitors. Three regimes can be identified. Both sufficiently small asteroids and large planetary bodies disrupt into discs with unaltered core mass fractions, as either half or none of their mass is ejected. In between, larger asteroids and dwarf planets eject primarily crustal and mantle material when they disrupt, resulting in a more core-rich tidal disc. 144

5.4 The rate at which mass is lost due to collisions from the tidal disc, a proxy for the accretion rate onto polluted white dwarfs, calculated according to scenario I. The lines correspond to either a differentiated 50 km (dotted), 120 km (dashed) or 300 km (solid) asteroid, with semi-major axes at 10 AU and a 30% core mass fraction (red line). The points indicate when half of the pollutant's mass has been accreted. In panel (a), the total collision rate first increases as fragment orbits begin to cross, and then decreases when the disc becomes depleted. In panel (b), the core mass fraction of the colliding material is shown to vary over time, leading to the asynchronous accretion of core and mantle components. 146

5.5 Scattering asymmetry of core and mantle fragments by a 10 $M_\oplus$ planet. In the top panels (a,b), the orbit of the planet and its chaotic zone are indicated by the red band. The red particles are susceptible to getting scattered, while brown (mantle) and black (core) particles are safe. On average, core fragments are more likely to be scattered by a planet, and the difference is greatest for larger asteroids and dwarf planets from the outer disc. 149

5.6 Photospheric abundances of calcium and iron in our white dwarf sample. The colours indicate the diffusion timescale of iron in the white dwarf atmospheres, computed with models by Koester et al. (2020). Lines of constant abundance ratios relative to iron are overplotted. 151
5.7 Cumulative distribution of steady-state accretion rates (Eq. 5.9) of iron relative to calcium, showing that white dwarf polluting material is iron-rich. The magenta curve corresponds to bulk white dwarf pollutant compositions (white dwarfs with $\tau_{\mathrm{Fe}} >$ Myr), while the black curve corresponds to abundances of nearby FGK stars (Brewer et al., 2016). The dotted lines indicate reported values, and the solid lines are built from a sampling with white dwarf measurement errors. 153

6.1 Schematic overview of how the asynchronous accretion of an ice-rich comet onto a white dwarf can appear either volatile-rich or dry, depending on when the system is observed. Left panel: an undifferentiated comet tidally disrupts, producing wet fragments. If these fragments dry out before they collide, a short water-rich accretion phase is followed by a longer, dry accretion phase. Right panel: an ice-rock differentiated comet tidally disrupts, producing both icy and dry fragments. The icy fragments are ejected in greater proportions (see chapter 5). The bound ice rapidly sublimates - before most fragments catastrophically collide and accrete, again leading to a short, volatile-rich early accretion phase and a longer, dry, second accretion phase. An accompanying version of this figure that details asynchronous core-mantle accretion is shown in chapter 5. 160
6.2 Numerically calculated timescales for the sublimative erosion of large, km-sized fragments (solid lines), compared to the energy-limited approximation (dashed lines, Eq. 6.4c). Fragments composed of water ice (blue) sublimate efficiently within $10^4 - 10^6$ yr around warm stars, and the two curves largely overlap. Fragments composed of refractory species like forsterite (brown) and iron (black) only begin to sublimate around the hottest white dwarfs, and re-radiate most of the incident stellar flux back to space, causing a divergence from the energy-limited curves. 164

6.3 Evolution of elemental abundances (black, left axis) and the implied water mass fraction (blue, right axis) when white dwarfs with hydrogen-dominated atmospheres accrete a comet with 20% ice. In this model, ice accretes at a constant rate until $t_{\rm sub}$ (Eq. 6.4c), and dry rocks accrete in 1 Myr. The water fraction implied by assuming steady state accretion appears discontinuous at $t_{\rm sub}$ due to the short diffusion timescales (days here, from Koester et al. (2020) with $\log(g) = 8$). The real bulk water content of the object (blue dotted curve) only matches the implied value if $t_{\rm sub} >= t_{\rm acc}$ yr, as is the case in panel c, at 10,000 K. 167

6.4 Same calculation as shown in Fig. 6.3, repeated for stars with helium-dominated atmospheres. The squares indicate the sinking timescales of oxygen, while the brown and blue areas indicate the accretion zones of ice and dry rocks, respectively. The implied water content peaks highest for hot stars and is highly dependent on the accretion state, with it increasing further when accretion has stopped and elements sink downwards (declining state). 168

6.5 Oxygen excesses of white dwarfs in our sample (star; hydrogen-dominated, square; helium-dominated), compared with Solar System bodies (Mercury: Hauck et al. 2013; Nittler et al. 2018, Earth: McDonough 2003, Vesta: Steenstra et al. 2016, CI chondrites & Solar photosphere Lodders 2003, FGK stars (grey band; Brewer et al. 2016)). The three blue points signal white dwarfs with significant ($\geq 2\sigma$) oxygen excesses in the default, state-corrected calculation (see Section 6.4.2). These labelled systems are 1: WD1425+540, 2: GALEXJ2339, and 3: WD1232+563. 174

6.6 Comparison of oxygen-rich pollutants ($\geq 2\sigma$, blue) to a sample of nearby FGK stars (grey band, Brewer et al. 2016), plotted relative to oxygen, relative to the Solar ratio. Filled markers represent measured abundances (square; WD1425+540, triangle; GALEXJ2339, circle; WD1232+563), while open markers are any non-measured abundances, inferred by `PyllutedWD`. . . . 174

A.1 Dependence of the prograde spin-up over time on numerical parameters. Top: variation of the filling factor of the simulation box between $10^{-4} \leq f \leq 10^{-1}$. The runs correspond to $N_{\rm n} = 5000$ numerical particles and are run at 5 AU. Bottom: variation of the number of numerical particles $10^3 \leq N_{\rm n} \leq 10^4$, computed with a filling factor of $f = 10^{-3}$. The magnitude of prograde spin-up is found to be insensitive to these numerical parameters. 192

A.2 Quiver plot of initial velocities in the co-moving frame for three setups used in this paper. While our simulations use spherical clouds, this plot shows their cross sections at z=0. The arrow sizes correspond to the magnitude of the particle velocities and the colors correspond to the rotational contribution (from Eq. A.2c). The left panel (a) indicates the Keplerian setup (A.3), which yields a total prograde rotation equal to $L_{\rm rot} \simeq 0.1 M_{\rm cl} \omega_0 R_{\rm cl}^2$. The middle panel (b) corresponds to the zero-rotation initial condition (Eq. A.4), while the right panel (c) corresponds to uniform rotation with the same initial rotational angular momentum as the Keplerian setup. 193

A.3 Overview of the collapse of a uniform cloud in orbit around a central mass (same as Fig. 2.5), shown in a co-moving frame. The spherical cloud is initiated with size $R_{\rm H}$ and without any rotation. The central mass is located left from the cloud. The velocity directions (magnitudes not to scale) and trajectory of the particles are highlighted for an interior and exterior particle that both wrap around the centre-of-mass in a prograde fashion. 196

B.1 Pebble growth tracks (a), their resulting pebble opacity (b), and produced dust opacity (c) for a standard set of model runs at 5 AU (see Table 3.1). This figure is the same as Fig. 3.4, but now the mass is fixed at the default 5 $M_\oplus$ and the limiting velocity (Eq. 3.13) is varied a logarithmically between $0.4 - 40$ m/s. 200

C.1 Snapshots indicating the spreading of fragments in a tidal disc after the disruption of a small asteroid ($a_{\rm ast} = 3$ AU, $R_{\rm ast} = 1$ km). The inner and outer fragments re-align after nearly precisely one spreading timescale, as defined by Eq. C.7b. 203

C.2 Top: model spectrum of WD J0914+191, generated with the model of Koester et al. (2020). Bottom: force ratio of the radiation pressure on atoms and ions around SDSS J0914+1914, relative to gravity. The radiation pressures are calculated at the strongest line for a given state, as compiled by Verner et al. (1994). Neutral hydrogen can experience intense radiation pressure relative to stellar gravity ($\beta \gg 1$), but the radiation pressures on C, Ca, and Mg atoms also exceed unity. Only helium feels a negligible radiation pressure relative to the gravitational force of the star. 207

C.3 Posterior distribution of the accretion states in our runs with `PyllutedWD`, ordered by their diffusion timescales (short-long). The histograms for the build-up and declining states share the same scaling on their x-axis from 0 to 3 oxygen diffusion timescales. The histograms of steady-state accretion in the middle panels have a custom x-scale, depending on the modelled length of the accretion event ($t_{\rm acc}$). The blue labels indicate systems with a significant oxygen excess above 2σ. 210

C.4 Posterior distribution of the oxygen excess in our runs with `PyllutedWD`, ordered by their diffusion timescales (short-long). The blue histograms and labels indicate systems with a significant (2σ) oxygen excess. No systems were found to be reduced in oxygen with the same threshold for significance. 211

List of tables

3.1 Descriptions and values of the default model parameters. 68

6.1 Mechanical and thermal properties of forsterite (Mg_2SiO_4), iron (Fe), and crystalline water ice (H_2O). 163
6.2 All 9 white dwarfs with previously suggested oxygen excesses. The state-corrected calculation accounts for the likelihood distribution of different accretion states (see Section 6.4.2). For systems in blue, we find oxygen excesses with $\geq 2\sigma$ significance with this state-corrected calculation. No new systems with significant oxygen excesses were found. 170

C.1 Properties and abundances of white dwarfs in the sample for chapter 5, ordered by type and effective temperature 212
C.2 Properties of white dwarfs used in our sample for chapter 6, ordered by their oxygen diffusion timescales (short to long) 218
C.3 Abundances of white dwarfs used in our sample for chapter 6. 219

Chapter 1

Introduction

"Here is a commandment for you: seek happiness in sorrow. Work, work tirelessly."
- Fyodor Dostoevsky, The Brothers Karamazov, 1880

The study of planetary astronomy has ancient roots that stretch back long before the invention of modern science. As early as the 17th century BC[1], the rising and setting of Venus was documented in the Babylonian tablet of Ammisaduqa (Koch-Westenholz, 1995), although the physical interpretation of a different planet orbiting the sun would not be understood for over three millennia (Evans, 1998). By the 7th century BC, Mesopotamian astronomy had progressed sufficiently that tablets are found with the diaries for six out of the eight Solar System planets (Sachs, 1974), along with the weather conditions during which the observations were taken. Further observational progress would need to wait more than two millennia, until the development of telescopes in Europe. The next definite sighting of a planet, Uranus, was only performed in 1690 (Wright, 1987), when it was initially mistaken for a star. By 1781, the development of more advanced reflecting telescopes allowed it to be re-characterized, first as a comet, and finally correctly as the seventh planet (Miner, 1990). The discovery of Neptune would wait another 65 years, until the development of more accurate perturbation theory, ultimately completing the list of Solar System planets in 1846 (Airy, 1846; Galle, 1846).

The search for ever more planets has only accelerated since then, and in 1992, the discovery of two planets orbiting around a pulsar provided the first definite proof of an extra-solar remnant planetary system (Wolszczan & Frail, 1992). Soon, this discovery was followed by the detection of 51 Pegasi b, the first exoplanet to be found orbiting around a main-sequence star (Mayor & Queloz, 1995). This now-famous exoplanet is around half as

[1]The tablet of Ammisaduqa itself dates to the 7th century BC, but it is a copy of an original that is thought to date to the second millennium BC, to the reign of king Ammisaduqa (Koch-Westenholz, 1995).

massive as Jupiter, but orbits at nearly 1/100th of its orbital distance, producing a strong, oscillating radial force on the host star. The periodic radial velocity that this induces, was used to infer the orbit of the planet, and the same method has now been used to identify over 1000 exoplanets, most of them also heavy and close to their host star (exoplanet.eu, 2023). Additionally, large-scale surveys like Kepler and TESS have looked for exoplanets by studying the partial occultation of stars via planetary transits (Borucki et al., 2010; Howell et al., 2014; Ricker et al., 2015). This method has proven to be extremely successful, yielding nearly 4000 exoplanets to date (exoplanet.eu, 2023). Some exoplanets have also been found on wider orbits, often via the analysis of gravitational lenses, where a planet's gravity slightly perturbs the lens created by the host star (Mao & Paczynski, 1991; Yang et al., 2022). Possibly most exciting, a number of planets have even been detected directly via their thermal emission or scattered light, despite the huge contrast ratio between planets and host stars (Jung et al., 2022; Marois et al., 2008). In total, 5313 planets are known to exist at the time of writing this thesis (exoplanet.eu, 2023), with upcoming missions like PLATO expected to significantly add to this number (Heras et al., 2020; Rauer et al., 2014). Future investigations are also expected to find planets around younger stars, which are more variable, ultimately promising to provide an observational basis for planetary evolution through time (Zhou et al., 2022).

The great expansion of known planets and their ever-improved characterization has also motivated an intense theoretical effort over the last two decades to explain the wide array of observed planetary characteristics. Specialized fields of study have sprung up to investigate the orbital evolution of planets and their satellites, their compositions and internal thermodynamics, their birth environments, and the structure of planetary systems as a whole. Many of these new developments have been aided substantially by the improvements in computing power that has become readily available to researchers. In this thesis, I add to this drive, and present ideas relating to the formation and destruction of planets. The first idea (chapter 2) relates to the formation of planetesimals, large rocks that are plausible planetary building blocks. The second part of the thesis is focused on the subsequent growth stage (chapter 3), and the final part of the thesis takes place at the end of a planet's life (chapters 4,5,6). In order to provide context around the work presented in these chapters, and to introduce the research questions, I begin by presenting a brief, chronological overview of the current state of knowledge on planetary formation and evolution. Rather than to attempt a comprehensive review of planetary astronomy, I focus specifically on the planetary life stages and processes that feature in this thesis. For each topic that is discussed here, additional background information and motivation is also presented at the start of the relevant chapter.

1.1 The early stages of star and planet formation

1.1.1 Proto-planetary discs

Stars in our galaxy form out of the dust and gas contained in molecular cloud cores; dense regions within the cool molecular clouds. The majority of stars form as part of stellar clusters containing hundreds to thousands of stars, with the individual stars often also part of binary or multiple systems, especially when they are heavy (Lee et al., 2012; Lee & Hennebelle, 2016b; McKee & Ostriker, 2007; Offner et al., 2022). Molecular cloud cores themselves are not dynamically homogeneous, and contain density and velocity fluctuations due to the presence of turbulence and structural rotation (Larson, 1981). Whenever a star forms in a self-gravitating infall of dust and gas, these inhomogeneities result in a non-zero angular momentum, whose direction usually aligns with that of the stellar cluster if the cloud core had a substantial rotational component, and is random if turbulence dominates (Corsaro et al., 2017; Lee & Hennebelle, 2016a). The angular momentum of the dust and gas is too high for everything to accrete directly onto the star, and some of the dust and gas settles into a plane around the star, known as a protoplanetary disc.

As a protostar evolves on its way to the main sequence, it accretes mass from the surrounding disc, and it goes through different structural phases. The initial embedded class 0/I phases are relatively short, lasting less than 0.5 Myr (Dauphas & Chaussidon, 2011; Evans et al., 2009). When the system reaches the class II phase, the disc appears fully formed, and emits a characteristic, shallow IR excess. Protoplanetary discs can endure for long periods of time, with median lifetimes estimated around 5-10 Myr (Pfalzner et al., 2022), but disc lifetimes tend to be shorter around more massive stars. The observed mass distribution of class II discs indicates that they likely contain insufficient dust mass to explain the observed distribution of giant planets (Tobin et al., 2020; Tychoniec et al., 2020). Based on this, it has been suggested that the planet formation process, where dust surface area is gradually lost, likely already starts early, in the embedded class 0/I phases (Cridland et al., 2022).

With the improvement in resolving power made possible by ALMA, it has also become clear that proto-planetary discs also show a remarkable degree of sub-structure (Benisty et al., 2022). This substructure was first seen in the form of multiple sets of concentric bright rings around the young star HL Tau (ALMA Partnership et al., 2015), but has since been observed around 73 of the 355 known protoplanetary discs (Bae et al., 2022). For the subsample of discs that are observed at high angular resolution (more than 10 angular bins per disc), the fraction of systems with substructure increase to 95% (Bae et al., 2022). It has been suggested that these substructures are caused by the formation of massive planets (Zhu, 2019), in which case giant planets must commonly form on wide orbits between 10-500 AU.

While there is currently little supporting observational evidence of the existence of such a population, previous observational surveys have not been sensitive to such wide orbits and young stars. Alternatively, if wide-orbit giant planets are indeed rare, migration onto closer orbits could potentially reconcile the old and young populations (Lodato et al., 2019).

1.1.2 Dynamics and growth of solid particles

Within proto-planetary discs, the planets form out of an environment that initially contains between 90-99% gas (mostly H_2 and He), and 1-10% more refractory dust (Kama et al., 2020). In the standard theory of core accretion (Pollack et al., 1996), the first stages of planet formation begin with the agglomeration of dust grains into larger structures. Laboratory experiments have shown that slow collisions between grains with relative velocities below a few m/s indeed cause small particles to stick together (Blum, 2018; Gundlach & Blum, 2015; Musiolik & Wurm, 2019), making this process feasible.

Gas molecules orbiting a central star are partially supported by gas pressure, which increases towards the star, causing the gas to move at sub-Keplerian velocities. As a result, gas drag slows down the orbits of dust particles, which move closer to Keplerian speeds, causing them to spiral inward. There are two regimes to consider in calculating the gas drag felt by disc particles. In the Epstein regime, applicable to small grains whose size is less than the mean-free path of gas molecules in the disc, gas drag scales proportionally to the particle size. In the Stokes regime for larger particles, the gas around the particles behaves like a fluid, and the drag force scales quadratically with the particle cross-section. Relative velocities induced by gas drag and turbulence can periodically fragment the dust grains via collisions, or cause particles to bounce rather than stick, limiting their sizes to centimetre to decimetre-sizes, depending on the internal strength (Drazkowska et al., 2022).

Also, problematically, gas drag begins to effectively drain orbital angular momentum when solids grow to centimetre to metre-sized bodies, causing them to quickly spiral inward. At this stage, in between planetesimal-sized and dust-sized, the so-called *pebbles* both feel a strong azumuthal drag (as opposed to well-coupled grains), and are still small enough to be slowed down by it. Together with the aforementioned fragmentation barrier, this drift barrier prevents growth beyond metre-sized objects, making the formation of planetesimals by continuous growth difficult. One potential solution to the drift and fragmentation barriers, is to suppose that grains maintain a high degree of porosity during their initial growth stages. Porous dust conglomerates are suggested to have far more efficient sticking properties (Okuzumi et al., 2012), and have increased cross-sections, making growth faster. However, even these features may not be sufficient to overcome the fragmentation and drift barriers

(Estrada et al., 2022), and porous particles are additionally sensitive to erosion by the small grains encountered in the disc (Schräpler et al., 2018).

1.1.3 Planetesimal formation via gravitational collapse

One way in which the fragmentation and drift barriers can be overcome, is for large planetesimals to form directly out of clouds of smaller dust grains, bypassing the intermediate growth stages entirely. The first suggestions for such a mechanism were proposed by Safronov (1969) in Soviet literature, and independently by Goldreich & Ward (1973) in Western literature. In this initial version of the theory, planetesimals were thought to form out of a thin layer of solids, created by efficient settling. It is now known that the formation of a sufficiently thin layer is likely impossible due to the Kelvin-Helmholtz instability, which is triggered by the higher velocity of the dusty mid-layer relative to the gas above and below, producing vertical motion that reduces the concentration of solids in the mid-layer (Youdin & Shu, 2002).

Modern planetesimal formation theories exploit this interaction between solids and gas to their advantage, making a gravitational collapse possible in certain circumstances. A popular example is the streaming instability, first suggested by Youdin & Goodman (2005). In the simplest version of this theory, dust is treated like a pressureless fluid that slowly drifts inwards, without feeling vertical stellar gravity or any self-gravity. Due to aerodynamic interactions between the dust and gas, the system exhibits growing instabilities, that lead to dust concentrations with sufficient density to gravitationally collapse (Johansen et al., 2014). In newer simulations, the instability is modelled with many different particle species (known as the polydisperse streaming instability), which is known to reduce the efficiency of the mechanism (Krapp et al., 2019; Lyra et al., 2023; Paardekooper et al., 2020, 2021), but likely does not prevent it entirely (Zhu & Yang, 2021).

In addition to the streaming instability, a number of other instabilities could be responsible for the formation of planetesimals (see Lesur et al. (2022) for a recent review). One possibility that intersects with the observation of disc substructure discussed in Sect. 1.1.1 is the clumping of particles in so-called pressure bumps. Planets are known to be able to perturb the disc, locally inverting the pressure gradient to be decreasing towards the star (Dullemond et al., 2018). This makes the gas orbit super-Keplerian in a pressure bump, reversing the drift process discussed in the last subsection. This in turn leads to grains oscillating within the pressure bump, causing a build-up of density that is prone to collapse (Carrera et al., 2021; Pinilla & Youdin, 2017). Alternatively, the increased sticking efficiency of icy grains may lead to a pile-up of pebbles just outside the snow-line, triggering planetesimal formation in a small radial region (Drążkowska & Alibert, 2017; Schoonenberg et al., 2019; Schoonenberg & Ormel, 2017). The driver of this pile-up is the larger size of icy grains, which quickly drift

inwards until they reach the ice line. It is currently not clear which exact collapse mechanism is dominant in the formation of planetesimals (Lesur et al., 2022).

1.1.4 Rotation of planetesimals and binaries

In addition to the theoretical arguments mentioned previously, the formation of planetesimals via gravitational collapse also seems consistent with two distinct characteristics of planetesimals in the Solar System. First, observational studies of the Kuiper belt have shown that most dynamically cold asteroids are part of binaries (Fraser et al., 2017; Grundy et al., 2019), which show strong colour correlations (Benecchi et al., 2009, 2011; Marsset et al., 2020), meaning they likely share the same composition. Second, it seems that the spins of asteroids and the binaries in which they are found are not random, and still contain a trace of their formation histories. In particular, the most dynamically pristine subset of binaries, the so-called Cold Classicals in the Kuiper belt, have binary orbits that are preferentially in the prograde direction - aligned with their orbit around the Sun (Grundy et al., 2019). Many of these binaries have mass ratios near unity, and contain substantial amounts of angular momentum, consistent with the collapse of a cloud similar in size to its Hill sphere (Robinson et al., 2020). Most strikingly, hydrodynamical simulations of the streaming instability show a remarkable agreement with the observed prograde-leaning spin distribution of these binaries (Nesvorný et al., 2021, 2019). So far, it is not clear, however, what physically causes this prograde bias to appear, or whether it is unique to the streaming instability. In Chapter 2, I will explore the underlying reasons for why gravitational collapses produce asteroids with prograde rotation.

1.2 From planetesimals to planets

1.2.1 Collisional growth and traditional models

The current resolution of streaming instability simulations is not yet sufficient to resolve physical sizes, but expected sizes for freshly formed planetesimals range up to 100s of km (Liu & Ji, 2020), with most of the mass contained in the more massive bodies (Rucska & Wadsley, 2021; Simon et al., 2016, 2017). At this point, planetesimals are no longer sensitive to gas drag, but they must still grow by several orders of magnitude to become planet-sized. For planetesimals smaller than about 600 km, the main growth mechanism is the collisional merging with other planetesimals within their feeding zone (Ormel & Klahr, 2010), a process that is enhanced by gravitational focussing (Lissauer & Stewart, 1993; Safronov, 1972). however, when planetesimals grow larger than about 600 km, they begin to dynamically

stir the orbits of nearby bodies, reducing their accretion efficiency (Ormel & Klahr, 2010). At this stage, known as the oligarchic phase, the growth rate of planetesimals slows down, scaling as $\dot{M} \propto M^{2/3}$ rather than as $\dot{M} \propto M^{4/3}$ in the early growth phase (Drazkowska et al., 2022)). In the outer protoplanetary disc, the growth rate expected from planetesimal mergers is likely prohibitively slow to form planet-sized objects. In the Solar System, this poses a particularly severe problem for the formation of Uranus and Neptune, which have acquired masses around 15 $M_\oplus$ at orbits as wide as 30 AU.

1.2.2 Planetary growth via pebble accretion

To solve the problem of slow planetary growth, researchers have looked for mechanisms via which growth timescales can be reduced. In modern planet formation models, the growth rate of planetesimals and planets is significantly enhanced by the accretion of drifting pebbles. While collisions between planetesimals are purely driven by gravity, pebbles are affected by gas drag with the protoplanetary disc during the encounter, slowing the pebbles down, at which point they can fall onto a planet or planetesimal (Lambrechts & Johansen, 2012; Ormel & Klahr, 2010). The accretion rate from pebble accretion is determined by the product of the radial flux of pebbles and the accretion efficiency. This efficiency parameter can reach around 10% for Earth-mass planets, scaling proportionally with the planet mass in the 3D regime, and less steeply in the 2D regime of efficiently settled pebbles ($\dot{M}/M \propto M^{-1/2}$ or $M^{-1/3}$ (Liu & Ormel, 2018; Ormel & Liu, 2018). When a planet grows to around 25 $M_\oplus$, it can perturb the disc sufficiently to locally invert the pressure gradient, stopping the accretion of pebbles entirely (Ataiee et al., 2018; Bitsch et al., 2018; Lambrechts et al., 2014; Liu et al., 2019).

Because pebbles are much smaller than planetesimals, their composition can quickly be altered when exposed to high temperatures. This property of pebbles has two important implications. First, pebbles are expected to sublimate any ice contained in their interior when they cross an ice line in the proto-planetary disc (Morbidelli et al., 2015; Schoonenberg & Ormel, 2017). Second, pebbles are also prone to sublimation during their accretion onto planets, where they have to pass through dense and hot atmospheres. In the first models to account for this, the expectation was that only ices would sublimate during the accretion process (Venturini et al., 2016, 2015). However, since the temperature of planetary envelopes can easily exceed several thousand Kelvin, refractory pebble components are equally susceptible to ablation (Alibert, 2017). As a result, planets that grow via pebble accretion likely form with envelope structures more complex than a central heavy core, surrounded by just hydrogen and helium(Brouwers & Ormel, 2020; Brouwers et al., 2018; Ikoma & Hori, 2012), and their interiors likely contain a compositional gradient (Ormel et al., 2021). This paradigm of pebble accretion is consistent with what the *Galileo* and

Juno missions have taught us about Jupiter, whose heavy elements are distributed broadly through its envelope (Debras & Chabrier, 2019). Further thermodynamic consequences of pebble accretion include increased interior temperatures and thermal reservoirs, as well as substantially delayed cooling (Bodenheimer et al., 2018; Ormel et al., 2021).

1.2.3 Gas accretion & giant planet formation

While planetesimals and small planets are exclusively composed of refractory materials and ices, larger planets also accrete hydrogen and helium from the protoplanetary disc during their formation. While in the proto-planetary disc, gas accretion begins at the characteristic Bondi mass, when the planet's escape velocity exceeds the thermal velocity of the gas. The envelope that forms around a planet can be modelled by solving the stellar structure equations without nuclear reactions (Pollack et al., 1996). As a planet gains mass, the envelope expands and compresses, with more nebular gas flowing in. Gas accretion also occurs without the further accretion of solids, as the planet's envelope cools and contracts, making space for more gas (Lambrechts & Lega, 2017; Lee & Chiang, 2015). When the mass of hydrogen and helium in the envelope becomes comparable to the accreted mass of heavier elements, the envelope begins to collapse, triggering runaway gas accretion, and the formation of a giant planet (Ormel et al., 2021).

The cooling timescale of an envelope is defined by its thermal reservoir and by its opacity, which determines how quickly heat can be lost. This opacity is, therefore, a key variable that needs to be constrained to know how much gas a forming planet accretes. Some previous studies have looked in detail at the opacity from grains in planetary envelopes (Movshovitz et al., 2010; Movshovitz & Podolak, 2008; Podolak, 2003), but only focused on the special case of Jupiter. They found that grains quickly coagulate, and that envelope opacities tend to be low. Simpler analytical (Mordasini, 2014) and numerical (Ormel, 2014) models with a single characteristic grain size at a given height have been able to replicate this main result, but it is unclear to what planets this generalizes. In Chapter 3, we build a new model for the opacity of solids, and apply the model across a wide parameter space to explore and map out the resulting opacity as a function of distance, planet mass and accretion rate.

Alternatively, it is also possible that some giant planets directly form via the gravitational collapse of a portion of the disc (Boss, 1998, 2021). These collapses are on a larger scale than those in the streaming instability, and involve both the gas and dust components. If this channel of planet formation via gravitational collapse indeed operates, it is expected to form planets more massive than Jupiter, and only in the cooler areas of massive discs (Deng et al., 2017). This characteristic of the gravitational instability, that it operates in the cooler regions

of discs, makes it an interesting complementary channel to that of gradual planet growth (also known as core accretion), whose growth timescale increases with the orbital time.

Mass-loss from planetary envelopes

While giant planets keep most of their hydrogen and helium during their lifetime, smaller planets can lose these components when the protoplanetary disc dissipates. Two mechanisms have been suggested as the main driver of H/He mass-loss. The first is EUV/X-ray photoevaporation (Lopez & Fortney, 2013; Owen, 2019; Owen & Wu, 2017), where the energy source is a flux of high-energy photons from the host star. Because the flux of high-energy photons decreases over time, photoevaporation is predicted to be most efficient in the first $\sim$ 100 Myr after the disc dissipates (Rogers et al., 2021). The second suggested channel for H/He loss is known as core-powered mass-loss (Ginzburg et al., 2018; Gupta et al., 2022; Gupta & Schlichting, 2018). In this model, the energy source driving the mass-loss is a combination of stellar luminosity and the internal heat of the planet. A potential caveat for the latter theory is that it has yet to be evaluated on envelopes more complex than analytically constructed, pure H/He atmospheres. Since core-powered mass-loss operates on Gyr timescales, the two scenarios could potentially be distinguished by comparing populations of young exoplanets when this data becomes available (Rogers et al., 2021), and work in this direction is ongoing with THYME: the TESS Hunt for Young and Maturing Exoplanets (Mann et al., 2020).

1.3 The observed exoplanet population

The planet formation process described above ultimately produces a population of exoplanets, only a portion of which can be observed with current instrumentation. Bias-corrected estimates rates predict that planets are more common than the stars they orbit, with occurrence rates around 140-200 % (Hsu et al., 2019; Mulders et al., 2019; Zhu & Yang, 2021). Exoplanets are often categorized by their properties relative to those found in the Solar System. The smallest planets with radii $\lesssim 1.25 R_\oplus$ are certainly too small to bind primordial atmospheres, but are not typically referred to with a distinct term. Planets with radii between $R_\oplus \lesssim R \lesssim 2R_\oplus$ are often referred to as super-Earths, and are likely still rocky or icy in composition. Planets more similar in size to Neptune are also observed, but not yet on orbits as wide as the Solar System's ice giants. Such planets are often referred to as warm Neptunes. Giant planets are usually split in terminology between hot and cold Jupiters, referring to orbits shorter than $\sim$ 10 days, or longer than $\sim$ 100 days, respectively. A small population of warm Jupiters with orbits within this range has also been found.

1.3.1 Low-mass planets

In the population of exoplanets that have currently been observed, smaller planets like super-Earths and warm Neptunes dominate the occurrence rates. These types of planets are commonly found across various stellar types, and around 30 % of solar-type stars are orbited by at least one super-Earth (Zhu et al., 2018). Comparing between different stellar types, however, makes clear that their occurrence rates increase significantly when the stellar mass is reduced (Howard et al., 2012; Mulders, 2018; Sabotta et al., 2021). For M-dwarfs, the occurrence rates of super-Earths and warm Neptunes seem to be a factor 2-3 higher than around Solar-mass stars (Hsu et al., 2020; Yang et al., 2020). Similarly, the mass of a typical planet around a star scales proportionally with the stellar mass (Pascucci et al., 2018). Perhaps the most striking system to represent these trends is that of *TRAPPIST-1*, where seven planets with radii similar to Earth orbit in a very compact configuration around a 0.08 $M_\odot$ star.

The distribution of smaller planets is characterized by a pronounced dearth of planets with radii between 1.5-2 $R_\oplus$ (Fulton & Petigura, 2018; Fulton et al., 2017; Van Eylen et al., 2018). The exact physical cause of this radius valley is subject to much ongoing debate, but it likely corresponds to a change in composition from entirely refractory to a significant H/He envelope (Ho & Van Eylen, 2023), or from rocky to icy (Luque & Pallé, 2022). The former interpretation has historically been most commonly suggested, and can be motivated in two ways. One possibility is that the planets with smaller radii formed late in the evolution of a protoplanetary disc, when little gas remains to be accreted (Lee & Connors, 2021; Lee et al., 2022). Alternatively, if the two populations of planets formed at similar times, the smaller planets may have lost their H/He layers due to either photoevaporation (Jin & Mordasini, 2018; Owen & Wu, 2017), or via outflows driven by internal heat (Ginzburg et al., 2018; Gupta et al., 2022). One potential issue with all of these theories is that combinations of H/He and refractories do not seem to match the density distribution that is observed. Modelling the density of planets around the radius valley as a function of mass seems to suggest that it arises from a split between purely rocky planets that formed inside the ice-line, and half-icy planets that formed outside it, and then migrated inward (Luque & Pallé, 2022).

1.3.2 Giant planets

Giant planets such as Jupiter are less common than their smaller counterparts, but planets more massive than Jupiter are still seen around 6% of stars (Fernandes et al., 2019). A large fraction of giant planets identified so far are hot Jupiters; heavily irradiated planets located close to their host star. However, these planets are mostly found due to the ease of

their detection with radial velocity surveys, rather than due to high occurence, and they are estimated to represent less than 1% of giant planets (Howard et al., 2012). Correcting for observational biases, the occurrence rate of giant planets appears to increase with semi-major axis (Santerne et al., 2016; Wittenmyer et al., 2020), until the distribution reaches a peak around 2-6 AU (Fulton et al., 2021).

While smaller planets exhibit minimal correlation with host star metallicity, giant planets are far more often found around stars with high metallicity values (Fischer & Valenti, 2005; Fulton et al., 2021). Furthermore, planets that contain a giant planet are quite likely ($\sim 30\%$) to contain a second (Wittenmyer et al., 2020). Cold Jupiters are even more closely associated with intermediate-mass planets. At least half of the systems with a cold Jupiter also contains at least one super-Earth or warm Neptune on a closer orbit (Bryan et al., 2019; Zhu et al., 2018).

1.4 White dwarf pollution

1.4.1 Post-main sequence planetary survival

When stars eventually exhaust the hydrogen in their cores, and they leave the main-sequence, their mass, radius, and luminosity all change significantly (e.g., Benacquista, 2013). With no more hydrogen remaining in the core, it begins to contract, while hydrogen continues to burn in a shell that slowly moved away from the core, causing the envelope to expand. The helium core in the centre becomes degenerate as it contracts, and heats up significantly. At $\sim 10^8$ K, helium begins to fuse to form carbon and oxygen, which occurs smoothly for stars above 2 $M_\odot$, and with a runaway helium flash for low-mass stars. In both cases, the stars enter the red giant branch (RGB) with a helium-burning core, an expanding envelope, increased mass-loss, and an increase in luminosity by orders of magnitude. When the helium in the core is exhausted, the star enters the asymptotic giant branch (AGB) with a carbon-oxygen core, surrounded by a shell of helium, and hydrogen. The nuclear burning alternates between the hydrogen and helium shells, and the star experiences a series of pulses, with its radius increasing and decreasing. During the RGB and the AGB, the star can lose as much as 80% of its mass, expand up to several AU in size, and increase its luminosity by orders of magnitude (Veras, 2016). For stars less massive than 8 $M_\odot$, the stellar envelope is ultimately blown away entirely, and the remaining core becomes a white dwarf (WD).

The post-main sequence evolution of the host star has significant implications for any circumstellar bodies, including planets and planetesimals. The orbit of the planet can either expand or contract, as it is affected by two competing processes. Stellar mass-loss will

cause orbits to expand, while simultaneously, orbits can also begin to contract due to tidal interaction with the star (Duncan & Lissauer, 1998; Mustill & Villaver, 2012; Veras, 2016; Villaver & Livio, 2009; Villaver et al., 2014). Close-in planets within a few AU are likely to be engulfed entirely, at which point they may spiral inwards or experience intense photo-evaporation (Bear & Soker, 2011). Some planets and planetesimals likely survive the RBG and AGB, however, as orbits outside a few AU may expand sufficiently quickly due to the stellar mass-loss to become protected from the increased stellar flux (Veras, 2016; Veras & Tout, 2012; Veras et al., 2011). Perhaps surprisingly, even water ice can resist the stellar luminosity of the RGB and AGB, provided that it is locked in sufficiently large bodies on wide orbits (Malamud & Perets, 2016, 2017a,b).

1.4.2 Compositional analysis of polluted white dwarfs

White dwarfs are interesting objects to study in the context of planet formation because a significant fraction between 25% - 56% of systems show metal lines in their spectra (Koester et al., 2014; Wilson et al., 2019; Zuckerman et al., 2003, 2010). These objects are known as *polluted white dwarfs*, and the standard interpretation is that these stars are sampling the remains of old planetary systems (Farihi, 2016; Jura, 2003; Jura & Young, 2014; Veras, 2021). High surface gravity leads to chemical stratification of their outer layers, with elements heavier than H/He sinking out of sight within days to millions of years, depending on white dwarf type and age (Heinonen et al., 2020; Koester, 2009). In many cases, the accretion of planetary material must, therefore, be ongoing or relatively recent. So far, the presence of 21 different heavy elements has been detected in white dwarf photospheres, with 19 of these found in the single system GD 362 (Melis & Dufour, 2017; Xu et al., 2013, 2017; Zuckerman et al., 2007). Recently, ongoing accretion of heavy elements has independently been confirmed for one system via the detection of X-rays emitted during the accretion process (Cunningham et al., 2022).

Observations of polluted white dwarfs with multiple identified photospheric elements are of special significance because they provide the only direct compositional measurement of exoplanetary material. In most cases, the inferred pollutant abundances roughly resemble those of Earth (Doyle et al., 2019; Klein et al., 2010; Xu et al., 2019, 2014; Zuckerman et al., 2007), although in some cases they hint at substantially different geological histories (Putirka & Xu, 2021). Notably, several systems contain increased levels of volatile elements (O, C, N), possibly indicating the accretion of cometary material that condensed in the outer regions of planetary discs (Farihi et al., 2013; Raddi et al., 2015; Xu et al., 2017). Other pollutants contain more refractory species (Ca, Ti) and likely formed on closer orbits (Xu et al., 2014). In GD362, the particularly high ratio of Mn/Na could indicate a history of

post-nebula volatilization (Harrison et al., 2021b), similar to the process experienced by Mars and the Moon (Palme & O'Neill, 2003; Siebert et al., 2018)

In addition to probing volatility trends, polluted white dwarfs can also reveal the proclivity of differentiation in exo-planetesimals (Bonsor et al., 2020; Hollands et al., 2017, 2021; Jura et al., 2013; Swan et al., 2019a; Zuckerman et al., 2011). Objects differentiate when their interiors become hot enough to partially melt, and chemical species separate into an iron-rich core and a magnesium-silicate-rich mantle. The decay of short-lived radioactive nuclei, such as ^{26}Al, as witnessed in the Solar System, can fuel large-scale melting in asteroids larger than $\sim$ 10 km (Hevey & Sanders, 2006; Lichtenberg et al., 2016). When a white dwarf's photosphere contains an over-abundance of iron and other siderophile (iron-loving – Ni, Cr) elements, it indicates that the star has swallowed a core-rich body (Gänsicke et al., 2012; Hollands et al., 2018, 2021; Melis et al., 2011; Wilson et al., 2015). High abundances of lithophile (rock-loving – Ca, Mg, Si) elements instead hint at the accretion of predominantly mantle material, although this can be difficult to distinguish from a post-accretion (declining) phase (Buchan et al., 2022; Harrison et al., 2021a, 2018). Pollutant abundances towards either extreme indicate that the parent body formed early or large enough to be differentiated and then experienced collisional processing. In the newest models, accounting for pressure-sensitivity of different elements allows the size of the parent body of pollutants to be constrained as well (Buchan et al., 2022).

1.4.3 Accretion onto white dwarfs

The analysis of polluted white dwarfs is a relatively young field, and some major questions remain to be solved. In particular, it is currently poorly understood how planetesimals or fragments of larger planetary bodies can make it onto the surface of white dwarfs. For material to accrete onto a white dwarf, it must travel from a distance of several AU to within the physical radius of the white dwarf, which is similar in scale to Earth. It is unlikely that accretion occurs as a direct strike because the Roche radius of a white dwarf is much larger than its physical radius. The first stage of accretion, after the planetesimal has been scattered onto a highly eccentric orbit, is likely a tidal disruption, producing an extremely eccentric disc with fragments (Malamud & Perets, 2020a,b; Nixon et al., 2020; Veras et al., 2021, 2014a). It is yet unclear how these fragments circularize and accrete onto the white dwarf surface. Among the processes suggested are Poynting-Robertson drag (Veras et al., 2015a), drag interactions with pre-existing material around the star (Grishin & Veras, 2019; Malamud et al., 2021) and magnetic Alfvén-wave drag (Zhang et al., 2021).

From an observational perspective, there are a few constraining factors. First, it is known that only around 3 percent of polluted white dwarfs show detectable infrared excesses (Farihi

et al., 2016; Rocchetto et al., 2015; Wilson et al., 2019). The discs that likely generate this infrared excess are highly variable on >yr timescales in the mid-infrared (Swan et al., 2019a, 2020), but not in the warmer near-infrared (Rogers et al., 2020). Only white dwarfs cooler than about 27,000 K have been found to exhibit an infrared excess (Bonsor et al., 2017), which corresponds to the limit where a white dwarf's Roche radius equals the sublimation radius of common minerals (Steckloff et al., 2021), consistent with the idea that any dust is generated by a tidal disruption. Second, around 4 pct of white dwarfs with infrared excesses have also been observed with double-peaked gaseous emission lines of Ca II (Gänsicke et al., 2008, 2007, 2006; Manser et al., 2020). These lines show some eccentricity, and precess with periods between 1.4-30 yr (Dennihy et al., 2018; Manser et al., 2016a,b; Wilson et al., 2015), indicating that the gas is on an eccentric orbit within the Roche radius of the star. Third, some systems are observed with transits with various periods between 23 minutes and 25 hrs (Farihi et al., 2022; Rappaport et al., 2016; Vanderburg et al., 2015). Finally, studies have estimated a simple empirical estimate of the accretion event lifetime between 0.1-10 Myr by combining the heavy element mass contained in atmospheres of white dwarfs with long sinking timescales with the instantaneous accretion rates observed onto stars with short diffusion timescales (Cunningham et al., 2021; Girven et al., 2012).

These four observational characteristics have yet to be consistently incorporated with the theory of material accretion onto white dwarfs. This is not only important for the sake of obtaining a self-consistent picture, but also because the accretion process itself could potentially modify the composition of the material that accretes onto a white dwarf, which would produce a huge caveat for any compositional interpretation. Chapters 4, 5, and 6 in this thesis are dedicated to the white dwarf accretion process, with the last two chapters focusing on the possibility that elements contained in a planetesimal accrete onto the white dwarf over different periods of time.

1.5 Thesis layout

In this thesis, I contribute to the field of planetary astronomy by discussing new ideas relating to the formation and destruction of planetary bodies. The thesis chapters are organized chronologically according to a planet's lifetime, beginning in chapter 2 with a theory on the spin-up of objects that form via gravitational collapse. In this chapter, I try to discern whether the spin distribution of Kuiper belt binaries can be explained via this mechanism. In chapter 3, I move on to the formation of the planets themselves, and discuss how planetary growth via the rapid accretion of small pebbles has implications for the atmospheric opacity, an important quantity that predicts the rate of heat loss and gas accretion. I try to answer

how much opacity is generated by the accretion of pebbles during the formation process. Finally, chapters 4, 5, and 6 skip forward in time by several billion years to the time when a planet's host star has left the main sequence, and has since become a white dwarf. At this late stage, there is strong observational evidence that stars begin to swallow their planets, providing a unique opportunity for astronomers to directly study planetary compositions. In chapter 4, I discuss how planetary material might arrive onto white dwarfs, and what observational signatures different accretion scenarios may have. In chapters 5 and 6, I question whether the composition seen in white dwarf atmospheres indeed reflects that of the accreted planetesimals, if different elements within a planetesimal may accrete over different periods of time. I summarize my work and discuss avenues for further research in chapter 7.

Chapter 2

Prograde spin-up during gravitational collapse

"Old stories are like old friends, she used to say. You have to visit them from time to time."
-George R. R. Martin, A Storm of Swords, 2000

In this chapter, a mechanism is described via which collections of particles can gain a prograde rotational component when they collapse or contract while in orbit around an external, central force. The proposed mechanism is simple, and relies on the geometry of an orbit. In summary, the relative shear between particles on curved orbits moves their shared centre-of-mass slightly inward and toward the external potential during a collapse, transferring orbital angular momentum into aligned (prograde) rotation. We perform illustrative analytical and N-body calculations to show that this process of prograde spin-up proceeds quadratically in time ($\delta L_{\rm rot} \propto t^2$) until the collapse nears completion. The work is initially presented without direct reference to planets and planetesimals, as it may be applicable to other settings as well. At the end of the chapter, we highlight an application to the Solar System, where prograde spin-up could explain the frequency of binary objects in the Kuiper belt with prograde rotation.

2.1 Introduction

Across a wide range of astrophysical scales, from asteroids to stars and beyond, many kinds of objects tend to form via the gravitational collapse of larger structures. The rotation of these objects, which tends to manifest as increased velocities when their moments of inertia decrease, is a key tool for investigating the physics of their formation. When inferring

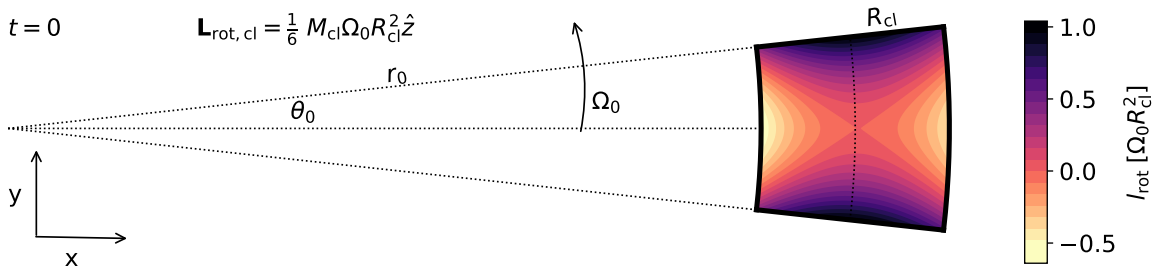

Fig. 2.1 Schematic setup of our analytical calculation (Sect. 2.2). We consider a two-dimensional cloud of mass $M_{\rm cl}$ in a stationary frame, whose origin lies on the central mass $M_{\rm C} \gg M_{\rm cl}$ (where the dotted lines cross). The initial shape of the cloud is that of a partial annulus, bounded by inner and outer circles with radii $r_0 \pm R_{\rm cl}$ and radial lines at angles $\pm\theta_0$. We follow the position $(\bar{x}_{\rm cl}, \bar{y}_{\rm cl})$ and velocity $(\bar{v}_{\rm x,cl}, \bar{v}_{\rm y,cl})$ of the cloud's centre-of-mass over time and calculate the specific rotational angular momentum of cloud particles (in direction $\hat{z}$) relative to this point as $l_{\rm rot} = (xv_{\rm y} - yv_{\rm x}) - (\bar{x}_{\rm cl}\bar{v}_{\rm y,cl} - \bar{y}_{\rm cl}\bar{v}_{\rm x,cl})$, shown in the colour plot at $t = 0$. The initial velocities of the cloud particles correspond to circular, Keplerian motion. Particles that start on the x-axis initially contribute retrograde rotation due to shear, whereas particles on the y-axis contribute prograde rotation due to curvature. The integrated result is a net initial prograde rotational angular momentum that increases over time if the cloud orbits freely (see Eq. 2.14b).

rotational trends from observations, it is often difficult to disentangle the system's rotation at birth from its later dynamical evolution. In some cases, however, systems with largely primordial rotational distributions still contain important historical clues about the processes by which they formed.

At the smallest scale of relevance here, asteroids and comets are long since thought to form in gravitational collapses within proto-planetary discs (see e.g., Goldreich & Ward, 1973; Morbidelli et al., 2009; Youdin & Shu, 2002), for instance via a small-scale mechanism now known as the streaming instability (Johansen et al., 2007, 2009; Schäfer et al., 2017; Simon et al., 2016; Youdin & Goodman, 2005). Whether traces of their primordial spins remain depends chiefly on the class and size of the asteroids that are studied. At the lower end of the size distribution, smaller asteroids have a largely isotropic spin distribution, with traces of their prior rotation wiped out by intense collisional processing (see e.g., Bottke et al., 2005a,b; Davis et al., 1989; Fraser, 2009; Pan & Sari, 2005) or by radiation induced changes in spin such as the YORP effect, (Medeiros et al., 2018; Pravec et al., 2008; Rubincam, 2000). Similarly, the largest bodies, such as Ceres and Vesta, may have accreted most of their prograde spin during later stages by pebble accretion (Johansen & Lacerda, 2010; Visser et al., 2020). In between, however, an intermediate class of asteroids with diameters between ~ 100 and 500 km likely still contains key information about their rotation at birth (Steinberg & Sari, 2015). Within the Solar System, the most dynamically pristine subset of these objects belong

to the group of "cold classicals" that reside in the Kuiper belt. Besides being characterized by low inclinations and eccentricities, this group contains a high fraction of binary pairs (Fraser et al., 2017; Grundy et al., 2019; Noll et al., 2008) which often have strong colour correlations (Benecchi et al., 2009, 2011; Marsset et al., 2020), reinforcing the idea that they formed in a single gravitational collapse - rather than by later capture. Interestingly, many of the binaries are found to have mass ratios near unity - which means that the collections of particles, or "clouds," from which they formed must have contained substantial amounts of rotational angular momentum (Nesvorný et al., 2010; Robinson et al., 2020). Their binary orbits are not distributed isotropically and express a preferential (prograde) alignment with their centre-of-mass orbit around the Sun (Grundy et al., 2019). Recently, hydrodynamic simulations have shown that such a distribution can indeed arise as the result of streaming instabilities (Nesvorný et al., 2021, 2019), but the underlying physical origin of the strong spin-orbit alignment remains poorly understood.

The trend of spin-orbit alignment continues at the scale above asteroids, where all the planets in the Solar System except Venus and Uranus rotate in the prograde direction. Theoretically, the prograde rotation of gas giants is readily explained in the context of core accretion by the torque during runaway gas accretion (Dittmann, 2021; Machida et al., 2008), but systematic explanations of terrestrial spin have proven more problematic (Lissauer & Safronov, 1991). Planetesimal accretion is found to deliver insufficient rotation to the accreting planet (Dones & Tremaine, 1993a; Lissauer & Kary, 1991), and later giant impacts fail to produce an anisotropic distribution (Dones & Tremaine, 1993b; Safronov, 1966). Pebble accretion could potentially provide a large, systematically prograde spin to planets (Johansen & Lacerda, 2010; Visser et al., 2020), although this remains to be validated for accretion onto proto-planets with substantial envelopes, where pebbles face intense drag and sublimation (Alibert, 2017; Brouwers et al., 2021; Johansen & Nordlund, 2020).

In the alternative theories to core accretion, planetary rotation could again find its origin in gravitational collapse. It is possible that in the outer regions of protoplanetary discs, giants can form directly from gravitational instabilities of cold gas (see e.g., Boss, 1998, 2021; Cameron, 1978; Kuiper, 1951). The spins of these larger planets on wide orbits are just beginning to be measured. Their rotation is certainly not always prograde, as HD 106906 b appears to spin on its side (Bryan et al., 2021). Recent smoothed-particle-hydrodynamics (SPH) and hydrodynamic simulations show that gravitational cloud collapse in gravito-turbulent discs can yield obliquities of up to 90 degrees (Jennings & Chiang, 2021), although most objects seem to form with more alignment (Hall et al., 2017). For now, more observations beyond the two known cases are required to resolve the statistical spin distribution of this class of planets.

At the scale of stars, it is thought that most stars form in clusters via the collapse of dense substructures within molecular clouds, which often fragment into several thousand stars per cluster (see e.g., Lee et al., 2012; Lee & Hennebelle, 2016b; McKee & Ostriker, 2007). The mutual alignment of stars in these clusters has been studied in a limited context, with differing results. In the first spectroscopic studies of the young, low-mass open clusters Pleiades and Alpha Per, no spin alignment was found in the population of G,K-, or M-type stars (Jackson et al., 2018; Jackson & Jeffries, 2010). This seems consistent with the older idea that stellar spins depend intimately on the local turbulence (see e.g., Belloche, 2013; Fleck & Clark, 1981), which itself is ultimately induced by differential galactic rotation (Renaud et al., 2013; Rey-Raposo et al., 2015; Rey-Raposo & Read, 2018). Recently, however, astro-seismological measurements of red giants in the higher-mass clusters NGC 6791 and NGC 6819 were found to exhibit a strong inter-cluster spin alignment (Corsaro et al., 2017). High-resolution simulations indicate that such a spin-alignment can arise for stars above 0.7 $M_{\odot}$ when their natal star-forming clump contains more than 50% of its kinetic energy in rotation (Corsaro et al., 2017; Lee & Hennebelle, 2016a). Although this rotational support might be rare (Caselli et al., 2002; Pirogov et al., 2003), mutual stellar spin alignment in such cases points to a spin-orbit alignment within the cluster, similar to the prograde rotation of asteroids and planets around a central star. Finally, we add that in the well-studied galaxies M33 and M51, the larger molecular clouds that host the star-forming clumps also seem to possess structural prograde rotation around the galaxy itself (Braine et al., 2020, 2018).

The preceding overview seems to suggest that objects which form via a gravitational collapse in the presence of an external gravitational field tend to exhibit a preferential alignment between their spins and orbital motions. Up to the present, the possibility that such a spin-orbit alignment exists across different scales has received little scientific attention. Perhaps the most relevant contribution to the topic is that of Mestel (1966), who considered the instantaneous condensation of patches from a differentially rotating disc ($\omega(r) \propto r^n$). His work showed that any closed, two-dimensional patch of a disc with an increasing rotation curve ($n \geq -1$) always contains prograde spin about its centre-of-mass, whereas patches from a Keplerian disc ($n = -3/2$) can yield spin in either direction, depending on their shape. However, in many cases, the collapse will not proceed from a fully ordered state. If the relevant clouds are formed by a process in which turbulent motions play an important role, the initial rotational setup of the collapsing cloud will be much more randomized, making it unclear from the potential alone what the spin direction will be. In addition, Shmidt (1957) realized that the centre-of-mass of a patch - and therefore its orbital angular momentum - could evolve during its collapse and that the final rotational direction would formally be set by the conservation of total angular momentum and energy. In his work, prograde rotation was

interpreted as the result of a collapse with sufficient thermal energy loss. These calculations were later extended by Safronov (1962, 1972) but ultimately proved inconclusive due to the problem of unknown thermal losses.

In this work, we provide a different, geometrically motivated approach to the rotational evolution of collapsing clouds in orbit around an external potential, most similar to the tidal torque theory that seeks to explain galactic spins (Hoyle, 1951; Peebles, 1969). We show that because particles that orbit in any non-rigid cloud shear away from one another over time - and do so on curved paths - their combined centre-of-mass moves toward the source of the external potential during a gravitational collapse. The orbital angular momentum that is thus liberated, adds a prograde component to the spin of the object that forms. This mechanism of prograde spin-up is most effective when the clouds are low in density prior to their collapse and when individual particles are on circular orbits, although the effect persists across a wide range of setups.

The structure of the chapter is organized as follows. We begin in Sect. 2.2 with an illustrative analytical calculation of prograde spin-up with two-dimensional, circular orbits around a point source. In Sect. 2.3, we numerically verify the main analytical trends by including self-gravity, and present a more visual analysis by showing the spin-up of a cloud without any initial rotation. In Sect. 2.4, we apply the mechanism of prograde spin-up to the formation of binary asteroids/comets, provided that these objects form via gravitational collapse. Finally, we discuss the broader implications of our findings in Sect. 2.5 and conclude in Sect. 2.6.

2.2 Analytical evaluation of prograde spin-up

In this section, we perform a calculation without self-gravity to illustrate how shear can transfer orbital angular momentum to rotation based on the orbital geometry. The idea behind this calculation is that objects form at the centres-of-mass of collapsing clouds, which orbit in the potential of larger objects or structures. While the nonlinear nature of a cloud collapse in the presence of an external potential is generally unsuitable for analytical modelling, the main trends can be elucidated by following cloud particles without treating self-gravity, at least while the collapse is not yet in full swing. The setup of this analytical calculation is sketched in Fig. 2.1. We consider a two-dimensional cloud with a uniform density $\sigma_{\rm cl}$ that integrates to a total mass $M_{\rm cl}$. The particles in the cloud move around a stationary central mass $M_{\rm C} \gg M_{\rm cl}$ on circular orbits with angular velocity $\omega = \sqrt{GM_{\rm C}/r^3}$ at distance r. We conveniently let the initial shape of the cloud be that of a partial annulus, bounded by inner

and outer circles at $r_0 \pm R_{\rm cl}$ and angles $\pm\theta_0$, with $R_{\rm cl} = \theta_0 r_0$, such that the cloud consists of radially separated differential arcs with length $l_{\rm arc}(r) = 2R_{\rm cl} r/r_0$.

2.2.1 Position and velocity of shearing radial arcs

First, we calculate the positions and velocities of the different radial arcs. Their angular velocities vary slightly depending on their radial separation, causing deviations between arcs that grow over time. In a stationary frame, the upper (θ_+) and lower (θ_-) bounding angles of an arc are given by:

$$\theta_\pm = \pm\theta_0 + \omega_0 \left(\frac{r}{r_0}\right)^{-\frac{3}{2}} t, \tag{2.1}$$

where t is time after initiation. The centre-of-mass of an arc can be calculated in Cartesian coordinates with their origin on $M_{\rm C}$ ($\bar{x}_{\rm arc}, \bar{y}_{\rm arc}$) to lie at:

$$\bar{x}_{\rm arc} = \frac{1}{2\theta_0} \int_{\theta_-}^{\theta_+} r \cos\left(\theta'\right) d\theta', \tag{2.2a}$$

$$= \frac{r \sin(\theta_0)\ \cos\left[\omega_0 \left(\frac{r}{r_0}\right)^{-\frac{3}{2}} t\right]}{\theta_0}, \tag{2.2b}$$

$$\bar{y}_{\rm arc} = \frac{1}{2\theta_0} \int_{\theta_-}^{\theta_+} r \sin\left(\theta'\right) {\rm d}\theta' \tag{2.3a}$$

$$= \frac{r \sin(\theta_0)\ \sin\left[\omega_0 \left(\frac{r}{r_0}\right)^{-\frac{3}{2}} t\right]}{\theta_0}. \tag{2.3b}$$

As expected, it is initially located on the x-axis and subsequently orbits in a circular motion as a function of time. Its velocity components follow from the time derivatives as:

$$\bar{v}_{\rm x,arc} = -\omega_0 \left(\frac{r}{r_0}\right)^{-\frac{3}{2}} \bar{y}_{\rm arc}\ ,\ \bar{v}_{\rm y,arc} = \omega_0 \left(\frac{r}{r_0}\right)^{-\frac{3}{2}} \bar{x}_{\rm arc}. \tag{2.4}$$

2.2.2 Trajectory of the cloud's centre-of-mass

Next, we combine the positions of different arcs to find the centre-of-mass of the whole cloud. We first note that without self-gravity, its area, being the integral over the differential arcs, remains constant over time and follows from subtracting the two partial disc areas as $A_{\rm cl} = 4R_{\rm cl} r_0 \theta_0 = 4R_{\rm cl}^2$. The position ($\bar{x}_{\rm cl}, \bar{y}_{\rm cl}$) and velocity ($\bar{v}_{\rm x,cl}, \bar{v}_{\rm y,cl}$) of the cloud's centre-

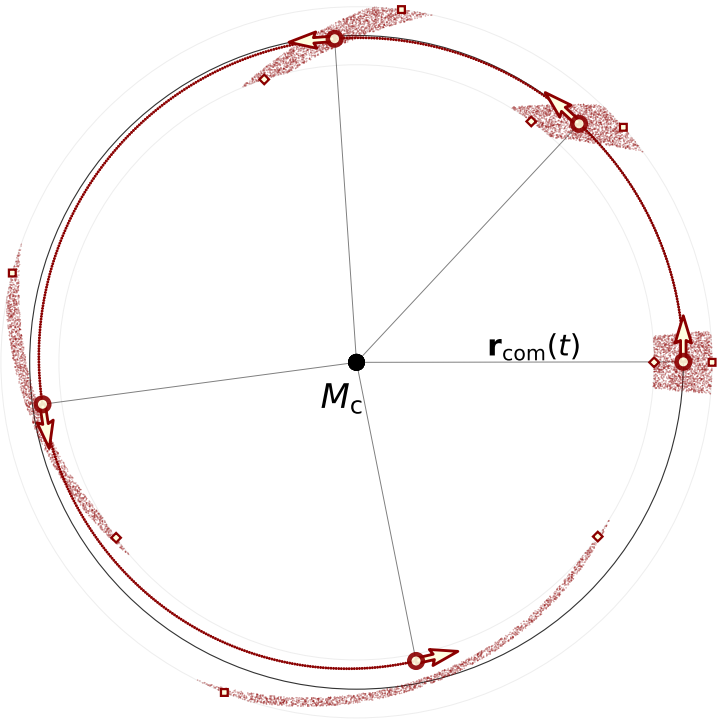

Fig. 2.2 Illustration of the inward centre-of-mass shift in our analytical example. The particles follow circular orbits around a central mass without mutual interactions. As the particles shear out over time, the ensemble deforms into an increasingly extended single arc, shifting the centre-of-mass position (open circular dot) closer to the orbital midpoint.

of-mass can be found by radially integrating over Eqs. 2.2b, 2.3b, and 2.4, which yields:

$$\bar{x}_{\mathrm{cl}}(t) = \frac{1}{A_{\mathrm{cl}}} \int_{r_0-R_{\mathrm{cl}}}^{r_0+R_{\mathrm{cl}}} \bar{x}_{\mathrm{arc}}(r) l_{\mathrm{arc}}(r) dr \tag{2.5a}$$

$$\simeq r_0 \cos(\omega_0 t) + \frac{R_{\mathrm{cl}}^2}{24 r_0} \left[\left(4 - 9\omega_0^2 t^2\right) \cos(\omega_0 t) + 9\omega_0 t \sin(\omega_0 t) \right], \tag{2.5b}$$

$$\bar{y}_{\rm cl}(t) = \frac{1}{A_{\rm cl}} \int_{r_0-R_{\rm cl}}^{r_0+R_{\rm cl}} \bar{y}_{\rm arc}(r) l_{\rm arc}(r) dr \tag{2.6a}$$

$$\simeq r_0 \sin(\omega_0 t) + \frac{R_{\rm cl}^2}{24 r_0} \left[\left(4 - 9\omega_0^2 t^2\right) \sin(\omega_0 t) - 9\omega_0 t \cos(\omega_0 t) \right], \tag{2.6b}$$

with the corresponding velocities given by the time derivatives:

$$\bar{v}_{\rm x,cl}(t) \simeq -\omega_0 r_0 \sin(\omega_0 t) + \frac{\omega_0 R_{\rm cl}^2}{24 r_0} \left[\left(5 + 9\omega_0^2 t^2\right) \sin(\omega_0 t) - 9\omega_0 t \cos(\omega_0 t) \right], \tag{2.7a}$$

$$\bar{v}_{\rm y,cl}(t) = \simeq \omega_0 r_0 \cos(\omega_0 t) + \frac{\omega_0 R_{\rm cl}^2}{24 r_0} \left[-\left(5 + 9\omega_0^2 t^2\right) \cos(\omega_0 t) - 9\omega_0 t \sin(\omega_0 t) \right]. \tag{2.8a}$$

These integrals are calculated with Mathematica 12.0 and each have exact solutions in the form of long sums. We provide the Maclaurin series with the variable $\theta_0 \ll 1$ in order to maintain some brevity. To zeroth order, the centre-of-mass follows a simple circular motion at distance r_0 from the central mass. The strongest deviation is a second-order term that includes a small initial off-set from r_0 as well as a time-dependent factor. From Eqs. 2.5b and 2.6b, we can calculate how the distance of the cloud's centre-of-mass ($\bar{r}_{\rm cl}$) evolves over time:

$$\delta \bar{r}_{\rm cl}(t) = \sqrt{\bar{x}_{\rm cl}^2(t) + \bar{y}_{\rm cl}^2(t)} - \sqrt{\bar{x}_{\rm cl}^2(t=0) + \bar{y}_{\rm cl}^2(t=0)} \tag{2.9a}$$

$$= -\frac{3R_{\rm cl}^2 \omega_0^2 t^2}{8 r_0}. \tag{2.9b}$$

Interestingly, we find that the centre-of-mass in this setup moves inward with a quadratic time dependence. We show the geometrical origin of this change in Fig. 2.2 where we sketch the position of a cloud of particles in Keplerian motion. As the cloud shears out and angular differences increase, its shape deforms from a partial annulus into an increasingly extended single arc. Due to the curvature inherent to circular motion, the centre-of-mass of this arc shifts toward the star as a function of time. If the system is evolved for a sufficiently long period of time, the centre-of-mass ultimately coincides with the position of the central mass.

We can further investigate the trajectory of the cloud's centre-of-mass by calculating its semimajor axis ($\bar{a}_{\rm cl}$), which follows from the energy balance as:

$$\bar{a}_{\rm cl}(t) = \frac{\omega_0^2 r_0^3}{2}\left(\frac{\omega_0^2 r_0^3}{\bar{r}_{\rm cl}(t)} - \frac{\bar{v}_{\rm x,cl}^2(t) + \bar{v}_{\rm y,cl}^2(t)}{2}\right)^{-1}. \tag{2.10}$$

Again, we are mainly interested in its evolution from the initial value as a function of time, so we compute this difference ($\delta\bar{a}_{\rm cl}$):

$$\delta\bar{a}_{\rm cl}(t) = \bar{a}_{\rm cl}(t) - \bar{a}_{\rm cl}(t=0) \tag{2.11a}$$

$$= -\frac{3R_{\rm cl}^2\omega_0^2 t^2}{2r_0}. \tag{2.11b}$$

We have verified that the form of Eq. 2.11b is unchanged when the shape of the cloud is altered. For example, the pre-factor of 3/2 becomes 1/8 for a cloud in the shape of a closed disc, remains 3/2 for a radial line and tends to zero for a tangential line, whose particles do not experience shear.

2.2.3 Transfer of orbital angular momentum to rotation

If an object forms at the centre-of-mass of a cloud, its shrinking semimajor axis and increasing eccentricity during the collapse reduce its orbital angular momentum ($\bar{L}_{\rm cl}$), which points in the $\hat{z}$-direction in this two-dimensional example:

$$\bar{L}_{\rm cl}(t) = M_{\rm cl}\left[\bar{x}_{\rm cl}(t)\bar{v}_{\rm y,cl}(t) - \bar{y}_{\rm cl}(t)\bar{v}_{\rm x,cl}(t)\right] \tag{2.12a}$$

$$\simeq M_{\rm cl}\omega_0 r_0^2\left[1 - \frac{1}{24}\left(\frac{R_{\rm cl}}{r_0}\right)^2\left(1 + 18\omega_0^2 t^2\right)\right]. \tag{2.12b}$$

While the orbital angular momentum associated with the centre-of-mass orbit declines, the total angular momentum of the cloud ($L_{\rm tot,cl}$) remains constant over time, equal to:

$$L_{\rm tot,cl} = \int_{r_0-R_{\rm cl}}^{r_0+R_{\rm cl}} \omega_0\left(\frac{r}{r_0}\right)^{-\frac{3}{2}} l_{\rm arc}(r)\sigma_{\rm cl} r^2 dr \tag{2.13a}$$

$$\simeq M_{\rm cl}\omega_0 r_0^2\left[1 + \frac{1}{8}\left(\frac{R_{\rm cl}}{r_0}\right)^2\right]. \tag{2.13b}$$

As a thought experiment that represents the simplest model for cloud collapse, we can envision a cloud of material that initially evolves without self-gravity up to time t and then

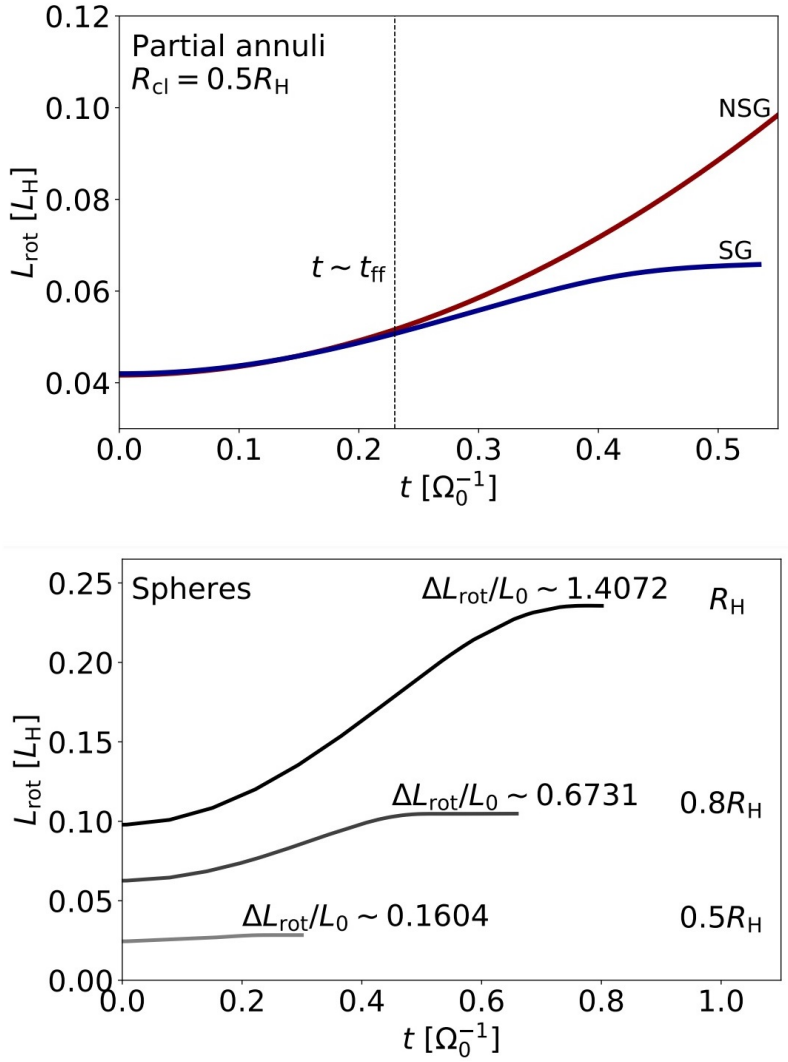

Fig. 2.3 The amount of spin-up over time for clouds shaped as partial annuli and spheres. Top: Simulated prograde spin-up of clouds in the shape of partial annuli that orbit around a central mass with (blue, SG) and without (red, NSG, Eq. 2.14) self-gravity enabled. When self-gravity and collisions are included, the prograde spin-up levels off around the free-fall timescale (plotted here for an equivalent sphere), when cloud shear comes to a halt. Bottom: Same calculation, computed with spherical clouds and varying initial densities. Their initial rotation scales as $L_0 \propto (R_{cl}/R_H)^2$, whereas the prograde spin-up during their collapse scales as $L_{rot} \propto (R_{cl}/R_H)^5$ (see Sect. 2.2.3). As a result, sparse clouds with $R_{cl} \simeq R_H$ accumulate most of their rotation during their collapse, whereas the rotation of denser clouds remains largely unchanged.

instantly collapses to form an object with position and velocity equal to the cloud's centre-of-mass. Conserving total angular momentum, the deficit between the total and orbital angular momentum can be interpreted as this object's rotation and is given by:

$$L_{\rm rot,cl}(t) = L_{\rm tot,cl} - \bar{L}_{\rm cl}(t) \tag{2.14a}$$

$$\simeq \left(\frac{1}{6} + \frac{3}{4}\omega_0^2 t^2\right)\left(\frac{R_{\rm cl}}{R_{\rm H}}\right)^2 L_{\rm H}, \tag{2.14b}$$

where we use the Hill radius ($R_{\rm H}$) and Hill rotation ($L_{\rm H}$) as natural normalization factors in this context (sometimes referred to as Roche units), defined by:

$$R_{\rm H} = r_0\left(\frac{M_{\rm cl}}{3M_\star}\right)^{\frac{1}{3}} \ , \ L_{\rm H} = M_{\rm cl}\omega_0 R_{\rm H}^2. \tag{2.15}$$

The key outcome of our analytical calculation is represented by Eq. 2.14b. Again, we have numerically verified that the shape of this key equation is unchanged for different cloud shapes. The pre-factors (1/6, 3/4) become (1/8, 9/16) for a disc, (-1/6, 3/4) for a horizontal line and (1/3, 0) for a vertical line. Our result agrees with the finding by Mestel (1966) that both a partial annulus and a disc of particles on circular orbits around a point source have prograde spin around their centre-of-mass. But more importantly, it shows that a cloud accumulates additional prograde rotational angular momentum over time during its collapse, scaling as $\delta L_{\rm rot} \propto t^2$. This rotational angular momentum builds up due to the curvature inherent to orbital motion, which moves the centre-of-mass of a cloud toward an increasingly contracted orbit that contains less orbital angular momentum, producing a deficit filled by increased prograde rotation. While we will show in Sect. 2.4.1 that the rate of prograde spin-up depends on the velocity distribution of the cloud, this analytical model is sufficient to discern the main scaling relations, which are as follows. First, we note that the typical timescale to evaluate the prograde spin-up on is the free-fall timescale, which we roughly approximate with the expression for a uniform sphere:

$$t_{\rm ff} = \frac{\pi}{\sqrt{24}}\left(\frac{R_{\rm cl}}{R_{\rm H}}\right)^{\frac{3}{2}}\omega_0^{-1}. \tag{2.16}$$

After substituting this timescale into Eq. 2.14b, we find that the rotational build-up during collapse scales as $\delta L_{\rm rot} \propto t_{\rm ff}^2 (R_{\rm cl}/R_{\rm H})^2 \propto (R_{\rm cl}/R_{\rm H})^5$. The Hill radius can be thought of as the interface between shear and self-gravity, as clouds bigger than $R_{\rm H}$ shear out before they collapse. It is really at this interface of shear and self-gravity that the mechanism of rotational gain discussed here is most significant, and its importance rapidly reduces for

clouds that begin their collapse at $R_{\rm cl} < R_{\rm H}$. Second, we note that if the cloud collapses from the Hill radius, the specific rotation of the object that forms, follows a mass scaling of $l_{\rm H} = L_{\rm H}/M_{\rm cl} \propto M_{\rm cl}^{2/3}$, matching the universal rotational trend followed by Solar System asteroids and planets identified by Goldreich & Peale (1968).

2.3 Numerical evaluation of cloud collapse in orbit

In this section, we perform numerical simulations of cloud collapse in orbit, using the N-body code REBOUND (Rein & Liu, 2012). The settings and numerical convergence of the runs are explained in detail in Appendix A. First, we numerically demonstrate the validity of our main analytical findings. Next, we present a second geometrical argument where the relative position of cloud particles, rather than their shared centre-of-mass, is used to illustrate the prograde spin-up during a gravitational collapse.

2.3.1 Comparison with analytical formulation

The main simplification of our analytical example, besides its fixed two-dimensional geometry, is that it approximates the prograde spin-up without accounting for the orbital changes induced by self-gravity. In the left panel of Fig. 2.3, we numerically compute the same example including self-gravity to illustrate the spin-up of a cloud that actually collapses. The two curves initially follow the same trend of $\delta L_{\rm rot} \propto t^2$ during the early phase of the collapse. Then, the spin-up of the collapsing cloud begins to level off as it contracts sufficiently. The process of prograde spin-up eventually halts entirely when the cloud becomes a rigid body, and it can no longer shear out. Nevertheless, the analytical example provides a decent approximation when the spin-up is evaluated at $t_{\rm ff}$.

Our analytical arguments predict that prograde spin-up scales as $\delta L_{\rm rot} \propto (R_{\rm cl}/R_{\rm H})^5$, more steeply than the cloud's initial rotation, which scales as $L_0 \propto (R_{\rm cl}/R_{\rm H})^2$ (see Eqs. 2.14b, 2.16). To test this trend, we perform numerical simulations of uniform, spherical clouds with different initial sizes, again initialized on circular, Keplerian orbits. We show the prograde spin-up of these runs in the right panel of Fig. 2.3 for initial cloud sizes between $0.5 - 1 R_{\rm H}$. As predicted, the spin-up can exceed the initial rotation in scale, but only when the cloud nearly fills its Hill radius prior to collapse. Indeed, the fraction of accumulated rotation drops from $\delta L_{\rm rot}/L_0 = 1.40$ to $\delta L_{\rm rot}/L_0 = 0.16$ when the cloud's initial size is halved. This factor of ~ 9 decline is similar to the factor of 8 predicted analytically and reiterates our finding that, while the rotation of dense ($R_{\rm cl} \ll R_{\rm H}$) clouds remains largely unchanged during

their collapse, clouds that fill their Hill sphere prior to collapse gain a substantial prograde component to their spins.

2.3.2 Visualization of the prograde spin-up mechanism

In this section, we visualize the prograde spin-up during a gravitational collapse differently, by tracking the relative motion of a cloud's inner- and outermost particles.

Two-particle dynamics without self-gravity

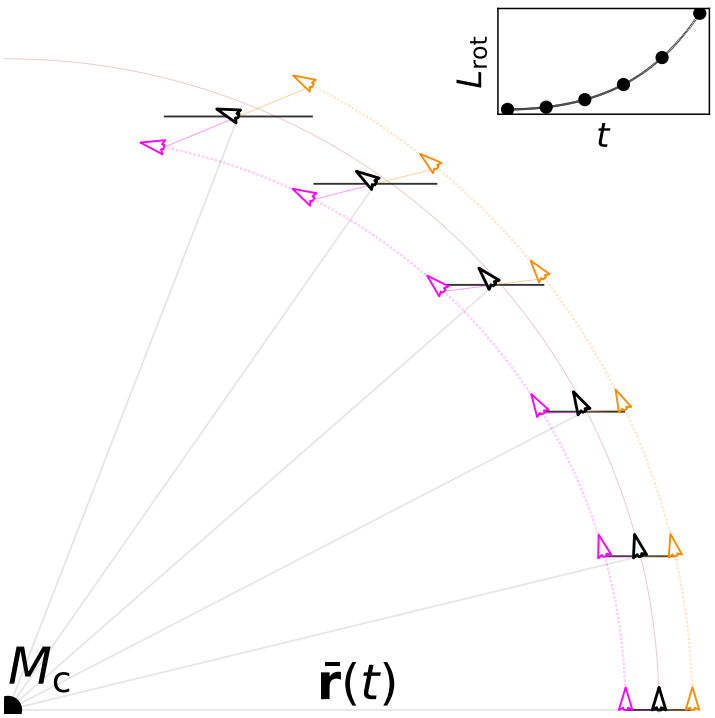

Fig. 2.4 Orbital evolution of two non-interacting particles and their centre-of-mass, initiated without rotation. Over time, both the interior (magenta arrow) and the exterior (orange arrow) particles start to revolve around their mutual centre-of-mass (black arrow) in a prograde fashion, as shown by the angular displacement that develops relative to the horizontal dashed line. The quadratic prograde spin-up over time is additionally shown in the inserted panel, with the rotation at the different snapshots depicted by the black dots.

The prograde spin-up during collapse is most striking in clouds that have no initial rotation, which we ensure by initiating all particles with (vector) velocities equal to that of their shared centre-of-mass (see Appendix A). Prior to showing the rotational build-up in an

N-body collapse, we first illustrate the underlying process in Fig. 2.4, where we consider the orbital motion of two horizontally aligned, non-interacting particles in a stationary frame. Their shared centre-of-mass coordinate is shown with a black arrow and is initiated with a non-eccentric Keplerian velocity.

Rather than focusing on the inward shift of the centre-of-mass shift due to shear, which is not always visible relative to the cloud's scale, we focus here on the relative motion of the particles. The innermost particle is more tightly bound to the central mass and traces out an elliptical orbit that is characterized by a greater angular velocity ($\dot{\theta}$) than that of the outermost particle. As a result of the orbital geometry, where its y-coordinate is modulated by a factor $\sin(\theta)$ in this stationary frame, the inner particle begins to drop below the exterior one. Consequently, it is seen to effectively wrap below their shared centre-of-mass in a prograde fashion. This behaviour is mirrored in reverse by the outer particle, whose angular velocity is lower and, therefore, wraps around their centre-of-mass from the top, again producing a prograde rotation. We emphasize this relative movement visually in Fig. 2.4 with a horizontal dashed line, drawn through the centre-of-mass. In the inserted panel, the rotation relative to the centre-of-mass is seen to rise quadratically over time, producing the same trend of prograde spin-up as a derived in Sect. 2.2.

N-body collapse of a spherical cloud

We now perform a cloud collapse, using the same initial condition without rotation, but this time for a uniformly packed cloud with size R_{H} and with self-gravity and collisions enabled in REBOUND. We visualize the evolution of the collapsing cloud in Fig. 2.5[1], again shown in a stationary frame. If we compare the stages of collapse over time with Fig. 2.4, we observe that the general behaviour remains unchanged. The difference is caused by the addition of self-gravity, which draws all particles toward their shared centre-of-mass over time. In the intermediate stages of the collapse, this self-gravity reshapes the cloud into an aligned bar, as is the case when any rotating spheroid collapses (Lin et al., 1965). Just like in the two-particle example, the interior particle drops below the centre-of-mass - while those exterior remain above it. As the cloud contracts further and self-gravity intensifies, this prograde wrapping of particles on either side of the centre-of-mass translates into a real prograde rotation of the object that forms.

[1]Fig. 2.5 shows the collapse in a stationary frame that is centred on a much more massive central mass. This poses the visual difficulty that any collapsing cloud is tiny in comparison to the scale of its orbit. To circumvent this, we place subpanels at the corresponding centre-of-mass positions where we zoom in. The cloud scale is, therefore, exaggerated for clarity, but the collapse evolution is still visualized in a stationary frame.

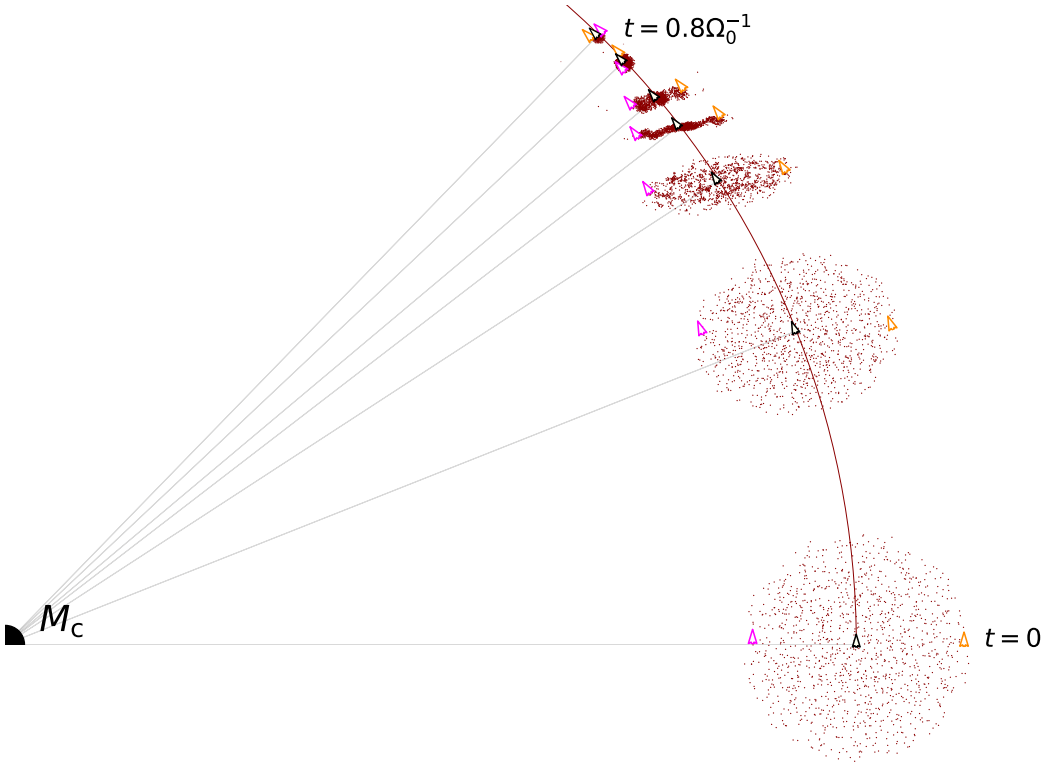

Fig. 2.5 Overview of the collapse of a uniform cloud in orbit around a central mass, shown in a stationary frame. The spherical cloud is initiated with size R_H and without any rotation. The snapshots from t = 0 to $t = 0.8\ \omega_0^{-1}$ are enlarged in scale for clarity. We highlight the positions and directions of two particles; one that is initiated closest to the central mass (magenta arrow) and one that starts the furthest away from the central mass (orange arrow). We also indicate the position and direction of the cloud's centre-of-mass (black edged arrow) and plot its initial distance (dark red semicircle). At the end of the collapse, the centre-of-mass has shifted slightly inward toward the central mass, and the two particles have performed half a prograde revolution, confirming the prograde rotation of the object that is formed.

2.4 Application: Formation of planetesimals

We highlight the formation of planetesimals as a small-scale example of a scenario where particle clouds form and then collapse due to their self-gravity while subject to a strong external force, in this case gravity from a central star. An example of a mechanism that triggers gravitational collapse is the streaming instability. In this theory, small over-densities in the proto-planetary disc locally accelerate the gas, producing dense filaments where small solids concentrate and collapse to form planetesimals (Johansen et al., 2007, 2009; Youdin & Goodman, 2005). Hydrodynamic simulations of the streaming instability in the proto-Kuiper belt have shown that it is possible to create equal-mass binaries in this manner (Nesvorný et al., 2010), which naturally seem to form with a strong preference for prograde rotation

(Nesvorný et al., 2021, 2019). These simulations provide a striking agreement with the observed abundance of prograde, equal-mass binaries in the dynamically cold class of Kuiper belt objects (Fraser et al., 2017; Grundy et al., 2019; Noll et al., 2008).

In this section, we evaluate whether the mechanism of prograde spin-up can drive this bias in rotational direction. Similar to Robinson et al. (2020), we model the final collapse stage of a pebble cloud with N-body simulations, and do not investigate the hydrodynamic onset of the collapse itself. Instead, we take a range of representative initial conditions and calculate the rotational gain in each of these scenarios. The effect of gas drag in this final collapse phase is neglected in this calculation, which is reasonable if the cloud has a dust-to-gas ratio exceeding unity (Nesvorný et al., 2010).

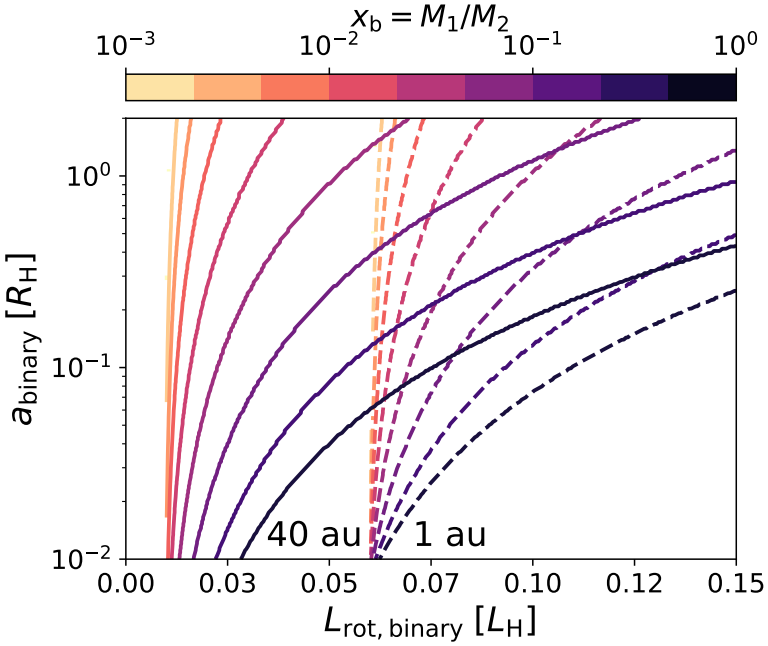

Fig. 2.6 Possible binary configurations for a given rotational angular momentum budget ($L_{\mathrm{rot,binary}}$) at two distances from the central star (40 au, solid; 1 au, dashed), assuming that the components themselves spin at near-breakup rates with density $\rho_{\mathrm{p}} = 1$. When $L_{\mathrm{rot,binary}} < 0.06\ L_{\mathrm{H}}$, only single planetesimals are formed at 1 au as the break-up spin exceeds the angular momentum budget, whereas this critical value lies between 0.02-0.03 L_{H} at 40 au. Large amounts of rotational angular momentum $\gtrsim 0.1 L_{\mathrm{H}}$ can only be contained in binaries with increasingly wide mutual orbits and increasingly similar masses, especially in the outer disc.

2.4.1 Binary formation criterion

We first examine how much rotational angular momentum is required to form a binary. If a spherical asteroid has a uniform density ρ_p, its moment of inertia for rotation is $I_\mathrm{p} = (2/5)M_\mathrm{p}R_\mathrm{p}^2$. If the asteroid's material strength is neglected - a reasonable assumption based on their low typical internal strengths (see e.g., Burns, 1975; Carbognani, 2017; Degewij & Gehrels, 1976; Persson & Biele, 2021) - its spin can at most reach the breakup limit of $\omega_\mathrm{crit} = \sqrt{4\pi G\rho_\mathrm{p}/3}$ (Pravec & Harris, 2000). The amount of angular momentum contained in a single asteroid's spin can then be written as a fraction of this limit:

$$L_\mathrm{spin,p} = I_\mathrm{p}\omega_\mathrm{spin} \tag{2.17a}$$

$$\simeq 0.06\, L_\mathrm{H} \left(\frac{d}{\mathrm{AU}}\right)^{-\frac{1}{2}} \left(\frac{M_\star}{\mathrm{M}_\odot}\right)^{\frac{1}{6}} \left(\frac{\rho_\mathrm{p}}{1}\right)^{-\frac{1}{6}} \frac{\omega_\mathrm{spin}}{\omega_\mathrm{crit}}, \tag{2.17b}$$

where $\omega_\mathrm{spin} \leq \omega_\mathrm{crit}$. Any excess rotational angular momentum can be accounted for by ejecting a portion of the mass, or by forming a binary (with mass ratio $x_\mathrm{b} = M_1/M_2$ and separation a_b), rather than a single planetesimal. In the idealized case without mass ejection, the complete rotational angular momentum budget gets divided into two spin terms around the respective asteroid centres (that sum to $L_\mathrm{spin,p1} + L_\mathrm{spin,p2} = L_\mathrm{spin,binary}$), as well as an orbital term for the motion of the binary around their shared centre-of-mass ($L_\mathrm{orb,binary}$). The spin component follows from the moments of inertia as:

$$L_\mathrm{spin,binary} = L_\mathrm{spin,p}\,(1+x_\mathrm{b})^{-\frac{5}{3}} \left(1 + x_\mathrm{b}^{\frac{5}{3}}\right), \tag{2.18}$$

while the orbital rotation around the binary's centre-of-mass can be calculated from their angular velocity ($\omega_\mathrm{b} = \sqrt{GM_\mathrm{p}/a_\mathrm{b}^3}$):

$$L_\mathrm{orb,binary} = M_1\omega_\mathrm{b}a_1^2 + M_2\omega_\mathrm{b}a_2^2 \tag{2.19a}$$

$$= L_\mathrm{H}\frac{x_\mathrm{b}}{(1+x_\mathrm{b})^2}\left(\frac{a_\mathrm{b}}{R_\mathrm{H}}\right)^{\frac{1}{2}}. \tag{2.19b}$$

Assuming that the collapse forms a bound system of at most two objects, the sum of Eqs. 2.18 and 2.19b specifies the possible binary configurations $(x_\mathrm{b}, a_\mathrm{b})$ for a given budget of rotational angular momentum. We examine these configurations in Fig. 2.6 at the location of the Kuiper belt (40 au) and at the location of Earth (1 au). The objects in the binaries are assumed to spin at breakup rate, in agreement with most Solar System asteroids (see e.g., Carbognani, 2017; Persson & Biele, 2021).

The first thing to note is that the formation of binaries is more likely at greater distances from the central star, where more angular momentum is available. This is due to the fact that the total rotational angular momentum generated in a collapse is constant across the disc in Hill units, which represent increasing angular momentum at greater orbital separations ($L_{\rm H} \propto r_0$). Furthermore, we note that the more equal the mass of the binary components, the more rotational angular momentum the combined system can store. When binaries are formed, therefore, they more commonly form with equal mass ratios in the outer disc. This trend is indeed reflected in the Solar System's asteroid and comet population. In the next subsection, we take a closer look at the magnitude of the rotational accumulation with different initial conditions for the collapsing cloud.

2.4.2 Dependence of spin-up on initial conditions

The magnitude of prograde spin-up during a gravitational collapse depends on the initial conditions of the cloud, including its size (Sect. 2.3.1), velocity distribution and distance from the central star. We now examine the importance of the latter two variables by running an array of N-body collapses. We vary the semimajor axis between $a_0 \in [10^{-1}, 10^2]$ au and vary the cloud mass between the equivalent of planetesimals with radii $R_{\rm p} \in [10, 10^3]$ km, assuming $R_{\rm cl} = R_{\rm H}$. We run this grid for four different rotational initial conditions for the cloud particles. Particles are either released on circular orbits referred to as the "Keplerian IC", with the same velocity as their centre-of-mass ("zero-rotation IC"), or with a uniform rotation relative to their centre-of-mass ("uniform rotation IC"). For the latter, we take the magnitude of the initial rotation equal to that of the Keplerian initial setup, but now with constant angular velocity around the centre-of-mass, and in both prograde and retrograde directions. A detailed description of these initial conditions is given in Appendix A.

We show the results in Fig. 2.7, where we indicate the prograde spin-up as well as the corresponding inward shift in the semimajor axis. Consistent with our analytical prediction, the rotational build-up is both scale-invariant and distance-invariant when expressed in Hill units. As predicted, the reduction of the cloud's semimajor axis during the collapse scales positively with the cloud mass and is proportional to its distance to the central star. Interestingly, the initial distribution of velocities in the cloud makes a large difference in the magnitude of the rotational gain. Whereas a cloud that begins with circular, Keplerian velocities attains an additional prograde rotation of $\delta L_{\rm rot} \simeq 0.15 L_{\rm H}$, clouds that begin with uniform rotation only gain $\delta L_{\rm rot} \simeq 0.05 L_{\rm H}$. This difference can be explained by the fact that prograde spin-up is driven by shear between the particles. If the initial conditions reflect more uniform motion, the cloud shears out to a less extended arc during the collapse, and the rotational gain is reduced. Nevertheless, even clouds that start without any rotation

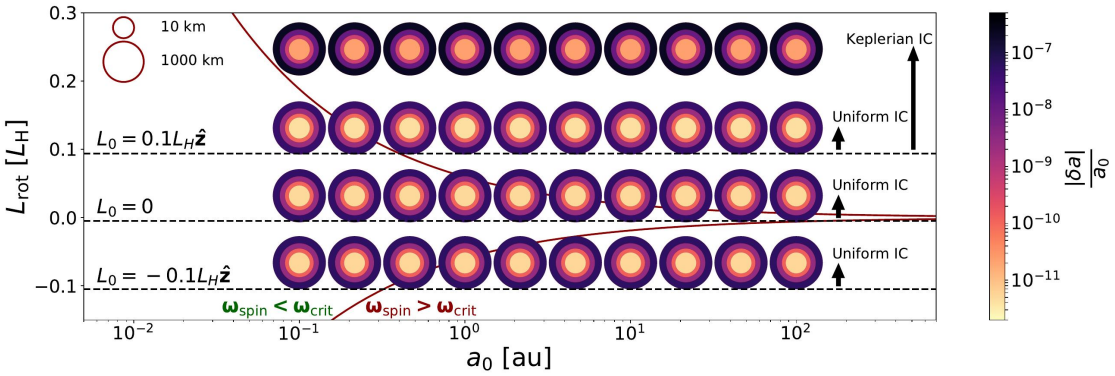

Fig. 2.7 Prograde spin-up in the collapse, visualized for a wide range of orbital separations, asteroid sizes and initial conditions. The dashed horizontal lines tangent to the circles represent the rotation prior to collapse, while the arrows indicate the magnitude of prograde spin-up. The ringed circles represent the size of the asteroid that forms, and their colours show the total centre-of-mass displacement during the collapse δa. The systems within the dark red lines represent cases where there is insufficient rotational angular momentum to form binaries ($\omega_{\rm spin} < \omega_{\rm crit}$). The systems above and below the red lines show the formation of prograde and retrograde binaries, respectively. The preference for prograde binary formation is clearly visible, especially in the outer disc.

accumulate a substantial prograde value of $L_{\rm rot} \simeq 0.05 L_{\rm H}$, which is enough to trigger unequal-mass binary formation outside a few astronomical units. In the case of Keplerian initial conditions, the rotational gain (to total $L_{\rm rot} \simeq 0.25 L_{\rm H}$) is enough to form equal-mass binaries across the proto-planetary disc (see Fig. 2.6).

2.5 Discussion

The mechanism of prograde spin-up is generally applicable to the gravitational contraction of any clouds that in orbit around an external, central potential. In any context, the key observational signature of this mechanism is a preferential alignment between the spin and orbital vectors of the objects that form. However, the rotational gain scales steeply as $\delta L_{\rm rot} \propto (R_{\rm cl}/R_{\rm H})^5$, such that only clouds whose sizes are set by the interplay of tidal shear and self-gravity ($R_{\rm cl} \sim R_{\rm H}$) experience significant spin-up when they collapse.

2.5.1 Comparison to hydrodynamic simulations of binary formation in the Kuiper belt

We presented a simple application of prograde spin-up to the formation of planetesimals via gravitational collapse, where we used a set of idealized initial conditions to show how perturbations by Solar gravity could provide enough rotation to form prograde binary systems. In reality, however, such clouds have morphologies and velocity distributions that are set in a more complex manner by interactions between the nebular gas and the solids, including back-reactions (Johansen et al., 2007, 2009; Youdin & Goodman, 2005). These processes were accounted for in more detail in the works by Nesvorný et al. (2021, 2019), who simulated the onset of the instability and initial stages of collapse using the hydrodynamics code ATHENA (Stone et al., 2008), prior to simulating high-resolution binary formation in the final collapse stage with the N-body code PKDGRAV (Stadel, 2001). Notably, Nesvorný et al. (2021, 2019) exclude stellar gravity in their PKGRAV simulations, but include it in their ATHENA runs, allowing their results to be influenced by prograde spin-up during the key early collapse stage. A comparison with their results illustrates two points: First, the broad distribution of scaled angular momenta that is generated by their ATHENA simulations, both in magnitude and direction, emphasizes the importance of modelling the onset of the streaming instability when considering the initial conditions of the collapse. Second, the fact that our simple model replicates their key result, namely the tendency of streaming instabilities to form prograde binaries, indicates that our suggested mechanism of prograde spin-up may well drive the rotational outcome in both models. Indeed, this suggestion is reinforced by the data shown in the supplementary Fig. 4 of Nesvorný et al. (2019), which indicates that the prograde bias only appears when the bound clumps collapse to form binary systems.

Rather than investigate the precise morphologies of these binary systems that form in SI, as was done with high-resolution studies by Robinson et al. (2020) and Nesvorný et al. (2021), we studied the mechanism behind the rotational evolution of material during the collapse. Conveniently, the prograde spin-up is largely independent of the chosen resolution or physical parameters such as coefficient of restitution and the particle size (see Appendix A), at least without accounting for the effects of gas drag. We should note, however, that the possibility of material ejection during the late stages of collapse means that not all the rotational angular momentum built up by the material necessarily ends up in the binary. The details tend to be more sensitive to parameter variations (Nesvorný et al., 2021; Robinson et al., 2020), and high-resolution simulations remain necessary to study the precise configurations that can form.

2.5.2 Relevance of prograde spin-up during planet formation

At the scale of planets, the mechanism of prograde spin-up might be applicable to the formation of giant planets by gravitational instability (see e.g., Boss, 1998; Cameron, 1978; Kuiper, 1951). The spins of these large planets on wide orbits are only just beginning to be uncovered, with the only two currently known cases pointing to moderate or large obliquities (Bryan et al., 2020, 2021). One notable difference with asteroid formation is that a collapse that forms a gas giant is halted by gas pressure, rather than collisions between solids. In both cases, however, these arresting forces become relevant only when the collapse is almost complete and significant prograde spin-up has already taken place. Alternatively, in the framework of core accretion (see e.g., Mizuno, 1980), gas giants could have accreted most of their mass and prograde angular momentum during the stage of runaway gas accretion (Dittmann, 2021; Machida et al., 2008). In this case too, the nebular gas accretes onto the planet from a range of non-eccentric orbits while exposed to stellar gravity, allowing for prograde spin-up to increase planetary rotation. Further work is required to resolve the statistical spin distribution of this class of planets and to investigate the role that prograde spin-up plays in setting their rotation.

The relevance of prograde spin-up to the formation of terrestrial planets is yet more difficult to assess. While their embryos may have formed in via gravitational collapse, terrestrial planets likely accreted most of their mass and rotation from nearby planetesimals (see e.g., Pollack et al., 1996), from the aerodynamic capture of pebbles (Lambrechts & Johansen, 2012; Ormel & Klahr, 2010), or possibly from late giant impacts (see e.g., Canup, 2012; Wetherill, 1985). Seen from a rotational perspective, however, none of these scenarios seem to offer satisfactory explanations for the scale or prograde bias of planetary spins. The accretion of planetesimals fails to deliver sufficient rotation (Dones & Tremaine, 1993a; Lissauer & Kary, 1991) while stochastic, giant impacts lead to isotropic spin distributions (Dones & Tremaine, 1993b; Safronov, 1966). Pebble accretion has been found to produce large, prograde rotation in some regimes (Johansen & Lacerda, 2010; Visser et al., 2020), although this may be dampened when protoplanetary envelopes are accounted for. There is, however, an alternative formation scenario that does involve a terrestrial-scale gravitational collapse. In the inside-out formation channel suggested by Cai et al. (2022); Chatterjee & Tan (2014); Hu et al. (2018, 2016); Mohanty et al. (2018), terrestrial cores are proposed to form out of dense pebble traps at the edges of dead zones. If planet formation indeed sometimes proceeds through this channel, the rotation of the planets it produces will likely be affected by prograde spin-up.

2.5.3 Potential application to molecular clouds and stars

Star formation is a hierarchical process that involves collapse on different scales, with potential applications for prograde spin-up at different levels. The process begins with the formation of a molecular cloud, the largest of which are observed to be concentrated toward galactic spiral arms (Blitz & Rosolowsky, 2005; Lee et al., 2001; Stark & Lee, 2005), where they form out of the interstellar medium, likely via gravitational instability driven by both stars and gas (Ballesteros-Paredes et al., 2007). At this scale, some prograde spin-up could be driven by the gravitational potential of the galaxy and contributes to an alignment between the rotation of the molecular cloud and its galactic orbit. Observations of molecular clouds in M33 and M51 do appear to have prograde biases in their rotation (Braine et al., 2020, 2018). It is not clear what fraction of their rotation can be attributed to prograde spin-up, though, as both M33 and M51 have rising velocity curves that already naturally lead to prograde rotation when a section of the disc contracts. Interestingly, Jeffreson et al. (2020) performed numerical simulations of molecular cloud formation in the dynamical galactic environment and found that the prograde bias remains even when the galactic rotation curve is declining and shear is expected to yield retrograde orbits. This persisting prograde bias fits the mechanism of prograde spin-up, but more work is required to investigate a potential connection. Moving down in scale, most stars are known to form in dense, gravitationally bound substructures within molecular clouds (see e.g., Lee et al., 2012; Lee & Hennebelle, 2016b; McKee & Ostriker, 2007), often referred to as star-forming clumps. When these clumps collapse and fragment, they form proto-clusters which often contain many thousand stars (see e.g., Lee et al., 2012; Lee & Hennebelle, 2016b; McKee & Ostriker, 2007). For the stars that form, the gravity from the star-forming clump itself could act as the external, central force necessary for prograde spin-up, which will act to align the angular momentum of the stellar spin (or binary orbit) with any orbital angular momentum within the cluster. While the available angular momentum is expected to reduce during star formation via magnetic breaking, the sign of the spin is maintained. If a star-forming clump contains systematic rotation, a spin-orbit alignment will translate to a correlation between the stellar spins in the cluster. Until recently, there had been no evidence of such a correlation, and the first spectroscopic studies of the young, low-mass open clusters Pleiades and Alpha Per were observed to be isotropic (Jackson et al., 2018; Jackson & Jeffries, 2010). However, recent astroseismological measurements have shown that red giants in the higher-mass clusters NGC 6791 and NGC 6819 exhibit a strong inter-cluster spin alignment (Corsaro et al., 2017), pointing to an imprint of spin-orbit alignment during their formation. Hydrodynamic simulations indicate that this spin-alignment can indeed arise when the star-forming clumps are mostly rotationally supported prior to their global collapse (Corsaro et al., 2017; Lee &

Hennebelle, 2016a), though further numerical simulations that track the rotational evolution during the key early collapse of the star-forming clump are required to assess the relative importance that prograde spin-up plays in this process.

2.6 Conclusions

Larger asteroids, planets, stars in some clusters, as well as molecular clouds seem to possess a preferential alignment between their spins and orbital vectors. In this work, we describe a process that can cause spin-orbit alignment based on the gravitational collapse of clouds in orbit around an external, central potential. We perform illustrative analytical and N-body calculations to show that a cloud's rotational angular momentum relative to its centre-of-mass is not conserved when it contracts next to such a potential, even if no material is ejected. Instead, because particles in a cloud shear away from one another over time - and do so on curved paths - their combined centre-of-mass moves inward toward the source of the potential (See Fig. 2.2). The orbital angular momentum, that is thus liberated, adds a prograde component to the spin of the object that forms. Equivalently, the process of spin-up can be understood from the prograde wrapping of inner and outer particles around the cloud's centre-of-mass, which we visualize in both a stationary (Figs. 2.4, 2.5) and corotating (Fig. A.3) frame. The basic properties of the prograde spin-up mechanism are as follows:

1. Clouds that orbit around external, central potentials build up prograde rotation when they collapse due to self-gravity. The spin-up develops quadratically over time ($\delta L_{\rm rot}/L_{\rm H} \propto t^2$), before slowing down when the collapse completes ($t \sim t_{\rm ff}$).

2. We find that the total rotational gain scales as $\delta L_{\rm rot}/L_{\rm H} \propto t_{\rm ff}^2 \propto (R_{\rm cl}/R_{\rm H})^5$. The fifth-order scaling means that prograde spin-up is only quantitatively important for clouds with lower densities prior to their collapse.

3. If the external potential is generated by a point mass and the initial cloud is spherical, we find a total increase in rotational angular momentum around $\delta L_{\rm rot} \simeq 0.05 - 0.15\, M_{\rm cl}\omega_0 R_{\rm cl}^2$. Out of the studied initial conditions, the magnitude of prograde spin-up is greatest when the cloud's particles orbit with circular velocities prior to the collapse, allowing for efficient shear.

When applied to the Solar System, we suggest that this mechanism of prograde spin-up could provide an explanation for the observed spin-orbit alignment of trans-Neptunian binaries (Grundy et al., 2019), provided that they formed in streaming instabilities (Johansen et al., 2007, 2009; Youdin & Goodman, 2005). As such, prograde spin-up could operate to drive

the recent simulation results of Nesvorný et al. (2021, 2019), who recently replicated this preferential spin-orbit alignment. The relevance of prograde spin-up to the formation of objects by gravitational collapse on larger astrophysical scales remains open for further investigation. Compared to the rotation contained in shear: $L_{\mathrm{rot}}/L_{\mathrm{H}} \propto (R_{\mathrm{cl}}/R_{\mathrm{H}})^2$, prograde spin-up becomes important when the size of the cloud prior to collapse is comparable to the Hill radius. For objects that form in this interface between self-gravity and shear, prograde spin-up can produce a spin-orbit alignment, even in an environment of retrograde shear.

Chapter 3

Envelope opacity generated by pebble accretion

"In order to solve this differential equation, you look at it until a solution occurs to you"
-George Polyá, How to solve it, 1945

In this chapter, we move on to the growth stage of planets, where they are accreting a mix of planetesimals and smaller pebbles. The accretion of pebbles has known consequences for the composition of the envelope, as they are sensitive to thermal ablation. However, it is also possible that pebbles contribute to the opacity of planetary envelopes by physically blocking photons trying to escape. The amount of nebular gas that a planet can bind is limited by its cooling rate, which is set by the opacity of its envelope. To gauge the importance of pebbles in this process, we design a simple model that accounts for the growth, fragmentation, and erosion of pebbles during their sedimentation. We formulate analytical expressions for the opacity of pebbles and dust and map out their trends as a function of depth, planet mass, distance, and accretion rate.

3.1 Introduction

Pebble accretion is a version of core accretion, where planets grow primarily by intercepting a stream of sub-centimetre sized particles (Lambrechts & Johansen, 2012; Ormel & Klahr, 2010). Previous works have mainly considered its dynamical aspects and have demonstrated that it can provide a rapid channel for growth (Chambers, 2014; Morbidelli & Nesvorny, 2012), especially when pebbles are settled in the mid-plane and accretion proceeds in a 2D manner (Liu & Ormel, 2018; Ormel & Liu, 2018). A key feature of pebble accretion is

that smaller particles are naturally prevented from reaching the planet once it has grown sufficiently large to perturb the surrounding disc (Bitsch et al., 2018; Eriksson et al., 2020; Morbidelli et al., 2015). This has been suggested as a way of discerning gas and ice giant formation (Lambrechts et al., 2014) and of limiting the growth of super-Earths around low-mass stars (Chen et al., 2020; Liu et al., 2019).

Besides these global effects, the accretion of smaller particles also has important consequences for a planet's internal structure. So far, most inquiries have focused on compositional changes, as the rapid vaporization of pebbles (Love & Brownlee, 1991; McAuliffe & Christou, 2006) naturally leads to the deposition of significant amounts of vapour, which can be stored in the deep interior (Iaroslavitz & Podolak, 2007; Lozovsky et al., 2017). This naturally limits the size of central cores (Alibert, 2017; Brouwers et al., 2018) and results in a dense, polluted interior (Bodenheimer et al., 2018; Iaroslavitz & Podolak, 2007; Lozovsky et al., 2017; Venturini et al., 2016). The traditional rigid core-envelope structure of these planets is replaced by the natural emergence of a compositional gradient (Ormel et al., 2021; Valletta & Helled, 2020; Vazan et al., 2020). This seems to be in line with Juno's measurements of Jupiter's gravitational moments of inertia, which imply such a dilute core structure (Debras & Chabrier, 2019; Debras et al., 2021; Wahl et al., 2017).

Before pebbles get to these inner regions, however, they must first sediment through the tenuous outer layers, where their combined surface area can contribute to the opacity. This influence of pebbles on the outer envelope is still largely unexplored but has important thermodynamic consequences. The more opaque an envelope, the less heat is able to escape it and the less gas it can gravitationally bind. By regulating the pace of cooling, the opacity is a key variable that directly affects the outcome of planet formation. The quantitative importance of the opacity is often understated in current formation models, where a lack of physically motivated values is still a serious issue. It is common practice to adopt conveniently high ISM-like opacities or values that are arbitrarily scaled down, with important consequences for the outcome of these models. One of the reasons that envelope opacity values are currently poorly constrained is that previous grain growth models focused specifically on the formation of Jupiter at 5 AU. In the most detailed of these, Podolak (2003), Movshovitz & Podolak (2008) and Movshovitz et al. (2010) calculated grain growth with numerical models that solve the Smoluchowski equation under the assumption that grains stick when they collide. They found that grain growth effectively reduces the dust opacity as a function of depth, with the opacity declining by around three orders of magnitude from the outer layers of the envelope to the inner radiative-convective boundary (RCB). Simpler analytical (Mordasini, 2014) and numerical (Ormel, 2014) models with a single characteristic grain size at a given height have been able to replicate this main result. However, because proto-planetary discs

are thermodynamically very different across distances and masses, it is not clear that these results can be applied generally to planets of varying sizes throughout the disc.

In addition, whether a planet is predominantly accreting sub-centimeter pebbles or 100 km planetesimals is clearly important for the abundance of grains in the outer envelope. The assumption of grain growth models that planetesimals deposit large amounts of small grains in the upper layers is in conflict with impact simulations, which predict that most of their mass is released close to the planet's central cores, far below the RCB (Brouwers et al., 2018; Valletta & Helled, 2019, 2020). In contrast, Ali-Dib et al. (2020) and Johansen & Nordlund (2020) have recently shown that pebbles are very susceptible to erosion by small dust grains when they enter planetary envelopes, especially when they are accelerated further by convective cells. It was also pointed out by Ormel et al. (2021) that even without any size evolution, milimeter-sized pebbles can contribute a significant opacity to planetary envelopes if they accrete at a sufficiently high rate.

The total envelope opacity is a sum of the contributions of solids and gas ($\kappa = \kappa_s + \kappa_{gas}$). In this study, we formulate a model for the contribution of solids, which often dominates over the gas during accretion. In Sect. 3.2, we develop a physical opacity model that accounts for the main processes that influence the evolution of solids in planetary envelopes. We consider a variation of the single-size approximation, where we model the populations of both small dust (κ_d) and larger pebbles (κ_{peb}). The characteristic size of the pebbles in our model is either determined by their growth from sticking collisions (coalescence) at low velocities or limited by fragmentation and erosion at high velocities, depending on the local thermodynamic conditions. When pebbles travel at speeds below the erosion velocity, they sweep up dust grains without experiencing mass loss (Krijt et al., 2015; Schräpler et al., 2018). We assume a constant dust size and calculate its steady state abundance between dust sweep-up and production, which can occur as a by-product of collisions between pebbles or via erosion. In Sect. 3.3, we then formulate simple, physically motivated analytical expressions for the opacity from solids, similar to what was done by Mordasini (2014). We apply our opacity model across a wide parameter space to explore and map out the resulting opacity as a function of distance, planet mass and accretion rate in Sect. 3.4. We then present the implications of these findings for the formation of gas and ice giants in Sect. 3.5. We discuss our model in relation to contemporary works, list potential model improvements, and contrast the scenarios of pebble and planetesimal accretion in Sect. 3.6. Finally, we conclude our work in Sect. 3.7. In Appendix B.1, we derive an expression for the non-isothermal critical metal mass that we use to study the onset of runaway growth. In the final Appendix (B.2), we vary the limiting velocity, the parameter in our model that represents the onset of fragmentation as well as erosion by micron-sized grains.

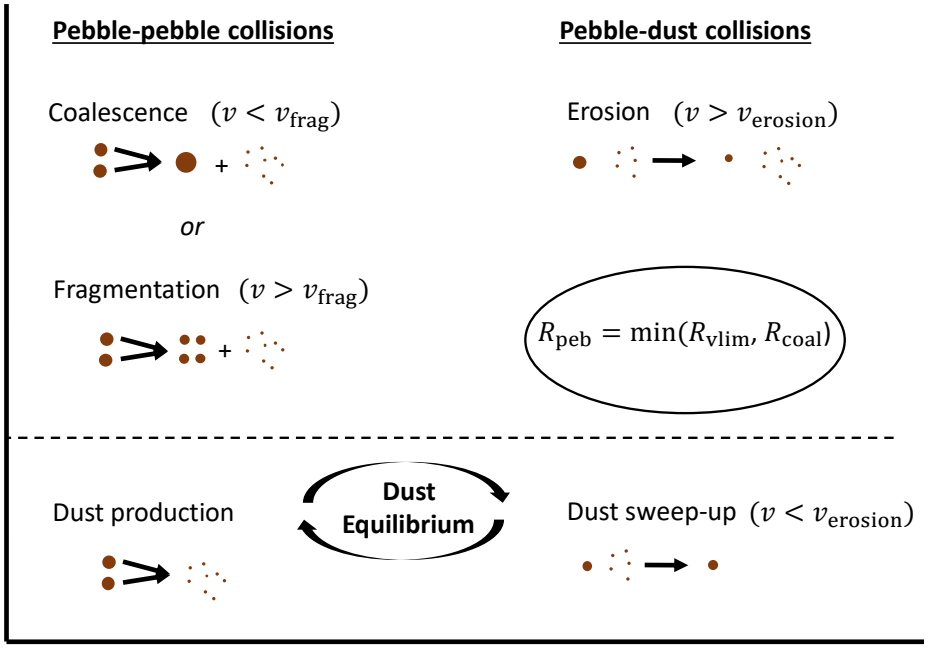

Fig. 3.1 Schematic diagram of our two-population opacity model. Depending on the velocities of sedimenting pebbles, they can experience growth (coalescence), fragmentation, or erosion. In the growth-limited regime, the pebble size in the interior is regulated by the collision and sedimentation timescales ($R_{\mathrm{peb}} = R_{\mathrm{coal}}$). In the velocity-limited regime, fragmentation and/or erosion restrict the pebble size below the growth potential ($R_{\mathrm{peb}} = R_{\mathrm{vlim}} < R_{\mathrm{coal}}$). In our model, dust grains of constant size are produced in collisions between pebbles or in high-velocity pebble-dust encounters (erosion), while they are lost by sticking encounters with slow-moving pebbles (dust sweep-up), leading to a local steady state in their abundance.

3.2 Model description

3.2.1 Two-population approach

Growing proto-planets are supplied with a flux of solid particles that enter their envelopes by two distinct mechanisms. The first is the drag-assisted capture of sub-centimetre pebbles that drift toward the central star (Lambrechts & Johansen, 2012; Ormel & Klahr, 2010), supplemented by the accretion of larger, km-sized planetesimals (Alibert et al., 2018; Guilera et al., 2020). The second source is the population of small, micron-sized dust grains that are coupled to the nebular gas and that enter the planet's envelope when it is massive enough to bind one.

In two recent works, Ali-Dib et al. (2020) and Johansen & Nordlund (2020) have shown that the interaction between dust and pebbles is crucial in evaluating their relative abundances, as high-velocity collisions between the two can significantly erode the incoming pebbles

and add to the dust population (Krijt et al., 2015; Schräpler et al., 2018). This erosion is a runaway process and is only halted at the pebble size, where collisions switch to sticking and the dust abundance begins to drop. In our model, we incorporate both dust and pebbles in a simple manner, where each is represented with a single characteristic size. The pebble size is determined locally by collisions within the population (growth or fragmentation), as well as collisions with the dust (sweep-up and erosion). The size of individual dust particles is a parameter in our model, which we keep constant as motivated by the ongoing production and sweep-up of these smaller grains in the envelopes. Fig. 3.1 provides a qualitative overview of our model, which we work out in the next subsections.

3.2.2 Sedimentation of solids

Particles referred to as dust and pebbles are small enough to be effectively slowed down by gas drag and sink at speeds close to their terminal velocities ($v_{\rm fall}$) relative to the local medium. We adopted a simple, continuous two-regime approximation to the drag force, where the transition from free molecular (Epstein) to continuum flow (Stokes) is set at the canonical value $l_{\rm mfp}/R_{\rm s} = 4/9$ and the terminal velocity is given by (Weidenschilling, 1977a):

$$v_{\rm fall} = \frac{gR_{\rm s}\rho_\bullet}{\rho_{\rm g} v_{\rm th}} \max\left(\frac{4{\rm R_s}}{9{\rm l_{mfp}}}, 1\right), \tag{3.1}$$

where g and $\rho_{\rm g}$ are the local gravitational acceleration and gas density at a distance from the planet's centre r and the subscript s refers to either population of solids (pebbles with size $R_{\rm peb}$ and dust with size $R_{\rm d}$), which share the same material density $\rho_\bullet$. We take the standard ideal gas expressions for the thermal velocity $v_{\rm th}$ and the mean free path of molecules $l_{\rm mfp}$. The second component to the sedimentation velocity of solids is given by the downward flow of gas. Because we are mostly interested in the planet's upper layers that only contain a fraction of the envelope mass, we can approximate this gas velocity ($v_{\rm gas}$) from mass conservation of the gas accretion rate ($\dot{M}_{\rm xy}$) as:

$$v_{\rm gas} = \frac{\dot{M}_{\rm xy}}{4\pi r^2 \rho_{\rm g}}. \tag{3.2}$$

When the solids are small enough, as is the case for the micron-sized dust particles in our model, the local downward flow of gas dominates their total sedimentation velocity. This was described as the advection regime in the work by Mordasini (2014). For larger particles, the free-fall term instead dominates and, generally, the total sedimentation velocity relative

Table 3.1 Descriptions and values of the default model parameters.

Parameter	Description	Value
$M_{\rm p}$	Total planet mass	$5\ {\rm M}_\oplus$
$M_{\rm c}$	Central core mass	$2\ {\rm M}_\oplus$
$\rho_{\rm c}$	Central core density	$3.2\ {\rm g/cm^3}$
$\rho_\bullet$	Dust and pebble density	$3.2\ {\rm g/cm^3}$
$\dot{M}_{\rm peb}$	Pebble accretion rate	$10^{-6}\ {\rm M}_\oplus{\rm /yr}$
$\dot{M}_{\rm xy}$	Gas accretion rate	$10^{-7}\ {\rm M}_\oplus{\rm /yr}$
$R_{\rm d}$	Dust monomer radius	$1\ \mu{\rm m}$
F	Dust replenishment constant	0.1
$v_{\rm frag}$	Fragmentation velocity	0.8 m/s
$T_{\rm vap}$	Sublimation temperature	2500 K
d	Orbital distance	5 AU
$M_\star$	Mass of the central star	$1\ {\rm M}_\odot$
$\rho_{\rm disc,5AU}$	disc density at 5 AU	$5\times10^{-11}\ {\rm g/cm^3}$
$T_{\rm disc,5AU}$	disc temperature at 5 AU	150 K
$\mu_{\rm xy}$	Molecular weight nebular gas	$2.34\ {\rm m_H}$
$\nabla_{\rm ad}$	Adiabatic temperature gradient	0.31

Notes: The disc conditions are adopted from the Minimum Mass Solar Nebula and scale as $T_{\rm disc} \propto d^{-1/2}$, $\rho_{\rm disc} \propto d^{-11/4}$ (Hayashi, 1981; Weidenschilling, 1977b).

to the planet's core is a sum of the two:

$$v_{\rm sed} = v_{\rm fall} + v_{\rm gas}. \tag{3.3}$$

We consider quasi-static envelopes, where the grain transport timescale is assumed to be short relative to the timescale on which the envelope's thermodynamic conditions change. This is a good assumption in the outer layers, provided that the total envelope mass is dominated by the planet's polluted interior. If the solids additionally enter in a spherically symmetric manner, their volume density is given by:

$$\rho_{\rm s} = \frac{\dot{M}_{\rm s}}{4\pi r^2 v_{\rm sed}}, \tag{3.4}$$

which represents radial mass conservation. We do not include large-scale convective motions (Popovas et al., 2019, 2018) in our model, which could locally transport clumps of solids and alter their collision velocities (Ormel & Cuzzi, 2007).

3.2.3 Dust-pebble collisions

Erosion at high velocities

The sizes of pebbles that enter planetary envelopes are determined by their growth, fragmentation and radial drift in the proto-planetary disc (i.e., Drazkowska et al., 2021; Liu & Ji, 2020). The observational evidence points toward typical sizes between 100 μm – 1 cm (i.e., Birnstiel et al., 2010; Carrasco-González et al., 2019; Hull et al., 2018; Kataoka et al., 2016; Ohashi et al., 2020; Tazzari et al., 2020b), which generally decrease with distance to the central star (Tazzari et al., 2020a). During their capture by the planet, pebbles are subject to additional gravitational acceleration and begin to collide with dust at increasing velocities. It was pointed out by Ali-Dib et al. (2020) and Johansen & Nordlund (2020) that if this velocity crosses the threshold for erosion, the dust particles begin to chip off pebble material. This process was measured by Schräpler et al. (2018) to begin at:

$$v_{\mathrm{erosion}} = 2.4\ \mathrm{m/s} \left(\frac{R_{\mathrm{d}}}{1\ \mu\mathrm{m}} \right)^{\frac{1}{1.62}}, \tag{3.5}$$

with an erosive mass loss per collision $\Delta m_{\mathrm{erosion}}$ of:

$$\frac{\Delta m_{\mathrm{erosion}}}{m_{\mathrm{d}}} = 4.3 \left(\frac{v}{10\ \mathrm{m/s}} \right) \left(\frac{R_{\mathrm{d}}}{1\ \mu\mathrm{m}} \right)^{-0.62}, \tag{3.6}$$

which requires a mass ratio below $\sim 10^{-2}$ (Krijt et al., 2015). The proportionality of the erosion efficiency to the collision velocity was also found in numerical investigations (Planes et al., 2017; Seizinger et al., 2013). The fragments that are produced are generally similar or smaller than the projectiles, which in our model are dust grains with mass m_{d}. Because the produced fragments add to the dust population, the erosion of pebbles is a runaway process up to a characteristic size, at which point they slow down sufficiently due to their increased susceptibility to gas drag. In our model with linear downward sedimentation, this is set by the condition that $v_{\mathrm{peb,fall}} = v_{\mathrm{erosion}}$ (assuming $v_{\mathrm{fall,d}} \ll v_{\mathrm{fall,peb}}$):

$$R_{\mathrm{erosion}} = \begin{cases} \dfrac{\rho_{\mathrm{g}} v_{\mathrm{th}} v_{\mathrm{erosion}}}{g \rho_{\bullet}} \ (\mathrm{Epstein}) \\ \\ \dfrac{3}{2} \left(\dfrac{\rho_{\mathrm{g}} v_{\mathrm{th}} l_{\mathrm{mfp}} v_{\mathrm{erosion}}}{g \rho_{\bullet}} \right)^{\frac{1}{2}} \ (\mathrm{Stokes}). \end{cases} \tag{3.7}$$

In order to estimate how rapidly pebbles erode, we formulate the radial equations of mass transfer and size evolution. The typical distance that pebbles travel before they encounter a

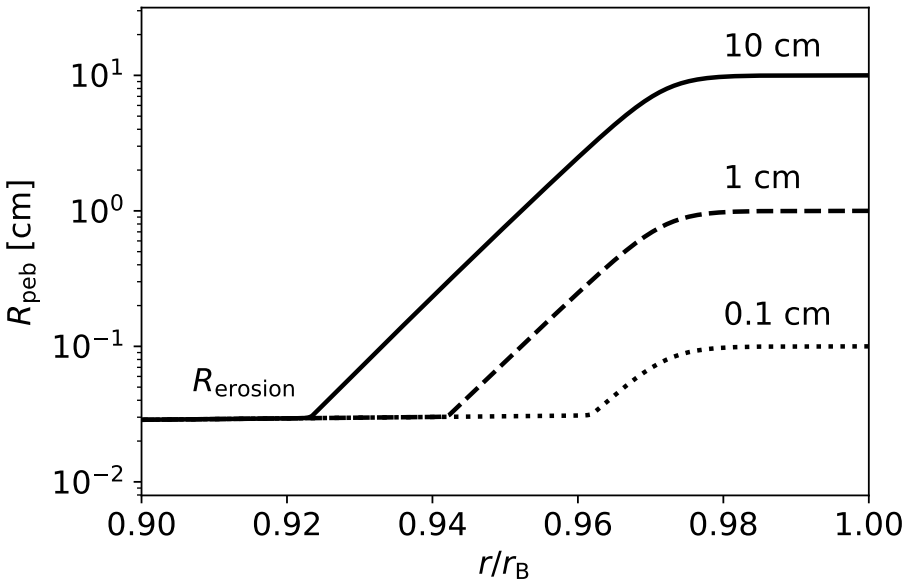

Fig. 3.2 Erosive mass loss of pebbles that enter the envelope of a growing planet at its Bondi radius ($r_{\rm B}$). The parameters of the planet are shown in Table 3.1. The three lines correspond to initial pebble entry sizes of 0.1 cm (dotted), 1 cm (dashed) and 10 cm (solid). Due to the positive feedback of erosive mass-loss on the dust abundance, the pebbles rapidly converge to the size $R_{\rm erosion}$ (Eq. 3.7) where collisions with dust grains switch from causing mass loss via erosion to sticking (sweep-up).

dust particle is given by:

$$l_{\rm sweep,peb} = \frac{m_{\rm d}}{\rho_{\rm d}\sigma_{\rm peb}} \left(1 - \frac{v_{\rm sed,d}}{v_{\rm sed,peb}}\right)^{-1}, \tag{3.8}$$

where $\sigma_{\rm peb} = \pi R_{\rm peb}^2$ is the pebble cross-section. The equations for mass transfer and shrinkage follow as:

$$\left.\frac{d\dot{M}_{\rm peb}}{dr}\right|_{\rm erosion} = \frac{\dot{M}_{\rm peb}}{l_{\rm sweep,peb}} \frac{\Delta m_{\rm erosion}}{m_{\rm peb}}, \tag{3.9a}$$

$$\left.\frac{d\dot{M}_{\rm d}}{dr}\right|_{\rm erosion} = -\frac{d\dot{M}_{\rm peb}}{dr}, \tag{3.9b}$$

$$\left.\frac{dm_{\rm peb}}{dr}\right|_{\rm erosion} = \frac{\Delta m_{\rm erosion}}{l_{\rm sweep,peb}}, \tag{3.9c}$$

where $\dot{M}_{\rm peb}$ is the pebble mass flux. In this simple model, the increase in dust abundance and decrease in pebble size from erosion can be very rapid, even without assuming any additional

acceleration from convective eddies. As an example, we integrate Eqs. 3.9a-3.9c from the Bondi radius inward for a nominal planet of 5 $M_\oplus$ at 5 AU with a disc dust-to-gas ratio of 10^{-3} (see Table 3.1 for all default parameters). The resulting size evolution curves are shown in Fig. 3.2 for three different pebble entry sizes. In all the runs, the pebbles quickly erode down to a characteristic size, at which point their velocity decreases below the threshold for erosion, and they are safe. In this manner, erosion essentially cancels out the upper range of the initial pebble size distribution to more uniform pebble entry sizes, limited by their erosion at the Bondi radius.

Sweep-up at low velocities

If the pebbles are reduced in size below $R_{\rm erosion}$, the relative velocities between the dust and the pebbles drop below $v_{\rm erosion}$ and dust can stick to the pebbles without dislodging additional material. In this sweep-up regime, Eqs. 3.9a - 3.9c still apply with $\Delta m = -m_{\rm d}$:

$$\left.\frac{d\dot{M}_{\rm d}}{dr}\right|_{\rm sweep-up} = \frac{\dot{M}_{\rm peb}}{l_{\rm sweep,peb}}\frac{m_{\rm d}}{m_{\rm peb}}, \tag{3.10}$$

Now, the presence of pebbles acts to reduce the dust abundance, rather than increase it. In Sect. 3.3.2, we will discuss the scenario where the production of dust via erosion and pebble-pebble collisions is in equilibrium with the sweep-up of dust, providing a steady state dust abundance.

3.2.4 Pebble-pebble collisions

When considering straight downward sedimentation, collisions between two pebbles can occur either through Brownian motion or by differential settling (coalescence). The timescale of the latter process decreases with increasing particle size, such that coalescence easily dominates their mutual collision rate when the pebbles are larger than several microns (Boss, 1998; Mordasini, 2014; Nayakshin, 2010; Ormel, 2014). As identical particles settle with the same speed, coalescence within a population formally arises from the parameterized width in the size distribution. In our model, we follow the works by Rossow (1978) and Mordasini (2014), who set the typical mass ratio of collisions to 0.5. Although a simplification, Krijt et al. (2016) and Sato et al. (2016) show that this is a good approximation to the average mass ratio found in coagulation simulations that treat a complete size distribution. When combined with Eq. 3.3, it leads to collisional velocities in the range of $0.21 < v_{\rm col}/v_{\rm fall} < 0.37$ depending on the drag regime. In our model, we neglect this order unity difference in favour of a continuous collision velocity across drag regimes and approximate it as $x_{\rm R} \equiv v_{\rm col}/v_{\rm fall} \simeq 1/3$.

Growth by coalescence at low velocities

When the collision velocities are sufficiently low, contact between pebbles leads to sticking and growth (Dominik & Tielens, 1997). To work out the rate of this growth, the typical travel distance between pebble collisions ($l_{\mathrm{col,peb}}$) can be related to their local size, abundance, and velocity as:

$$l_{\mathrm{col,peb}} = \frac{m_{\mathrm{peb}}}{\rho_{\mathrm{peb}} \sigma_{\mathrm{peb}}} \frac{v_{\mathrm{sed,peb}}}{v_{\mathrm{col,peb}}}. \tag{3.11}$$

Eq. 3.11 scales positively with pebble size, which indicates that smaller particles collide more often. By equating $l_{\mathrm{col,peb}}$ to the scale height $H = k_{\mathrm{b}} T_{\mathrm{g}} / (\mu_{\mathrm{g}} g)$, which represents the characteristic length scale in an envelope, it is possible to approximate the maximum sizes (R_{coal}) to which solids can grow as they sediment:

$$R_{\mathrm{coal}} = \begin{cases} \left(\dfrac{3 x_{\mathrm{R}} H \dot{M}_{\mathrm{peb}} v_{\mathrm{th}} \rho_{\mathrm{g}}}{16 \pi G M_{\mathrm{p}} \rho_{\bullet}^2} \right)^{\frac{1}{2}} \text{(Epstein)} \\ \\ \dfrac{3}{4} \left(\dfrac{x_{\mathrm{R}} H \dot{M}_{\mathrm{peb}} v_{\mathrm{th}} l_{\mathrm{mfp}} \rho_{\mathrm{g}}}{\pi G M_{\mathrm{p}} \rho_{\bullet}^2} \right)^{\frac{1}{3}} \text{(Stokes)}, \end{cases} \tag{3.12}$$

where we assumed that their total velocities are dominated by the terminal component rather than by inward gas flow. In the regime where growth by coalescence provides the limit to their size, the pebbles are typically large enough ($R_{\mathrm{peb}} \gtrsim 100\ \mu$m) that this is indeed a good assumption. The scaling of Eq. 3.12 with the pebble accretion rate shows that a greater mass flux of pebbles leads to more collisions and faster growth. Its dependence on the planet's mass is more complicated. More massive planets have a stronger gravitational pull, which increases the distance at which they can bind gas and, therefore, extends the envelope ($r_{\mathrm{B}} \propto M_{\mathrm{p}}$). This lowers the gravitational acceleration at the planet's outer boundary as a function of mass ($g \propto M_{\mathrm{p}} / r_{\mathrm{B}}^2 \propto M_{\mathrm{p}}^{-1}$). Taken together, the collision distance scales as $l_{\mathrm{col,peb}} \propto M_{\mathrm{p}}$, which balances with the increasing scale height $H \propto M_{\mathrm{p}}$ and leads to a constant value of R_{coal} across planetary masses.

Collisional fragmentation at high velocities

At higher velocities, collisions between pebbles lead to bouncing or even fragmentation. Collision experiments typically find that silicate particles begin to fragment if their collision velocity is larger than 1 m/s (Güttler et al., 2010; Schäfer et al., 2007; Wurm et al., 2005), and up to 10 m/s for water ice grains (Gundlach & Blum, 2015; Musiolik & Wurm, 2019). This fragmentation criterion can be combined with the velocity for the onset of erosion (see

Eq. 3.5) to yield a limit on the terminal velocities of pebbles:

$$v_{\rm lim} = \min\left(v_{\rm erosion}, v_{\rm frag}/x_{\rm R}\right). \tag{3.13}$$

Depending on the dust size and the pebble's material properties, either fragmentation or erosion can be the limiting factor to pebble growth. For simplicity, we take a default dust size of 1 μm and a fragmentation velocity of 0.8 m/s, for which the two velocity limits on the pebble's terminal velocity are both equal to $v_{\rm fall,peb} = v_{\rm lim} = 2.4$ m/s. In Appendix B.2, we vary the limiting velocity within a wider range. We refer to the velocity-limited pebble size as $R_{\rm vlim}$ and it can be found from Eq. 3.1 as:

$$R_{\rm vlim} = \begin{cases} \dfrac{\rho_{\rm g} v_{\rm th} v_{\rm lim}}{g \rho_\bullet} \text{ (Epstein)} \\ \\ \dfrac{3}{2}\left(\dfrac{\rho_{\rm g} v_{\rm th} l_{\rm mfp} v_{\rm lim}}{g \rho_\bullet}\right)^{\frac{1}{2}} \text{ (Stokes)}. \end{cases} \tag{3.14}$$

The dependence of $R_{\rm vlim}$ at the Bondi radius is visualized in Fig. 3.3, with comparison to the limit set by the growth rate. In contrast to $R_{\rm coal}$, the value of $R_{\rm vlim}$ scales positively with the planet's mass. Hence, the sizes of pebbles in small envelopes are typically velocity-limited via erosion or fragmentation, whereas pebbles in more massive envelopes are typically only limited by their rate of growth. Close to the central star, the disc is relatively dense and pebbles of the same size sediment more slowly. Consequently, pebbles erode or fragment down to the smallest sizes when they accrete onto low-mass planets that reside in the outer disc.

Besides limiting the sizes to which pebbles can grow, collisions between pebbles can also potentially result in production of small dust as collisional by-products. In our two-component model, we include this with a fractional dust production efficiency F, which can theoretically be between 0 (no dust production) and 1 (all growth beyond $R_{\rm vlim}$ is turned into dust). Physically, F is a measure for the number of pebble-pebble collisions needed to completely grind down a pebble. The rate at which this dust is produced is then given by the pebble collision rate as:

$$\left.\frac{d\dot{M}_{\rm d}}{dr}\right|_{\rm frag} = -F\frac{\dot{M}_{\rm peb}}{l_{\rm col,peb}}, \tag{3.15a}$$

$$\left.\frac{dm_{\rm peb}}{dr}\right|_{\rm frag} = F\frac{m_{\rm peb}}{l_{\rm col,peb}}. \tag{3.15b}$$

We will discuss reasonable values for the parameter F in Sect. 3.3.3.

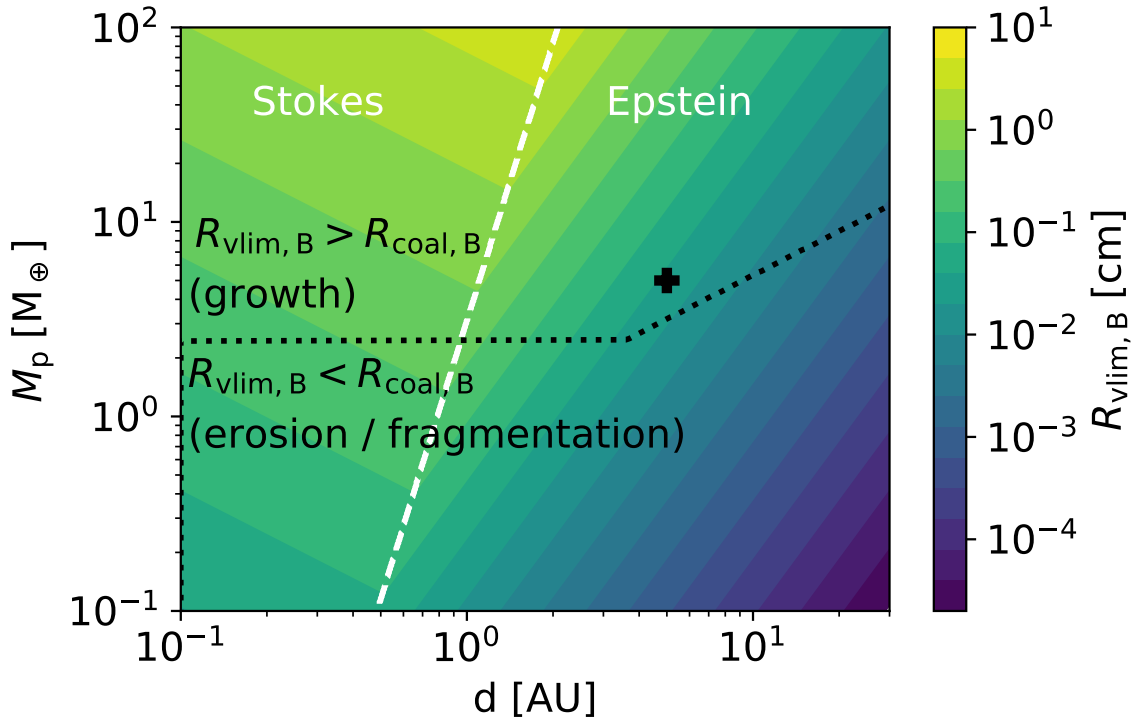

Fig. 3.3 Characteristic pebble size limits at the Bondi radius, plotted with the parameters of Table 3.1. The colours indicate the pebble size where $v_{\mathrm{fall,peb}} = v_{\mathrm{lim}} = 2.4$ m/s, the common limit set via erosion with micron-sized grains and fragmentation. The white dashed line separates the Stokes and Epstein regimes, while the dotted line indicates the regions where either growth rate or erosion/fragmentation limits the local pebble size. The plus sign marks the default planet mass (5 $M_\oplus$) and distance (5 AU).

3.3 Analytical opacity expressions

In this section, we formulate analytical expressions for the opacity contributions from pebbles and dust. For the pebbles, these follow from the previously identified pebble size limits in different regimes ($R_{\mathrm{coal}}, R_{\mathrm{vlim}}$). The basic expression for the Rosseland mean opacity from solids (κ_{s}) is:

$$\kappa_{\mathrm{s}} = \frac{3 Q_{\mathrm{eff}} \rho_{\mathrm{s}}}{4 \rho_\bullet R_{\mathrm{s}} \rho_{\mathrm{g}}}, \tag{3.16}$$

where the extinction efficiency Q_{eff} can be approximated as $Q_{\mathrm{eff}} \simeq \min\left(0.6\pi R_{\mathrm{s}}/\lambda_{\mathrm{peak}}, 2\right)$, with the peak wavelength of the emitted photons by the local gas $\lambda_{\mathrm{peak}}(\mathrm{cm}) = 0.290/T_{\mathrm{g}}$ (Wien's law). Laboratory experiments provide a more detailed temperature scaling of Q_{eff}, as well as a factor of ~ 2 between different species (Bitsch & Savvidou, 2021; Movshovitz & Podolak, 2008). We do not include these additional details here, but do account for the most important opacity difference between species, which is that solid particles are only present in

layers of planetary envelopes that are sufficiently cool for the solids to escape sublimation. In the case of silicates, which we consider as the default composition of pebbles and dust, this threshold is positioned deep inside planetary envelopes around ~ 2500 K.

3.3.1 Pebble opacity expression

The first opacity regime is the growth-limited regime, which applies when pebbles are travelling relatively slowly through planetary envelopes and experience sticking collisions, rather than erosion or fragmentation. In this case, their size can be approximated by R_{coal} (Eq. 3.12) and their opacity contribution is independent of their accretion rate. It follows the same equation in both drag regimes:

$$\kappa_{\mathrm{coal}} = \frac{Q_{\mathrm{eff}}}{x_{\mathrm{R}} H \rho_{\mathrm{g}}}, \tag{3.17}$$

which was the main finding of Mordasini (2014). As indicated by Fig. 3.3 at the Bondi radius, this growth-limited regime is mainly applicable in the envelopes of more massive planets, whose larger envelopes allow pebbles to sediment more slowly. The required planetary size to enter this regime at the same accretion rate is an increasing function of distance from the central star, as pebbles in the tenuous outer disc sediment faster than those closer in. When the conditions are such that the terminal velocity of pebbles exceeds v_{lim}, the size to which solids can grow becomes limited to R_{vlim} (Eq. 3.14) by either fragmentation or erosion. In this regime, the pebble opacity is instead given by:

$$\kappa_{\mathrm{vlim}} = \frac{3 Q_{\mathrm{eff}} \rho_{\mathrm{peb}}}{4 \rho_{\bullet} R_{\mathrm{vlim}} \rho_{\mathrm{g}}} \tag{3.18a}$$

$$= \begin{cases} \dfrac{3 Q_{\mathrm{eff}} \dot{M}_{\mathrm{peb}} g}{16 \pi r^2 \rho_{\mathrm{g}}^2 v_{\mathrm{th}} v_{\mathrm{lim}} (v_{\mathrm{lim}} + v_{\mathrm{gas}})} \ (\text{Epstein}) \\ \\ \dfrac{Q \dot{M}_{\mathrm{peb}}}{8 \pi r^2 (v_{\mathrm{lim}} + v_{\mathrm{gas}})} \left(\dfrac{g}{\rho_{\bullet} \rho_{\mathrm{g}}^3 v_{\mathrm{th}} v_{\mathrm{lim}} l_{\mathrm{mfp}}} \right)^{\frac{1}{2}} \ (\text{Stokes}). \end{cases} \tag{3.18b}$$

In combination, the pebble opacity can be approximated analytically from the expressions above by determining the appropriate regime based on the characteristic sizes, which have to

be evaluated locally in the envelope:

$$\kappa_{\rm peb} = \begin{cases} \kappa_{\rm vlim} \text{ if } R_{\rm vlim} < R_{\rm coal} \\ \\ \kappa_{\rm coal} \text{ if } R_{\rm vlim} > R_{\rm coal}. \end{cases} \tag{3.19}$$

For completeness, we also include the simplest scenario where solids enter a planetary envelope with a constant size that remains unchanged during their sedimentation. While we follow the more physically motivated expressions from Eq. 3.19 in the rest of this work, the scenario of a constant pebble size might be applicable if pebbles are both sufficiently small to escape fragmentation and bounce rather than stick upon contact, as is the case if the pebbles are modelled as small molten chondrules, rather than dust agglomerates. Under this assumption, the opacity follows from Eq. 3.16, 3.3 as (see also the work by Ormel et al. 2021):

$$\kappa_{\rm peb,cst} = \frac{3 Q_{\rm eff} \dot{M}_{\rm peb}}{16\pi r^2 \rho_\bullet \rho_{\rm g} R_{\rm peb} v_{\rm sed,peb}}. \tag{3.20}$$

3.3.2 Steady state between dust replenishment and sweep-up.

In previous grain growth models (Mordasini, 2014; Ormel, 2014), a large influx of small dust grains in the envelope's outer layers was found to quickly diminish due to mutual sticking collisions. Hence, even when a significant fraction of the pebble mass is transferred to dust grains upon entry by efficient erosion (sect. 3.2.3), the smallest particles soon disappear from the envelope, growing to the same limiting sizes as pebbles that we discussed in the previous section. The diminishing of the small grains abundance is further hastened by the sweep-up of pebbles below their erosion size. In order to maintain a dust population, therefore, it must be supplied by either continued erosion of pebbles that grow beyond the erosion limit, or by fragmentation. If that happens, the dust abundance has both a source and a sink term, generating a steady state when they are equal and opposite:

$$\left.\frac{d\dot{M}_{\rm d}}{dr}\right|_{\rm sweep-up} = -\left.\frac{d\dot{M}_{\rm d}}{dr}\right|_{\rm frag}, \tag{3.21}$$

from which their respective volume densities follow as

$$\frac{\rho_{\rm d}}{\rho_{\rm peb}} = F x_{\rm R} \left(1 - \frac{v_{\rm sed,d}}{v_{\rm sed,peb}}\right)^{-1}. \tag{3.22}$$

Eq. 3.22 implies that in a steady state between fragmentation/erosion and sweep-up, most of the radial mass flux is generated by the larger sedimenting pebbles. But if F is near unity, the volume density of grains can nevertheless be comparable to that of the pebbles due to their slower sedimentation.

3.3.3 Dust opacity in steady state

The dust opacity in steady state between dust production and sweep-up is given by (assuming $R_{\rm d} \ll R_{\rm peb}$):

$$\kappa_{\rm d} = \frac{3 Q_{\rm eff,d} \rho_{\rm d}}{4 \rho_\bullet R_{\rm d} \rho_{\rm g}} \tag{3.23a}$$

$$= \kappa_{\rm peb} \frac{Q_{\rm eff,d}}{Q_{\rm eff,peb}} \frac{R_{\rm peb}}{R_{\rm d}} F x_{\rm R}. \tag{3.23b}$$

Eq. 3.23b is proportional to the pebble opacity, only differing from its trends due to the additional dependence on the pebble size. Because the opacity in planetary envelopes is generally far more variable than the pebble size, the opacity from dust in steady state generally follows a very similar trend to that of the pebbles. The parameter F is largely unconstrained, and can vary between $0-1$, with a value around unity more appropriate in the erosion-limited regime where any pebble growth beyond the erosion limit is converted into dust. Lower values, where collisions convert a smaller fraction of their mass into dust, are likely more appropriate in cases where either fragmentation or growth (both pebble-pebble interactions) limits the pebble size. We show in the next section that with our default value of $F = 0.1$ the dust opacity is typically comparable to the pebble contribution.

3.4 Envelope opacity trends

In this section, we apply our model for the opacity of solids to a broad parameter space in order to investigate the trends in envelopes of planets throughout the disc. We first detail our envelope model and then evaluate the opacity of dust and pebbles as a function of depth (Figs. 3.4-3.6) for a range of planetary masses, distances and pebble accretion rates. After that, we consider the opacity at the boundary between radiative and convective zones to visualize the same trends in a single graph (Fig. 3.7).

3.4.1 Envelope structure

We focus our modelling efforts on the outer envelope down to the polluted region, ulterior to which no significant sublimation occurs and the opacity of solids is relevant. We refer to an accompanying paper by Ormel et al. (2021) and independent studies by Bodenheimer et al. (2018) and Valletta & Helled (2020) for detailed numerical models of polluted envelope interiors. The structure of the outer envelope is simple by contrast, as it shares its gaseous composition with the surrounding disc and is unaffected by self-gravity prior to the onset of runaway accretion. In quasi-hydrostatic equilibrium, its structure equations read:

$$\frac{\partial m}{\partial r} = 4\pi r^2 \rho_{\rm g}, \tag{3.24a}$$

$$\frac{\partial P_{\rm g}}{\partial r} = -\frac{G M_{\rm p} \rho_{\rm g}}{r^2}, \tag{3.24b}$$

$$\frac{\partial T_{\rm g}}{\partial r} = \frac{\partial P_{\rm g}}{\partial r}\frac{T_{\rm g}}{P_{\rm g}} \min\left(\nabla_{\rm rad}, \nabla_{\rm ad}\right), \tag{3.24c}$$

where

$$\nabla_{\rm rad} = \frac{3\kappa L P_{\rm g}}{64\pi\bar{\sigma} G M_{\rm p} T_{\rm g}^4} \tag{3.25}$$

is the radiative temperature gradient, which contains the gravitational and Stefan-Boltzmann constants ($G, \bar{\sigma}$) and is a function of the luminosity L and the total Rosseland mean opacity κ. In our model, we assume a constant (global) accretion luminosity equal to $L = GM_{\rm c}\dot{M}_{\rm peb}/r_{\rm c}$ as is commonly done. However, we note the caveat issued by Ormel et al. (2021), that this term can in reality vary substantially, as refractory material can be absorbed before sinking to the core and a significant portion of the gravitational energy can be processed in envelope mixing or used to heat the surrounding gas.

The total envelope opacity is defined as the sum of the gas, dust, and pebble contributions ($\kappa = \kappa_{\rm gas} + \kappa_{\rm d} + \kappa_{\rm peb}$). The gas opacity is often taken from lookup tables (i.e., Freedman et al., 2014, 2008) that contain contributions from different gaseous species. We do not model this contribution here, but choose to take a simple reference value of $\kappa_{\rm gas}$ as an analytical scaling of the molecular opacity from Bell & Lin (1994):

$$\kappa_{\rm mol} = 10^{-8} \rho_{\rm g}^{\frac{2}{3}} T_{\rm g}^3 \ {\rm cm^2 g^{-1}}, \tag{3.26}$$

which was also used in Brouwers & Ormel (2020); Brouwers et al. (2018). A simple molecular opacity scaling has the advantage that trends in the opacity from solids, which we seek to characterize here, can be more easily isolated in the results.

In order to compute the opacity within the planetary envelope, we radially integrate the envelope structure equations (Eqs. 3.24a-3.24c) together with the steady-state opacity equations (Eqs. 3.19, 3.23b, 3.26). We use the ideal gas equation to relate the local density to the pressure and temperature, which is justified in the upper layers of the atmosphere that are evaluated here. For the outer boundary of the integration, we take the conventional choice of the minimum between the Hill and Bondi radii, where molecules are kinetically and thermally bound to the planet. The outer boundary conditions are equal to the local disc environment, for which we assume the simple temperature and density relations from the Minimum Mass Solar Nebula (see Table 3.1) (Hayashi, 1981; Weidenschilling, 1977b). For the inner boundary of our integration, we stop at 2500 K, where the saturated vapour pressure of silicate becomes similar to the hydrostatic pressure of the planetary envelope (Brouwers & Ormel, 2020; Ormel et al., 2021). Beyond this point, our model ceases to be valid, as the composition of the envelope becomes substantially altered by silicate vapours, which increases the molecular opacity (Freedman et al., 2014), but rapidly diminishes the contribution from solids. The integration itself is performed with a fourth-order Runge-Kutta scheme, whose radial step is dynamically set to tolerate a maximum change in radius, pressure, temperature and opacity of 10^{-3} per step.

3.4.2 Trend with planet mass

In Fig. 3.4, we plot the pebble sizes (panel a) along with their opacity (b), and the dust opacity (c) of our steady state model for a range of masses that we logarithmically vary between 0.5-20 $M_\oplus$. The other parameters in the runs share the default values from Table 3.1. We first discuss the top panel, which shows two separate trends depending on the process that limits the pebble size. In the velocity-limited regime ($R_{\rm peb} = R_{\rm vlim}$, yellow colour range), the pebble size is limited by either the erosion with small dust grains or by collisions with other pebbles. Because the Bondi radius is positioned closer to the core in low-mass planets, pebbles of the same size are able to sediment faster ($g \propto M_{\rm p}^{-1}$) and the same terminal velocity limit leads to larger pebbles in more massive planets. Once the planet becomes massive enough that $R_{\rm vlim} > R_{\rm coal}$, the pebble size ceases to be velocity-limited and instead becomes only limited by the rate of growth. In this growth regime, the pebble size is nearly invariant with a further increase in the planet mass (see Sect. 3.2.4).

Regardless of the regime, we find that the opacity from solids declines steeply when planets become more massive. This can be explained with two competing processes. As planets accrete material, the surface area of their Bondi sphere increases quadratically with mass, and the same pebbles obscure a smaller fraction of the envelope. Part of this trend is compensated by the slower sedimentation of pebbles in more massive planets, but the

net result is that the pebble volume density scales as $\rho_{\rm peb} \propto M_{\rm p}^{-1}$ at the Bondi radius. If the pebble size is instead limited via erosion and fragmentation, in which regime their sizes also scale positively with planet mass, the opacity from solids is an even steeper declining function. The pebble and dust opacity trends are almost identical because they are nearly proportional to one another (Eq. 3.23b).

The difference in opacity between the low- and high-mass planets begins at around three orders of magnitude at the Bondi radius, and these differences increase further with depth. Most of this increase is due to the transition from Epstein to Stokes drag that occurs in the more massive envelopes, where larger pebbles enter a denser medium. With this, the difference at the Bondi radius is extended further, to over six orders of magnitude between the plotted values ($0.5 - 20\,{\rm M}_\oplus$) at the RCB.

3.4.3 Trend with orbital separation

Next, we evaluate the importance of the planet's distance to the central star in Fig. 3.5, where we plot five lines that indicate semimajor axes between 0.1-30 AU. The distance to the central star determines the local thermodynamic conditions of the surrounding disc. In our model, we use the Minimum Mass Solar Nebula, where the temperature and density scale as $T_{\rm disc} \propto d^{-1/2}$, $\rho_{\rm disc} \propto d^{-11/4}$ (Hayashi, 1981; Weidenschilling, 1977b). While the local conditions will also generally differ between different disc types and models, the general trend of lower densities and temperatures in the outer regions that receive less light is universal. This trend is important, because a more tenuous medium allows pebbles of the same size to sediment faster. The velocity-limited sizes, therefore, decrease with distance from the star. Pebbles also experience fewer collisions, reducing their rate of growth as well. This trend is reflected in Fig. 3.5, where the opacity of solids at the Bondi radius is seen to increase with orbital separation, regardless of the regime.

The opacity trend with distance becomes more complex at greater depth, where the opacity of solids at the RCB is seen to converge to similar values for the parameters in Fig. 3.5. In these runs, the pebble sizes of planets in the outer disc increase with depth as the surrounding medium becomes denser, and the same velocity limit allows for larger pebbles. As a result, the opacities also decline with depth until they are surpassed by the molecular contribution near the RCB, where the local pebble sizes become limited by growth with the parameters plotted here. For smaller planets in the outer disc, or those that are accreting pebbles at a higher rate, the pebble sizes at the RCB instead remain limited by fragmentation and erosion. We will look into the distance trend of this velocity-limited opacity regime in Sect. 3.4.5.

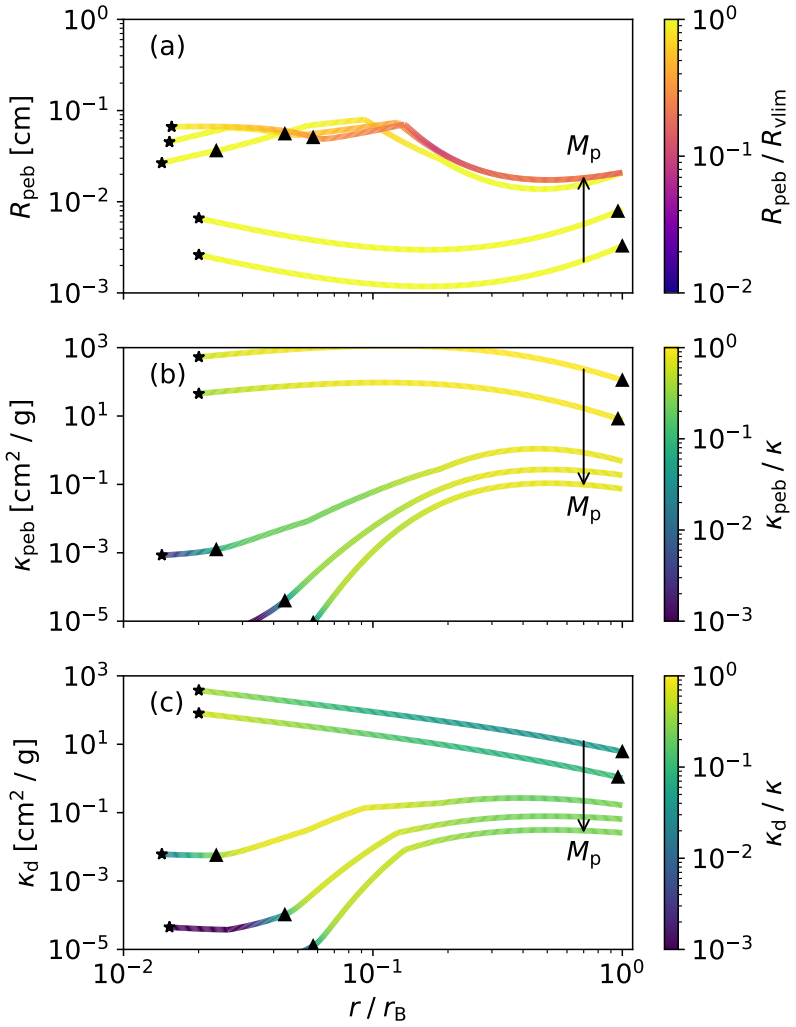

Fig. 3.4 Pebble growth tracks (a), their resulting pebble opacity (b), and produced dust opacity (c) for a standard set of model runs at 5 AU (see Table 3.1). The different lines indicate a range of planet masses, with the arrow indicating a logarithmic progression from $0.5 - 20\ M_\oplus$. The triangles indicate the location of the RCB, while the stars indicate the depth where the ambient temperature exceeds the sublimation temperature (2500 K) and the opacity from solids vanishes. The colours in the top panel show the ratio of the pebble size in the model relative to R_{vlim} (Eq. 3.14). The colours in the two lower panels show the relative value of the indicated opacity to the total opacity.

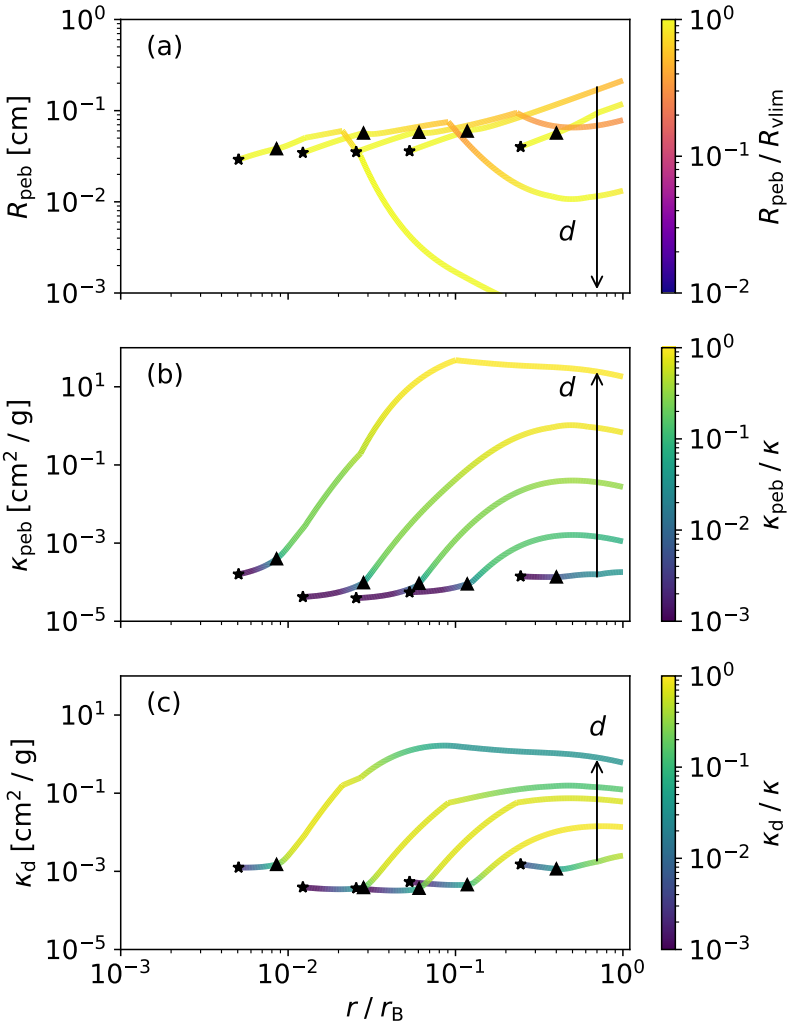

Fig. 3.5 Pebble growth tracks (a), their resulting pebble opacity (b), and produced dust opacity (c) for a standard set of model runs at 5 AU (see Table 3.1). This figure is the same as Fig. 3.4, but now the mass is fixed at the default 5 $M_\oplus$ and the planet's distances from the star are varied logarithmically from $0.1 - 30$ AU.

3.4.4 Trend with pebble accretion rate

Finally, we examine the opacity trend with the pebble accretion rate in Fig. 3.6, where it is varied between $10^{-7} - 10^{-4}$ $M_\oplus$/yr. This probes both the variation in solid mass flux and accretion luminosity, which are proportional ($L = GM_c\dot{M}_{peb}/r_c$) in our model. The effect on the pebble sizes (top panel) can be divided into two regimes, depending on whether the pebble size is limited by growth (orange colour range) or velocity (yellow colour range). In the former case, the pebble size scales positively with the accretion rate, as an increased pebble mass flux increases the number of collisions during their sedimentation and allows for faster growth. In this regime, the pebble opacity (per Eq. 3.17) is not explicitly dependent on the mass flux, aside from the extinction efficiency which is higher for larger pebbles in these conditions. The second effect is that a higher luminosity increases the local radiative temperature gradient, which alters the conditions of the local medium, ultimately affecting the opacity as well.

When the accretion rate is increased beyond $\sim 10^{-5}$ $M_\oplus$/yr for the plotted default parameters, the pebble size becomes velocity-limited at the fragmentation-erosion barrier. At this point, any additional material no longer increases the pebble size and directly increases their volume density, allowing the opacity to rise sharply. The increased opacity in these runs with high pebble accretion rates turns the envelopes almost entirely convective (see the upper two curves), with RCB locations at or close to the Bondi radius.

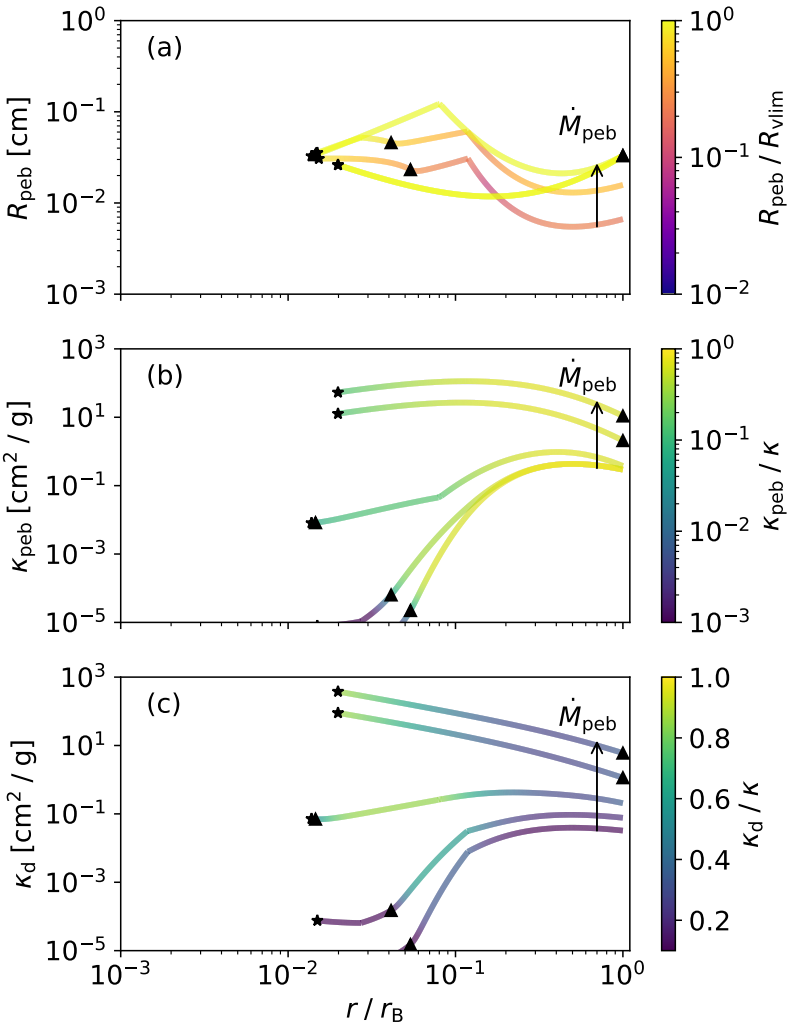

Fig. 3.6 Pebble growth tracks (a), their resulting pebble opacity (b), and produced dust opacity (c) for a standard set of model runs at 5 AU (see Table 3.1). This figure is the same as Fig. 3.4, but now the mass is fixed at the default 5 $M_\oplus$ and the pebble accretion rates are varied logarithmically from $10^{-7} - 10^{-4}$ $M_\oplus$/yr.

3.4.5 Description of three opacity regimes

In order to visualize the broad opacity trends more clearly, we also evaluate a large 2D grid of envelope opacities at the RCB (κ_{rcb}) as a function of their distance to the star and planetary mass. While the opacity throughout the entire radiative zone is relevant for the envelope's structure, its value at the boundary between the radiative and convective zones is generally considered the most important. This is both because most of the radiative portion of the envelope's mass is contained near the RCB and because it controls the rate at which the convective interior cools (i.e., Ginzburg et al., 2016; Lee & Chiang, 2015).

The results of these runs are shown in Fig. 3.7, ordered into four panels that correspond to different pebble accretion rates, which typically increase as planets grow and capture pebbles more efficiently (Lambrechts & Johansen, 2012; Liu et al., 2019; Ormel & Klahr, 2010). The opacity trends reflect the discussions of the previous subsections but also contrast the opacity of solids and molecules, which generally follow a dichotomy based on the planet's distance and mass. Hot molecules contribute most of the envelope's opacity in the warm and dense inner disc, where solids sediment slowly and coalesce to form larger agglomerates. Because the molecular opacity increases with both temperature and density, this provides a clear contrast based on orbital separation. The molecular opacity at the RCB is not very sensitive to planet mass, as can be seen from the nearly vertical opacity contours. In contrast, the opacity from solids declines steeply as planets grow more massive and particles sediment more slowly due to the higher densities.

Fig. 3.7 shows that the total envelope opacity can be divided into three regimes. First, the molecular opacity regime applies to higher-mass planets in the inner disc that are accreting pebbles at a low rate. In this regime, the opacity at the RCB is almost independent of planet mass and steeply declines with orbital separation. Second, the growth-limited solids opacity regime applies to higher-mass planets in the outer disc that are accreting pebbles at a low rate. In this regime, the RCB opacity is almost independent of distance and declines steeply with planet mass. The opacity is invariant to an increase in the mass flux, as any additional mass just adds to pebble growth. However, the RCB opacity scales positively with the accretion luminosity. Third, the velocity-limited solids opacity regime applies to lower-mass planets that are accreting pebbles at a sufficiently high rate. It is typically characterized by fully convective envelopes, with the plotted RCB located at the Bondi radius. A higher pebble accretion rate increases the volume density of solids in this regime, and greatly increases the parameter range where it applies (to include larger M_p and smaller d).

One caveat to this third regime is that if the entire outer envelope is convective, the envelope density remains relatively low and, as pointed out by Johansen & Nordlund (2020), the envelope can then locally become radiative at the depth where solids sublimate (2500 K in our model). At this point, which roughly coincides with the dissociation temperature of molecular hydrogen, only the molecular contribution to the opacity remains. If there are sufficient free electrons to ionize the hydrogen and produce H^-, this becomes the dominant opacity component (Lee & Chiang, 2015). The situation in this regime is further complicated by the balancing effect of a compositional gradient that also begins to form at these temperatures (Bodenheimer et al., 2018; Müller et al., 2020), in which the Ledoux criterion (Ledoux, 1947) has to be used to evaluate stability against convection, rather than

the Schwarzschild criterion. The thermodynamic consequences of this transition region are an active topic of investigation (Ormel et al., 2021; Valletta & Helled, 2020) and are outside the scope of this opacity study, where we focus specifically on the opacity of solids in the outer envelope. We provide a broader discussion of this potential zone in Sect. 3.6.

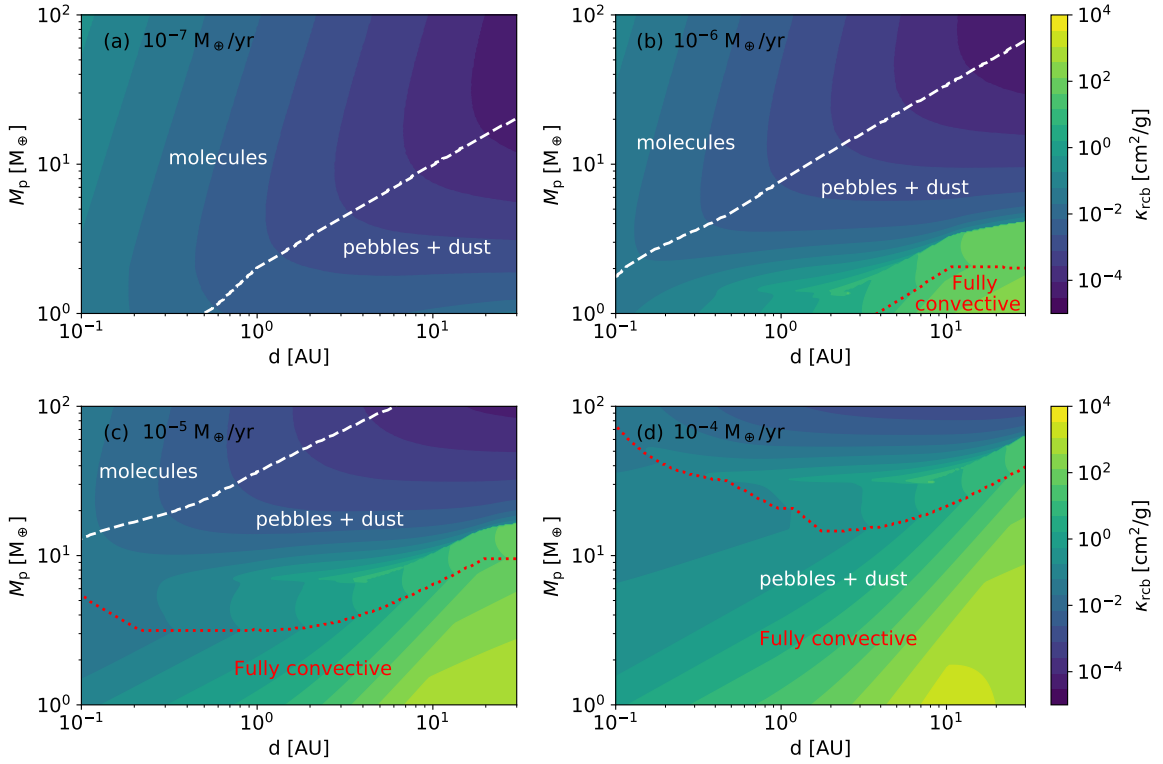

Fig. 3.7 Compilation grid of 10^6 runs, where the colours indicate the opacity at the RCB as a function of the planet's semi-major axis and mass at four different pebble accretion rates. The white dashed lines divide the zones where different opacity contributions dominate. The red dotted lines mark the parameter space where the entire envelope is convective due to high opacities in the velocity-limited regime.

3.5 Implications for giant planet formation

Planets transition from slow to runaway gas accretion when they reach a critical point, where their self-gravity begins to exceed the envelope's pressure support. A transparent envelope is characterized by more efficient radiative energy transport in the outer regions, which results in faster cooling and more rapid gas accretion. As a result, both analytical and numerical works (e.g., Lee & Chiang, 2015; Mizuno, 1980; Movshovitz et al., 2010; Pollack et al., 1996; Stevenson, 1982) have shown that the mass at which planets transition to runaway

growth scales positively with the envelope's opacity. In this section, we apply our model to examine this trend across the proto-planetary disc.

3.5.1 Trends in the critical metal mass

In a previous work (Brouwers & Ormel, 2020), we showed that the traditional criterion of a critical core mass becomes meaningless if the growth of the core is limited. For this reason, we introduced and derived an analogous criterion called the "critical metal mass", which measures the total metal content of a planet at the onset of runaway gas accretion. It shares the opacity dependence with previous expressions for the critical core mass, but is additionally an explicit function of the core mass itself. One limitation of our previous work was that we modelled envelopes with an isothermal radiative layer, which is a good assumption for grain-free envelopes, but which becomes invalid for envelopes with higher opacities due to the presence of solids. In order to correctly account for thermodynamic changes in the radiative part of the envelope, we slightly modify the analytical structure model of Brouwers & Ormel (2020) in Appendix B.1 to be applicable to envelopes with non-isothermal radiative regions. The critical metal mass, defined as the total mass of solids accreted at the onset of runaway accretion, then becomes an explicit function of both $T_{\rm rcb}$ and $\kappa_{\rm rcb}$:

$$M_{\rm z,crit} \approx 5.5\,{\rm M}_\oplus \left(\frac{\kappa_{\rm rcb}}{0.01\ {\rm g\ cm^{-2}}}\right)^{\frac{1}{6}} \left(\frac{d}{\rm AU}\right)^{\frac{7}{108}} \left(\frac{T_{\rm vap}}{2500\ {\rm K}}\right)^{\frac{8}{27}} \left(\frac{\dot{M}_{\rm peb}}{10^{-6}\,{\rm M}_\oplus\ {\rm yr^{-1}}}\right)^{\frac{1}{6}} \left(\frac{M_{\rm c}}{\rm M_\oplus}\right)^{\frac{1}{2}} \left(\frac{T_{\rm rcb}}{T_{\rm disc}}\right)^{-\frac{126}{972}}. \tag{3.27}$$

In line with the findings by Ormel et al. (2021), we assume core growth to be uniformly limited to 2 $\rm M_\oplus$, with the rest of the solids being absorbed in the deep envelope. We plot the resultant critical metal masses as a function of orbital separation for three accretion rates in Fig. 3.8. The black lines include the opacity from dust and pebbles, contrasted with the gray lines that assume entirely grain-free envelopes.

The general shape of the curves in Fig. 3.8 reflects the opacity trends described in the previous section. Molecules dominate the opacity of envelopes in the hot inner disc, where the critical mass is seen to decrease with orbital separation. In the grain-free curves, this downward trend continues toward the outer disc, where the critical mass reaches very low values of only a few Earth masses. Accounting for the opacity of pebbles and dust breaks this trend in the intermediate disc, where solids begin to dominate the opacity of the envelopes. This halts the decline of the critical mass, which then instead flattens toward the outer disc.

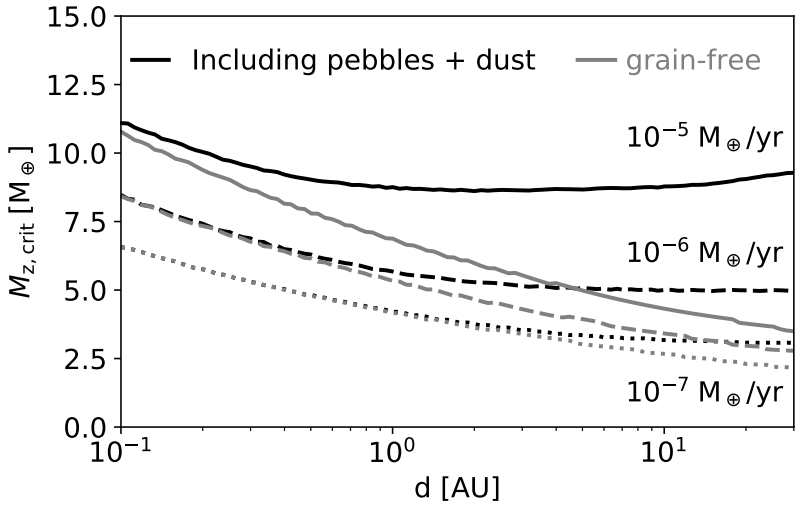

Fig. 3.8 Trends in the critical metal mass as a function of distance. The different lines correspond to a variation in solids accretion rates: 10^{-7} $M_\oplus$/yr (dotted), 10^{-6} $M_\oplus$/yr (dashed), 10^{-5} $M_\oplus$/yr (solid), with proportional gas accretion $\dot{M}_{\mathrm{xy}}/\dot{M}_{\mathrm{peb}} = 5$ and the remaining parameters set by Table 3.1. Planets with grain-free envelopes (gray lines) exhibit a downward trend with orbital separation because the molecular opacity scales positively with temperature. The opacity generated by pebbles and dust (black lines) increases the critical mass significantly in the outer disc, especially at higher accretion rates.

Besides its variation with distance, the critical metal mass is also positively dependent on the solids accretion rate. This is both due to the increased luminosity and the increased opacity from solids, although the two are linked thermodynamically (see Sect. 3.4.4). We note that in reality, a pebble-accreting planet would not experience a single pebble accretion rate during its evolution, but one that generally increases as it gains in mass and is able to capture pebbles more efficiently.

Physically, the trends in the critical metal mass translate to similar trends in the occurrence rates of gas giant planets. Data from the Kepler mission have provided good exoplanet abundance statistics up to about 1 AU in semimajor axis (Batalha et al., 2013; Borucki et al., 2010, 2011), which show a general increase in the abundance of giant planets with distance in this range (Dong & Zhu, 2013; Howard et al., 2012; Santerne et al., 2016). When combined with data from radial-velocity measurements (Mayor et al., 2011), it shows a break in the giant planet occurrence rate between 2-3 AU, with a declining power law beyond this value (Fernandes et al., 2019). While other factors are certainly at play in planet formation across the proto-planetary disc, these trends are generally well-matched by the critical metal mass predicted by our opacity model.

3.5.2 Implications for the formation of Uranus and Neptune

Far out in the disc, one of the key theoretical challenges is to explain how Uranus and Neptune accreted their substantial masses of $\sim 15\ M_\oplus$ without entering runaway growth (Helled & Bodenheimer, 2014; Helled et al., 2020). In the model developed by Lambrechts et al. (2014), it is suggested that the accretion of solids continued throughout the disc lifetime, and that the heat from impactors kept the envelope stable during its evolution. However, the planet's cold birth environments and low molecular opacity means that their accretion luminosity is easily radiated away, causing grain-free envelopes to implode into gas giants before they have grown beyond a few Earth masses. In order to prevent runaway accretion, the planets must either form when most of the nebula is gone (Lee & Chiang, 2016; Ogihara et al., 2020), or their envelopes must still be sufficiently opaque that their heat does not escape so quickly. The common approach to this problem is to assume that the envelopes contain a large ISM-like opacity from small dust grains. In line with previous works on coagulation (Mordasini, 2014; Movshovitz et al., 2010; Movshovitz & Podolak, 2008; Ormel, 2014), our results indicate that such a high opacity is not realistic when grain growth determines the pebble sizes. It is possible, however, for planetary envelopes in the outer disc to attain these high opacities if the pebble sizes are velocity-limited by fragmentation or erosion. As we show in Fig. 3.7, this requires the planet to continuously accrete pebbles at a sufficiently high rate.

Alternatively, planets begin to carve partial gaps around their orbit when they grow beyond several Earth masses (Paardekooper & Mellema, 2004, 2006). When they continue to grow, they locally invert the pressure gradient in the disc and stop accreting pebbles, a criterion that is known as the pebble isolation mass (Ataiee et al., 2018; Morbidelli et al., 2015; Morbidelli & Nesvorny, 2012). As shown by Bitsch et al. (2015) and Bitsch et al. (2018), it is important to account for the cooling of the Solar nebula and the reduced disc scale height over time. In these simulations, the pebble disc scale height is found to reduce sufficiently in the first few Myrs that both Uranus and Neptune can reach their isolation mass and stop accreting pebbles. This introduces a new issue, however, as ceasing the supply of accretion heat can again easily trigger cooling and rapid gas accretion. Unlike the close-in super-Earths and mini-Neptunes, which can be prevented from accreting gas by entropy advection (Ali-Dib et al., 2020; Cimerman et al., 2017; Kurokawa & Tanigawa, 2018; Moldenhauer et al., 2020; Ormel et al., 2015), the ice giants will rapidly accrete gas due to their Kelvin-Helmholtz contraction. The solution offered by Alibert et al. (2018) and Guilera et al. (2020) is that the reduction in pebble accretion can be compensated by the accretion of planetesimals, which could naturally form at the surrounding pressure bump. In a similar vein, Lambrechts & Lega (2017), Chen et al. (2020), and Bitsch & Savvidou

(2021) reason that while centimetre-sized pebbles are easily blocked by a local pressure bump, small dust ($\leq 200\ \mu$m) is sufficiently coupled to the gas to pass through (Bitsch et al., 2018; Haugbølle et al., 2019; Pinilla et al., 2016; Weber et al., 2018) and provide the required opacity to prevent rapid cooling. Our results indicate that this solution essentially faces the same problem as continuous pebble accretion: Regardless of whether the mass is supplied by pebbles or planetesimals, the opacity from solids is insufficient to prevent runaway growth without a high accretion rate. In fact, the required planetesimal accretion rate is even higher than the equivalence in pebbles because the abundance of small solids is insufficient to reach the velocity-limited regime and the envelope opacity thus remains low.

The implication is that regardless of whether the ice giants became isolated from the pebble flow, their formation requires the constant accretion of material at high rates if they formed in-situ. This introduces a timescale problem, as they must then have formed in the window where they had enough time to accrete their observed masses, but not too early such that they accreted too much material and became gas giants. Accurately estimating the duration of this formation window requires more detailed models of the ice giant's interiors, which are currently not yet well constrained (Helled et al., 2020; Vazan et al., 2020). In addition, it is important to account for the cooling of the solar nebula over time. The cooling of the surrounding disc has the same general effect as increasing the planet's distance from the central star (reduced $T_{\rm disc}, \rho_{\rm disc}$), which we showed increases the envelope opacity contribution of solids.

3.6 Discussion

3.6.1 Comparison with contemporary works

In this work, we focused on the growth and destruction of solids as they travel through planetary envelopes, ignoring their evolution prior to accretion. A contrasting approach was taken in a contemporary work by Bitsch & Savvidou (2021), who modelled the size distribution of solids in the disc similar to Savvidou et al. (2020), with the assumption that their distribution and opacity in the disc mid-plane also apply to the envelope's interior. We present evidence that the opacities at the RCB are actually very different from the disc due to a typically much higher gas temperature and density, as well as the significant size evolution of solids in the envelope. Larger pebbles fragment or face erosion when they enter planetary envelopes, while the lower end of the accreted size distribution experiences significant growth during sedimentation. Effectively, we predict much smaller envelope opacities in the growth-limited regime than Bitsch & Savvidou (2021), although high opacities remain possible in the

velocity-limited regime. Nevertheless, while we argue that the sizes of solids in the envelope are disconnected from their size distribution in the disc, modelling their size evolution in the disc remains important for physical estimates of their accretion rates and efficiency.

An alternative approach to modelling the envelope opacity is presented by Chachan et al. (2021), which is based on the work by Lee & Chiang (2015). The authors argue that the sublimation of dust leads to a second radiative zone at the sublimation front, with an inner boundary around 2500 K, where dissociation of H_2 provides a new opacity source in the form of H^-. The appearance of this inner radiative zone is based on the assumption that the envelope's outer layers are convective due to a high dust opacity. The requirement of free elections to form H^- means that the opacity studied by Chachan et al. (2021) is proportional to the local metallicity of the gas, which the authors take equal to the local dust-to-gas ratio of the disc, yielding an opacity minimum at intermediate distances (1-10 AU). While this is an interesting result, we note that the interior region around 2500 K is highly complex due to the compositional gradient that forms at this temperature, which affects the criterion for convective stability (Ledoux, 1947; Müller et al., 2020). The precise value of the metallicity at 2500 K is, therefore, hard to constrain without a detailed interior model that accounts for the saturated vapour pressure of the sublimated solids, which determines the envelope absorption of metals and is highly variable with temperature and composition (Ormel et al., 2021). Besides the compositional complexity, the appearance of a second radiative region furthermore requires a high dust opacity in the outer envelope, which we show is significantly reduced when coalescence is accounted for. Nevertheless, the work by Chachan et al. (2021) hints at a more complex scenario for the fully convective envelopes that we encounter in the velocity-limited opacity regime. The details of a potential deeper RCB are likely crucial in any model where it appears. It is, therefore, warranted to engage in a detailed study that also accounts for the important effects in this temperature range, including the varying composition of the envelope.

3.6.2 Pebble versus planetesimal accretion

Our work also highlights the difference between the formation of planets with pebbles or planetesimals. Whereas pebbles naturally provide an abundance of small grains in the outer envelope, planetesimals are much larger (>1 km, typically several hundred km, (i.e., Klahr & Schreiber, 2020; Li et al., 2019; Rucska & Wadsley, 2021) and only produce smaller grains when they experience significant mass loss or a dynamical fracture, where the pressure on the front of the planetesimal exceeds its strength and the planetesimal bursts apart. For this to occur, the planetesimal must be moving at very high velocity through a region with sufficient density, a condition that is only fulfilled near a planet's central core and far below the RCB

(Brouwers et al., 2018; Mordasini et al., 2015; Pinhas et al., 2016; Podolak et al., 1988; Valletta & Helled, 2019). Similarly, mass ablation through frictional heating is inversely effective with planetesimal mass and only becomes important for planetesimal-sized objects close to the planet's central core. Besides this, the localized nature of planetesimal impacts also makes it more difficult to effectively obscure an envelope, allowing unaffected parts to continue radiating away energy.

3.6.3 Model caveats and improvements

The main simplification of our opacity model is the assumption that the distribution of the solids in a planetary envelope can be modelled with a characteristic local pebble size, supplemented with a constant-size dust population. This assumption has been shown to provide good agreement with coagulation simulations (Mordasini, 2014) and we argue that it is also justified when the pebbles are limited by a velocity threshold and pile up at a single size. Modelling a more complex size distribution self-consistently during sedimentation would require a computationally intensive approach with a large number of size bins and experimental data on the redistribution function of grains produced by both erosion and collisions. Furthermore, grains of different compositions are characterized by different strengths and sublimation temperatures, meaning that the maximum grain size will in reality fluctuate depending on the temperature regime where different species can survive. Finally, we considered quasi-static envelopes and did not model any convective overshoot from the envelope's deeper regions, which can potentially return a portion of the particles to the surface (Popovas et al., 2019, 2018) after they experience collisional grind-down from the additional acceleration (Ali-Dib et al., 2020; Johansen & Nordlund, 2020).

3.7 Summary and conclusions

In the scenario of pebble accretion, planets grow by the subsequent accretion of solids (micron-sized dust + larger pebbles) and gas. The amount of gas that a planet is able to bind at a certain mass depends on its cooling rate. This, in turn, is set by the envelope's opacity. In this work, we designed an opacity model that incorporates the main physical processes that influence the evolution of solids in planetary envelopes. Our approach can be considered an extension to previous works by Mordasini (2014) and Ormel (2014) as we model two populations of solids instead of one and add the effects of pebble erosion, fragmentation, and dust sweep-up by pebbles to a grain growth prescription. We formulate convenient analytical expressions for the pebble opacity in different regimes (Eqs. 3.17-3.20), and we estimate the

dust opacity in a steady-state between dust sweep-up and production (Eq. 3.23b). Finally, we apply our model across a wide parameter space to map out the resulting opacity trends as a function of distance, planet mass and accretion rate. Our main findings are that:

1. The initial size distribution of solids that a planet accretes is not an accurate representation of their sizes within the envelope. At the upper end of the distribution, we corroborate the recent findings by Ali-Dib et al. (2020) and Johansen & Nordlund (2020) that larger pebbles are prone to erosion by dust grains when they accrete onto planetary envelopes. This erosion occurs as a result of the additional gravitational acceleration by the planet, and does not require violent convective gas motion. The size limit at entry varies from a few microns in envelopes of small planets in the outer disc to several centimetres for more massive planets that are located closer to the central star.

2. Within the envelope, the pebble sizes are limited by their rate of growth or by the velocity at which they begin to erode or fragment. The growth-limited regime applies to larger planets that are accreting pebbles at a low rate. As found by Mordasini (2014) and Ormel (2014), the opacity in this regime drops far below ISM values, especially at greater depth or in the envelopes of more massive planets. Any additional pebbles that a planet accretes in the growth-limited opacity regime only lead to larger pebbles, and do not increase the opacity, other than through any added luminosity. Nevertheless, the contribution of solids typically still dominates over the molecules, except for higher-mass planets in the inner disc (see Fig. 3.7). Smaller planets at greater distance from the star or those that are accreting pebbles at a sufficiently high rate enter the velocity-limited regime, where pebble growth is restricted by erosion or fragmentation. In this regime, a higher pebble accretion rate further increases the pebble abundance and the opacity is able to remain high throughout the envelope, typically turning it entirely convective.

3. One proposed solution for the fact that Uranus and Neptune accreted their substantial masses of $\sim 15\ M_\oplus$ without entering runaway gas accretion is that they had a high envelope opacity during formation. However, we find that the commonly made assumption of an ISM-like opacity from small dust grains is not realistic when grain growth is accounted for. High envelope opacities remain possible if the pebble accretion rate is sufficiently high and the pebble sizes become limited by fragmentation or erosion, rather than by their rate of growth. However, this introduces a timescale problem, as the planets must have formed at the right time to grow to their current sizes at a sufficiently rapid pace without becoming gas giants.

Chapter 4

A road-map to white dwarf pollution: tidal disruption, eccentric grind-down, and dust accretion

"Non est ad astra mollis e terris via" - There is no easy way from the earth to the stars
-Seneca, Hercules furens, 1st century AD

In this chapter, we move to the end of a star's active lifetime, when it has left the main sequence and become a white dwarf. A significant fraction of these white dwarfs show metal lines indicative of pollution with planetary material, and this information can be used to infer the pollutant's composition. In this chapter, we illustrate several potential routes for white dwarf pollution, and link these paths to observational outcomes. We propose a scenario where accretion begins with the tidal disruption of a scattered asteroid and the formation of a highly eccentric tidal disc. Larger fragments are ground down to small dust, which circularizes and accretes onto the white dwarf via drag forces. We show that optically thin dust accretion by PR drag produces large infrared excesses when the accretion rate exceeds 10^7 g/s. We hypothesize that around white dwarfs accreting at a high rate, but with no detected infrared excess, dust circularization requires enhanced drag – for instance due to the presence of gas near the disc's pericentre.

4.1 Introduction

While the study of polluted white dwarfs has blossomed into a field of its own, the processes via which planetary material accretes, remain poorly understood. We know that the initial

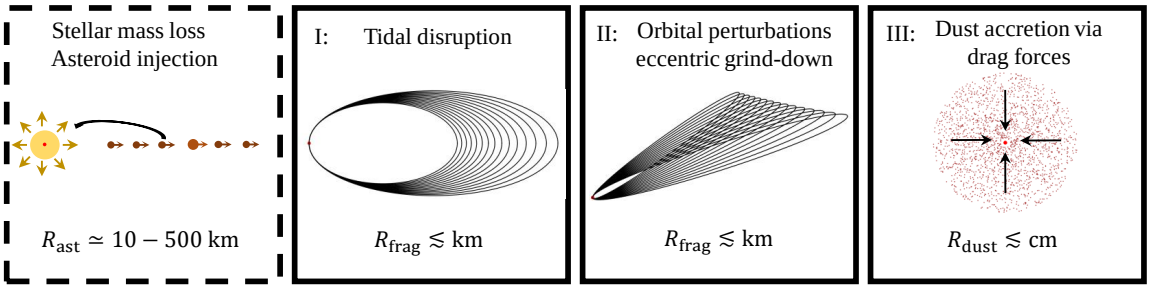

Fig. 4.1 Schematic diagram of the main road to white dwarf pollution examined in this work. In the precursor to its pollution, the star sheds its outer layers during post-main sequence evolution (dashed border). This widens and destabilizes the orbits of surrounding bodies and causes some asteroids to be scattered towards the star through interactions with nearby planets. In the first stage of accretion, asteroids that cross the Roche radius tidally disrupt and form eccentric structures with an orbital spread, which we refer to as (eccentric) *tidal discs*. The orbits of the surviving fragments are perturbed via various processes, including differential precession, causing high-velocity collisions and grind-down within the eccentric tidal disc (stage II). The resulting dust then circularizes and accretes onto the star via various drag forces (stage III).

trigger for pollution is likely to be stellar mass loss, which widens planetary orbits and strengthens the interactions between planets. This can destabilize tightly-packed planetary systems, even if they were previously stable (Debes & Sigurdsson, 2002; Maldonado et al., 2020, 2021), while systems with more space between the planets likely survive intact (Duncan & Lissauer, 1998; Veras et al., 2016). If the planetary system contains an asteroid belt, a single massive planet orbiting interior to the belt can scatter large numbers of asteroids within its expanding chaotic zone (Bonsor et al., 2011; Mustill et al., 2018). An outer planet can be similarly effective and scatter asteroids around expanding interior mean motion resonances (Antoniadou & Veras, 2016; Debes et al., 2012). Asteroids or planets that pass within the Roche radius tidally disrupt into highly eccentric discs whose shapes range from narrow if the asteroid was small (Nixon et al., 2020; Veras et al., 2021, 2014a), to wider and even partially unbound if the object was terrestrial-sized (Malamud & Perets, 2020a,b).

From this point on, the evolution of the fragments remains more obscured. As an end-point of their evolution, observations show that a minority of polluted white dwarfs are surrounded by dust (Farihi, 2016; Rocchetto et al., 2015; Rogers et al., 2020; Wilson et al., 2019), whose emission typically varies within several years at mid-infrared (Farihi et al., 2018; Swan et al., 2019b, 2020), but less commonly at near-infrared (Rogers et al., 2020). Some of these systems also show evidence of ongoing gas production (Gänsicke et al., 2008, 2007, 2006; Manser et al., 2020) and they occasionally contain larger, transiting bodies (Budaj et al., 2022; Farihi et al., 2022; Guidry et al., 2021; Manser et al., 2019;

Vanderbosch et al., 2020, 2021; Vanderburg et al., 2015). While no complete description of the accretion process currently exists, the general hypothesis is that small fragments circularize via Poynting-Robertson (PR) drag (Rafikov, 2011a; Veras et al., 2015a,b), while larger fragments require a prior phase of collisional grind-down (Jura, 2003; Jura et al., 2007; Li et al., 2021; Wyatt et al., 2011). Other mechanisms that induce orbital changes after disruption are the Yarkovski force (Malamud & Perets, 2020b; Veras et al., 2015a,b), potential interactions with pre-existing material around the star (Grishin & Veras, 2019; Malamud et al., 2021) and magnetic Alfvén-wave drag (Zhang et al., 2021).

In this chapter, we systematically investigate how planetary material accretes onto white dwarfs. We eventually produce a road-map illustrating several potential routes for white dwarf pollution with links to observational outcomes (Fig. 4.17). The main path to accretion that we examined (see Fig. 4.1) begins with the tidal disruption of a scattered asteroid to form a highly eccentric tidal disc (Sect. 4.2). We evaluate its morphology and constrain the upper and lower bounds of their fragment sizes due to radiative and tidal forces. Then, we present a short intermezzo where we consider the merits and limitations of a simple collision-less evolution model via PR drag (Sect. 4.3), which we find cannot drive sufficiently rapid accretion, even under the most optimistic assumptions. We continue our main road to pollution in Sect. 4.4, where we discuss how various processes induce high-velocity collisions between fragments. These collisions take place while the fragments still travel along the highly eccentric orbits ($e > 0.999$) on which they are released. This notion is fundamentally different from previous models that calculated collisions between fragments that were already supposed to have circularized (Kenyon & Bromley, 2017a,b; Swan et al., 2021). In Sect. 4.5, we present a simple but quantitative calculation of eccentric collisional grind-down based on the fragment's differential rates of apsidal precession, a process that likely induces collisions in all tidal discs on this scale. We then enter the third stage of our accretion scenario, where we model the geometry and emission of the dust that is produced (Sect. 4.6). We discuss variations of this model as well as alternative paths to white dwarf pollution in Sect. 4.7, including observational outcomes when they are sufficiently well understood. Finally, we conclude our work in Sect. 4.8

4.2 Stage I: from asteroid to tidal debris disc

4.2.1 The tidal disruption criterion

The outer edge of the disruption zone is set by the distance where an asteroid's internal strength and self-gravity are overcome by tidal forces. The details of this process depend on

the asteroid's shape and composition, as well as on its path and potential rotation (Davidsson, 2001, 1999; Dobrovolskis, 1982, 1990). We content ourselves here by considering an idealized case of breakup by tensile failure, likely the most common type of tidal disruption for solid bodies. We adopt a similar approach as Bear & Soker (2015) and Brown et al. (2017) and identify the breakup criterion for a spherical, non-rotating asteroid of size $R_{\rm ast}$ and density $\rho_{\rm ast}$ as the point where the summed forces from the tensile strength ($F_{\rm S}$) and self-gravity ($F_{\rm SG}$) first fail to compensate the tidal force induced by the gravitational gradient ($F_{\rm T}$):

$$F_{\rm S}+F_{\rm SG}+F_{\rm T}\simeq -SR_{\rm ast}^2-\frac{GM_{\rm ast}^2}{R_{\rm ast}^2}+\frac{2GM_{\rm WD}M_{\rm ast}R_{\rm ast}}{r^3}=0, \tag{4.1}$$

where G is the gravitational constant, is r is the distance to the white dwarf and S is the material's tensile strength. The masses of the white dwarf and the asteroid are indicated by $M_{\rm WD}$ and $M_{\rm ast}$, respectively. In the gravity-dominated regime ($|F_{\rm SG}| \gg |F_{\rm S}|$), the distance at breakup is mostly independent of the asteroid's size and occurs at the classical Roche radius (e.g. Bear & Soker, 2013; Davidsson, 1999; Malamud & Perets, 2020a,b; Veras et al., 2014a):

$$r_{\rm Roche}=\left(\frac{2\rho_{\rm WD}}{\rho_{\rm ast}}\right)^{\frac{1}{3}}R_{\rm WD}. \tag{4.2}$$

To quantify Eq. 4.2, it is necessary to specify the white dwarf density $\rho_{\rm WD}$. Neglecting the slight temperature dependence, this relationship can be approximated by (Nauenberg, 1972):

$$R_{\rm WD}=0.0127\ {\rm R}_\odot\left(\frac{M_{\rm WD}}{{\rm M}_\odot}\right)^{-1/3}\left(1-0.607\left(\frac{M_{\rm WD}}{{\rm M}_\odot}\right)^{4/3}\right)^{\frac{1}{2}}. \tag{4.3}$$

The Roche radius amounts to roughly 1 $\rm R_\odot$ for a 0.6 $\rm M_\odot$ white dwarf. If they are monolithic (as opposed to rubble-pile aggregates, see below), smaller asteroids can survive a certain distance within the Roche radius until the extra barrier of their internal strength is overcome. Accounting for this, Eq. 4.1 can be solved to yield a maximum object size ($R_{\rm max}$) that can survive at a distance r from a WD:

$$R_{\rm max}=\frac{3}{4\pi\rho_{\rm ast}}\left(\frac{S}{G\left[\left(\frac{r_{\rm Roche}}{r}\right)^3-1\right]}\right)^{\frac{1}{2}}. \tag{4.4}$$

Chondrite asteroid samples indicate that the upper end of tensile strengths is around 0.1-10 MPa (Pohl & Britt, 2020; Scheeres et al., 2015; Veras & Scheeres, 2020) but it is understood to vary by orders of magnitude depending on an asteroid's formation history

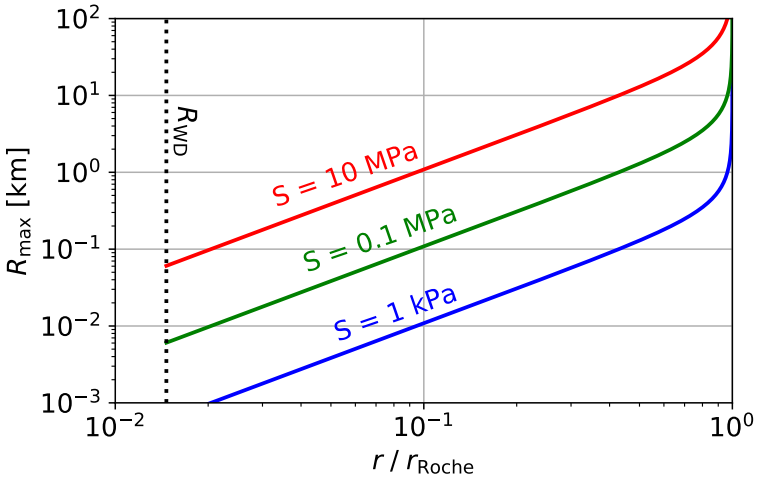

Fig. 4.2 The maximum sizes of objects that are safe from tidal disruption at a distance r from a 0.6 $M_\odot$ white dwarf, plotted for three different tensile strengths. Large asteroids (>100 km) always disrupt close to the Roche radius of the star, whereas smaller fragments ($\ll$ km) can survive deep pericentre passages ($r \ll r_{\rm Roche}$) due to their material strength.

and composition. For instance, estimates from modelling of cometary material composed of ice-coated interstellar silicate grains indicate sub-kP strengths (Davidsson, 1999; Greenberg et al., 1995; Gundlach & Blum, 2016). A formation via the gentle sticking of constituent particles can even result in so-called rubble piles with near-zero effective strength. Such an object is for instance invoked to explain the rapid breakup of Shoemaker-Levy 9 in Jupiter's outer envelope (Asphaug & Benz, 1994). To visualize these differences, we plot the maximum intact object size as a function of distance for a range of tensile strengths in Fig. 4.2. The figure illustrates the dichotomy that arises based on the asteroid's size. Large (> 100 km) asteroids always fragment at the Roche radius, regardless of their tensile strength. In contrast, because the tidal force scales as $F_{\rm T} \propto R^4$ and $F_{\rm S} \propto R^2$, smaller km-sized granite rocks can reach as close as a few percent of the Roche radius before they are torn apart.

4.2.2 Tidal disc morphology

As the main body begins to break up, its fragments stray from the initial orbit and spread out over a range of energies. Malamud & Perets (2020a,b) simulated this process for terrestrial-sized bodies and showed how the breakup typically proceeds in stages. Pericentre passages that are close to the Roche radius typically result in partial disruption and require several orbits in order to completely destroy the object. Each passage can add spin to the surviving object and progressively weaken it. The fragments that break off begin to form a stream that

can gravitationally collapse perpendicular to its direction of motion. After several orbits, this produces a fully formed tidal disc of interlaced elliptical annuli.

While the details of the breakup process lead to some variation in the tidal disc, its basic morphological features agree with the simple impulse approximation method. In this framework, the disruption is assumed to occur instantaneously at a location r_B from the star, which for simplicity we take as the pericentre of the object's orbit. As the object disintegrates, its fragments are no longer guided by the centre of mass and continue on orbits corresponding to their energy at the point of separation. The ones facing the white dwarf are more gravitationally bound than their velocity warrants and move to a tighter orbit, while those on the other side of the asteroid migrate away from the white dwarf. Neglecting the small effect of binding energy in asteroid-sized objects, their specific energy (ε_i) can be expressed as a sum of the kinetic ($\varepsilon_\mathrm{k,i}$) and potential ($u_\mathrm{G,i}$) parts:

$$\varepsilon_\mathrm{i} = \varepsilon_\mathrm{k,i} + u_\mathrm{G,i} \tag{4.5a}$$

$$= \frac{1}{2} G M_\mathrm{WD} \left(\frac{2}{r_\mathrm{B}} - \frac{1}{a_0} \right) - \frac{G M_\mathrm{WD}}{r_\mathrm{i}}, \tag{4.5b}$$

where r_B is the breakup distance of the asteroid's centre to the white dwarf and $r_\mathrm{i} = r_\mathrm{B} + x R_\mathrm{ast}$ is the distance corresponding to the individual fragments (with $-1 < x < 1$) and a_0 is the asteroid's semi-major axis. Correspondingly, the fragment's new semi-major axes (a_i) are spread along

$$a_\mathrm{i} = -\frac{G M_\mathrm{WD}}{2\varepsilon_\mathrm{i}} \tag{4.6a}$$

$$= a_0 \left(1 + 2 a_0 \frac{r_\mathrm{B} - r_\mathrm{i}}{r_\mathrm{B} r_\mathrm{i}} \right)^{-1}, \tag{4.6b}$$

with eccentricities (e_i) equal to

$$e_\mathrm{i} = \left(1 - \frac{r_\mathrm{i}}{a_\mathrm{i}} \right). \tag{4.7}$$

The asteroid moves parallel to the plane of motion of its centre-of-mass prior to its breakup. This means that fragments get imparted an inclination (i_i) depending on their vertical position that varies between $0 < i < R_\mathrm{ast}/r_\mathrm{i}$. With this, the tidal debris discs have an approximate height of $2R_\mathrm{ast}$ at pericentre, which grows to many times the size of the body at apocentre, where it can be estimated at $H_\mathrm{apo} \sim 4 R_\mathrm{ast} a_0 / r_\mathrm{B}$. In our subsequent modelling, we take the inclination constant as a function of time, although the vertical evolution of these tidal discs currently remains poorly understood.

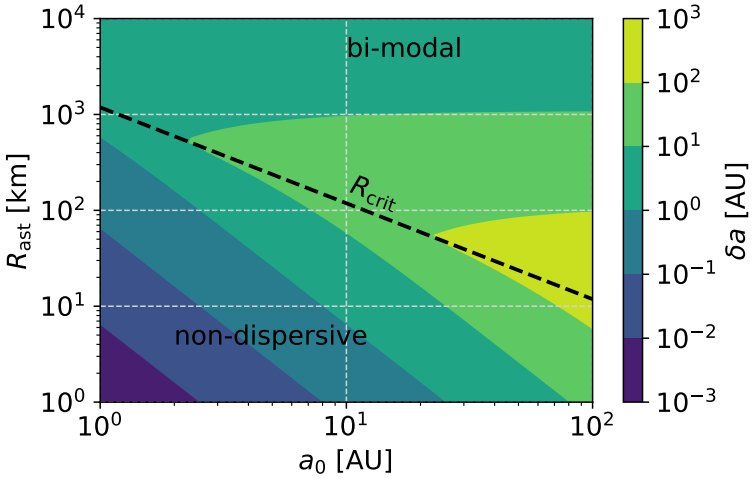

Fig. 4.3 Orbital width (δa) that contains 90 % of the bound fragments around a 0.6 $M_\odot$ white dwarf. Small asteroids on tight orbits experience non-dispersive breakup and form a non-dispersive stream. The width of the tidal disc increases with the progenitor size and its orbital separation. Very large objects like planets with $R \gg R_{\rm crit}$ experience bimodal breakup with half of their mass being ejected from the system.

Depending on the size and semi-major axis of the asteroid prior to breakup, the tidal discs described as by Eqs. 4.6a - 4.7 form with various shapes. Asteroids that originate from wide orbits are only loosely bound to the star and when their size exceeds the threshold of $R_{\rm crit} \simeq \frac{r_{\rm B}^2}{2a_0 - r_{\rm B}}$ (Malamud & Perets, 2020a), some of its fragments become unbound after breakup ($a_{\rm i} < 0$), with up to half of the material being expelled from the system in the most extreme case. These highly dispersive tidal disruption events have previously been linked to planetesimal seeding of other systems (Rafikov, 2018). The fragments that remain on bound orbits spread out over a range in semi-major axes, approximately distributed evenly in the energy range of Eq. 4.5b (Malamud & Perets, 2020a). Since the orbital energy scales as a^{-1}, most bound fragments become clustered on tight orbits. Therefore, we can use the inner ($a_{\rm in}$) and outer ($a_{\rm out}$) bound fragments to define an effective width δa of the tidal disc as

$$\delta a = \frac{\chi a_{\rm in}(a_{\rm out} - a_{\rm in})}{\chi a_{\rm in} + (1-\chi) a_{\rm out}}, \tag{4.8}$$

where χ is the mass fraction of bound fragments included in the width of the disc. We plot this effective disc width for a range of semi-major axes and asteroid sizes in Fig. 4.3, which shows the clear dichotomy between the non-dispersive and bimodal regimes. We also visualize three examples of the different regimes in Fig. 4.4. The top panel (a) indicates the tidal disc that forms when a small asteroid (1 km from 3 AU) disrupts, similar to the

models by Debes et al. (2012), Veras et al. (2014a), and Nixon et al. (2020). As described by these authors, the result is a completely bound but spaghettified orbital structure. If the size of the asteroid and its semi-major axis are increased (panel b), the orbital band broadens until $\delta a >> a_0$ and almost half of the original material is ejected (panel c). In this bimodal regime, any further increase of the impactor size or semi-major axis begins to increase the concentration of orbits closer to the star and effectively reduces the width of the tidal disc (see top part of Fig. 4.3).

4.2.3 Debris size distribution

Immediately after the main body breaks up, its fragments become exposed to the same tidal force that broke up their progenitor. These fragments are smaller than the original body and thus require a lower tensile strength to resist further breakup and initially remain stable. However, if the asteroid was scattered onto an orbit with its pericentre closer to the star than its initial original breakup distance, the fragments experience an increased peak tidal force and may disrupt again. In this simple picture, the maximum fragment size $R_{\rm max}$ follows from Eq. 4.4 with $r = r_{\rm peri}$ and can be identified from Fig. 4.2. Because asteroids are most likely to be scattered to orbits with pericentres near the edge of the Roche radius (Veras et al., 2021), it may be expected that the largest fragment is typically similar to the size of the asteroid itself. It is not necessary that this happens in practice, however, as tighter orbits or rubble pile asteroids composed of smaller constituent particles may not lead to any large surviving fragments. In addition, the fragments can be spun up, making them easier to break up (Malamud & Perets, 2020b). In our model, we take $R_{\rm max}$ as a free parameter due to the large associated uncertainty, with a baseline value of 1 km, corresponding to the size where fragments with a 1 kPa strength survive near the Roche radius. We assume the same density for the fragments as we do for the asteroid.

On the other end of the distribution, the lower limit for bound fragments corresponds either to the scale of the smallest dust grains that splinter off during breakup or to the blow-out size where radiation pressure from the stellar luminosity $L_{\rm WD}$ pushes the dust out of the system. This blow-out criterion provides an absolute lower limit to the fragment sizes and can be estimated from the ratio of radially oriented forces (Burns et al., 1979):

$$\frac{F_{\rm rad}}{F_{\rm G}} = 0.0013 \left(\frac{R}{\mu{\rm m}}\right)^{-1} \left(\frac{\rho_{\rm frag}}{2.7\ {\rm g/cm^3}}\right)^{-1} \left(\frac{L_{\rm WD}}{0.01\ L_\odot}\right) \left(\frac{M_{\rm WD}}{0.6\ M_\odot}\right)^{-1} \left(\frac{<Q>}{1}\right), \tag{4.9}$$

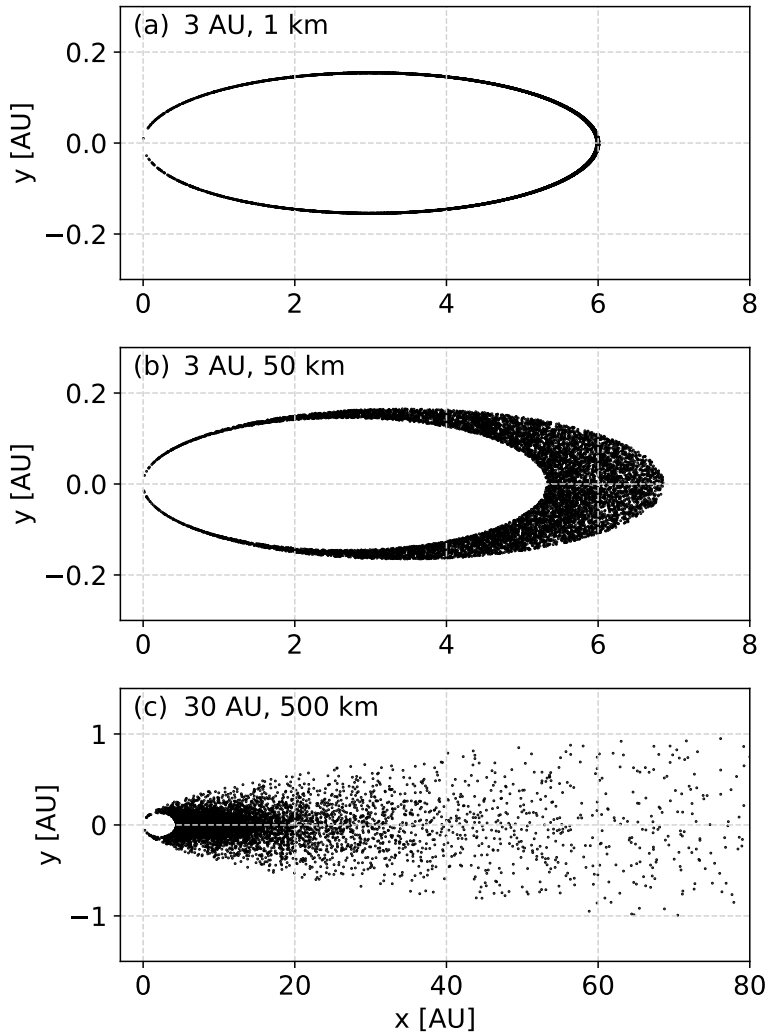

Fig. 4.4 Post-breakup orbits after a strengthless asteroid tidally disrupts near a 0.6 $M_{\odot}$ white dwarf. Panel (a) indicates the tidal disc that forms when a small (1 km from 3 AU) asteroid disrupts, yielding a thin orbital spread. Panel (b) corresponds to a 50 km asteroid from 3 AU, which produces a wider – but still completely bound disc. When both the asteroid size and semi-major axis increase to 500 km and 30 AU (c), the outcome is a bimodal disruption event, with nearly half of the material becoming unbound from the white dwarf.

where $< Q >$ is the radiation pressure coefficient, averaged over the stellar emission. While white dwarfs are not luminous enough to blow out micron-sized grains on circular orbits, the near-unity eccentricities of the fragments after the tidal disruption make these grains susceptible. We can estimate a typical blow-out size by taking the orbital parameters of the original asteroid, with a breakup point at its pericentre. The smallest fragments follow unbound orbits when $F_{\rm rad}/F_{\rm G} > 0.5(1-e)$, which, when combined with Eq. 4.7, reduces to:

$$R_{\rm blow} = 1.51\ \mu{\rm m}\ \left(\frac{a_0}{\rm AU}\right)\left(\frac{r_{\rm B}}{R_\odot}\right)^{-1}\left(\frac{L_{\rm WD}}{0.01\ {\rm L}_\odot}\right) \left(\frac{M_{\rm WD}}{0.6\ {\rm M}_\odot}\right)^{-1}\left(\frac{\rho_{\rm frag}}{2.7\ {\rm g/cm^3}}\right)^{-1}, \tag{4.10}$$

assuming geometric scattering ($< Q >= 1$), which is valid for grains larger than the reduced peak stellar wavelength $\lambda_{\rm peak}/2\pi \simeq 0.02 - 0.1\ \mu$m, depending on the stellar temperature. We plot the blow-out size across a range of white dwarf temperatures for three asteroid semi-major axes in Fig. 4.5. The figure indicates that the sizes typically range between 1-100 μm, depending on the white dwarf temperature and the asteroid's orbit. We note, however, that if they are produced during the tidal disruption, a population of grains much smaller than $R_{\rm blow}$ can still remain in the system due to their reduced interaction with light at stellar wavelengths. We do not consider these tiny grains here because their properties also make them resistant to PR drag.

The distribution of fragments between $R_{\rm min}$ and $R_{\rm max}$ is determined by the fracture lines, the amount of sequential breakups and mergers, as well as the short collisional phase that follows (Malamud & Perets, 2020a) and currently remains poorly constrained. We therefore opt to insert a truncated power-law for the fragment sizes:

$$\frac{dN}{dR} = CR^{-\alpha}, \tag{4.11}$$

where α is the scaling factor of the size distribution and the constant C is set by mass conservation. Because $R_{\rm max} \gg R_{\rm min}$ and assuming that $\alpha < 4$, it can also be written as

$$\frac{dM}{dR} = \frac{(4-\alpha) f_{\rm bound} M_{\rm ast}}{R_{\rm max}}\left(\frac{R}{R_{\rm max}}\right)^{3-\alpha}, \tag{4.12}$$

where $f_{\rm bound}$ is the mass fraction of post-breakup fragments that are bound to the white dwarf, a factor that follows from Eq. 4.6b. In the case of a scale-independent collisional cascade, the power law follows $\alpha = 3.5$ and large fragments dominate the mass budget, while the smaller particles dominate the cross-section (Dohnanyi, 1969; Tanaka et al., 1996; Wyatt et al., 2011,

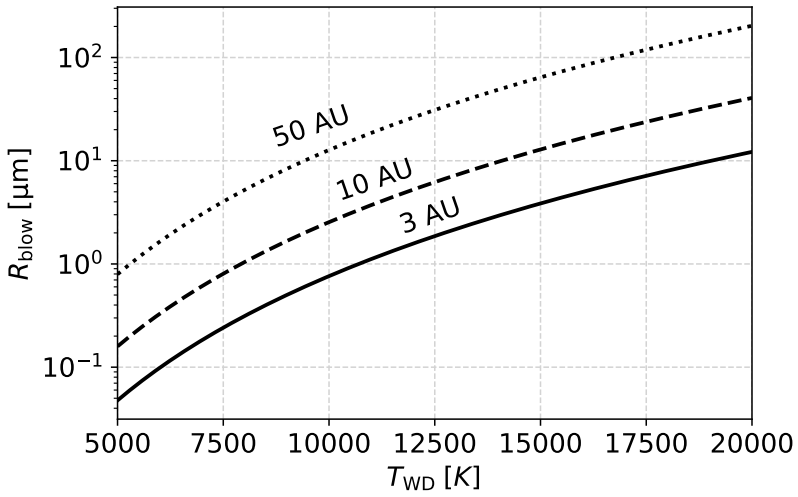

Fig. 4.5 The smallest dust grains (R_{blow}) that interact with the stellar light ($< Q >= 1$) and can remain bound despite the star's radiation pressure. The figure assumes the disruption of a strengthless asteroid at the Roche radius of a 0.6 $M_{\odot}$ white dwarf (from Eq. 4.10). The three lines correspond to different asteroid semi-major axes, and the tidal disruption is assumed to occur at the orbit's pericentre.

2007). We take this as our default value in our subsequently presented calculations, but note that simulations of collisional cascades that account for scale-dependent effects suggest a slightly lower value of alpha. If the mass is instead more evenly distributed over the size bins, the value of α is closer to 3.

4.3 Intermezzo: collision-less evolution via PR drag

Before we consider collisions between larger fragments, we first evaluate the potential of perhaps the simplest scenario, where fragments accrete via PR drag alone. We derive accretion rates as a function of the bounded size distribution and point out the limitations of this simple scenario.

4.3.1 PR contraction timescale and accretion rate

The main contribution from PR drag on a highly eccentric orbit occurs near the pericentre where the stellar flux is highest. In this calculation, we will make the a-priori assumption that the tidal disc is optically thin, which we later evaluate in Sect. 4.6. The averaged orbital

equations of motion are described by Veras et al. (2015a,b):

$$< \frac{da}{dt} > = -\frac{3 < Q > L_{\rm WD}(2+3e^2)}{16\pi\rho_{\rm frag} R a c^2 (1-e^2)^{\frac{3}{2}}}, \tag{4.13a}$$

$$< \frac{de}{dt} > = -\frac{15 < Q > L_{\rm WD} e}{32\pi\rho_{\rm frag} R a^2 c^2 (1-e^2)^{\frac{1}{2}}}, \tag{4.13b}$$

where we again substitute $< Q >= 1$ and use the simple relation

$$L_{\rm WD} \simeq 3.26\, L_{\odot} \left(0.1 + \frac{t_{\rm WD}}{\rm Myr}\right)^{-1.18} \tag{4.14}$$

to relate the white dwarf's luminosity to its age $t_{\rm WD}$ based on Mestel theory (Mestel, 1952), with the same parameters as in Bonsor & Wyatt (2010). This prescription is valid up to 9 Gyr when the white dwarf undergoes crystallization and the cooling slows dramatically (Althaus et al., 2010). While more detailed cooling codes are available (Salaris et al., 2013), Mestel's relation captures the essential cooling trend for the first few Gyrs, which is sufficient for our purposes here.

The equations of motion (Eqs. 4.13a-4.14) are coupled and generally need to be solved numerically to obtain the accretion time as a function of fragment size $t_{\rm acc}(R)$. Because a white dwarf's luminosity remains approximately constant for a similar period of time as its age, a fragment's accretion time in the window $t_{\rm acc} < t_{\rm WD}$ is proportional to its size. For a size distribution $3 < \alpha < 4$, this leads to an accretion rate of:

$$\dot{M}_{\rm PR} = \frac{dM}{dR}\left(\frac{dt_{\rm acc}}{dR}\right)^{-1} \tag{4.15a}$$

$$= \frac{(4-\alpha) f_{\rm bound} M_{\rm ast} t_{\rm acc}^{3-\alpha}}{t_{\rm acc,max}^{4-\alpha}}, \tag{4.15b}$$

where $t_{\rm acc,max}$ is the accretion time of the largest fragment. We plot the PR accretion rates (accounting for stellar cooling) for 100 km asteroids that originate from 3 and 10 AU in Fig. 4.6, assuming three different values of α. In agreement with Eq. 4.15b, the accretion rate declines as a function of time unless $\alpha < 3$. The smallest fragments, therefore, typically determine the peak accretion rate in a collision-less scenario, even if large fragments contain most of the mass. The steeper the fragment size distribution, the higher the peak accretion rate and the steeper its decline as a function of time. Furthermore, we find that the accretion rate is only marginally dependent on the orbital parameters of the fragments. For a given value of α, the PR accretion rate can also be written as a simple scaling function. For the

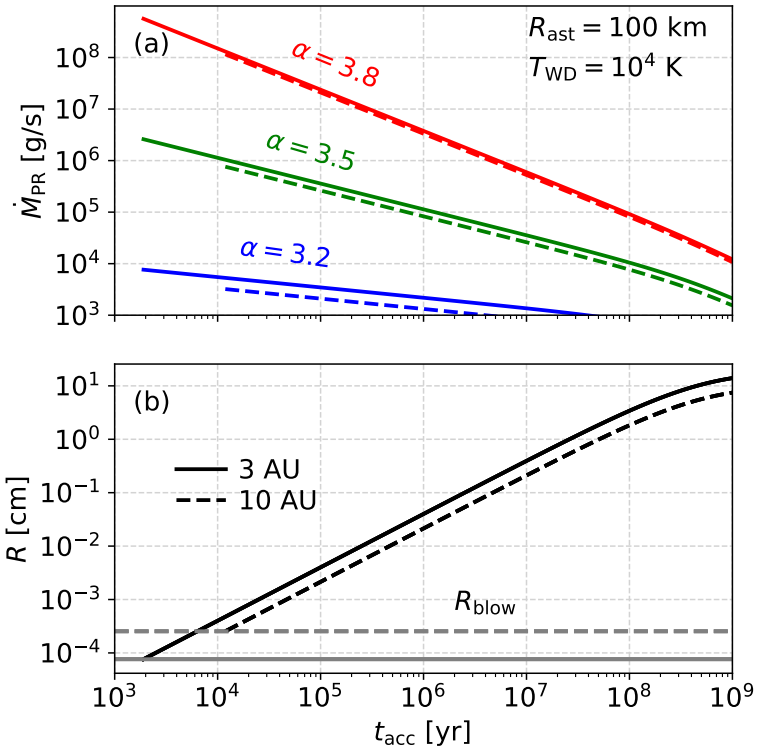

Fig. 4.6 Collision-less mass accretion rates of asteroid fragments via PR drag onto a 0.6 $M_\odot$ white dwarf. The top panel (a) shows how the accretion rate varies with the size distribution (different colours) and orbital separation (line style). The lower panel (b) indicates what fragments reach the star via PR drag after a certain time (t_{acc}). Accretion starts with the smallest bound fragments R_{blow}, as bigger fragments take longer to circularize. The curves flatten over time due to the declining luminosity of the cooling star (Eq. 4.14), meaning that fragments larger than $1 - 10$ cm cannot be accreted via PR drag alone.

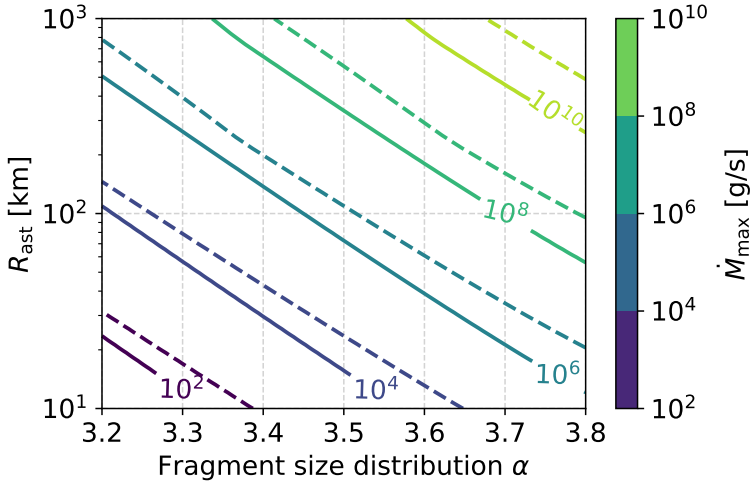

Fig. 4.7 Peak collision-less accretion rates via PR drag onto a warm (10^4 K) 0.6 $M_\odot$ white dwarf as a function of asteroid radius and fragment size distribution. The solid and (dashed) lines correspond to asteroid semi-major axes of 3 and (10 AU). Explaining observed implied accretion rates beyond 10^9 g/s (Farihi et al., 2012) by PR drag alone requires large asteroids ($R_{\rm ast} > 500$ km) to break up into a steep fragment size distribution ($\alpha > 3.6$).

standard case of $\alpha = 3.5$, this is:

$$\dot{M}_{\rm PR,3.5} \simeq 2.3 \cdot 10^6 \text{ g/s} \left(\frac{t_{\rm acc}}{10^4 \text{ yr}}\right)^{-\frac{1}{2}} \left(\frac{L_{\rm WD}}{0.01 \text{ L}_\odot}\right) \left(\frac{R_{\rm max}}{1 \text{ km}}\right)^{\frac{1}{2}} \left(\frac{R_{\rm ast}}{100 \text{ km}}\right)^{3} \left(\frac{f_{\rm bound}}{1}\right) \left(\frac{\rho_{\rm ast}}{2.7 \text{ g/cm}^3}\right) \left(\frac{\rho_{\rm frag}}{2.7 \text{ g/cm}^3}\right)^{\frac{1}{2}}. \tag{4.16}$$

If the fragment size distribution is steeper and $\alpha = 3.8$, the PR rate becomes:

$$\dot{M}_{\rm PR,3.8} \simeq 2.0 \cdot 10^8 \text{ g/s} \left(\frac{t_{\rm acc}}{10^4 \text{ yr}}\right)^{-\frac{4}{5}} \left(\frac{L_{\rm WD}}{0.01 \text{ L}_\odot}\right) \left(\frac{R_{\rm max}}{1 \text{ km}}\right)^{\frac{4}{5}} \left(\frac{R_{\rm ast}}{100 \text{ km}}\right)^{3} \left(\frac{f_{\rm bound}}{1}\right) \left(\frac{\rho_{\rm ast}}{2.7 \text{ g/cm}^3}\right) \left(\frac{\rho_{\rm frag}}{2.7 \text{ g/cm}^3}\right)^{\frac{4}{5}}. \tag{4.17}$$

4.3.2 Peak accretion rates by collision-less PR drag

The peak accretion rate by PR drag occurs soon after the asteroid disrupts and the smallest fragments with size $R_{\rm blow}$ (Eq. 4.10) begin to reach the white dwarf. We evaluate these peak rates in Fig. 4.7 for a range of asteroid sizes and size distributions. We take a warm white dwarf with temperature $T_{\rm WD} = 10^4$ K, which is characterized by both rapid PR-

circularisation compared to cooler stars but also a larger blow-out size (Eq. 4.10). Of these two, the luminosity effect is more important, so the plotted rates can be seen as upper values that decrease slightly for cooler stars. Fig. 4.7 shows that collision-less accretion via PR drag can at least briefly supply the lowest detectable accretion rates around 10^6 g/s in the standard case of $\alpha = 3.5$. The higher values of observed inferred accretion rates beyond 10^9 g/s (Farihi et al., 2012) are more difficult to explain with PR drag alone and require large asteroids ($R_{\rm ast} > 500$ km) to break into sufficiently small particles ($\alpha > 3.6$). In addition, the problem of explaining the high accretion rates by PR drag alone is exacerbated for cooler stars with lower luminosities.

In any case, PR drag alone is unable to accrete fragments above ~ 10 cm before the star cools down (see Fig. 4.6). Most of the fragment mass is contained in much larger bodies, unless the size distribution is incredibly steep ($\alpha \geq 4$). If we consider the default value of $\alpha = 3.5$ and a maximum fragment size of 1 km, the total mass fraction that can be accreted via PR drag is only $(10\,{\rm cm}/R_{\rm max})^{1/2} = 0.01$. Because of this accretion inefficiency, the model is in conflict with the higher observed average accretion rates for some DBZ white dwarfs with longer sinking timescales (Farihi et al., 2012) and an additional process is required to explain the observed accretion rates. We will examine how collisions can play a role in increasing accretion efficiency in the next sections.

4.4 Stage IIa: collisions induced by orbital perturbations

We propose the collisional grind-down of larger fragments into dust as a solution to the difficultly in obtaining high accretion rates. In this section, we discuss several processes that naturally lead to the required collisions between fragments soon after an eccentric tidal disc forms.

4.4.1 Differential geodetic precession

Collisions between fragments only occur when their relative orbits are altered sufficiently from their initial trajectories that they begin to overlap. One way in which these changes could be induced, is from the fact that orbits do not precisely follow Newtonian tracks. Instead, their pericentres precess over many orbits according to GR (to the lowest order) at a rate ($\dot{\phi}_{\rm GR}$) of (e.g. Ragozzine & Wolf, 2009; Venkatraman Krishnan et al., 2020):

$$\dot{\phi}_{\rm GR} = \frac{3}{c^2(1-e^2)} \left(\frac{G^3 M_{\rm WD}^3}{a^5} \right)^{\frac{1}{2}}, \tag{4.18}$$

which can lead to the build-up of apsidal differences between fragment orbits over time. In the context of white dwarf pollution, differential apsidal precession was first mentioned by Debes et al. (2012) and further examined by Veras et al. (2014a), who suggested it can be triggered by orbital differences induced by PR drag. Because the precession rate is highest for the most eccentric orbits and those with short periods, apsidal precession translates orbital differences into angular differences. However, as we discussed in Sect. 4.2.2, the tidal breakup process already spreads the fragments along a range of semi-major axes and eccentricities. This means that no additional process is required and that the fragments start differentially precessing as soon as they form. The inner fragments precess more quickly than those on wider orbits, with the timescale for complete differential precession of the inner and outer ring (1 and 2) is given by Eq. 4.18:

$$\delta\tau_{\rm precess} = \frac{2\pi}{\dot{\phi}_{\rm GR,1} - \dot{\phi}_{\rm GR,2}} \tag{4.19a}$$

$$\simeq \frac{2\pi c^2 r_{\rm B}^3}{9R_{\rm ast}} \left(\frac{a_0}{G^3 M_{\rm WD}^3}\right)^{\frac{1}{2}}, \tag{4.19b}$$

in the non-dispersive limit where $R_{\rm ast} << R_{\rm crit}$. For partially unbound orbits, the precession timescale is instead given by $2\pi/\dot{\phi}_{\rm GR}$. We visually indicate the differential apsidal precession of an eccentric tidal disc in Fig. 4.8, where we plot the fragment orbits of a 100 km asteroid that originates from 3 AU (corresponding to the inner boundary of the zone that is not swallowed by the progenitor star during post main-sequence evolution, see Mustill & Villaver 2012) at 0.1 and 1 Myr. While this is less than the timescale of complete orbital precession ($\sim$ 20 Myr), the highly eccentric nature of the tidal disc means that collisions already occur at small angular differences. Initially, the orbit crossings are restricted to the pericentre and apocentre of the orbit. The relative fragment velocities scale with the angular differences and increase as a function of time. As the angular differences increase, the locations of orbit crossings eventually spread out over a wide range in space.

Differential precession vs coherent precession

Before we proceed with modelling the collisional grind-down induced by differential apsidal precession in the next section, we should note that not all eccentric astrophysical discs are observed to precess at differential rates. For instance, the asymmetric nucleus of the Andromeda Galaxy (M31) likely consists of an eccentric disc (Lauer et al., 2005; Tremaine, 1995) that does not show signs of differential precession, even though its stellar ages ($\sim$ Gyr) far exceed the timescale of differential apsidal precession ($\sim$ Myr). We should, therefore, first investigate whether the same processes that act here could cause the orbits of fragments

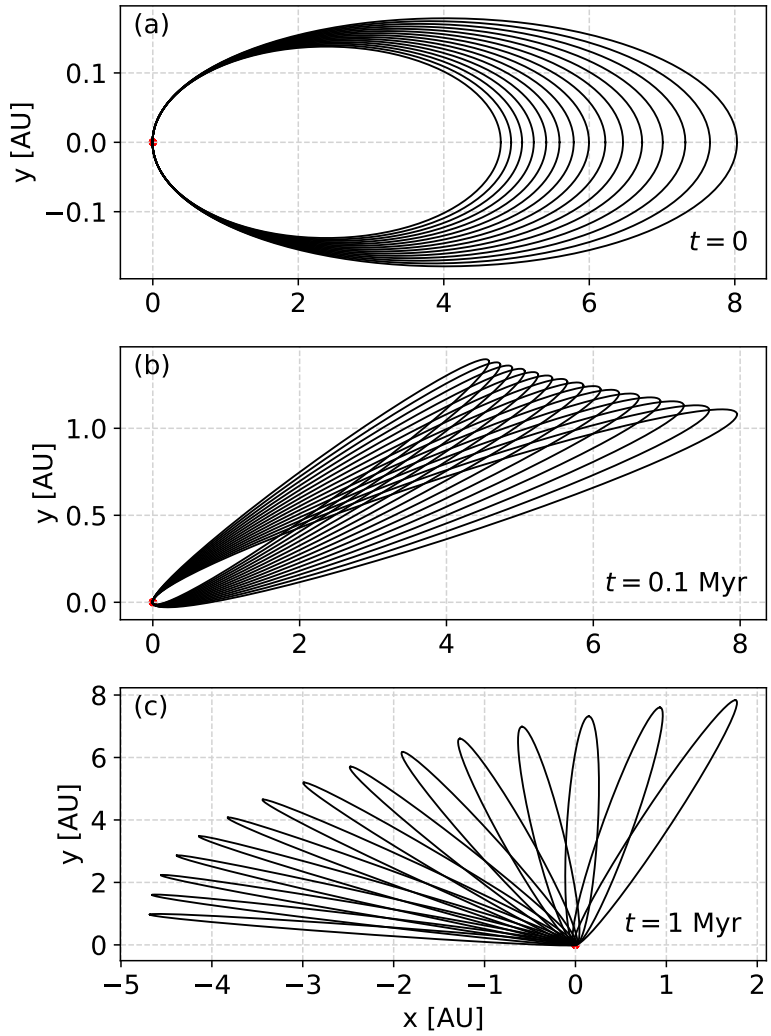

Fig. 4.8 Differential apsidal precession of fragment orbits from a 100 km asteroid originating from 3 AU. The orbits do not cross at $t = 0$ (panel a) but angular differences increase as a function of time, and at 0.1 Myr (panel b) the orbits cross at both pericentre and apocentre. At 1 Myr (panel c), both the relative angles and collision velocities have grown further, and the collision locations are spread out over a wider range in space.

around white dwarfs to precess coherently as well. The process that has been suggested to explain the coherent precession of M31 is a dynamical oscillation of the eccentricities as a result of self-gravity (Madigan et al., 2018; Wernke & Madigan, 2019). Physically, any orbits that precess faster than the bulk of the disc are pulled back, while orbits that lag behind are pulled forward. This force torques the orbit and changes its angular momentum and eccentricity, generating an oscillation. Based on the calculations of Madigan et al. (2018), the typical period of these oscillations is the secular timescale $t_{\rm sec} = P\left(\frac{M_{\rm central}}{M_{\rm disc}}\right)$, which is on the order of 100 orbits for M31. In the case of a disruption of an asteroid around a white dwarf, the mass ratio of the central object is much larger, however. Even in the case of a disrupting Earth-mass planet, the mass ratio ($0.6\,{\rm M}_\odot/{\rm M}_\oplus$) leads to a characteristic scale around 10^5 orbits, too long to prevent orbit crossings via differential apsidal precession.

A second option is that differential precession may be inhibited by continual collisions between fragments. If enough collisions occur at small relative angles and velocities, their exchange of angular momentum could prevent further differential precession, similar to what happens in eccentric gaseous discs. For this process to be effective, the disc needs to contain a sufficient fraction of small particles to generate a large collisional cross-section. In the case of the tidal discs that form from tidal disruptions around white dwarfs, this is unlikely due to the blow-out of the smallest fragments (Sect. 4.2.3) and the typically rapid accretion of slightly larger dust grains. Hence, it seems safe to assume that differential apsidal precession does indeed proceed uninhibited for the larger fragments contained in the tidal debris discs around white dwarfs.

4.4.2 Gravitational perturbations by a planet

Besides the gravitational perturbations from the central star, gravitational interactions with surrounding planets can also drive collisions between the eccentric fragments. Polluted white dwarfs are thought to be surrounded by whole planetary systems - including potentially gas- and ice giants as well as rocky planets (see Veras (2021) for a recent review). Because the tidal disc that forms in a disruption event centres around the asteroid's prior orbit, interactions with the planet that scattered it will continue to perturb the surviving fragments.

The effectiveness of this continued scattering likely depends on the geometry of the tidal disc. Any fragments whose orbits either cross the path of the planet or whose apocentre is close to the planet's semi-major axis will continue to be scattered. The width of this chaotic zone ($\delta a_{\rm chaos}$) around the planet has been studied in detail in previous works - albeit with far less eccentric orbits - and is around $\delta a_{\rm chaos} = C\, a_{\rm pl}\left(\frac{M_{\rm pl}}{M_\star}\right)^{\frac{2}{7}}$ with constant $1.3 < C < 2$ (Chiang et al., 2009; Duncan et al., 1989; Quillen & Faber, 2006; Wisdom, 1980). If the

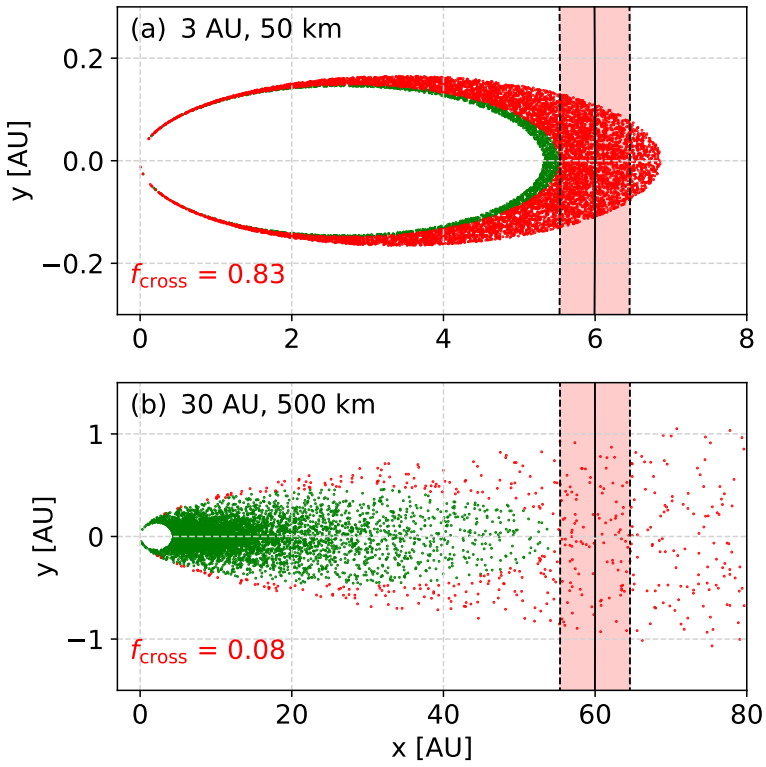

Fig. 4.9 Continued scattering of fragments that cross the chaotic zone of a planet ($M_{\mathrm{pl}} = 10\,\mathrm{M}_{\oplus}$) that resides at the apocentre of a scattered asteroid. This figure depicts the eccentric tidal disc, dividing the fragments between those that are likely to be directly re-scattered by the planet (red) and those that now lie outside the planet's chaotic zone (green). The top panel (a) shows that most fragments from a 50 km asteroid from 3 AU are susceptible to scattering (fraction f_{cross}). Fragments from a larger 500 km asteroid that originates from 30 AU (panel b) are spread bimodally (see Sect. 4.2) and are mostly safe from further scattering.

planet is located at the apocentre of the fragment orbits, any fragments with semi-major axes beyond $\delta a_{\mathrm{i,cross}}$ are susceptible to scattering:

$$a_{\mathrm{i,cross}} \geq \frac{a_{\mathrm{pl}}}{2}\left[1 - C\left(\frac{M_{\mathrm{pl}}}{M_{\star}}\right)^{\frac{2}{7}}\right], \tag{4.20a}$$

where we use that the eccentricities of fragments in these tidal discs are close to unity. We visualize the range of this scattering for 50 and 500 km-sized asteroids with semi-major axes of 3 and 30 AU in fig. 4.9. If the asteroid is small and originates from the inner zone, it will form a narrow orbital band and most of its fragments lie within the chaotic zone. Larger asteroids or those from further out are less likely to be perturbed directly, as the fragment

orbits begin to follow a bimodal bound-unbound distribution, with up to half of the fragments tightly bound to the star with orbits that are safe from direct scattering. Nevertheless, slower perturbations of these inner orbits are also possible around interior mean-motion resonances or via secular perturbations if the planetary orbit is not entirely circular, as discussed by Veras et al. (2021).

Over time, these orbital perturbations will lead to collisions between fragments and facilitate faster collisional grind-down. In addition, some fragments will be scattered out of the system, while others scatter to bound orbits with reduced pericentre distances. We suggest that fragment scattering in this way can provide a separate avenue for white dwarf pollution. Instead of having to lose angular momentum through stellar light, some fragments will collide with the white dwarf directly. Others scatter into the sublimation zone, where the vapour pressure of their material becomes significant and they and disintegrate over several orbits.

4.4.3 Drag-assisted circularization via pre-existing material

Thirdly, fragments can change their orbits by interacting with pre-existing gaseous or dusty material inside the Roche radius (Grishin & Veras, 2019; Malamud et al., 2021; O'Connor & Lai, 2020), such as has been observed around a substantial minority of systems (Farihi et al., 2016; Rocchetto et al., 2015; Wilson et al., 2019). The near-unity eccentricities of fragments mean that their pericentre velocities are typically on the order of several 100 km/s, yielding an extremely violent interaction with any dust or gas that is encountered. In a detailed study, Malamud et al. (2021) showed that this interaction can significantly alter fragment orbits. Firstly, the fragments lose kinetic energy and become more tightly bound to the star. Interestingly, the orbital contraction already becomes significant when the mass of the central compact disc is several orders of magnitude below that of the tidally disrupted asteroid. The smallest fragments circularize the fastest, typically within a few orbits. Larger fragments require additional passages through the disc, causing increased orbital differences that again accelerate the onset of orbit crossings via differential apsidal precession. In addition, regardless of whether the pre-existing disc contains dust or gas, each fragment passage though the central compact disc erodes away a mass similar to the mass that is encountered. Complete circularization of a fragment requires colliding with a similar amount of mass as the fragment itself, and therefore also leads to its complete disintegration. In the presence of such a massive central compact disc, fragments can accrete onto the white dwarf without the necessity for collisional grind-down.

4.4.4 Orbital changes due to the Yarkovski effect

Finally, larger fragments ($\geq$ 0.1-100 m) may either gain or lose angular momentum over time due to the Yarkovski effect (Bottke et al., 2006; Veras et al., 2015a,b). The idea is that while a fragment orbits the white dwarf, its side that faces the star is more strongly irradiated. Subsequent re-emission occurs with a time lag that, coupled with a rotation, leads to either an accelerating or braking term. If the fragment spins sufficiently quickly, its temperature gradient smooths out and the term disappears. While the Yarkovski effect likely dominates over PR drag in larger fragments, its derived terms are highly dependent on poorly constrained fragment parameters like the spin period (see Veras et al. 2015a, 2019). While a first attempt at constraining the spin distribution was made by Malamud & Perets (2020b), current simulations are not yet able to resolve them for physical fragment sizes. These characteristics of the Yarkovski effect currently make a useful inclusion in a collisional model unfeasible. However, it is clear that by increasing or decreasing the orbital momentum of different fragments, the Yarkovski effect will both facilitate collisions directly and induce orbital differences that accelerate the process of differential apsidal precession.

4.5 Stage IIb: calculation of eccentric collisional grind-down

In this section, we formulate a crude but quantitative calculation of collisional grind-down within the highly eccentric tidal discs that form after asteroids tidally disrupt around a white dwarf. Our model is based on the angular differences that are induced by differential apsidal precession (Sect. 4.4.1), which in turn originate from the orbital spread imparted at the moment of tidal breakup (Sect. 4.2.2). As discussed in the previous section, there are many additional mechanisms that also drive orbital differences between fragments. We take differential precession as the sole perturbing process here to make the calculation tractable and because it is universally applicable to tidal discs around white dwarfs, that all start with the required orbital spread.

4.5.1 Numerical setup

We opt for a simple computational approach where we divide the fragments into a 2D grid along semi-major axis and fragment size and model the collisions with a particle-in-a-box method. The fragments are assumed to be spread evenly across energy bins, with semi-major axes and eccentricities that lie between the bounds specified by Eq. 4.6a-4.7. Their initial

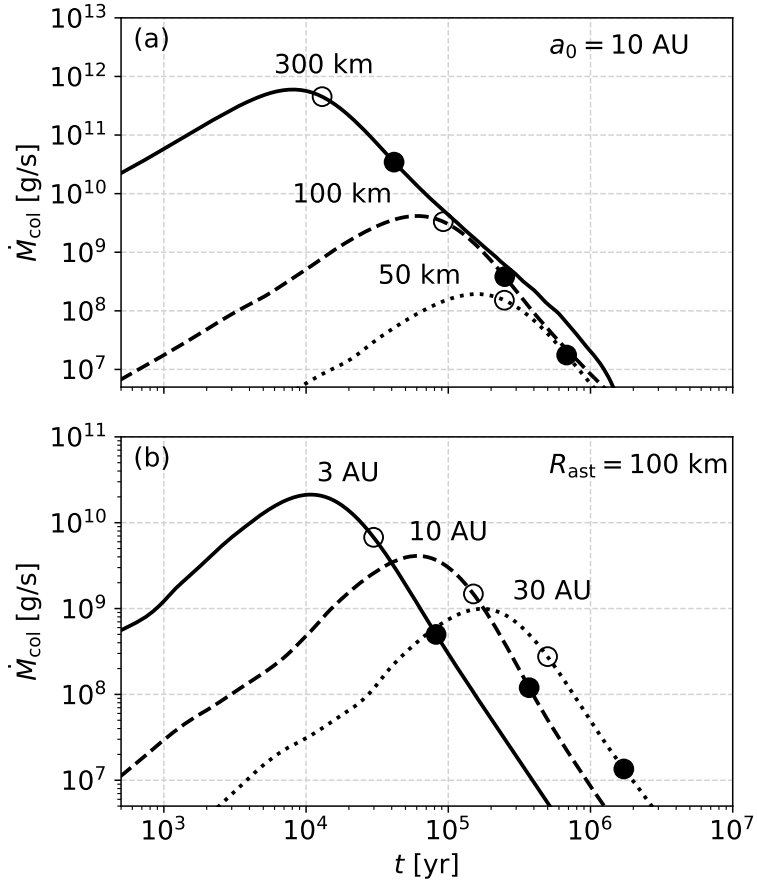

Fig. 4.10 Time evolution of the collision rate ($\dot{M}_{\rm col}$) from our model of eccentric collisional grind-down induced by differential apsidal precession (see text for details). In the top panel (a), we take asteroids from 10 AU and vary their size between 50-500 km. In the bottom panel (b), we take 100 km asteroids and vary their initial semi-major axis between 3-30 AU. The open and filled dots indicate the points where a total of 50% and 90% of the fragment mass has catastrophically collided, respectively. Larger asteroids on tighter orbits disrupt to form tidal discs whose fragments collide within the shortest period of time.

sizes are assumed to follow the collisionally evolved distribution of Eq. 4.11 with $\alpha = 3.5$ as a typical value, meaning that most of the mass is contained in the larger fragments, whereas their surface area is dominated by the smaller fragments. As described in Sect. 4.4.1, the orbits precess at different rates depending on their eccentricities and semi-major axes (Eq. 4.18), leading to orbit crossings. We estimate the rate of collisions in a projected 2D plane, where the collision points can be identified at radius $r_{\rm col}$ and true anomaly $\theta_{\rm col}$ for any two bins with indices i, j from the criterion that $r_{\rm i}(\theta_{\rm col}, \phi_{\rm i}) = r_{\rm j}(\theta_{\rm col}, \phi_{\rm j}) = r_{\rm col}$, where the velocity $v_{\rm i}$ and distance $r_{\rm i}$ are given by the standard equation of the ellipse in polar form:

$$r_{\rm i}(\theta) = \frac{a_{\rm i}(1-e_{\rm i}^2)}{1-e_{\rm i}\cos(\theta_{\rm i}-\phi_{\rm i})}, \tag{4.21a}$$

$$v_{\rm i}(r) = \left(GM_{\rm WD}\left(\frac{2}{r_{\rm i}} - \frac{1}{a_{\rm i}}\right)\right)^{\frac{1}{2}}. \tag{4.21b}$$

While all collisions exchange some angular momentum, only those that are sufficiently violent lead to the (partial) destruction of fragments. Accounting for the angular momentum changes in sub-catastrophic collisions is not possible with our method due to the large number of additional spacial bins it would create. Hence, we do not include these less violent collisions in our calculation and only focus on the collisional grind-down from catastrophic collisions. The required specific energy for catastrophic fragmentation $Q = \frac{1}{2}(\vec{v}_{\rm i} - \vec{v}_{\rm j})^2 \frac{m_{\rm j}}{m_{\rm i}}$ is known as the dispersion threshold and can be estimated as a scaling relation (Benz & Asphaug, 1999; Durda et al., 1998):

$$Q^\star = Q_{\rm a} R^{-a} + Q_{\rm b} R^b, \tag{4.22}$$

where the first term accounts for the material strength of a fragment and the second term corresponds to the gravitational binding energy that has to be overcome. We take the constants $a = 0.3$, $b = 1.5$ and $Q_{\rm a} = 6.2 \cdot 10^7$ erg/g, $Q_{\rm b} = 5.6 \cdot 10^{-2}$ erg/g from Löhne et al. (2008) and Wyatt et al. (2011). In our simulations, fragments of different sizes that reside in the same orbital bin experience the same collisional velocities when they cross paths with fragments in other bins. This means that Eq. 4.22 also directly specifies the minimum fragment size $R_{\rm j,crit}$ that can catastrophically collide with a fragment of size $R_{\rm i}$, depending on its collisional velocity:

$$R_{\rm j,crit} = \left(\frac{2Q^\star}{v_{\rm col}^2}\right)^{\frac{1}{3}} R_{\rm i}. \tag{4.23}$$

Generally, only fragment pairs with size ratio's below two orders of magnitude collide catastrophically.

The collision rate $P_{\rm ij}$ of two bins with fragment sizes $R_{\rm i}, R_{\rm j}$ and $N_{\rm i}, N_{\rm j}$ fragments can be estimated from a standard particle-in-a-box approach as:

$$P_{\rm ij} = \frac{< T_{\rm box,i} >}{T_{\rm orb,i}} \frac{< T_{\rm box,j} >}{T_{\rm orb,j}} \frac{N_{\rm i} N_{\rm j} \sigma_{\rm ij} v_{\rm col,ij}}{V_{\rm box}}, \tag{4.24}$$

where $\sigma_{\rm ij} = \pi(R_{\rm i} + R_{\rm j})^2$ is the collision cross-section, $V_{\rm box}$ is the volume of the collision box and $< T_{\rm box,i} >, < T_{\rm box,j} >$ are the average periods of time that fragments of bins i and j spend there. We approximate these collision volumes as locally straight boxes with volume $V_{\rm box} \simeq l_{\rm i} l_{\rm j} H \sin(\alpha_{\rm ij})$ where $\alpha_{\rm ij} = |\vec{v}_{\rm i} \times \vec{v}_{\rm j}|/(|\vec{v}_{\rm i}||\vec{v}_{\rm j}|)$ is the angle between the orbits and H is the local height of the tidal disc. We estimate this height based on a typical orbital inclination $\bar{i}$ as $H_{\rm i} = 2\bar{i} r_{\rm col} = 2R_{\rm ast} r_{\rm col}/r_{\rm B}$ (see Sect. 4.2.2), assuming that the inclination remains constant over time. The widths $l_{\rm i}$ and $l_{\rm j}$ cancel from the time spent in the box $<T_{\rm box,i}> = l_{\rm i}/|\vec{v}_{\rm i}|$, which gives:

$$P_{\rm ij} = \frac{\pi N_{\rm i} N_{\rm j} (R_{\rm i} + R_{\rm j})^2 |\vec{v}_{\rm i} - \vec{v}_{\rm j}|}{T_{\rm orb,i} T_{\rm orb,j} H |\vec{v}_{\rm i} \times \vec{v}_{\rm j}|}. \tag{4.25}$$

The total collision rate of bin i is set by the binned sum over $P_{\rm i,j}$:

$$P_{\rm i} = \sum_{j_{\rm crit,min}}^{j_{\rm crit,max}} P_{\rm ij}, \tag{4.26}$$

which we evaluate numerically. Because we only track catastrophic collisions in this scheme, we register the first catastrophic encounter for any fragment and remove the pair involved in the collision for the rest of the simulation. Although this approach does not incorporate grind-down that can result from second generation fragments, larger fragments generally require more time to catastrophically collide, so our approach can still provide order-of-magnitude estimates. More importantly, even this crude model can illuminate important trends and biases that are inherent to the collisional phase, which we will describe in the next subsections.

4.5.2 General trends in eccentric grind-down rates

We explore the most important trends of eccentric fragment collisions in Fig. 4.10 where we simulate the grind-down of fragments from a range of asteroid progenitors. In the top panel (a), we take asteroids with fixed semi-major axes of 10 AU but with sizes between 50-500 km. In the bottom panel (b), we instead take fixed asteroid sizes of 100 km but vary their semi-major axis between 3-30 AU. The first thing to note is that their rates of grind-down follow similar temporal shapes. Initially, no fragments cross paths and the rate of collisions begins at

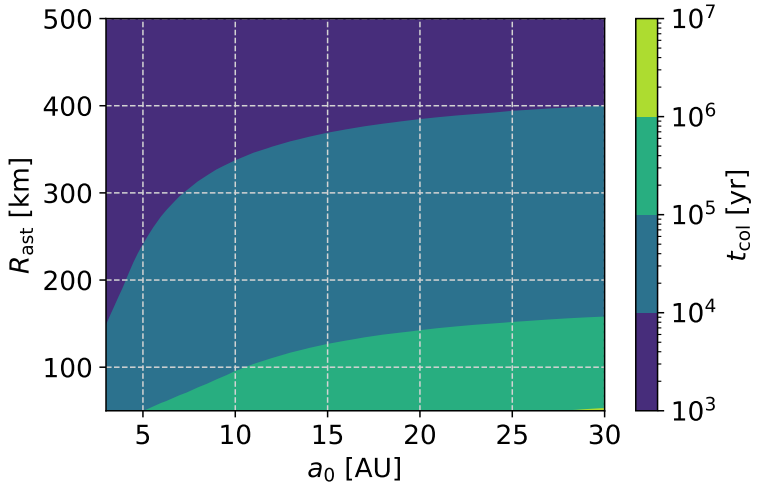

Fig. 4.11 Timescales for the collisional grind-down of fragments in eccentric tidal discs (t_{col}), calculated with our numerical model based on differential apsidal precession (see text for details). The grind-down timescale is defined as the time required for half of the mass to catastrophically collide. Fragments within tidal discs that form from large asteroid progenitors on tight orbits grind down within the shortest period of time.

zero. As the fragment orbits continue to precess at different rates, some orbits begin to cross, but the relative velocities are low and only similar-sized fragments catastrophically collide. After $10^2 - 10^4$ years, these relative velocities have increased sufficiently that catastrophic collisions occur for a wide range of relative fragment sizes and the collision rate shoots up. When around half of the fragment mass has collided (open dots), the rate decreases from its peak value and continues to drop as fewer and fewer intact fragments remain.

The most important variable in the rate of grind-down is the size of the asteroid progenitor. Larger asteroids provide more fragments that can collide (factor of R_{ast}^3), which additionally means that each fragment has more other fragments that it can collide with (also a factor of R_{ast}^3). Together, this predicts a scaling of the grind-down rate of $\dot{M}_{col} \propto R_{ast}^6$, similar to what we find in our simulations. In Fig. 4.10a, we find that the peak accretion rate increases from $\sim 10^8$ g/s for a 50 km asteroid from 10 AU to $\sim 10^{12}$ g/s for a 300 km asteroid with the same semi-major axis. This slightly flatter scaling ($\propto\sim R_{ast}^5$ instead of $\propto R_{ast}^6$) is due to the more disperse disc that forms when a larger asteroid disrupts (see Figs. 4.3 and 4.4). Some fragments of the 300 km progenitor are placed on unbound orbits and are ejected from the system, while others just follow wider orbits that take longer to collide. This general inverse scaling of the rate of grind-down with the semi-major axis of the asteroid is also shown in Fig. 4.10b, where a 100 km asteroid from 3 AU has a peak collision rate that exceeds the collision rate of an asteroid from 30 AU by around an order of magnitude.

4.5.3 Event lifetimes and peak accretion rates

In order to compare the results of our simulations to observationally inferred accretion event lifetimes, we simulate a grid of 400 tidal discs corresponding to asteroid sizes between 50-500 km that originate between 3-30 AU. Our results are shown in Fig. 4.11, where we indicate the time required to grind down half of the fragment mass (labelled $t_{\rm col}$). As explained in the previous subsection, our model yields a large variation in collisional timescales based on the asteroid size and its semi-major axis. Rather than try to produce an exact fit to the DAZ population from a crude model, we investigate the observability trends based on these parameters. The shortest grind-down timescales that we find are on the order of 10^3 years for asteroids that are several hundreds of kilometres in size. When the asteroid size drops to 50 km, the timescale increases by orders of magnitude to $10^5 - 10^6$ yr, depending on the orbital separation of the asteroid. From an observational perspective, typical accretion lifetimes of material around white dwarfs can most directly be inferred from differences in detection rates of DAZ and DBZ stars. In the pioneering study by Girven et al. (2012), the typical timescales are inferred to be between $10^4 - 10^6$ yr, based on dividing the average mass in DBs by the average accretion rates of DAs. More recently, this analysis was revisited by Cunningham et al. (2021) with updated photospheric modelling, which yielded an order of magnitude longer timescales between $10^5 - 10^7$ yr. Harrison et al. (2021a) took a different approach and estimated typical accretion event lifetimes around 10^7 yr based on a Bayesian analysis of the photospheric composition. When compared to our simulation results, lifetimes around $10^4 - 10^6$ yr match our computed grind-down timescales for asteroids up to 400 km in size, whereas we only find longer lifetimes of 10^7 yr when the asteroids are smaller than 50 km.

The highest inferred ongoing accretion rate to date is $10^{9.3}$ g/s for the most metal-rich DAZ (Farihi et al., 2012). If convective overshoot is accounted for, the inferred rates could increase by another order of magnitude (Cunningham et al., 2019). In Fig. 4.12, we examine whether such high accretion rates can be generated by the grind-down of asteroids with sizes between 100-300 km that originate from either 3 or 10 AU. The figure shows that this is indeed the case when any produced dust is rapidly accreted, as all lines show at least some period of grind-down rate beyond $10^{9.5}$ g/s. Within the context of our model, grind-down rates beyond 10^{11} g/s require asteroids with sizes that exceed 200 km.

The most extreme outliers of the inferred accretion rates have only been observed for DBZ stars. Farihi et al. (2012) identified six objects with inferred accretion rates above 10^{10} g/s, with the highest observation implying a record rate of $10^{11.5}$ g/s. Due to their longer sinking timescales, these are not observations of ongoing accretion rates, but represent an average over a longer time period. Based on their findings, Farihi et al. (2012) suggest that short periods of violent accretion that take between 10-100 years must occur at times to

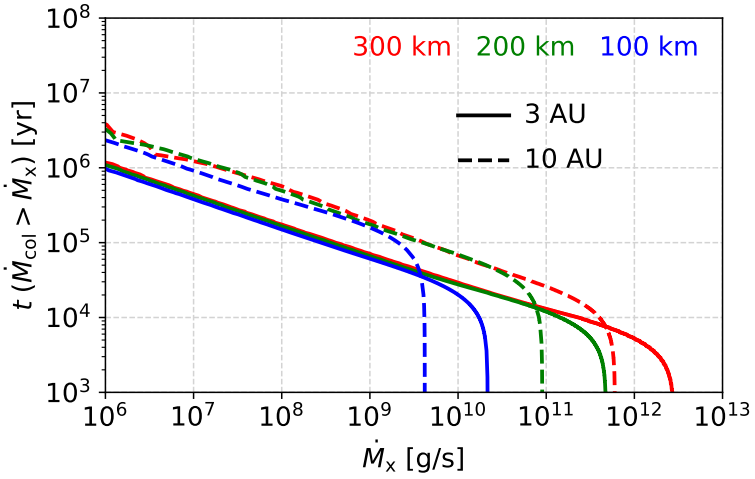

Fig. 4.12 Cumulative time when the rate of dust production from collisional grind-down lies above a certain rate $t(\dot{M}_{\rm col} > \dot{M}_{\rm x})$. The values correspond to calculations with our collisional model (see text for details). Larger asteroids produce more fragments, leading to more rapid grind-down and higher peak collision rates. Asteroids that originate from the inner zone of planetary systems (solid lines, 3 AU) generate higher peak collision rates compared to those on wider orbits (dashed lines, 10 AU) but they spend less time accreting at more moderate rates, making their pollution less likely to be observed if the subsequent accretion of small dust is sufficiently rapid.

explain the difference between DAZ and DBZ upper values. Within the context of our model, the dichotomy between the DAZ and DBZ upper values arises naturally. More massive asteroids produce more fragments that each collide within a shorter period of time, causing the accretion of the biggest asteroids to occur in short and intense bursts, provided that the accretion of the produced dust is sufficiently fast. In contrast, the grind-down of fragments that originate from smaller asteroids occurs over longer periods of time, making them more commonly detected in DAZ pollution, which measures ongoing accretion.

4.6 Stage III: infrared emission from accreting fragments or dust

A substantial minority of accreting white dwarfs exhibit detectable infrared excesses (Farihi et al., 2016; Rocchetto et al., 2015; Wilson et al., 2019). While the simplest canonical model computes emission from opaque dust on circular orbits (Jura, 2003), elliptical discs around white dwarfs have been modelled in response to observational clues to account for the reduced infrared excess around young stars (Dennihy et al., 2017) and also to explain the variability of the emission Nixon et al. (2020). The elliptical nature of the material is furthermore suggested by Doppler tomography of gas near the Roche radius (Manser et al., 2016b; Steele et al., 2021). From a physical perspective, it is similarly clear that the fragments are indeed expected to be released on orbits that are initially highly eccentric (see Sect. 4.2.2) and then slowly circularize over time. In our modelling, we compute the emission that is generated during the accretion of dust from such a highly eccentric structure. We do not follow the typical assumption that the disc is opaque to stellar light. Instead, we compute the distribution of dust and its re-emission under the a-priori assumption of an optically thin environment, the validity of which we then discuss after we calculate the radial optical depth.

With our model, we show that typically inferred accretion rates can indeed produce detectable infrared excesses when grains circularize in an optically thin disc via PR drag alone, but that the disc only remains optically thin if the orbital inclinations of the dust are increased over time. We then evaluate the results within our three-stage model and discuss how the disc geometry and circularization speed can affect the produced infrared excesses.

4.6.1 Infrared emission from a collision-less tidal disc

Before we calculate the infrared emission by dust grains from collisional grind-down, we first evaluate how much emission is produced just after a tidal disc forms and how this changes as fragments circularize. The emission produced by newly formed tidal discs was suggested by

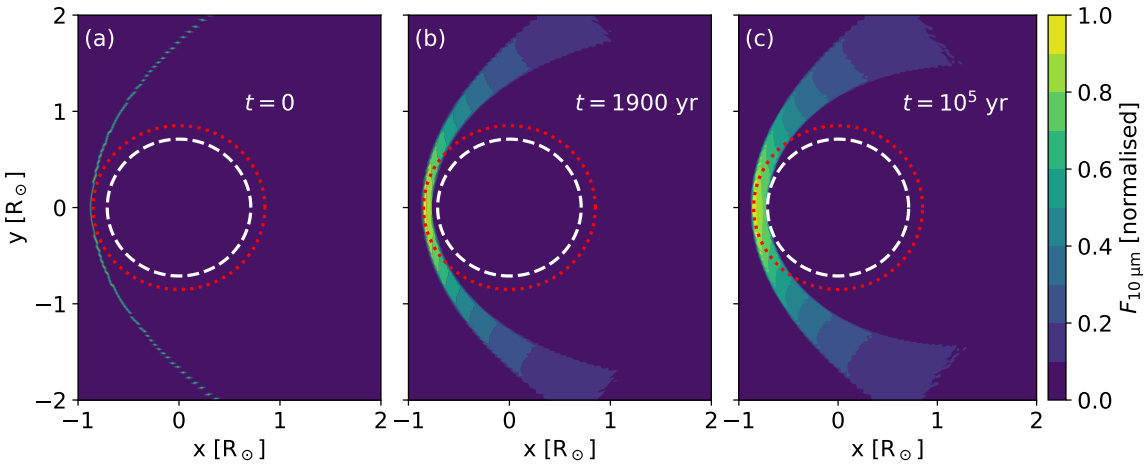

Fig. 4.13 Simulated emission per unit surface area at 10 μm from fragments accreting onto G29-38 (0.59 $M_\odot$, 11240 K, 17.5 pc) via collision-less PR drag, computed assuming optically thin properties (See Sect. 4.3.1 and Sect. 4.6.2 for details on PR drag and this emission). The three panels correspond to snapshots at different times after the tidal disruption event of an asteroid from 3 AU, and the colours are normalized individually per panel. Just after the tidal disruption event (a), the fragments are still highly eccentric, and their emission is minimal. The smallest fragments accrete just after 1900 yr (b), when their more contracted orbits begin to generate far more emission. The final panel corresponds to 10^5 yr, when all fragments smaller than 100 μm have already reached the star. The disc contains an elliptical inner gap because fragments are not yet fully circularized when they enter the sublimation distance (white dashed circle). The Roche radius is indicated with a red dotted circle, just outside the sublimation zone.

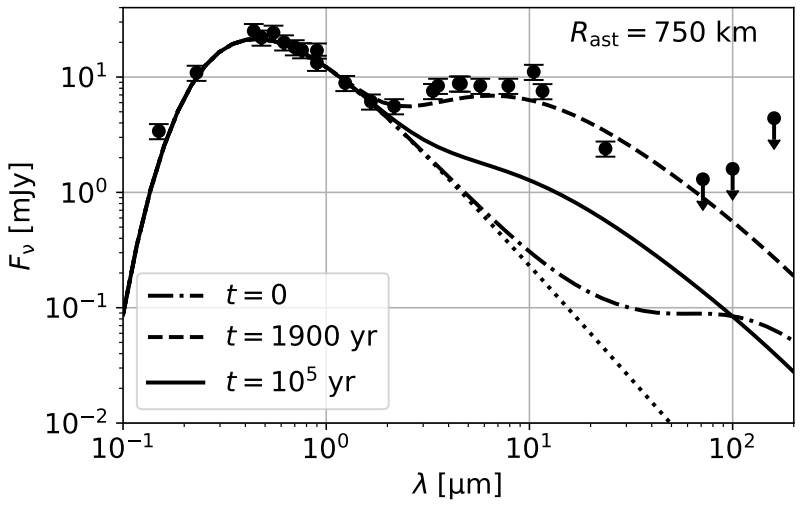

Fig. 4.14 Simulated emission spectra from a 750 km asteroid disruption around G29-38 computed by our model (see text), followed by collision-less and optically thin orbital contraction via PR drag. The dotted line indicates the contribution from the star, with the dash-dotted ($t = 0$), dashed ($t = 1900$ yr) and solid ($t = 10^5$ yr) lines including the emission from the fragments at different times. The points indicate the emission from the system as observed in several surveys (largely compiled by Farihi et al. (2014), original references in the text).

Nixon et al. (2020) as the source of observed infrared excesses based on normalized emission profiles.

As explained in Sect. 4.2.2, the fragments are placed on a range of orbits depending on the size of the asteroid, that share their pericentre but differ in their apocentre (see Fig. 4.4). In this calculation, we simplify the situation somewhat and assume that the fragments initially occupy a single orbital ring (a_0, e_0), given by the original orbit of the asteroid. Along this ring, the fragments experience different temperatures, which we approximate with radiative equilibrium:

$$T(r) = T_{\rm WD}\left(\frac{2r}{R_{\rm WD}}\right)^{-\frac{1}{2}}. \tag{4.27}$$

For simplicity, we ignore the super-heating of the smallest particles in this model (Chiang & Goldreich, 1997; Rafikov & Garmilla, 2012). The Planck emission per unit mass ($\mathscr{F}_\nu$) depends on the size of the fragments, which determines their ratio of area (A) to mass (M):

$$\mathscr{F}_\nu(R,T) = \frac{AB_\nu(T)}{M} \tag{4.28a}$$

$$= \frac{3B_\nu(T)}{\rho_{\rm frag}R}, \tag{4.28b}$$

where B_ν is the Planck function at a given frequency ν. In this simplified collision-less test case, fragments evolve towards the star via PR drag as a function of time, with their semi-major axes and eccentricities slinking at rates given by Eqs. 4.13a and 4.13b (Veras et al., 2015a,b). At any time t, fragments with different sizes R have already shifted away from their initial orbit and are now located at their own orbits $(a(t), e(t))$, which are most contracted for the smallest fragments. We take a linear grid of angular bins with size $d\theta$ between 0 and 2π, where fragments spend a time $dt = d\theta/\dot{\theta}(\theta)$. The average emission from a particular orbit per unit mass ($\mathscr{F}_{\nu,\mathrm{orbit}}$) is then weighed by the time spent at given angle θ as:

$$\mathscr{F}_{\nu,\mathrm{orbit}}(R,t) = \frac{1}{P(R,t)} \sum_{\theta=0}^{2\pi} \mathscr{F}_\nu(R,t,\theta) \frac{d\theta}{\dot{\theta}(\theta)}, \tag{4.29}$$

where P is the fragment's orbital period. The total emission ($F_{\nu,\mathrm{PR}}$) from the asteroid fragments is given by the sum over all the rings occupied by the different fragment sizes at time t:

$$F_{\nu,\mathrm{PR}}(t) = \sum_{R_{\min}}^{R_{\max}} \mathscr{F}_{\nu,\mathrm{orbit}}(R,t) \frac{dM}{dR}(R) dR, \tag{4.30}$$

where dM/dR is defined by the fragment size distribution. As explained in Sect. 4.2.3, we take a truncated power law with the default exponent $\alpha = 3.5$. The definite lower limit is set by the blow-out size (Eq. 4.10) and the upper limit is set at 1 km, corresponding to a rough indication of the breakup limit from the tidal force (Eq. 4.4).

We visualize the results by calculating the expected emission around G29-38, a 11240 K DAZ white dwarf at 17.5 pc with a well-documented infrared excess (Xu et al., 2018), first identified by Zuckerman & Becklin (1987). We compare our results to multi-wavelength fluxes, for which we take a supplemented version of the sample compiled by Farihi et al. (2014) with observations from Tokunaga et al. (1990), Reach et al. (2005), and Farihi et al. (2008). For our comparison here, we disrupt a large, 750 km asteroid with initial semi-major axis at 3 AU and let the fragments circularize in a collision-less, optically thin manner via PR drag. Without collisions, this scenario produces a peak accretion rate just above 10^9 g/s that occurs around 1900 yr after the disruption event. We show the geometry of the emitting fragments around the white dwarf in Fig. 4.13, plotted at three different times at an emission wavelength of 10 μm. Panel a ($t = 0$) corresponds to the moment after disruption, assuming that the fragments are spread uniformly over the orbit, which is known to only require a few orbits (Li et al., 2021; Malamud & Perets, 2020a; Veras et al., 2014a). Panel b is plotted at 1900 yr, just before the first fragments sublimate and accrete, which happens when their pericentre crosses the sublimation distance (white dashed circle), assumed to be located at 1500 K, corresponding to the temperature where the vapour pressure of silicates becomes

significant, and they begin to sublimate in vacuum (van Lieshout et al., 2014). Panel (c) corresponds to 10^5 yr after the disruption event, when fragments smaller than 100 μm have already accreted. In all three cases, the non-circular nature of the material is evident. Most emission at 10 μm occurs near the orbit's pericentre, or just away from it in the fragment's most eccentric initial state. Because the fragments enter the star's sublimation radius before they are entirely circular, the central gap has the form of an ellipse rather than a circle. The eccentricity of this ellipse increases for higher stellar temperatures and for lower sublimation thresholds.

In Fig. 4.14, we plot the emission spectrum of the fragments at the same snapshots in time. The first thing to note is that the emission varies greatly with time. The initial fragment orbits have semi-major axes similar to that of the original asteroid (3 AU here), and, therefore, have long orbital periods with most of their time spent at a distant apocentre. As a result, the emission from the orbit's pericentre is initially minimal, with emission only picking up at longer ($\sim$ 100 μm) wavelengths. Based on these calculations, we argue that newly formed tidal discs provide insufficient infrared emission to explain the observed excesses or variation, as was suggested by Nixon et al. (2020). We find that the emission from the disc quickly increases as the fragments circularize, peaking in this collision-less test case at the moment that the smallest fragments begin to reach the star. The emission then gradually decreases again as the smallest fragments reach the white dwarf, with the emission spectrum maintaining a similar shape. During the circularization process, the effective temperature of the emission slightly increases over time as fragments contract their orbits and spend more time at strongly irradiated locations.

4.6.2 Emission from collisional dust production

We can slightly modify the calculation of the previous subsection to calculate the emission produced by the accretion of small dust that is produced via collisional grind-down of larger fragments. With the same assumption of optically thin contraction via PR drag, we can calculate the average emission per unit mass ($\bar{\mathscr{F}}_\nu$) of a fragment from the moment of its production to its accretion by averaging over the different orbits $(a(t), e(t))$ that a dust grain occupies on its trajectory towards the star:

$$\bar{\mathscr{F}}_\nu(R) = \frac{1}{t_{\rm acc}(R)} \sum_{t'=0}^{t_{\rm acc}(R)} \mathscr{F}_{\nu,{\rm orbit}}(R,t')dt'(R,t'). \tag{4.31}$$

The time intervals dt' during which the different orbital bins are occupied follow from Eqs. 4.13a, 4.13b. We again sum the contributions of different fragments in the size distribution to

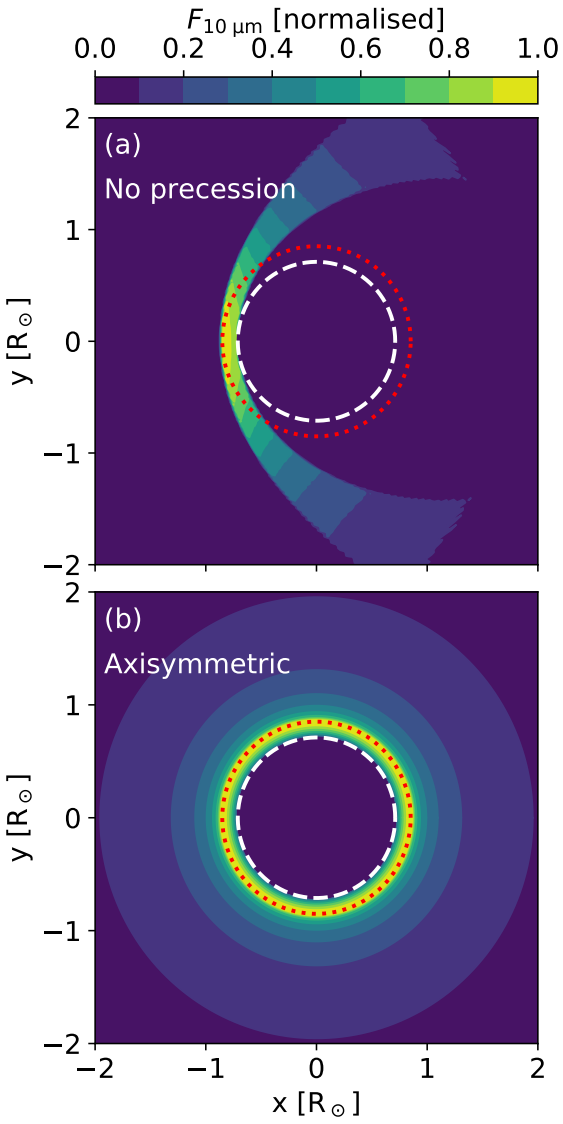

Fig. 4.15 Simulated emission per unit surface area at 10 μm from constant dust production and accretion at a rate of 10^7 g/s via PR drag, computed assuming optically thin properties. The top panel (a) shows the resulting emission without apsidal precession, and the bottom panel (b) shows the axisymmetrically averaged emission. The disc contains an elliptical inner gap because fragments are not yet fully circularized when they enter the sublimation zone (white dashed circle). The Roche radius is indicated with a red dotted circle, just outside the sublimation zone. Axisymmetrically averaged, the structure becomes visible as a ring-like structure mostly contained within the Roche radius.

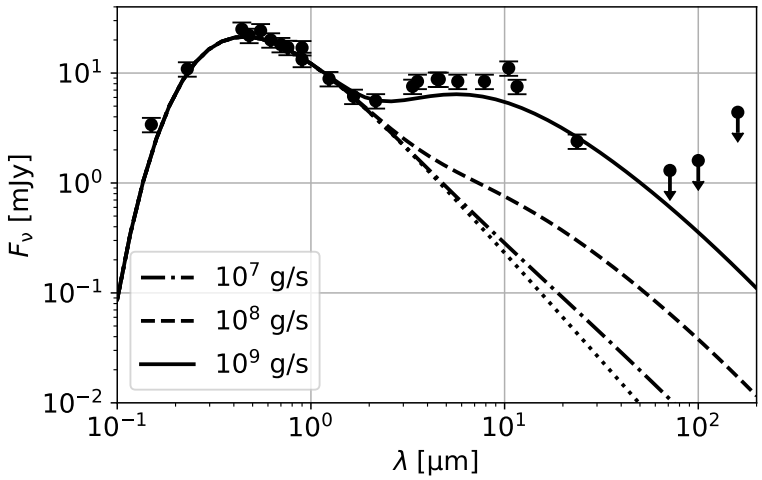

Fig. 4.16 Simulated emission spectra of G29-38, with dust accretion via PR drag at three different rates. The dotted line indicates the contribution from the star, with the dash-dotted (10^7 g/s), dashed (10^8 g/s) and solid (10^9 g/s) lines including the emission from circularizing dust at different accretion rates. The points indicate the observed emission from the system in several surveys (largely compiled by Farihi et al. (2014), original references in the text).

obtain the total emission ($\bar{F}_{\nu,\mathrm{PR}}$), but now for a given accretion rate rather than at a particular time:

$$\bar{F}_{\nu,\mathrm{PR}}(\dot{M}) = \sum_{R_{\mathrm{min}}}^{R_{\mathrm{max}}} \bar{\mathscr{F}}_\nu(R) t_{\mathrm{acc}}(R) \frac{d\dot{M}}{dR}(R) dR, \tag{4.32}$$

which, for a given accretion rate, notably yields a result that is independent of the fragment size distribution if the fragments are modelled as black bodies in thermal equilibrium [1]. We show the geometry of the emission in Fig. 4.15, which, as expected, shows a similarly asymmetric shape as the time evolution discussed in the previous subsection, with most of its emission originating from a narrow band near the pericentre of the orbit. If the collisions are induced by the differential apsidal precession of fragment orbits, the actual geometric shape of the disc will be different. We approximate this state in panel (b) of the same figure, where we neglect potential collisional circularization from inelastic collisions, yielding an axisymmetrically averaged structure when the fragment orbits are completely differentially precessed. The pericentre now appears as a bright narrow band up to the Roche radius, surrounded by a less luminous zone.

[1]The PR accretion time scales as $t_{\mathrm{acc}} \propto R$, while the area-to-mass ratio scales as $A/M \propto R^{-1}$. These contributions cancel out, meaning that the emission in a steady-state of dust production and accretion by PR drag is independent of R if the particles are modelled as perfect absorbers/emitters.

We plot the emission spectrum, which is not affected by asymmetric averaging, in Fig. 4.16, corresponding to accretion onto G29-38 at three different rates. Because the emission is proportional to the assumed accretion rate, the implication of this model is that an excess in the system's infrared emission is visible whenever the PR accretion rate is sufficiently high. While such an excess has indeed been observed for some rapidly accreting systems, the majority of polluted white dwarfs do not follow this trend. Hence, we must conclude that even if PR drag can supply high accretion rates of small dust, the majority of systems likely accrete their material differently. In the next subsection, we will evaluate the optical depth of the accretion via PR drag, which provides an additional constraint to the dust accretion process via discs with small inclinations.

4.6.3 Radial optical depth of the tidal debris disc

In the previous calculations regarding accretion via PR drag, we assumed that the dust and fragments around the white dwarf form an optically thin disc. Here, we investigate the validity of this assumption and compute the optical depth in the radial direction, where the disc is most opaque. We follow a similar procedure as in the previous subsection and begin by computing the radial optical depth contribution per unit mass ($\mathscr{T}$) as a function of the true anomaly for a given orbit:

$$\mathscr{T}(R,t,\theta) = \frac{\pi R^2}{MHdl}\frac{dt}{P} \tag{4.33a}$$

$$= \frac{3}{4\rho_{\mathrm{frag}} RH(R,t,\theta)P(R,t)v(R,t,\theta)}, \tag{4.33b}$$

where $P(R,t)$ is the period of a fragment at its given orbit. For this calculation, we assume the same constant inclination imparted at the moment of breakup of $i = R_{\mathrm{ast}}/r_{\mathrm{B}}$, which is around 10^{-4} for a 100 km asteroid (see Sect. 4.2.2). To obtain the optical depth contribution per unit mass ($\overline{\mathscr{T}}(R,\theta)$) for a fragment size bin, we again sum over the different orbital rings that are occupied during the orbital contraction, evaluated separately for every angle:

$$\overline{\mathscr{T}}(R,\theta) = \frac{1}{t_{\mathrm{acc}}(R)} \sum_{t'=0}^{t_{\mathrm{acc}}(R)} \mathscr{T}(R,t',\theta)dt'(R,t'). \tag{4.34}$$

The total optical depth is then determined by the sum over the size distribution:

$$\tau_{\mathrm{PR}}(\dot{M},\theta) = \sum_{R_{\mathrm{min}}}^{R_{\mathrm{max}}} \overline{\mathscr{T}}(R,\theta)t_{\mathrm{acc}}(R)\frac{d\dot{M}}{dR}(R)dR. \tag{4.35}$$

We are primarily interested in estimating the optical depth at pericentre because that is where the fragments are exposed to the most stellar light, even when corrected for travel time (Veras et al., 2015a,b). When we perform the calculation with the parameters of G29-38 for the star and assume a 100 km asteroid, we find that the disc becomes radially opaque at its pericentre when the accretion rate exceeds 10^7 g/s. This result still applies when the material in the disc is axisymmetrically averaged, meaning that the optical depth at pericentre is comparable to the average across the disc.

While stellar rays from more vertical directions can still reach the dust when it is radially opaque, our calculation suggests that the assumption of perfect optically thin accretion begins to fail at higher accretion rates. If the inclination of the dust remains small, the amount of stellar light that can reach the dust grains declines and circularization rates slow down (see also the models by Rafikov 2011a,b). However, if the inclination of the tidal disc does increase from its initial value, for instance due to interactions with neighbouring planets (Li et al., 2021), the disc can remain entirely optically thin and high dust accretion rates by PR drag are possible. This scenario could explain the few cases where infrared excesses are observed. Finally, several white dwarfs show the remarkable combination of both rapid ongoing accretion and no infrared excess. In the scenario of grind-down and dust accretion, we find that this requires faster dust circularization and accretion than is possible by PR drag alone, as was also suggested by Bonsor & Wyatt (2010). This finding points to the importance of additional circularization processes that could involve gas drag (Malamud et al., 2021) or the recently suggested mechanism of Alfvén-wave drag (Zhang et al., 2021).

4.7 Discussion

In this work, we studied how material accretes onto white dwarfs from their surrounding planetary systems and how this relates to observational quantities. Our baseline scenario begins with the tidal disruption of an asteroid close to the white dwarf, which forms a highly eccentric tidal debris disc. The fragment orbits are then perturbed via various processes, including differential apsidal precession, causing the larger fragments to collide on their eccentric orbits until only dust remains. In the final stage, the dust accretes onto the star by drag forces. Our suggested scenario can produce accretion rates as high as those observed ($\gtrsim 10^{11}$ g/s) from the disruption of $\gtrsim 200$ km asteroids. Both the presence and the absence of infrared emission can be explained depending on the rate of dust in-spiral and accretion, with drag rates faster than PR-drag, such as via additional gas or Alfvén-wave drag required to explain the absence of infrared emission in the majority of white dwarfs.

Nevertheless, we propose that no single accretion scenario explains the pollution of all white dwarfs. A range of different accretion channels are likely applicable, depending on the properties of both the central star and the accreted object. In this discussion, we will present a selection of different routes to white dwarf pollution, which are summarized in the form of a road-map in Fig. 4.17. We visualize this road-map as a series of forks that split into different accretion channels according to specified physical criteria. We also discuss the observational characteristics that belong to each of these channels wherever they are sufficiently well understood, noting that further detailed modelling is required in many cases. After presenting our road-map, we will discuss the limitations of our calculations relating to our suggested main path and suggest areas for improvement in our model.

4.7.1 Fork (1): direct asteroid impact, ejection or tidal debris disc formation

The first step towards white dwarf pollution starts with mass loss from the central star, which widens the chaotic zone around planets (Bonsor et al., 2011; Mustill et al., 2018) and can destabilize tightly-packed planetary systems (Debes & Sigurdsson, 2002; Maldonado et al., 2020, 2021). Nearby asteroids become subject to scattering from close encounters or strong perturbations in mean motion resonances. In principle, scattering events can have four possible outcomes, which we show at the first fork (1) of Fig. 4.17. Most commonly, the asteroid's eccentricity or semi-major axis are only altered slightly, and the asteroid continues on its way until it is scattered again. In a chain of scattering events, the asteroid can eventually attain such a high eccentricity that it enters the Roche radius of the star, and it disrupts into an eccentric tidal disc (red arrow). This corresponds to our suggested baseline model. Alternatively, the asteroid could either be scattered outwards and enter the influence of outer planets, become completely unbound from the system, or directly hit the surface of the white dwarf if its pericentre distance becomes sufficiently small.

This last possibility of a direct asteroid impact is worth mentioning as a separate channel of accretion, studied in detail by Brown et al. (2017) and McDonald & Veras (2021). It is the simplest method of mass accretion, as material almost instantly enters the star's photosphere. This near-instant accretion prevents any detectable infrared excess and also restricts the detection window of the pollution itself to a few sinking timescales of metals in the photosphere, making direct asteroid impacts unlikely to be detected in young DAZ stars. In any case, direct impacts should be rare events. Not only is the Roche radius significantly larger than the white dwarf itself, but Veras et al. (2021) show that most low mass (terrestrial)

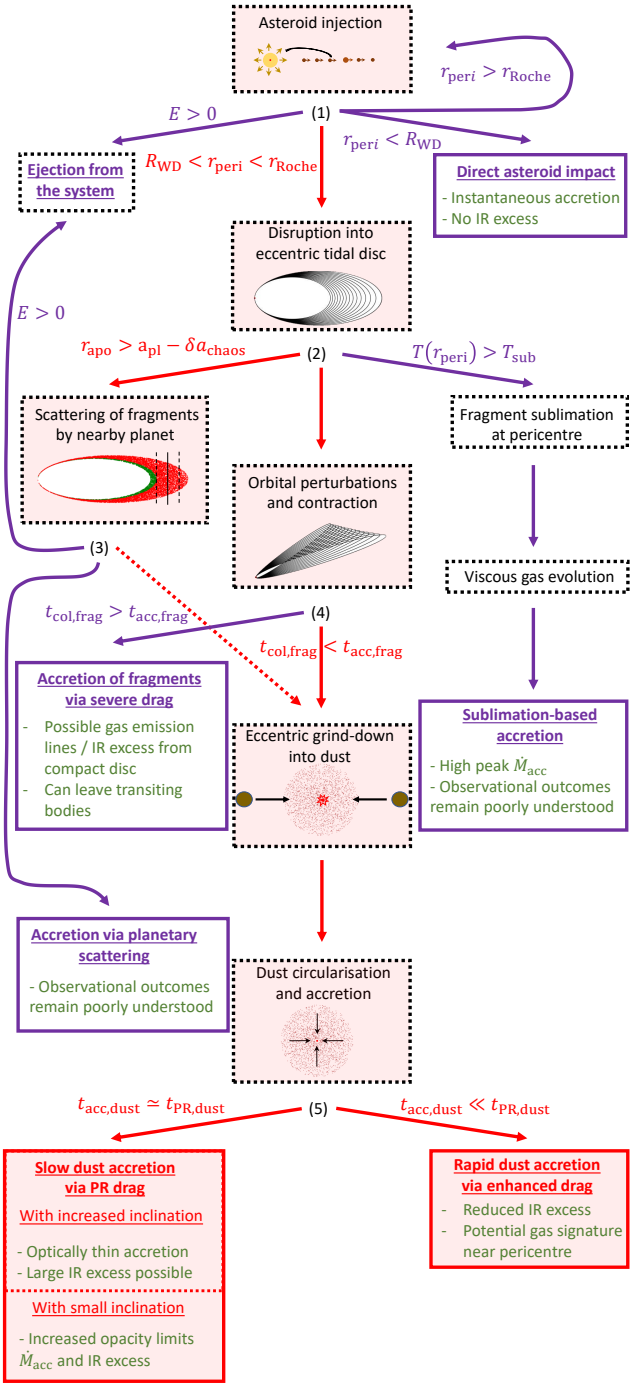

Fig. 4.17 Road-map outlining potential routes for planetary material to arrive in the atmospheres of white dwarfs. Our suggested main route (red arrows and boxes) begins with the injection of an asteroid into the stellar Roche radius, followed by a tidal disruption event, orbital perturbations, collisional grind-down, and finally dust accretion. Alternative accretion channels are shown in purple, with physical selection criteria at five numbered points. The detectable characteristics of these different accretion channels are listed in green, provided that they are sufficiently well-constrained.

planets provide small eccentricity kicks that marginally push asteroids into the white dwarf's tidal disruption zone.

4.7.2 Fork (2): sublimation, continued scattering by a planet or orbital perturbations and collisions

We continue along the main channel of our road-map (visualized as red in Fig. 4.17) with the formation of an eccentric tidal disc. Following the asteroid's disruption, its fragments can evolve in a number of ways, as indicated at the second fork (2). If the temperature at the disc's pericentre exceeds the sublimation threshold, its fragments quickly turn into gas. This is always the expected outcome around hot white dwarfs ($\gtrsim 27.000$ K), which are sufficiently luminous that rocky material begins sublimating at distances outside the star's Roche radius (Bonsor et al., 2017; Steckloff et al., 2021). However, in rarer cases, fragments can also sublimate around less luminous stars if their pericentre lies deep in the Roche sphere or when the fragments contain volatile components, which always sublimate within the Roche radius (Bonsor et al., 2017). Although it is clear that fragment sublimation leads to a distinct channel of accretion, further work is required to determine the full details. If the subsequent viscous evolution of the gas is sufficiently rapid, the gas can quickly accrete onto the star after it is produced, leading to a scenario of pure gas accretion with potentially detectable gas emission lines but no infrared emission. If the gas does not circularize sufficiently within a single orbit, it likely re-condenses on its way back towards apocentre, in which case dust exterior to the Roche limit could produce detectable infrared emission. In any case, this scenario is likely characterized by a high peak accretion rate as small fragments quickly sublimate and the presence of gas only adds to the circularization and accretion speeds of remaining solids.

For those tidal discs where sublimation does not occur, even at pericentre, we consider two further possibilities. If the asteroid was scattered by a planet, this planet could potentially re-scatter the disrupted material. This would occur for those fragments whose apocentre continues to approach that of the planet (See sect. 4.4.2). Otherwise, the fragments will evolve according to further orbital perturbations, including apsidal precession, leading to collisions. We separate these two scenarios because they potentially lead to different observational outcomes, as discussed next.

4.7.3 Fork (3): outcome of continued scattering by a planet

We visualize the possible outcomes of continued scattering after fork (3) of Fig. 4.17. Planets can either scatter fragments outwards, such that they are ejected, inwards, such that they graze

the star with reduced pericentre, or just perturb their orbits, leading to further collisional evolution. The likely outcome depends in part on the size of the asteroid and on its semi-major axis. Since larger asteroids and those that originate from an outer belt disrupt into wider tidal discs, strong scattering by a planet is unlikely for most of their fragments, such that we envisage continued collisional grind-down as the most likely pathway in these cases. This preference towards collisional evolution is further amplified for large asteroids due their fragment's shorter collisional time-scales. For smaller asteroids, collisions require more time and many fragments remain on planet-crossing orbits, making them instead susceptible to continued strong scattering. We predict that as the sublimation zone is significantly larger than the white dwarf, and the bodies are deep in the white dwarf's potential, inward scattering of fragments typically leads to their sublimation rather than a direct impact. In this sense, the accretion channel via planetary scattering might proceed similarly to the sublimation-based channel mentioned earlier. Understanding the full details will require further work, where a detailed understanding of gaseous evolution and condensation on the highly eccentric orbits will be crucial.

4.7.4 Fork (4): rapid circularization or collisional grind-down

We continue our suggested main road at fork (4) of Fig. 4.17 with the evolution of fragments that are not sublimated from the heat of the central star nor scattered by a planet. These fragments nevertheless have their orbits perturbed via various processes (see Sect. 4.4) until they either lose enough angular momentum to accrete onto the star intact, or until they collide with a different fragment. Whether their orbits can fully contract before a catastrophic collision occurs, depends mainly on the size of the asteroid progenitor and the time required for circularization. Larger asteroids produce more fragments and lead to faster collisions. Speed is key here and PR drag, the most suggested process for angular momentum loss, is clearly too slow. It was already shown by Veras et al. (2015b) that PR drag takes too long to accrete fragments above ~ 10 cm before the star cools down, let alone before they collide with other fragments. In our analysis of the tidal and material forces involved, we estimate that the upper limits to fragment sizes lie much higher, around 100 m – 10 km depending mainly on the strength of the asteroid (see Sect. 4.2).

There are, however, other processes that can contract orbits at a much greater pace than PR drag. One of these is the drag induced by fragment interactions with regions around the star that contain high concentrations of either gas or dust grains, for instance in the form of a compact disc that formed from in a prior accretion event. In a recent work, Malamud et al. (2021) showed that drag at the fragment's pericentre can even circularize km-sized bodies in several orbits, provided that a large second object already formed a massive pre-existing

disc around the star. If this disc only exists for a limited duration of time and is thick enough to circularize all but the very largest fragments, remaining km-sized boulders could survive into a new environment where they are relatively safe from collisional grind-down. This has been suggested as a channel to generate transiting material, as is observed around some systems (Manser et al., 2019; Vanderbosch et al., 2020, 2021; Vanderburg et al., 2015). However, an important argument against the significance of this accretion channel is the lack of observations of gaseous emission lines or large IR excesses belonging to the required pre-existing disc. An alternative scenario is that a small minority of fragments survive the stage of collisional grind-down because they are put on only marginally bound orbits after a tidal disruption. These few fragments are much less susceptible to collisions because each orbit takes much longer than for more strongly bound fragments.

4.7.5 Fork (5): the link between dust circularization and infrared excess

In our suggested main channel, we continue with the collisional grind-down of fragments into dust. In this final phase, the speed of the dust circularization leads to a split in possible observational outcomes. With our optically thin emission model, we show that slow dust circularization in a sufficiently inclined disc via PR drag leads to detectable infrared excesses at higher accretion rates ($\gtrsim 10^7$ g/s). This scenario could explain the minority of systems that show significant infrared excesses. If the inclination of the dust instead remains equal to the tiny value imparted during the tidal disruption event, the work done by stellar light becomes limited by the radial optical depth of the grains and the circularization of the shaded dust grains slows down, ultimately limiting accretion onto the star and limiting the IR excess.

However, the scenario of slow dust circularization via PR drag cannot be used to explain the majority of systems that show no detectable infrared excess, even at high accretion rates. We suggest, therefore, that PR drag is not the only force that drives dust circularization around most polluted white dwarfs. As was earlier suggested by Bonsor & Wyatt (2010), other drag forces - likely involving gas - are likely to play a key role. If the time required to circularize dust grains is reduced sufficiently by the gas drag, their accretion can occur without the accumulation of high grain abundances around the central star. In this manner, different circularization speeds of dust around different stars could break the proportionality between accretion rate and infrared excess. It is possible that the small quantities of gas required to accelerate the accretion of dust grains are readily produced in the grind-down process itself. Indeed, Doppler tomography shows that some systems contain gas near the Roche radius, likely as a consequence of collisional production (Manser et al., 2016b; Steele et al., 2021).

4.7.6 Main road: model caveats and improvements

Having discussed conceivable alternative paths to white dwarf pollution along with their physical selection criteria, we finally evaluate the model limitations of our suggested main road to accretion. The main uncertainty in the first stage relates to the fragment size distribution. As discussed in Sect. 4.2, the upper limit of the distribution is limited by our uncertain knowledge of the material strength. At the lower end, it is not clear whether the smallest grains are indeed produced in disruption events, and the slope is very poorly constrained. These factors severely limit the quantitative conclusions of our grind-down calculations, which are strongly related to our assumed size distribution.

Despite the great uncertainties relating to the fragment sizes, we argue that it is worthwhile to evaluate the grind-down to examine the process at order-of-magnitude scale and to investigate the trends and biases it involves. Our simple grind-down model of Sect. 4.5 should be interpreted in this way, rather than as an attempt to predict exact accretion rates. Firstly, it is based only on angular differences induced by differential apsidal precession and does not include any other perturbing processes. Clearly, these other perturbing forces would play an important role. However, the precession rates for differential apsidal precession are analytically known, such that these could be readily incorporated. We hypothesize that the general trends in collisional rates will follow a similar form. Secondly, the calculation only tracks catastrophic collisions and does not track the full collisional evolution of child orbits. This can be justified tentatively by the faster collisions of smaller fragments that result from the collisions, but it remains an important limitation of the model. A more self-consistent evolution is possible to simulate in theory, but is numerically difficult, considering the extreme eccentricity (~ 0.999) of the fragment orbits. Given our limited knowledge of the fragment size distribution, we did not consider that such a model would significantly improve our understanding of the processes involved. Although it could still be worthwhile to develop such a detailed model in the future, its predictive power will remain limited as long as the fragment size distribution after a tidal breakup event remains poorly constrained.

Similarly, our calculation of the infrared excess in the dust accretion stage is done in a simplified manner with the main goal to elucidate trends and show the two-dimensional morphology of the system rather than to predict precise excesses. Most importantly, we only performed calculations in the limiting case that the accreting dust is optically thin, whereas the discs become radially optically thick if the rate of dust production is greater than $\sim 10^7$ g/s and the disc's inclination remains small. Although it is clear that the inclination is directly linked to the observational outcome of dust accretion, further work is required to study how it evolves after the tidal disc has formed.

4.8 Summary and conclusions

The main aim of this chapter is to produce a road-map illustrating several potential routes for white dwarf pollution and to link these paths to observational outcomes (see Fig. 4.17). Our main route begins with the tidal disruption of a scattered asteroid and the formation of a highly eccentric tidal disc, followed by the collisional grind-down of fragments, which finally circularize and accrete onto the star as dust due to drag forces. Alternatives to this standard pathway for white dwarf pollution include a) the direct accretion of scattered asteroids/fragments of asteroids onto the white dwarf, b) the sublimation of dusty material and the accretion of gas, or c) the rapid circularization of fragments via pre-existing compact discs. While accretion likely proceeds through a combination of these channels, the alternative a) is statistically very unlikely to occur, even with a planet re-scattering fragments of a disrupted asteroid. Channel b) will occur only for material scattered sufficiently close to the hottest white dwarfs, while c) occurs only following previous disruption events.

Here we present detailed calculations of our suggested main road to white dwarf pollution. Our work includes simulations of collisional grind-down due to differential precession, as well as a model for the infrared excess of the dust that is produced. Our main findings are that:

1. The size distribution of fragments in a tidal disruption event around a white dwarf can range as many as 10 orders of magnitude. The smallest bound fragments are no smaller than the limit set by radiation pressure at 0.1-10 μm (Fig. 4.5), while fragments as large as 100 m-10 km also survive the tidal disruption depending on their material strength (Fig. 4.2). In the absence of a pre-existing compact disc or intense radiation, these larger fragments must be ground down before they can circularize and accrete by drag forces.

2. Large asteroids produce more fragments when they disrupt, causing rapid collisional grind-down and generating short and intense bursts of dust production, whereas smaller asteroids grind down over longer periods of time. If subsequent dust accretion is fast, this biases observations to detect ongoing accretion at intermediate rates by smaller asteroids. Rare peaks in accretion rates from large asteroids are short-lasting and only probable to be detected in the atmospheres of DBZ stars with longer sinking time-scales (Fig. 4.12).

3. Optically thin dust discs produce large amounts of infrared emission when their accretion rate exceeds 10^7 g/s. However, in order to remain completely optically thin at these high accretion rates, the inclination of the dust grains must be substantially

increased beyond the tiny value imparted at the moment of tidal disruption. Infrared excesses at high accretion rates can be avoided by more rapid dust circularization, for instance via enhanced drag due to the presence of gas near the disc's pericentre.

Chapter 5

Asynchronous accretion can mimic diverse white dwarf pollutants I: core and mantle fragments

"Where is all my wisdom, then? I behaved stubbornly, pursuing a semblance of order, when I should have known well that there is no order in the universe."

- Umberto Eco, The Name of the Rose, 1986

In this chapter, we continue the discussion of the accretion process of planetary material onto white dwarfs. We show that due to asymmetries in the accretion process, the composition of the material falling onto a star may vary with time during the accretion of a single planetary body. Consequently, the instantaneous photospheric abundances of white dwarfs do not necessarily reflect the bulk composition of their pollutants, especially when their diffusion timescales are short. In particular, we predict that when an asteroid with an iron core tidally disrupts around a white dwarf, a larger share of its mantle is ejected, and that the core/mantle fraction of the accreting material varies with time during the event.

5.1 Introduction

In order to accurately translate spectroscopic signatures into pollutant abundances, a detailed understanding of photospheric physics is required, with well-constrained diffusion timescales for different elements (Cunningham et al., 2021; Koester et al., 2014, 2020). It is equally important, however, to understand how accretion onto white dwarfs proceeds temporally. If different parts of a pollutant (e.g., core/mantle, volatile/refractory) enter the white dwarf's

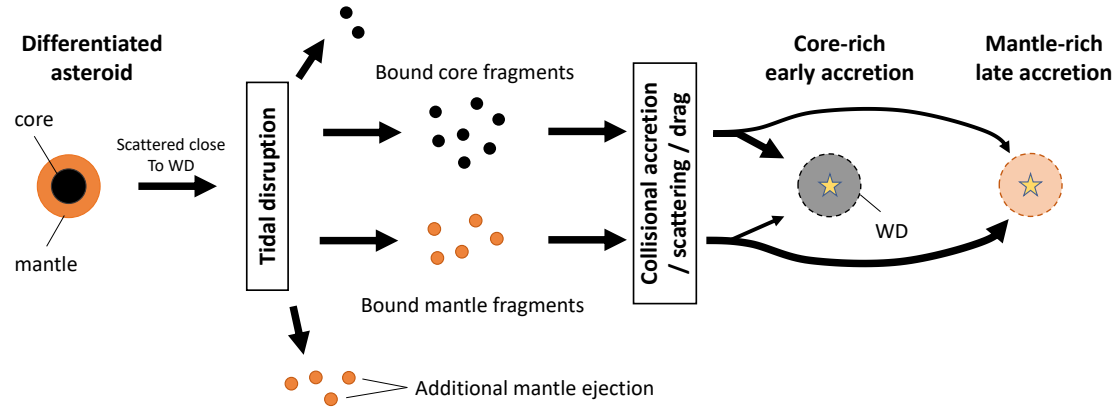

Fig. 5.1 Schematic overview of how the asynchronous accretion of a differentiated asteroid onto a white dwarf can mimic the photospheric signature of either a core- or mantle-rich object. In this simplified scenario, a differentiated asteroid tidally disrupts into fragments composed of core or mantle material. Mantle fragments are preferentially ejected out of the system in greater proportions, and bound core and mantle fragments occupy distinct orbital zones in the tidal disc (Section 5.2). Core fragments collide or scatter sooner on average, leading to a core-rich early accretion phase, followed by a mantle-rich late accretion phase (Section 5.3). The form of this figure was inspired by the conceptually similar Fig. 1 of Buchan et al. (2022). An accompanying version of this figure that details asynchronous ice-refractory accretion is presented in chapter 6.

photosphere at different times, this *asynchronous accretion* could mimic an identical signature of e.g., a core-rich or a volatile-rich body whose parts accrete synchronously (see Fig. 5.1). The implicit assumption in the current analyses of polluted white dwarfs – that accretion proceeds both synchronously and symmetrically – is clearly valid when a solid body directly strikes the white dwarf's surface (Brown et al., 2017; McDonald & Veras, 2021) but such instances are predicted to be exceedingly rare (Veras et al., 2021). Instead, the accretion process is thought to begin with a tidal disruption and the formation of an eccentric tidal disc (Debes et al., 2012; Malamud & Perets, 2020a,b; Nixon et al., 2020; Veras et al., 2014a), whose fragments can subsequently accrete via a range of processes (e.g., Brouwers et al., 2022; Li et al., 2021; Malamud et al., 2021; Veras et al., 2015a,b). In this work, we perform the first analysis of the synchronicity of accretion onto white dwarf photospheres. This chapter considers the accretion of core and mantle fragments from a differentiated pollutant. In the next chapter (5), we study the contrast in accretion between refractory materials and ices (e.g., H_2O, CO_2). Our results highlight that different elements are theoretically expected to accrete in proportions that vary over time, a finding that is supported by our analysis of the current sample of polluted whited dwarfs, and that can be corroborated further with upcoming large samples of young white dwarfs.

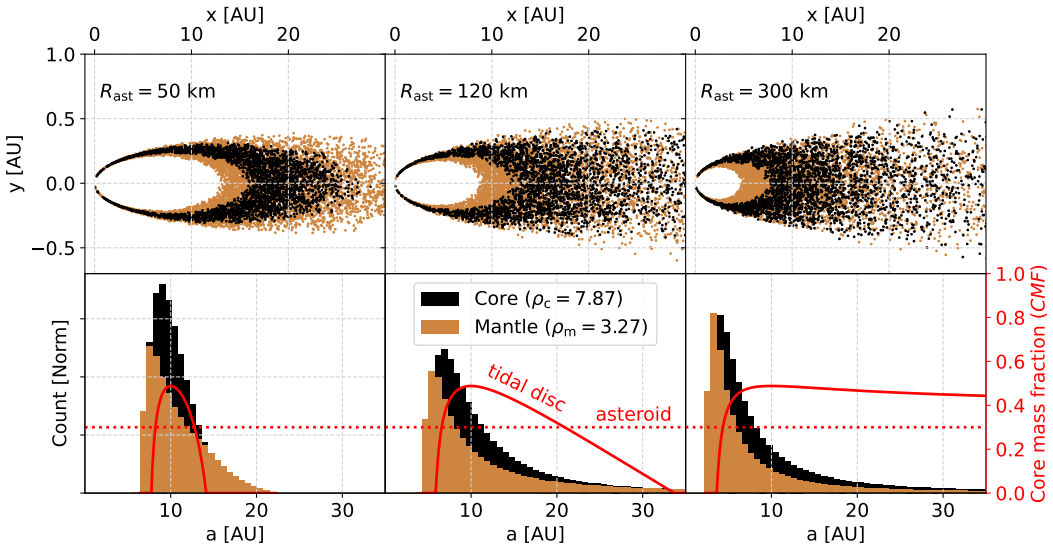

Fig. 5.2 Distribution of core and mantle fragments after the tidal disruption of a differentiated asteroid from 10 AU around a white dwarf. The top panels provide a top-down view of the tidal disc, and show that core (black) and mantle (brown) fragments are spread to distinct, but partially overlapping orbital ranges. The histogram plots in the lower panels show the distribution of material in more detail. The solid red line indicates the core mass fraction (*CMF*) at a given orbit, which can be compared to the 30% CMF of the asteroid progenitor (red dotted line). The innermost orbits of the tidal disc always contain exclusively mantle material, while the outer orbits are enhanced in core material if the asteroid was large (right panels), and depleted otherwise (left and middle panels).

This chapter is organized as follows. We first show in Section 5.2 how a tidal disruption unevenly spreads and ejects core and mantle fragments, providing an asymmetric starting point for the accretion process. We then consider the collisional grind-down of a differentiated asteroid in Section 5.3.1 and evaluate the relative scattering of core and mantle fragments by a planet in Section 5.3.2. In order to test the validity of our proposition, we investigate the accretion rate and abundance distribution of iron relative to lithophile elements in Section 5.4. We discuss our findings in Section 5.5 and conclude in Section 5.6.

5.2 Disruption of differentiated asteroids

The accretion process of planetary material onto a white dwarf is thought to begin with the perturbation of an asteroid or planetary body onto a highly eccentric orbit (e.g., Bonsor et al., 2011; Mustill et al., 2018; Smallwood et al., 2018). When the asteroid ventures too close to the star, its internal strength and self-gravity are overwhelmed by stellar gravity, and it

tidally disrupts (Debes et al., 2012; Malamud & Perets, 2020a,b; Veras et al., 2014a). In this section, we consider a simplified scenario where the disrupted body was differentiated into two radially separate layers: a central core, and an outer mantle. We first study how these components are geometrically spread in the tidal disc, and then trace their accretion onto the white dwarf as a function of time. If both components (core and mantle) accrete with a constant mass ratio over time, the composition of the photosphere remains unchanged. However, if the accretion of either component follows a different trend, and the accretion process is *asynchronous*, the composition of the photosphere varies with time during the accretion of a single body.

5.2.1 Geometry of core and mantle fragments in tidal discs

In the scenario that asteroids are torn apart by strong tidal forces close to the star, accretion is preceded by the formation of an eccentric tidal disc. Core and mantle fragments will occupy distinct orbits in this disc due to their different radial positions within the asteroid. In order to trace the distribution of these orbits, we consider a simplified, instantaneous tidal disruption at a distance $r_{\rm B} = 0.75\ {\rm R}_{\odot}$ from the star[1]. The energies of the fragments i depend on their distance $r_{\rm i}$ to the star, and their semi-major axes $a_{\rm i}$ become spread out along the range (e.g., Brouwers et al., 2022):

$$a_{\rm i} = a_{\rm ast}\left(1 + 2a_{\rm ast}\frac{r_{\rm B} - r_{\rm i}}{r_{\rm B} r_{\rm i}}\right)^{-1}, \tag{5.1}$$

with eccentricities $e_{\rm i} = 1 - r_{\rm i}/a_{\rm i}$. This calculation safely ignores the spin of the asteroid (see Appendix C.1). While the fragments initially form in a cluster, with core and mantle regions not necessarily disrupting simultaneously (Duvvuri et al., 2020; Malamud & Perets, 2020a; Veras et al., 2017), they shear out over time, and completely fill a tidal disc after a well-defined timescale (see Appendix C.2 for a derivation of this filling time). The width of the tidal disc that forms in this manner depends chiefly on the size of the asteroid and on its semi-major axis. The fragments of small asteroids that originate from a planetary system spread out along a narrow orbital band when they disrupt (Nixon et al., 2020; Veras et al., 2021, 2014a), while larger objects on wider orbits form a broader tidal disc, culminating in a completely bimodal disruption for planet-sized bodies, where half of their fragments eject from the system, and the rest become concentrated close to the star (Malamud & Perets, 2020a,b; Rafikov, 2018).

Fragments from different layers in the asteroid are spread to distinct orbits. Therefore, an asteroid that has any radial variation in its composition will form a tidal disc whose geometry

[1]Corresponding to the disruption of a strengthless or sufficiently large asteroid with a core mass fraction (*CMF*) of 0.3 around a 0.6 $M_{\odot}$ white dwarf (e.g., Bear & Soker, 2013; Davidsson, 1999).

retains a similar compositional variation. We illustrate this asymmetry in Fig. 5.2 for a range of asteroid sizes, assuming representative core and mantle densities of $\rho_c = 7.87\ \mathrm{g/cm^3}$ and $\rho_m = 3.27\ \mathrm{g/cm^3}$, respectively, corresponding to iron and forsterite. Small asteroids (left panel, $R_{ast} = 50$ km), disrupt into a tidal disc whose intermediate orbits contain additional core material, whereas both its inner and outer orbits consist entirely of mantle fragments. Larger asteroids of 120 km (middle panel) form tidal discs whose core fragments spread out over a wider range, although their innermost and outermost fragments still consist exclusively of mantle material. At $R_{ast} = 300$ km (right panel), a substantial fraction of the fragments become unbound from the stellar system and all except the closest orbits are enhanced in core material.

5.2.2 Ejection bias of mantle and crustal fragments

The parts of the asteroid that are furthest from the white dwarf during the tidal disruption are the easiest to eject. The outer layers of a differentiated asteroid are part of its mantle, and so the remaining material that forms the bound tidal disc can become dominated by the core. The dividing line between bound and unbound fragments is drawn at a distance R_{eject} from the asteroid's centre (Malamud & Perets, 2020a):

$$R_{eject} = \frac{r_B^2}{2a_{ast} - r_B}, \tag{5.2}$$

with all the material beyond R_{eject} lost into space. To compute the core mass fraction of the bound tidal disc, we compare the total volume fraction of the ejected material ($\chi_{ast} = V_{ast,unbound}/V_{ast}$) to the ejection fraction of the core ($\chi_c = V_{c,unbound}/V_c$):

$$\chi_{ast} = \frac{3}{4\pi R_{ast}^3} \int_{R_{ast,eject}}^{R_{ast}} \pi \left(R_{ast}^2 - x^2\right) dx \tag{5.3a}$$

$$= \frac{\left(R_{ast} - R_{ast,eject}\right)^2 \left(2R_{ast} + R_{ast,eject}\right)}{4R_{ast}^3}, \tag{5.3b}$$

$$\chi_c = \frac{3}{4\pi R_c^3} \int_{R_{c,eject}}^{R_c} \pi \left(R_c^2 - x^2\right) dx \tag{5.3c}$$

$$= \frac{\left(R_c - R_{c,eject}\right)^2 \left(2R_c + R_{c,eject}\right)}{4R_c^3}, \tag{5.3d}$$

where $R_{c,eject} = \min(R_{eject}, R_{c,ast})$ and $R_{ast,eject} = \min(R_{eject}, R_{ast})$. Combined, these expressions analytically specify the mass fraction of core material in the bound tidal disc (CMF_{disc}):

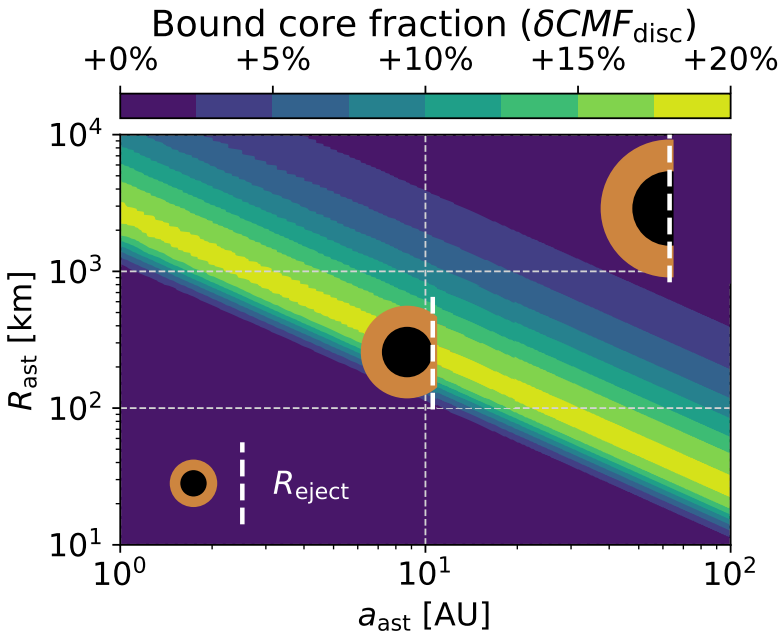

Fig. 5.3 Enhancement in bound core mass fraction ($\delta CMF_{\rm disc} = (CMF_{\rm disc} - CMF_{\rm ast})/CMF_{\rm ast}$, colours) of tidal discs compared to their asteroid progenitors. Three regimes can be identified. Both sufficiently small asteroids and large planetary bodies disrupt into discs with unaltered core mass fractions, as either half or none of their mass is ejected. In between, larger asteroids and dwarf planets eject primarily crustal and mantle material when they disrupt, resulting in a more core-rich tidal disc.

$$CMF_{\rm disc} = \frac{\rho_{\rm c}\left(V_{\rm c} - V_{\rm c,unbound}\right)}{\left(\rho_{\rm c} - \rho_{\rm m}\right)\left(V_{\rm c} - V_{\rm c,unbound}\right) + \rho_{\rm m}\left(V_{\rm ast} - V_{\rm ast,unbound}\right)} \tag{5.4a}$$

$$= \frac{1 - \chi_{\rm c}}{\left(\chi_{\rm ast} - \chi_{\rm c}\right)\left(1 - \rho_{\rm m}/\rho_{\rm c}\right) + \left(1 - \chi_{\rm ast}\right)/CMF_{\rm ast}}, \tag{5.4b}$$

where $CMF_{\rm ast} = M_{\rm c,ast}/M_{\rm ast}$ is the core mass fraction of the asteroid.

We show the core enhancement of the tidal disc in Fig. 5.3, which presents three distinct regimes as a function of asteroid size and semi-major axis. Fragments from sufficiently small or tight asteroids ($R_{\rm ast} < R_{\rm eject}$) remain entirely bound to the star, and the core mass fraction of their tidal discs is equal to that of their asteroid progenitors. Similarly, very large asteroids ($R_{\rm ast} \gg R_{\rm eject}$) disrupt in a bimodal manner where nearly half of their material is ejected, again leaving the bulk core fractions in the tidal disc largely unchanged. In between, however, intermediate-sized asteroids ($R_{\rm ast} \sim R_{\rm eject}$) eject almost exclusively mantle and crustal fragments, increasing the fraction of core material in their tidal disc by up to 20%.

The size range most affected by this ejection asymmetry lies between 100-1000 km in the inner disc (< 10 AU), which overlaps with the larger asteroids and dwarf planets in the Solar System's asteroid belt, like Vesta and Ceres. In the outer disc, the affected sizes shrink substantially to ~ 20 km at 100 AU. At this point, only the asteroids that formed sufficiently early will have differentiated, and so the importance of the ejection asymmetry gradually diminishes towards the far outer disc. Finally, we note that the ejection asymmetry, illustrated with core-mantle differentiated bodies, applies to any pollutant with a radial variation in composition. This includes the ejection of an increased portion of crustal material relative to both the core and mantle, as well as the ejection of additional ice when a comet contains an icy outer layer (see chapter 5). Therefore, when a differentiated object disrupts around a white dwarf, the material that accretes onto it will often not exactly match its bulk composition.

5.3 Asynchronous accretion of core and mantle fragments

In this section, we illustrate how the spatial asymmetry between core and mantle fragments in a tidal disc can cause these components to accrete asynchronously onto the white dwarf. We follow the road-map to accretion outlined by Brouwers et al. (2022), where accretion either proceeds via differential precession and collisional grind-down, or via the scattering of fragments by a planet (see also Li et al. 2021). In Section 5.5.3, we discuss how core-mantle accretion may play out in different accretion models.

5.3.1 Scenario I: differential precession and collisional grind-down

In this first scenario, we consider the three-stage accretion model suggested in the previous chapter. In the first stage, a tidal disruption spreads the fragments over a range of highly eccentric orbits, as discussed in the previous section. The orbits do not follow precise Keplerian tracks and their pericentres precess over time due to GR, at rates that depend on their semi-major axis and eccentricity (Debes et al., 2012; Veras et al., 2014a). Inner fragments precess more quickly than those on wider orbits and unless interactions allow the disc to precess coherently, significant apsidal differences between fragments build up over time, causing orbits to cross. In the second stage of the model, fragments grind into dust at the intersection points. Finally, the dust quickly accretes due to drag forces, preventing a large infrared excess. In our calculation, we divide the fragments into a two-dimensional grid along semi-major axis and fragment size. The semi-major axis grid points accommodate a constant portion of fragment mass when the tidal disc forms. The fragment orbits are set by Eq. 5.1, which we evaluate according to the spatial distribution of core and mantle material

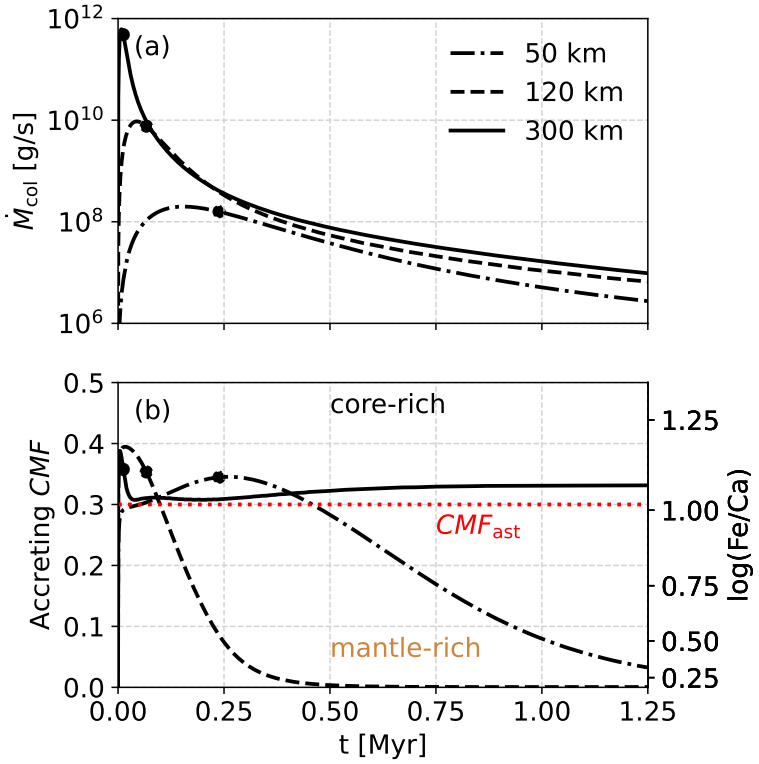

Fig. 5.4 The rate at which mass is lost due to collisions from the tidal disc, a proxy for the accretion rate onto polluted white dwarfs, calculated according to scenario I. The lines correspond to either a differentiated 50 km (dotted), 120 km (dashed) or 300 km (solid) asteroid, with semi-major axes at 10 AU and a 30% core mass fraction (red line). The points indicate when half of the pollutant's mass has been accreted. In panel (a), the total collision rate first increases as fragment orbits begin to cross, and then decreases when the disc becomes depleted. In panel (b), the core mass fraction of the colliding material is shown to vary over time, leading to the asynchronous accretion of core and mantle components.

in a spherical asteroid. Orbits whose fragments originate from the centre of the asteroid contain more core material, whereas orbits contain additional mantle material (See Fig. 5.2). The rate of catastrophic collisions is modelled with a particle-in-cell approach (Eqs. 22-26 of Brouwers et al. 2022), with the crude assumption that a catastrophic collision turns the entire fragment into dust, which then quickly accretes onto the star.

We show the evolution of the total catastrophic collision rate of core and mantle fragments combined in panel (a) of Fig. 5.4, plotted for disrupted asteroids of 50, 120 and 300 km in size. These simulations are run with 200 semi-major axis bins and 150 size bins, for a total of resolution of 30,000 fragments. As was shown in the previous chapter, the collision rate first builds up, due to an increase in orbit crossings, and then declines when the tidal disc

becomes depleted of fragments. The peak collision rate is much greater in more massive discs, as larger asteroids break up into more fragments that each collide more easily. In panel (b), we plot the core mass fraction of the accreting material as a function of time, with the equivalent Ca/Fe number ratio that would be observed in the photosphere if the core and mantle have Earth-like elemental abundances[2]. Core fragments in a tidal disc cluster on intermediate orbits, while those from the mantle mostly occupy the inner and outer orbits (see Fig. 5.2). As a result, collisions initially involve an increased fraction of core fragments. The fragments located on the outermost orbits can spend many years at their apocentres every orbit, and are the last to collide. In the 50 km and 120 km examples, these outermost orbits only contain mantle fragments, and the core fraction of their accreting material drops all the way to zero over time. This is not the case for the grind-down of a larger 300 km asteroid (see Section 5.2).

The instantaneous accretion rates in Fig. 5.4 indicate what would be observed in white dwarfs with short diffusion timescales, such as those with hydrogen-dominated atmospheres. The implied accretion rates and compositions will show reduced variability for older stars with helium-dominated atmospheres, as material remains in their atmospheres for longer, averaging over a portion of the accretion curve. When the diffusion timescale exceeds 1 Myr in this model, as is the case for helium-dominated envelopes cooler than 20,000 K, the entire accretion is averaged over, to a value closer to the asteroid's bulk composition.

5.3.2 Scenario II: scattering of core fragments by a planet

If a white dwarf is polluted by a planetesimal that was scattered onto a star-grazing orbit by a planet, it is likely that the planet continues to scatter the fragments after the main body is disrupted. This alternative accretion scenario was discussed by Brouwers et al. (2022) and studied with more numerical simulations by Li et al. (2021). When a fragment is scattered by a planet, it can either collide with the white dwarf, be ejected from the system, or just continue on a different orbit (Wyatt et al., 2017). In the scattering simulations by Li et al. (2021) with a Neptune-mass planet, most scattered fragments quickly hit the white dwarf. We suggest that core fragments are significantly more likely to be re-scattered by a planet due to their central positioning in the tidal disc, providing a second channel for asynchronous core-mantle accretion.

[2]Assuming steady-state accretion with a typical sinking timescale ratio between Ca and Fe of $\tau_{\mathrm{Ca}}/\tau_{\mathrm{Fe}} = 1.4$ (Koester et al., 2020). Earth's core mean molecular weight is taken as $\mu_{\mathrm{c}} = 53.79$, with core Ca and Fe mass fractions of $f_{\mathrm{Ca,c}} = 0\%$ and $f_{\mathrm{Fe,c}} = 88.8\%$ (Workman & Hart, 2005). Earth's mantle equivalents are taken as: $\mu_{\mathrm{m}} = 51.7$, $f_{\mathrm{Ca,m}} = 2.3\%$, and $f_{\mathrm{Fe,m}} = 6.4\%$ (Morgan & Anders, 1980).

In the example that we study here, a single planet of 10 $M_\oplus$ is located at the apocentre of the asteroid's orbit ($a_{\rm pl} = 2a_{\rm ast}$). The maximum allowed distance where fragments are re-scattered can be approximated from the width of the chaotic zone ($\delta a_{\rm chaos} = C\, a_{\rm pl} \left(\frac{M_{\rm pl}}{M_{\rm WD}}\right)^{\frac{2}{7}}$ (Chiang et al., 2009; Duncan et al., 1989; Quillen & Faber, 2006; Wisdom, 1980)), with constant $1.3 < C < 2$. The inner edge of the chaotic zone provides a minimum semi-major axis for re-scattering $a_{\rm i} > a_{\rm cross}$ (Brouwers et al., 2022), with:

$$a_{\rm cross} \geq \frac{a_{\rm pl}}{2}\left[1 - C\left(\frac{M_{\rm pl}}{M_{\rm WD}}\right)^{\frac{2}{7}}\right]. \tag{5.5a}$$

The semi-major axis of a fragment is related to its position relative to the star at the moment of disruption via Eq. 5.1. Using that $r_{\rm B} \ll a_{\rm ast}$, we can derive an analogous criterion to the ejection distance (Eq. 5.2) for the re-scattering of fragments by a planet. If the distance of a fragment to the white dwarf exceeds $r_{\rm B} + R_{\rm scat}$ at the moment of the tidal disruption, the fragment will cross the chaotic zone of the planet:

$$R_{\rm scat} = -\frac{r_{\rm B}^2\, \delta a_{\rm chaos}}{a_{\rm pl}(a_{\rm pl} - \delta a_{\rm chaos})}. \tag{5.6a}$$

These fragments that intersect a planet's orbit are susceptible to re-scattering. Similar to the calculation presented in Section 5.2.2, we can use this characteristic distance to compute the total volume fraction of fragments that can be scattered ($\widetilde{\chi}_{\rm ast} = V_{\rm tot,scat}/V_{\rm ast}$), and compare this to the fraction of core material liable to scattering ($\widetilde{\chi}_{\rm c} = V_{\rm c,scat}/V_{\rm c}$):

$$\widetilde{\chi}_{\rm ast} = \frac{3}{4\pi R_{\rm ast}^3}\int_{R_{\rm ast,scat}}^{R_{\rm ast,eject}} \pi\left(R_{\rm ast}^2 - x^2\right) dx \tag{5.7a}$$

$$= \frac{3R_{\rm ast}^2\left(R_{\rm ast,eject} - R_{\rm ast,scat}\right) - R_{\rm ast,eject}^3 + R_{\rm ast,scat}^3}{4R_{\rm ast}^3}, \tag{5.7b}$$

$$\widetilde{\chi}_{\rm c} = \frac{3}{4\pi R_{\rm c}^3}\int_{R_{\rm c,scat}}^{R_{\rm c,eject}} \pi\left(R_{\rm c}^2 - x^2\right) dx \tag{5.7c}$$

$$= \frac{3R_{\rm c}^2\left(R_{\rm c,eject} - R_{\rm c,scat}\right) - R_{\rm c,eject}^3 + R_{\rm c,scat}^3}{4R_{\rm c}^3}, \tag{5.7d}$$

where $R_{\rm c,scat} = \max(R_{\rm scat}, -R_{\rm c})$ and $R_{\rm ast,scat} = \max(R_{\rm scat}, -R_{\rm ast})$. Together, these expressions specify the mass fraction of core material that can be re-scattered ($CMF_{\rm scat}$) from the

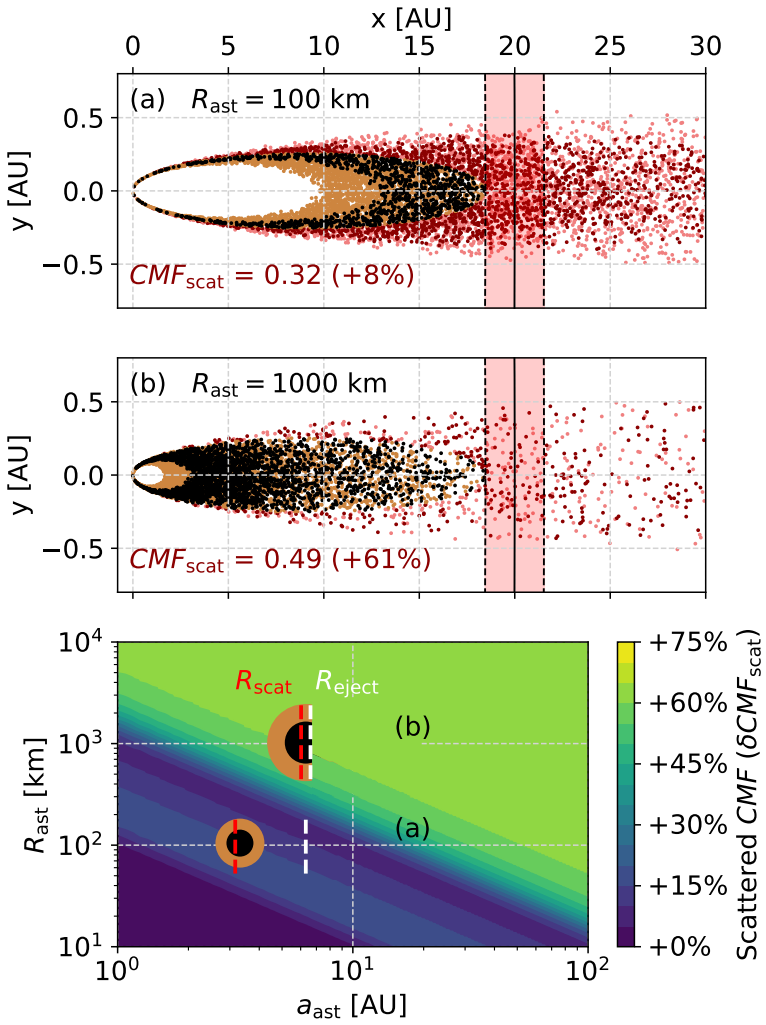

Fig. 5.5 Scattering asymmetry of core and mantle fragments by a 10 $M_\oplus$ planet. In the top panels (a,b), the orbit of the planet and its chaotic zone are indicated by the red band. The red particles are susceptible to getting scattered, while brown (mantle) and black (core) particles are safe. On average, core fragments are more likely to be scattered by a planet, and the difference is greatest for larger asteroids and dwarf planets from the outer disc.

tidal disc by a planet:

$$CMF_{\rm scat} = \frac{\rho_{\rm c} V_{\rm c,scat}}{(\rho_{\rm c} - \rho_{\rm m}) V_{\rm c,scat} + \rho_{\rm m} V_{\rm ast,scat}} \tag{5.8a}$$

$$= \frac{\widetilde{\chi}_{\rm c}}{(\widetilde{\chi}_{\rm c} - \widetilde{\chi}_{\rm ast})(1 - \rho_{\rm m}/\rho_{\rm c}) + \widetilde{\chi}_{\rm ast}/CMF}. \tag{5.8b}$$

We present the results of this calculation in Fig. 5.5. Panels (a) and (b) show the disruption of a 100 km and 1000 km asteroid, respectively. In both cases, core fragments are more susceptible to re-scattering via close encounters with the planet, with an additional scattered core mass fraction between 8% and 61% present in the relevant orbital range. Fragments that are sufficiently tightly bound to the star are protected from close encounters with the planet, while unbound fragments eject on hyperbolic orbits. The fragments that remain to be scattered originate from the core-rich middle of the asteroid. While the scattering asymmetry in terms of core/mantle ratio is greatest for the largest bodies, only a small percentage of the bound fragments are scattered if the body is too large. Therefore, like the ejection asymmetry discussed in Section 5.2.2, the scattering asymmetry is most important for asteroids and dwarf planets in the range between 100-1000 km in the inner disc, and down to 20 km at 100 AU.

5.4 Test of preferential mantle ejection

From the preceding arguments, the asymmetries in the accretion process of differentiated bodies onto white dwarfs lead to two observational predictions:

1. Mantle fragments are preferentially ejected in the tidal disruption that likely precedes accretion. This implies that the material that accretes onto white dwarfs from differentiated bodies is enriched in core material by up to 20%.

2. Core and mantle fragments spread to distinct orbital ranges after a tidal disruption, causing them to accrete in a proportion that varies over time. Core fragments likely accrete faster on average than mantle fragments, so the core mass fraction of the accreted material is expected to decline over time during a single accretion event.

In this section, we analyse with the current white dwarf sample to compare with this first prediction.

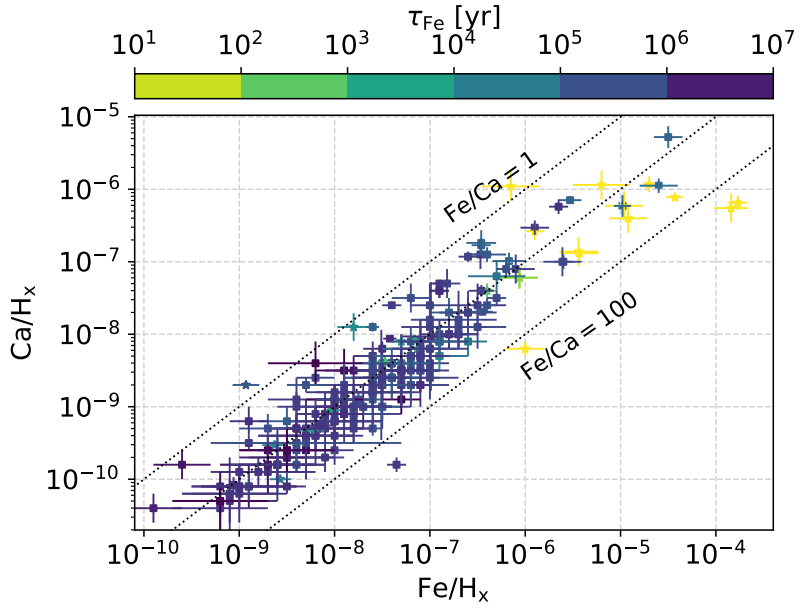

Fig. 5.6 Photospheric abundances of calcium and iron in our white dwarf sample. The colours indicate the diffusion timescale of iron in the white dwarf atmospheres, computed with models by Koester et al. (2020). Lines of constant abundance ratios relative to iron are overplotted.

5.4.1 White dwarf sample with Fe/Mg or Fe/Ca abundance ratios

To observationally study the accretion asymmetries between the core and mantle, we compile a sample of polluted white dwarfs with measured photospheric abundances of both iron and Ca. The sample is by no means uniformly selected, and contains all white dwarfs with these abundance ratios that we could find in the literature. The photospheric abundances of the sample are plotted in Fig. 5.6, and show about two orders of magnitude variation in the ratios of Fe/Ca.

5.4.2 Evidence for a core bias in the total accreted material

We first study the first prediction, that the preferential ejection of mantle fragments after a tidal disruption (Section 5.2.2) skews the accretion of material onto white dwarfs to core-rich compositions. As a test, we compare the accretion rate ratios $\dot{M}_{\rm Fe}/\dot{M}_{\rm Ca}$ in the sample of polluted white dwarfs to a second sample of 957 nearby FGK stars (Brewer et al., 2016; Harrison et al., 2018), which represent a pristine abundance ratio. Because planetary material forms from the same molecular clouds that form stars, stellar data are a useful proxy for certain pristine abundance ratios in a proto-planetary disc that are not altered by nucleosynthesis in the stars or incomplete condensation in the proto-planetary disc

(Adibekyan et al., 2021; Lodders, 2003). In our analysis, we limit the sub-sample studied to older white dwarfs, whose diffusion times are sufficiently long (>Myr) to average over the accretion process, allowing the bulk composition of the accreted material to be measured. Furthermore, we use Ca rather than Mg here because of significant differences in reported Mg abundance rates, depending on the constitutive physics used to model the atmospheres of cool, helium-dominated white dwarfs (Blouin, 2020; Hollands et al., 2017; Turner & Wyatt, 2020).

In an equilibrium between accretion and downward diffusion, the accretion rate of element El onto a white dwarf is given by:

$$\dot{M}_{\rm El} = {\rm El/H_x} \frac{\mu_{\rm El} M_{\rm cvz}}{\mu_{\rm H_x} \tau_{\rm El}}, \tag{5.9}$$

where $\rm El/H_x$ is the photospheric abundance of El relative to hydrogen or helium, $M_{\rm cvz}$ is the mass of the star's convective zone, $\mu_{\rm El}, \mu_{\rm H_x}$ are atomic weights and $\tau_{\rm El}$ is the diffusion timescale of El. In our sample, the abundances $\rm El/H_x$ are collated from the literature (see Table C.6), and $M_{\rm cvz}, \tau_{\rm El}$ are calculated with the module `timescale_interpolator` from the open source code `PyllutedWD`[3] (Buchan et al., 2022; Harrison et al., 2021a), based on updated white dwarf models from Koester et al. (2020). The photospheric abundances of Fe and Ca in white dwarfs are subject to significant errors. Assuming that these abundance errors are independent, and that the diffusion timescales are exactly known, the combined error on the accretion ratio is:

$$\sigma_{\log(\dot{\rm M}_{\rm Fe}/\dot{\rm M}_{\rm Ca})} = \sqrt{\sigma^2_{\log({\rm Fe/H_x})} + \sigma^2_{\log({\rm Ca/H_x})}}. \tag{5.10}$$

We follow a slightly modified Kolmogorov–Smirnov test procedure to compare the abundance ratios of white dwarfs to pristine material. The main issue in comparing the distributions of Ca/Fe in white dwarf pollutants and FGK stars, is that the measurement errors on both samples are not comparable. Whereas errors on the FGK abundances are very small relative to the reported abundances, reported errors on the white dwarf abundances are typically around 0.2 dex ($\sim 60\%$). Measurement errors in effect act to spread out the sampled distribution of CA/Fe ratio's for white dwarfs, making it wider than the underlying distribution. To account for this effect, we go through a procedure to apply these same measurement errors to the stellar sample. When the measurement errors of the white dwarf sample are applied to the FGK star data, the probability density $\rm PDF_{FGK}$ of an accretion rate

[3]https://github.com/andrewmbuchan4/PyllutedWD_Public

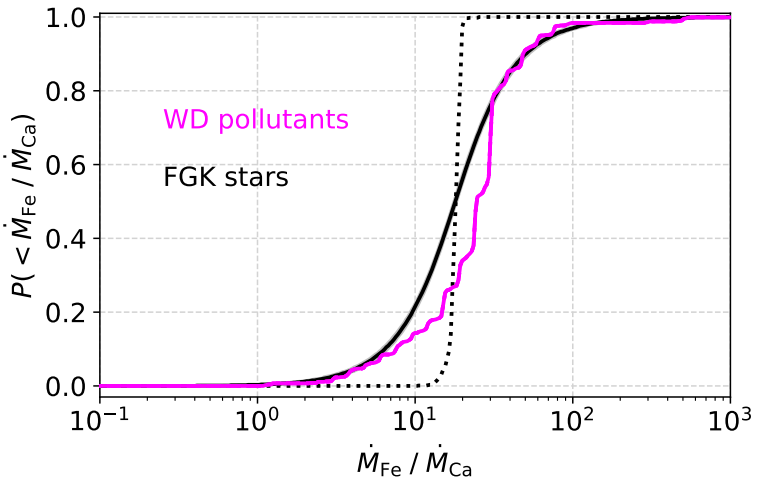

Fig. 5.7 Cumulative distribution of steady-state accretion rates (Eq. 5.9) of iron relative to calcium, showing that white dwarf polluting material is iron-rich. The magenta curve corresponds to bulk white dwarf pollutant compositions (white dwarfs with $\tau_{Fe} > \text{Myr}$), while the black curve corresponds to abundances of nearby FGK stars (Brewer et al., 2016). The dotted lines indicate reported values, and the solid lines are built from a sampling with white dwarf measurement errors.

ratio of white dwarfs can be computed for a sample of N stars:

$$\text{PDF}_{\text{FGK}} = \frac{1}{N}\sum_{i=0}^{N} \frac{1}{\sqrt{2\pi}\sigma_{\log(\dot{M}_{Fe}/\dot{M}_{Ca})_{WD,i}}} \exp\left[-\frac{1}{2}\left(\frac{\log(\dot{M}_{Fe}/\dot{M}_{Ca}) - \log(\dot{M}_{Fe}/\dot{M}_{Ca})_{FGK,i}}{\sigma_{\log(\dot{M}_{Fe}/\dot{M}_{Ca})_{WD,i}}}\right)^2\right]. \tag{5.11}$$

The error-corrected cumulative probability function (CDF_{FGK}) similarly follows from its integral as:

$$\text{CDF}_{\text{FGK}} = \frac{1}{2N}\sum_{i=0}^{N}\left[1 + \text{erf}\left(\frac{\log(\dot{M}_{Fe}/\dot{M}_{Ca}) - \log(\dot{M}_{Fe}/\dot{M}_{Ca})_{FGK,i}}{\sqrt{2}\sigma_{\log(\dot{M}_{Fe}/\dot{M}_{Ca})_{WD,i}}}\right)\right]. \tag{5.12}$$

We estimate asymmetric errors on CDF_{FGK} by repeatedly sampling white dwarf errors from the white dwarf distribution. For this comparison, we calculate the Kolmogorov–Smirnov test statistic (D) of the sampled white dwarf CDF, and the error-corrected FGK star CDF:

$$D = \max\left(|\mathrm{CDF}_{\mathrm{FGK}} - \mathrm{CDF}_{\mathrm{WD}}|\right). \tag{5.13}$$

This generates a list of values for D, corresponding to the different samplings of the white dwarf errors applied to the FGK stars. We then take the median of this distribution as a reasonable estimate of the test statistic D, which can be used to test whether the white dwarf pollutants and FGK stars follow similar distributions in CA/Fe ratios.

The comparison between white dwarf pollutants and pristine material is shown in Fig. 5.7. First, we find tentative evidence that the Fe/Ca ratios of WD pollutants and FGK stars follow different distributions, with a significance of 2.0 σ. Even corrected for errors, the white dwarf pollutants follow a broader distribution of $\dot{M}_{\mathrm{Fe}}/\dot{M}_{\mathrm{Ca}}$, compared to the FGK stars. Because the plotted sample is limited to older white dwarfs ($\tau_{\mathrm{Fe}} >$ Myr), that average over the accretion process, this indicates that the bulk content of white dwarf pollutants contains more compositional variation than is seen in the stellar sample, likely as a result of the collisional evolution of differentiated bodies prior to the accretion process (Bonsor et al., 2020). Alternatively, this widening could be caused by a spread in the accretion states of the white dwarfs (i.e. declining, build-up). Secondly, and more importantly, we find that the distribution of $\dot{M}_{\mathrm{Fe}}/\dot{M}_{\mathrm{Ca}}$ corresponding to white dwarf pollutants is off-set in the direction of increased core content. This direction cannot be explained by deviations from steady-state accretion, as a build-up state is unlikely for cool white dwarfs with helium-dominated atmospheres, and $\tau_{\mathrm{Ca}} > \tau_{\mathrm{Fe}}$. However, the preferential ejection of mantle fragments can increase the bound core mass fraction by up to 20% (see Fig. 5.3), which is enough to explain the off-set.

5.5 Discussion

5.5.1 Interpretation of photospheric abundances

The suggested asynchronous accretion of core and mantle material means that the age and type of white dwarfs should be accounted for when interpreting their photospheric abundances. For young white dwarfs with hydrogen-dominated atmospheres and short diffusion timescales, their photospheric composition may vary during the accretion of a single body. The positive implication of this hypothesis is that observers and geologists can more easily study the exoplanetary geology of their pollutants, as every differentiated body goes through a core and mantle-rich accretion phase, and catastrophic collisions between asteroids are not required in order to observationally sample these layers. The flip side of asynchronous accretion is that a pollutant's bulk composition cannot be confidently inferred

when the atmospheric diffusion timescale of a white dwarf is shorter than the timescale on which the accreted composition changes. In short, a young white dwarf with hydrogen-dominated envelope might sample the composition of a given layer of the pollutant, while older, helium-dominated white dwarfs with long diffusion timescales are more suited to infer the bulk composition of their pollutants. However, even old white dwarfs are not perfect spectrometers of white dwarf pollutants, as the preferential ejection of mantle fragments in a tidal disruption (Section 5.2.2) implies that the total material accreted by a white dwarf will be enriched in core material by up to 20% when it accretes a differentiated body. In addition, older white dwarfs come with their own inherent difficulties of a more poorly constrained accretion state and history, as they could potentially have swallowed multiple objects in a single diffusion time (Trierweiler et al., 2022; Turner & Wyatt, 2020; Wyatt et al., 2014).

5.5.2 Observational tests for asynchronous core-mantle accretion

Accretion asynchronicities can be directly studied observationally with a sufficiently varied white dwarf sample with well-constrained and diverse abundances. While a sufficiently good sample does not yet exist, it might be possible to study this process in the future. If the abundance ratios of core and mantle material vary over a characteristic time period during accretion, regression between the accretion rates of siderophile and lithophile elements will show a steep trend, but only for stars with diffusion times shorter than the typical accretion event. However, the current sample of young white dwarfs with hydrogen-dominated atmospheres is too small at 18 stars with diffusion timescales below 10^4 yr. A larger sample of around $\sim$ 100 young stars with both Fe and Ca detections is required to corroborate these findings. In addition, the identification of other siderophile elements like chromium in more white dwarfs would aid the comparison, as it will allow for an independent analysis of the same physical trend. In the future, upcoming large-scale spectroscopic surveys (4MOST/WEAVE/DESI/SDSS-V) will greatly increase the number of known, young white dwarfs with photospheric pollution. Studying the asynchronicity of the accretion process will put much-needed observational constraints on the white dwarf accretion process.

5.5.3 Asynchronous accretion in alternative models

In this work, we argue that core and mantle fragments of differentiated asteroids are expected to accrete onto white dwarfs in proportions that vary over time. We note, however, that the details and magnitude of this asynchronicity are intimately linked with the accretion process itself, which is still imperfectly understood. Most current theoretical studies share the idea that accretion begins with the tidal disruption of a pollutant (Brouwers et al., 2022; Hogg

et al., 2021; Li et al., 2021; Malamud et al., 2021; Malamud & Perets, 2020a,b; Trevascus et al., 2021; Veras et al., 2021; Zhang et al., 2021). We use energy arguments to show that such a disruption spreads core and mantle fragments to different orbits (see Fig. 5.2), leading to the preferential ejection of mantle material. This asymmetric distribution forms the starting point of asynchronous accretion in our models. For the subsequent accretion process, we considered two simple scenarios, each of which has its limitations.

In our first model of collisional grind-down, the main simplification is that it only tracks catastrophic collisions, rather than following the full collisional evolution of child orbits. As discussed in the previous chapter, it is possible that a more detailed tracking of the collision tree would yield either a reduced or increased asynchronicity between core and mantle fragments, or that this trend is altered when other sources of collisions are accounted for (e.g., gravitational stirring (Li et al., 2021), the Yarkovski effect (Veras et al., 2015a,b; Veras & Scheeres, 2020), Poynting-Robertson drag (Rafikov, 2011a)). Finally, the fragment size distribution could differ between core and mantle fragments, as iron is denser, stronger and more ductile than typical mantle minerals. Our analysis of fragment scattering by a planet is yet more simple and just serves to illustrate the idea that core fragments are more susceptible to close encounters with the planet, rather than produce an exact time evolution.

It is also conceivable that accretion begins with a tidal disruption, but then proceeds via different channels than the ones studied in this work. For instance, in chapter 5, we describe how the rapid sublimation of ices can cause a distinct accretion asynchronicity where volatiles reach the star faster than refractory components. Within the context of core-mantle accretion, Hogg et al. (2021); Zhang et al. (2021) suggest diamagnetic and Alfvén-wave drag as mechanisms to circularize and accrete magnetized fragments onto the star. In these cases too, however, there are asymmetries between more and less strongly magnetized fragments, which would translate to a conceptually similar, though quantitatively different core-mantle asynchronicity. A third possibility is that fragments circularize by interactions with a pre-existing disc, as suggested by Malamud et al. (2021). In this case, the accretion times of fragments are largely determined by their semi-major axes, which also vary between core and mantle fragments (see Fig. 5.2). As such, we argue that while the asynchronicity of core-mantle accretion is for now difficult to constrain theoretically, it is likely to affect relative white dwarf abundances in a wide range of accretion scenarios that involve a tidal disruption on a highly-eccentric orbit.

Asynchronous core-mantle accretion may also occur in the very different scenario where large objects circularize before they disrupt. Such a scenario might play out around some white dwarfs, considering the transits of disintegrating planetesimals seen in some systems (Budaj et al., 2022; Farihi et al., 2022; Manser et al., 2019; Vanderburg et al., 2015). In the

example of WD 1145+017, these transits are best modelled by differentiated planetesimals, whose mantles are shedding material, while their denser cores remain intact initially (Duvvuri et al., 2020; Veras et al., 2017).

5.6 Summary and conclusions

Polluted white dwarfs with multiple identified photospheric elements are often used to infer the composition of the planetary bodies that accrete onto them (e.g., Buchan et al., 2022; Farihi et al., 2011; Harrison et al., 2021a, 2018; Hollands et al., 2018; Klein et al., 2010; Putirka & Xu, 2021; Swan et al., 2019a; Xu et al., 2019, 2014, 2017; Zuckerman et al., 2007). In this chapter and the next, we argue based on theory and observations that the composition of the material accreting onto a white dwarf may vary with time during the accretion of a single planetary body. Consequently, photospheric abundance ratios of white dwarfs can fluctuate during a single accretion event, and the abundances of white dwarfs do not necessarily reflect the bulk composition of their pollutants, especially for young stars with hydrogen-dominated atmospheres. The potential consequences are particularly important for differentiated bodies, whose cores and mantles disrupt into distinct groups of fragments that follow different orbits, and could accrete over varying periods of time. In summary, we find that:

1. If a white dwarf accretes a core-mantle differentiated pollutant, the material accreted by white dwarfs will be enriched in core material by up to 20% due to the ejection of a larger portion of the mantle during the tidal disruption.

2. Both a collisional model and fragment scattering by a planet predict that accretion begins with an iron-rich phase, followed by a more Ca and Mg-rich second phase. This variation is caused by the geometry of a differentiated body during a tidal disruption, which implies that core fragments cluster around the centre of the disc that forms, while mantle fragments occupy both inner and outer orbits, and take longer to accrete on average.

3. There are more white dwarfs accreting material with high Fe/Ca ratios than low Fe/Ca, assuming that relative sinking timescales for Ca and Fe are accurate. This can be interpreted as evidence for the ejection of mantle material when a differentiated pollutant tidally disrupts.

Chapter 6

Asynchronous accretion can mimic diverse white dwarf pollutants II: water content

"And then her heart changed, or at least she understood it; and the winter passed, and the sun shone upon her"

-J.R.R. Tolkien, The Return of the King, 1955

In this chapter, we extend the discussion of asynchronous accretion onto white dwarfs to pollutants with an icy component. We study the accretion process, and find that ices may sublimate and accrete before more refractory minerals reach the star. As a result, a white dwarf's relative photospheric abundances may vary with time during a single accretion event, and do not necessarily reflect the bulk composition of a pollutant. We find that in the current sample, only three stars show statistically significant evidence of water at the 2σ level, due to large typical uncertainties in atmospheric abundances and accretion states. In the future, an expanded sample of polluted white dwarfs with hydrogen-dominated atmospheres will allow for the corroboration of our theoretical predictions. Our work also shows the importance of interpreting pollutant compositions statistically, and emphasizes the requirement to reduce uncertainties on measured abundances to allow for statistically significant constraints on their water content.

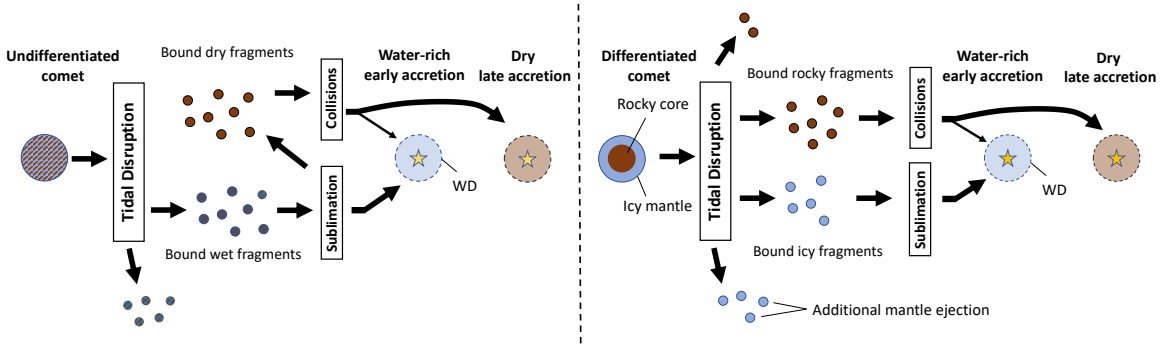

Fig. 6.1 Schematic overview of how the asynchronous accretion of an ice-rich comet onto a white dwarf can appear either volatile-rich or dry, depending on when the system is observed. Left panel: an undifferentiated comet tidally disrupts, producing wet fragments. If these fragments dry out before they collide, a short water-rich accretion phase is followed by a longer, dry accretion phase. Right panel: an ice-rock differentiated comet tidally disrupts, producing both icy and dry fragments. The icy fragments are ejected in greater proportions (see chapter 5). The bound ice rapidly sublimates - before most fragments catastrophically collide and accrete, again leading to a short, volatile-rich early accretion phase and a longer, dry, second accretion phase. An accompanying version of this figure that details asynchronous core-mantle accretion is shown in chapter 5.

6.1 Introduction

If multiple elements are detected in a white dwarf atmosphere, their relative abundances can be used to constrain the composition of the pollutants (e.g., Buchan et al., 2022; Harrison et al., 2021a, 2018; Hollands et al., 2018; Putirka & Xu, 2021; Swan et al., 2019a). Notably, the detection of oxygen together with the other major rock-forming elements (Fe, Si, and Mg) makes it possible to infer the water content of the accreted material (Farihi et al., 2013; Klein et al., 2010). The delivery of comets containing water may be crucial for habitable planet formation in dry inner regions (Albarède, 2009; Morbidelli et al., 2000; Raymond et al., 2009), and polluted white dwarfs offer a direct way to investigate the presence of water-rich material around other stars.

Analyses of individual white dwarfs indicate that, while most pollutants are made up of dry minerals (Gänsicke et al., 2012), nearly one in four systems with oxygen detections is inferred to contain a substantial amount of water ice (Farihi et al., 2013, 2016; Hollands et al., 2022; Hoskin et al., 2020; Klein et al., 2021; Raddi et al., 2015; Xu et al., 2019, 2017). Independently, volatile accretion has also been investigated using white dwarfs with helium-dominated atmospheres, where trace amounts of hydrogen record the cumulative accretion of water ice throughout their history (Gentile Fusillo et al., 2017; Izquierdo et al., 2018, 2021; Veras et al., 2014b). However, in the population studies by Jura & Xu (2012);

Jura & Young (2014) and Gentile Fusillo et al. (2017), water is found to be far more rare than indicated by the analysis of individual systems, with a fraction below 1% of the total metal mass accreted in the form of water. The origin of this apparent mismatch is not currently well understood, but could hint at the over-interpretation of water in the compositional analysis of individual white dwarfs.

Until now, studies that infer the composition of white dwarf pollutants make the assumption that the different parts of an object (e.g., core/mantle, volatile/refractory) enter the white dwarf in a constant proportion, such that ongoing accretion is always representative of its bulk content. In this work, we expand upon the previous chapter, to investigate the possibility that accretion occurs *asynchronously*, with some parts of a pollutant accreting faster than others. In particular, we study the scenario suggested by Malamud & Perets (2016), who hypothesized that the ices contained in a pollutant can sublimate and accrete before more refractory minerals reach the star. In this scenario, where sublimative erosion outpaces alternative accretion processes such as scattering, collisional grind-down and drag forces (e.g. Brouwers et al., 2022; Li et al., 2021; Malamud et al., 2021; Swan et al., 2021; Veras et al., 2015b), the ice and rock in a pollutant will largely accrete separately, and the photospheric abundances of white dwarfs do not necessarily reflect the bulk composition of their pollutants (see Fig. 6.1). We focus on defining observational predictions that result from this form of asynchronous accretion, and collate a white dwarf sample from the literature to test these predictions. In our compositional analysis, we confront the problem that to accurately infer the composition of accreting material, the star's accretion state (i.e. build-up/steady-state/declining) needs to be well-constrained. We demonstrate a procedure where a Bayesian model (`PyllutedWD`, Buchan et al. 2022; Harrison et al. 2021a) is used to quantify the uncertainties on the accretion state, with allows for a statistical constraint on the presence of water in the accreted material. Our results highlight the difficulty of making statistically strong statements regarding the composition of pollutants in white dwarfs, especially those with helium-dominated atmospheres, where accretion states are often subject to large uncertainties.

This chapter is organized as follows. We first compute the sublimative erosion of icy and rocky fragments in Section 6.2, and show how asynchronous accretion can affect white dwarf abundances in Section 6.3. To test the predictions of asynchronous accretion, we analyse the *oxygen excess* of white dwarf pollutants in Section 6.4. Finally, we discuss the results in Section 6.5 and conclude in Section 6.6.

6.2 Timescale of sublimative erosion

The accretion of planetary material onto a white dwarf is usually thought to begin with the tidal disruption of a pollutant (Debes et al., 2012; Malamud & Perets, 2020a,b; Nixon et al., 2020; Veras et al., 2014a), forming a highly eccentric disc with its fragments. If these fragments face intense radiation from the white dwarf, they can begin to lose their material to sublimation, similar to the fate of comets near the Sun (Binzel et al., 2004). The timescale for the sublimative erosion of a fragment can be estimated from the integrated stellar flux over a complete orbit, defined by Kepler's orbital equations of distance to a central star (r) with mass $M_{\rm WD}$:

$$r = \frac{a(1-e^2)}{1-e\cos(\theta)}\ ,\ \frac{d\theta}{dt} = \left[\frac{GM_{\rm WD}}{a^3\left(1-e^2\right)^3}\right]^{\frac{1}{2}}\left(1-e\cos(\theta)\right)^2, \tag{6.1}$$

where θ is the true anomaly (with the pericentre at $\theta = \pi$), and a, e are the fragment's semi-major axis and eccentricity. At any point on the orbit, the flux of stellar radiation through its surface ($J_{\rm WD}$) averages to:

$$J_{\rm WD} = \frac{(1-A)\sigma_{\rm sb}R_{\rm WD}^2T_{\rm WD}^4}{4r^2}, \tag{6.2}$$

where $\sigma_{\rm sb}$ is the Stephan-Boltzmann constant, A is the fragment's albedo, and $R_{\rm WD}, T_{\rm WD}$ are the stellar radius and temperature. Some of this flux is used to heat or sublimate the fragment, while a portion is re-radiated back to space. For ices with very low sublimation temperatures, the importance of thermal re-radiation is negligible, allowing for the simplification that all the incident flux is used for heating and sublimation. With this assumption, the shrinkage of a fragment's radius due to sublimative erosion ($dR_{\rm frag}/dt$) can be time-averaged over a complete orbit with period $P_{\rm frag} = 2\pi\sqrt{a_{\rm frag}^3/(GM_{\rm WD})}$, and is:

$$\frac{d\bar{R}_{\rm frag}}{dt} = -\frac{1}{P_{\rm frag}}\int_0^{2\pi}\frac{J_{\rm WD}}{H_{\rm sub}\rho_{\rm frag}}\left(\frac{d\theta}{dt}\right)^{-1}d\theta \tag{6.3a}$$

$$= -\frac{(1-A)\sigma_{\rm sb}T_{\rm WD}^4R_{\rm WD}^2}{4H_{\rm sub}\rho_{\rm frag}a_{\rm frag}^2\sqrt{1-e_{\rm frag}^2}}. \tag{6.3b}$$

where $H_{\rm sub}$ is the enthalpy of sublimation. Note that Eq. 6.3b is independent of the fragment's size. With this expression, the timescale for sublimative erosion $t_{\rm sub}$ of icy fragments follows

Table 6.1 Mechanical and thermal properties of forsterite (Mg_2SiO_4), iron (Fe), and crystalline water ice (H_2O).

Symbol	Forsterite (Mg_2SiO_4)	Iron (Fe)	Ice (H_2O)
$\mu^{(1)}$	140.69	55.85	18.02
$\rho^{(2)}$	3.27	7.87	1
$C_1^{(3)}$	$34.1^{(a,b)}$	$29.2^{(a,c)}$	$31.1^{(d)}$
$C_2^{(4)}$	$65308^{(a,b)}$	$48354^{(a,c)}$	$6135^{(d)}$
$H_{\rm sub}^{(5)}$	$8.1\cdot10^{10(e)}$	$8.3\cdot10^{10(e)}$	$2.7\cdot10^{10(f,\star)}$
$\eta_{\rm sub}^{(6)}$	$0.2^{(g,\dagger)}$	$1^{(a)}$	$0.2^{(d,h)}$

Parameters: $^{(1)}$ molecular weight [m_u] $^{(2)}$ density [cm^3 g^{-1}] $^{(3)}$ vapour pressure constant [no dim] $^{(4)}$ vapour pressure constant [K] $^{(5)}$ enthalpy of sublimation (heating + vaporization) [erg g^{-1}] $^{(6)}$ kinetic inhibition [no dim]

References: $^{(a)}$ Van Lieshout et al. (2014) $^{(b)}$ Nagahara et al. (1994) $^{(c)}$ Ferguson et al. (2004) $^{(d)}$ Gundlach et al. (2011) $^{(e)}$ Podolak et al. (1988) $^{(f)}$ Huebner et al. (2006) $^{(g)}$ Steckloff et al. (2021) $^{(h)}$ Beckmann & Lacmann (1982)

Notes: $^{(\star)}$ evaluated at an initial comet temperature of 0 K$^{(\dagger)}$ evaluated at 2400 K

as:

$$t_{\rm sub} = -\frac{R_{\rm frag}}{dR_{\rm frag}/dt} \tag{6.4a}$$

$$= \frac{4H_{\rm sub}\rho_{\rm frag}a_{\rm frag}^2\sqrt{1-e_{\rm frag}^2}R_{\rm frag}}{(1-A)\sigma_{\rm sb}T_{\rm WD}^4R_{\rm WD}^2} \tag{6.4b}$$

$$\simeq 6.9\cdot10^4\ {\rm yr}\left(\frac{T_{\rm WD}}{2\cdot10^4\ {\rm K}}\right)^{-4}\left(\frac{R_{\rm WD}}{{\rm R}_\oplus}\right)^{-2}\left(\frac{H_{\rm sub}}{2.7\cdot10^{10}\ {\rm erg/g}}\right) \tag{6.4c}$$
$$\left(\frac{r_{\rm B}}{{\rm R}_\odot}\right)^{\frac{1}{2}}\left(\frac{a_{\rm frag}}{3\ {\rm AU}}\right)^{\frac{3}{2}}\left(\frac{\rho_{\rm frag}}{1\ {\rm g/cm^3}}\right)\left(\frac{1-A}{1}\right)^{-1}\left(\frac{R_{\rm frag}}{\rm km}\right),$$

where in the last line we used that $1-e_{\rm frag}^2 \simeq 2r_{\rm B}/a_{\rm frag}$ because $1-e_{\rm frag} = r_{\rm B}/a_{\rm frag} \sim O({\rm R}_\odot/{\rm AU}) \ll 1$ in an eccentric tidal disc. The value $r_{\rm B}$ refers to the breakup distance of the asteroid, assumed equal to the pericentre of its orbit ($r_{\rm B} = a_{\rm frag}(1-e_{\rm frag})$). The largest fragments expected in the tidal disc are unlikely to exceed 1 km in size (Brouwers et al., 2022; Zhang et al., 2021), and might be significantly smaller if the inherent strength of the ice is sub-kP (Davidsson, 1999; Greenberg et al., 1995; Gundlach & Blum, 2016). Eq. 6.4c indicates that even the largest icy fragments are expected to sublimate fully within 1 Myr if the stellar temperature exceeds 10^4 K, and much faster if the star is warmer or the fragment is smaller. Around hot stars, the sublimation timescale is short compared to the typical duration of accretion events, as inferred from the statistical differences between hydrogen and helium

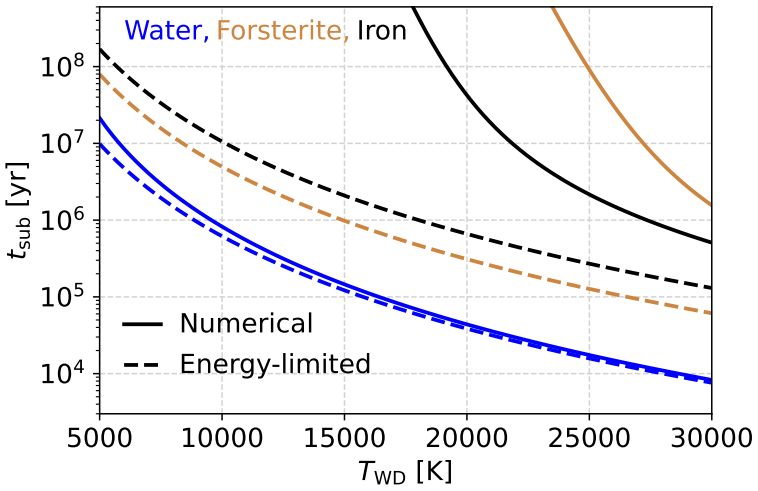

Fig. 6.2 Numerically calculated timescales for the sublimative erosion of large, km-sized fragments (solid lines), compared to the energy-limited approximation (dashed lines, Eq. 6.4c). Fragments composed of water ice (blue) sublimate efficiently within $10^4 - 10^6$ yr around warm stars, and the two curves largely overlap. Fragments composed of refractory species like forsterite (brown) and iron (black) only begin to sublimate around the hottest white dwarfs, and re-radiate most of the incident stellar flux back to space, causing a divergence from the energy-limited curves.

white dwarfs (Cunningham et al., 2021; Girven et al., 2012). In this case, icy fragments are expected to completely sublimate before the accretion process of more refractory components has completed.

6.2.1 Very slow sublimation of refractory minerals

To contrast the sublimative erosion of ices and more refractory species, we formulate a simple numerical model that accounts for the fragment's thermal re-radiation into space. The fragments are assumed to have uniform compositions, consisting either of core-like material (iron), mantle-like material (forsterite), or ice (water). The sublimation parameters for these materials are shown in Table 6.1. Furthermore, it is assumed that the heating of the fragments proceeds from a thin, hot outer layer, with negligible internal heat transport (see Appendix C.3).

The energy flux through the fragment's surface contains terms for the incident stellar radiation (J_{WD}, Eq. 6.2), as well as the re-radiation (J_{emit}) and sublimation (J_{sub}) from the

fragment's surface:

$$J_{\rm WD} = J_{\rm emit} + J_{\rm sub} \tag{6.5a}$$

$$\frac{(1-A)\sigma_{\rm sb} R_{\rm WD}^2 T_{\rm WD}^4}{4r^2} = \sigma_{\rm sb} T_{\rm s}^4 + H_{\rm sub} I_{\rm sub}, \tag{6.5b}$$

where $T_{\rm s}$ is the surface temperature, and both the fragment and the star are assumed to emit as perfect black bodies. The mass flux $I_{\rm sub}$ at the surface should account for the processes of sublimation and re-condensation. The kinetic theory of gases gives the following equation (Knudsen, 1909; Langmuir, 1913):

$$I_{\rm sub} = \eta_{\rm sub} P_{\rm vap} \left(\frac{\mu}{2\pi k_{\rm b} T_{\rm s}} \right)^{\frac{1}{2}}, \tag{6.6}$$

with saturated vapour pressure $P_{\rm vap}$. The kinetic inhibition $\eta_{\rm sub}$ describes the divergence of the sublimation from being the perfect inverse of condensation (Kossacki et al., 1999), and has to be determined experimentally. The same is true for the vapour pressure, which typically follows the empirical Clausius-Clapeyron relation (Clausius, 1850):

$$P_{\rm vap} = \exp\left(C_1 - \frac{C_2}{T_{\rm s}} \right) \ {\rm dyne/cm^2}, \tag{6.7}$$

with constants C_1, C_2 (see Table 6.1). We solve for the temperature of the fragment's outer layer from Eq. 6.5b with a root-finding procedure at every time-step across a full orbit, and calculate the mass loss via Eq. 6.6. The fragment's albedo is set equal to the canonical value of 0.04 for comets (Bernardinelli et al., 2021). To approximate the complete disintegration of a fragment, its sublimative mass-loss is integrated over one complete orbit, and this result is extrapolated, using the observation that sublimative shrinkage (of a fragment's radius) is independent of its remaining size.

The numerically calculated timescales for sublimative erosion are plotted in Fig. 6.2, with comparison to the energy-limited expression (Eq. 6.4c). The values for water ice accurately follow the analytical expression, while the two curves diverge for fragments composed of forsterite or iron. These refractory fragments lose the vast majority of their mass near the pericentre of their eccentric orbits, where they only spend a tiny fraction of their time. At distances further from the star, nearly all the stellar flux is re-radiated without substantial sublimation. Even with stellar temperatures of 20,000 K, the sublimative erosion of km-sized iron and forsterite fragments in a tidal disc requires more than 10^7 yr. Therefore, we find that while ices can rapidly sublimate around hot white dwarfs, fragments made of more refractory species are expected to remain intact until they are collisionally ground down to dust.

6.3 Implied water content during accretion

In the preceding section, we showed that icy fragments can face rapid sublimative erosion in the tidal discs where they are released. If sublimative erosion outpaces other accretion channels, most of the volatile ices will accrete onto the white dwarf before more refractory species arrive. In this section, we show how such an asynchronicity causes the star's relative photospheric abundances to vary over time during a single accretion event, which in turn affects the implied composition of its pollutants.

We imagine a simple scenario where a comet containing both minerals and ice tidally disrupts around a warm star. Both the rock and ice accretion are illustrative here, and do not include complexities such as the size distribution of fragments and their orbital spread. The rocky material is assumed to accrete evenly over 1 Myr, a typical value implied by comparing DA and non-DA pollution rates (Cunningham et al., 2021; Girven et al., 2012). The ice is also modelled to accrete at a constant rate, but with a shorter timescale given by Eq. 6.4c, assuming a typical fragment size of 1 km. The accretion rates of the different elements onto the star ($\dot{M}_{\rm O}, \dot{M}_{\rm Si}, ...$) follow from summing over icy and rocky accretion. The rocks have a modified, roughly bulk-Earth elemental composition, set to yield zero oxygen excess [1], while the ice is assumed to be pure water (H_2O). The number ratio of an element in the star's convective zone follows from an integration over the accretion rate, modulated by the diffusion timescale ($\tau_{\rm O}, \tau_{\rm Si}, ...$). This yields the following abundances at time $t_{\rm obs}$:

$$\mathrm{O/Hx}(t_{\rm obs}) = \frac{\mu_{\rm H_x}}{\mu_{\rm O} M_{\rm cvz}} \int_{t=0}^{t=t_{\rm obs}} \dot{M}_{\rm O}(t) e^{-(t_{\rm obs}-t)/\tau_{\rm O}} dt \tag{6.8a}$$

$$\mathrm{Si/Hx}(t_{\rm obs}) = \frac{\mu_{\rm H}}{\mu_{\rm Si} M_{\rm cvz}} \int_{t=0}^{t=t_{\rm obs}} \dot{M}_{\rm Si}(t) e^{-(t_{\rm obs}-t)/\tau_{\rm Si}} dt, \tag{6.8b}$$

$$...$$

where $\mathrm{H_x}$ refers to the dominant atmospheric element, either hydrogen or helium. To infer a pollutant's composition, the atmosphere is often assumed to be in a steady-state between accretion and diffusion. In such a steady-state, the total accretion rate $\dot{M}$ onto the white dwarf is given by:

$$= \dot{M} = \sum_{\text{elements El}_i} \mathrm{El_i/H_x} \frac{\mu_{\rm El_i} M_{\rm cvz}}{\mu_{\rm H_x} \tau_{\rm El_i}}, \tag{6.9}$$

where $\mu_{\rm i}$ is the atomic weight of element $\mathrm{El_i}$, and $M_{\rm cvz}$ is the mass of the star's convective zone. The diffusion timescales and $M_{\rm cvz}$ are calculated using the methods described in

[1] We take rocks with an Earth-like elemental composition (O:37.3%, Fe:30.0%, Si:15.1%, Mg:14.5%, Ca:1.6%, Al:1.5% by number McDonough 2003), slightly rescaled for illustrative purposes to yield zero oxygen excess.

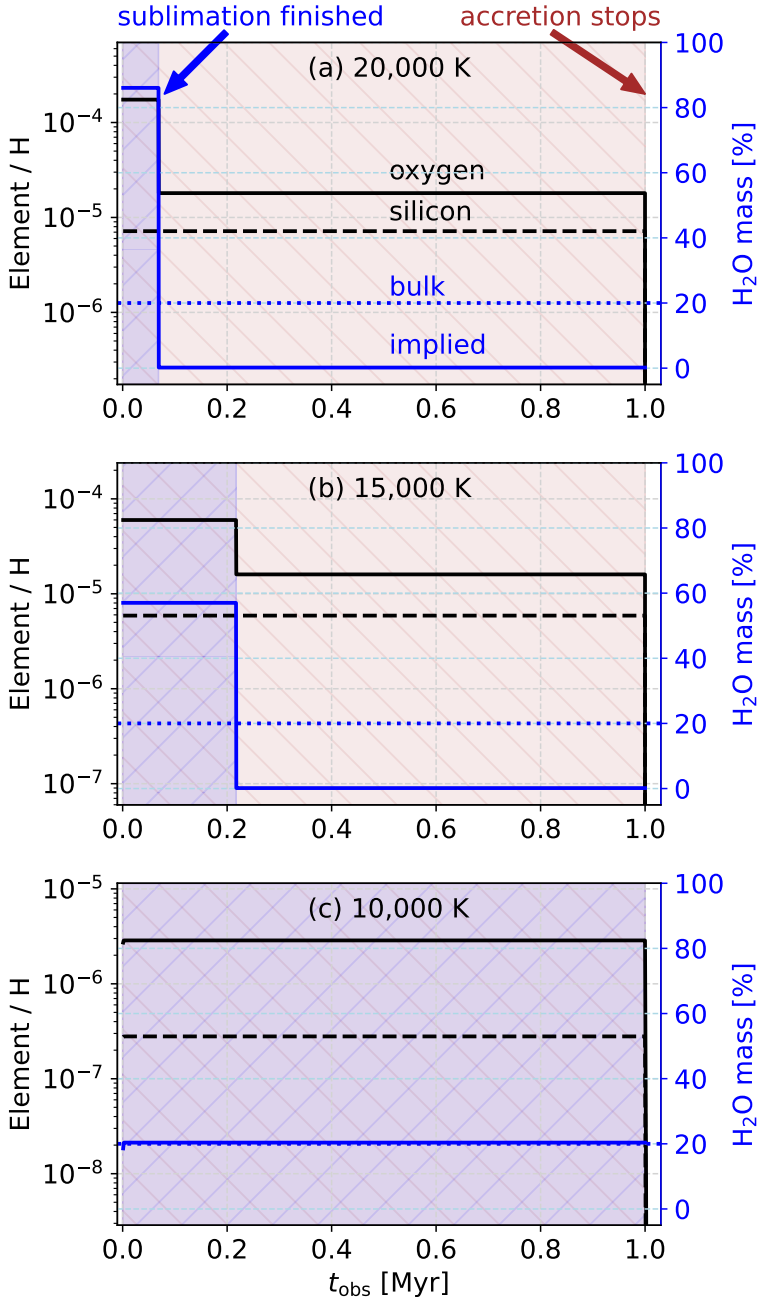

Fig. 6.3 Evolution of elemental abundances (black, left axis) and the implied water mass fraction (blue, right axis) when white dwarfs with hydrogen-dominated atmospheres accrete a comet with 20% ice. In this model, ice accretes at a constant rate until $t_{\rm sub}$ (Eq. 6.4c), and dry rocks accrete in 1 Myr. The water fraction implied by assuming steady state accretion appears discontinuous at $t_{\rm sub}$ due to the short diffusion timescales (days here, from Koester et al. (2020) with $\log(g) = 8$). The real bulk water content of the object (blue dotted curve) only matches the implied value if $t_{\rm sub} >= t_{\rm acc}$ yr, as is the case in panel c, at 10,000 K.

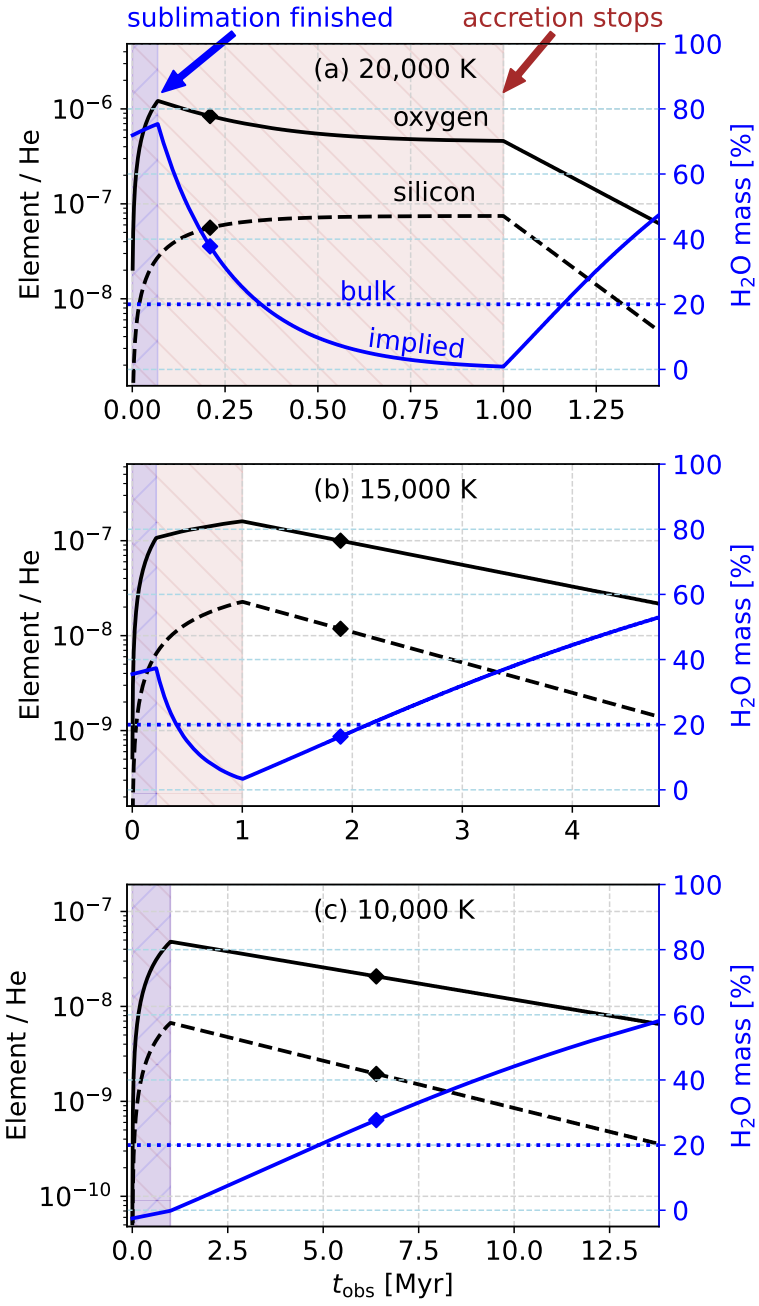

Fig. 6.4 Same calculation as shown in Fig. 6.3, repeated for stars with helium-dominated atmospheres. The squares indicate the sinking timescales of oxygen, while the brown and blue areas indicate the accretion zones of ice and dry rocks, respectively. The implied water content peaks highest for hot stars and is highly dependent on the accretion state, with it increasing further when accretion has stopped and elements sink downwards (declining state).

Koester et al. (2020)[2], using an overshoot prescription with one pressure scale height of additional mixing. Diffusion timescales vary over many orders of magnitude within the range of effective temperatures from 20,000 to 5,000 K; from days to Myr for hydrogen-dominated atmospheres, and between $10^4 - 10^8$ yr for helium-rich atmospheres. The oxygen excess associated with accretion refers to the fraction of oxygen atoms that remain after accounting for oxygen bindings in a pre-defined set of minerals. If an element $\mathrm{El_i}$ binds with n_i oxygen atoms in the minerals of the pollutant ($n_\mathrm{i} = 1$ in $\mathrm{FeO, CaO, MgO}$, $n_\mathrm{i} = 1.5$ in $\mathrm{Al_2O_3}$, and $n_\mathrm{i} = 2$ in $\mathrm{SiO_2}$), the remaining rate of excess oxygen accretion ($\delta\dot{M}_\mathrm{O}$) is:

$$\delta\dot{M}_\mathrm{O} = \mathrm{O/H_x}\frac{\mu_\mathrm{O} M_\mathrm{cvz}}{\mu_{\mathrm{H_x}}\tau_\mathrm{O}} - \sum_{\text{elements El}_\mathrm{i}} \mathrm{El_i/H_x}\frac{n_\mathrm{i}\mu_{\mathrm{El_i}} M_\mathrm{cvz}}{\mu_{\mathrm{H_x}}\tau_{\mathrm{El_i}}}. \tag{6.10}$$

Assuming that these excess oxygen atoms correspond to the accretion of water ice from the pollutant, its implied mass fraction of $f\mathrm{H_2O}$ (in steady-state) follows from:

$$f\mathrm{H_2O} = \frac{\delta\dot{M}_\mathrm{O}\,(1 + 2\mu_\mathrm{H}/\mu_\mathrm{O})}{\dot{M}}. \tag{6.11}$$

The evolution of a comet's implied water content during an asynchronous accretion event is illustrated in Figs. 6.3 and 6.4. For white dwarfs with hydrogen-dominated atmospheres (Fig. 6.3), which have short diffusion timescales ($\sim$ days), this produces two discontinuous accretion stages, indicated by the blue and brown areas in the figure. In the first stage, the comet's volatiles rapidly sublimate, and the white dwarf accretes material with a water fraction that far exceeds that of the comet. If the atmospheric abundances in this phase are used to infer the cometary composition, its water content would be over-estimated. In contrast, the second accretion phase is entirely dry, and if the star is observed during this period, the pollutant would incorrectly be identified as a dry asteroid. The figure shows that the effects of asynchronous accretion are greater around hotter stars (top panel), which trigger a short and intense phase of sublimative erosion, while the majority of the accretion event is dry.

For stars with helium-dominated atmospheres (Fig. 6.4), a similar argument applies, but the abundances are more averaged out due to the longer diffusion timescales, which means that their implied oxygen excess is not discontinuous. Instead, the implied oxygen excess peaks at t_sub, and decreases from there. However, with slow downward diffusion, heavy elements continue to be visible in helium-rich atmospheres after all accretion has stopped. During this *declining* phase, the implied oxygen excess generally increases over time, as the

[2]Extensive tables and more details of the calculations can be found at http://www1.astrophysik.uni-kiel.de/~koester/astrophysics/astrophysics.html

Table 6.2 All 9 white dwarfs with previously suggested oxygen excesses. The state-corrected calculation accounts for the likelihood distribution of different accretion states (see Section 6.4.2). For systems in blue, we find oxygen excesses with $\geq 2\sigma$ significance with this state-corrected calculation. No new systems with significant oxygen excesses were found.

System	State-corrected excess [%]	sig. [σ]	Steady-state excess [%]	Previous estimate [%]
GALEXJ2339$^{(\mathrm{He})}$	61^{+8}_{-12}	2.82	53^{+9}_{-14}	$\sim 66^{\star,(a)}$
WD1425+540$^{(\mathrm{He})}$	80^{+10}_{-19}	2.29	75^{+12}_{-23}	$55^{\star,\bullet,(b)}$
WD1232+563$^{(\mathrm{He})}$	57^{+14}_{-21}	2.14	53^{+15}_{-21}	$57^{\star,\ddagger,(c)}$
GD61$^{(\mathrm{He})}$	27^{+9}_{-12}	1.86	27^{+8}_{-10}	$42^{\star,(d)}$, $50^{\dagger,(d)}$
GD378$^{(\mathrm{He})}$	73^{+15}_{-36}	1.49	73^{+15}_{-35}	$\sim 66^{\star,(a)}$
WD1536+520$^{(\mathrm{He})}$	20^{+28}_{-44}	0.49	3^{+32}_{-48}	$< 0^{\star,(e)}$, $43^{\dagger,(e)}$
SDSSJ1242+5226$^{(\mathrm{He})}$	11^{+22}_{-30}	0.42	48^{+12}_{-16}	$57^{+7\star,(f)}_{-7}$
SDSSJ2047-1259$^{(\mathrm{He})}$	1^{+27}_{-36}	0.02	21^{+19}_{-26}	$16^{+20\star,(g)}_{-27}$
SDSSJ0956+5912$^{(\mathrm{He})}$	-20^{+50}_{-84}	-	53^{+19}_{-34}	$\sim 45^{\star,(h)}$

$^{(a)}$Klein et al. (2021), $^{(b)}$ Xu et al. (2017), $^{(c)}$Xu et al. (2019), $^{(d)}$Farihi et al. (2013),$^{(e)}$ Farihi et al. (2016), $^{(f)}$Raddi et al. (2015), $^{(g)}$Hoskin et al. (2020), $^{(h)}$Hollands et al. (2022)
Notes: $^{(\star)}$ Assuming steady-state accretion. $^{(\dagger)}$ Assuming accretion in a build-up phase (pre steady-state). $^{(\ddagger)}$ Corresponds to a more conservative oxygen assignment with Fe_2O_3 instead of FeO.$^{(\bullet)}$ Corresponds to a differently defined oxygen excess. Re-calculation with our definition yields an excess of 84%.

oxygen atoms sink more slowly than the other elements, and remain in the atmosphere for longer.

6.4 Observational tests of asynchronous ice-refractory accretion

From the preceding arguments, the asynchronous accretion of volatiles and refractories makes two observational predictions:

1. There is an anti-correlation between white dwarf temperature and the inferred fraction of wet pollutants. This trend should continue down to $t_{\mathrm{acc}} = t_{\mathrm{sub}}$ ($\sim 10,000$ K) for white dwarfs with hydrogen-dominated atmospheres, and down to $t_{\mathrm{acc}} = t_{\mathrm{sink}}$ for those with helium-dominated atmospheres ($\sim 15,000$ K).

2. Some hot white dwarfs will be found with volatile abundances that far exceed the plausible range for comets. These systems can be explained as examples where accretion is caught in the early phase of sublimative erosion.

In this section, we analyse with the current white dwarf sample to compare with these predictions.

6.4.1 Description of white dwarf sample

We compile a new sample of white dwarfs from the literature, which contains all currently identified white dwarfs with a published abundance of atmospheric oxygen, as well as measured abundances of Mg, Si, and Fe. Out of these stars, 9 were previously suggested to have accreted material with an oxygen excess. The complete sample is listed in Appendix C.7. It is by no means uniformly selected, as oxygen measurements are often performed as a follow-up of the most highly polluted or interesting systems. The majority of the sample has oxygen detections (28/32), with only 4 upper limits. The sample is skewed towards hot white dwarfs (median 14,754 K) with high levels of pollution and helium-dominated atmospheres (23/32), despite the fact that white dwarfs with hydrogen-dominated atmospheres are generally more common.

6.4.2 Calculation of oxygen excess with `PyllutedWD`

The amount of oxygen in excess of that required for metal oxides is determined based on the photospheric abundances of all other elements, adjusted to consider different rates of downward diffusion. When observing metals in the atmosphere of a white dwarf, it is not clear a-priori whether accretion is ongoing or finished, with the observed metals caught in the process of sinking out of sight. Whilst clues such as infrared emission, the presence of circumstellar gas or a short sinking timescale (days) might indicate that ongoing accretion is more likely, for most of the white dwarfs considered here, it constitutes a major uncertainty in interpreting the observed abundances.

In order to address this uncertainty here, and to interpolate any missing abundances (e.g. Ca, Al), we make use of the open-source python code `PyllutedWD`[3] (Buchan et al., 2022; Harrison et al., 2021a). `PyllutedWD` works from the principle that a range of accretion states might be consistent with the data within the error range, but that the observed abundances can provide clues as to the most likely values of the current accretion state. In this physical model, elements with different condensation temperatures (e.g. Ca relative to Mg or Na) or different affinities to enter the iron melt (e.g. Ca/Fe or Ni/Fe) can vary in ways appropriate to volatile loss and core-mantle differentiation. The only other process in this model that can alter key ratios of elemental pairs with similar condensation temperatures is relative sinking due to variations in the rate of downward diffusion. By considering only these processes, insights

[3]https://github.com/andrewmbuchan4/PyllutedWD_Public

regarding the most likely accretion state of the white dwarf pollutants can be determined, which for some individual systems constrain the accretion to be most likely in steady-state (or declining), whilst for others systems, a broad likelihood distribution of the accretion states can be obtained.

To calculate the oxygen excess of a pollutant, we go through the following procedure: First, we run `PyllutedWD` to find a posterior distribution of the accretion state (see Fig. C.3). Next, to account for the errors, we sample the pollutant's abundances 10^4 times from Gaussian functions centred on the reported or inferred values, taking a conservative error of 0.4 dex on any inferred minor abundances (Al, Ca). For each sampling, an accretion state is assigned by a weighted draw from the posterior distribution of accretion states, which is used to translate the photospheric abundances into pollutant abundances. Generalizing from Eqs. 6.8a and 6.8b, the accreted abundance ratio $\mathrm{El}_1/\mathrm{El}_2$ for elements 1 and 2 that accrete at a constant rate from $t = 0$ to $t = \min(t_{\mathrm{acc}}, t_{\mathrm{obs}})$ is:

$$\frac{\mathrm{El}_1}{\mathrm{El}_2} = \frac{\mathrm{El}_1(t_{\mathrm{obs}})}{\mathrm{El}_2(t_{\mathrm{obs}})} \frac{\tau_{\mathrm{El}_2}}{\tau_{\mathrm{El}_1}} e^{(\min(t_{\mathrm{acc}}, t_{\mathrm{obs}}) - t_{\mathrm{obs}})\left(1/\tau_{\mathrm{El}_2} - 1/\tau_{\mathrm{El}_1}\right)}. \tag{6.12}$$

Calculated for the complete posterior distribution of accretion states and abundance samplings, this produces 10^4 sets of equally likely abundances for each pollutant, adjusted for relative diffusion rates. Next, we follow the standard procedure outlined by Klein et al. (2010), where the major rock-forming elements are assigned to the minerals $\mathrm{FeO}, \mathrm{CaO}, \mathrm{SiO_2}, \mathrm{Al_2O_3}, \mathrm{MgO}$. A portion of the iron can also be present in metallic form, but this fraction is unknown. From the oxygen assignments to minerals, we obtain a histogram of oxygen excesses for each pollutant, expressed as a number fraction of the total oxygen abundance (see Fig. C.4). The oxygen excess is given as the median value of this distribution, with asymmetric 1 σ errors identified from the 15.8^{th} and 84.1^{st} percentiles. The total significance is given by the fraction of this distribution with a positive oxygen excess. Our statistical approach yields wide errors on the oxygen excesses of most systems, due to a combination of the uncertainties on abundances and accretion states. Nevertheless, we note that the true uncertainties on the calculated excesses are likely to exceed our quoted values, mainly due to additional expected inaccuracies in relative diffusion timescales (see Blouin 2020; Heinonen et al. 2020) that are not accounted for in this analysis. Further challenges are discussed in Section 6.5.4

6.4.3 Prediction I: oxygen excess and stellar temperature

The first prediction from asynchronous ice-refractory accretion is that there exists an anti-correlation between white dwarf temperature and the inferred fraction of wet pollutants. In Fig. 6.5, the oxygen excesses of all white dwarfs in the sample are plotted against stellar

temperature. We find that almost all systems are consistent with the accretion of dry rocks, with only three systems showing an oxygen excess at the $\geq 2\sigma$ level (shown in blue). This threshold is set at 2σ for practical reasons, as a lower level of 1σ yields too many expected false positives (4.4, against 0.62), and the uncertainties on abundances and accretion states are currently too great to reach 3σ for any system. The limited number of systems with oxygen excesses at even 2σ significance highlights that the uncertainties on the accretion states and relative abundances make it difficult to ascertain oxygen excesses with strong statistical certainty. In addition, we note that no systems in the sample showed evidence of being significantly reduced in oxygen, consistent with prior analysis by Doyle et al. (2020).

The three white dwarfs with oxygen-rich pollutants all have effective temperatures at or below the sample median of 14,500 K. While this can be interpreted as tentative evidence for the proposed anti-correlation between oxygen excesses and white dwarf temperature, the number of systems is currently too small for a statistical argument to be made. Furthermore, the three white dwarfs with significant oxygen excesses all have helium-dominated atmospheres with long diffusion timescales, making their accretion states subject to greater uncertainty. In the future, when oxygen lines are identified in a larger number of white dwarfs with hydrogen-dominated atmospheres, and abundance errors are reduced, this new sample would be ideally suited to investigate the proposed anti-correlation between white dwarf temperature and the volatile content in their accretion.

6.4.4 Prediction II: rare instances of near-pure ice accretion

The theoretical ‘smoking gun‘ for asynchronous ice-refractory accretion is a hot white dwarf that appears to be accreting material with an almost entirely icy composition (see Figs. 6.3,6.4). Most comets are a mixture of refractories and ice, with the maximum volatile content occurring when material of pure solar (stellar) composition condenses to form dust and ices. If some white dwarfs are accreting material with relative oxygen abundances exceeding stellar values, this is expected by this model as a result of the sequential accretion of volatiles and refractories. To see if any of the pollutants in the sample match near-pure ice accretion, we compare the abundances of the oxygen-rich systems with nearby FGK stars in Fig. 6.6. The FGK sample was compiled by Brewer et al. (2016) and represents a plausible compositional range for pristine comets with complete condensation.

Out of the three white dwarfs with significant oxygen excesses, one system (WD1425+540) is found to be highly oxygen-rich. When compared to Solar elemental ratios, the composition of WD1425+540’s pollutant is enhanced in oxygen relative to the other major rock-forming elements, but it still falls within the plausible range of FGK stars. If these pollutant abundances represent the bulk content of a comet, it must have undergone minimal thermal processing

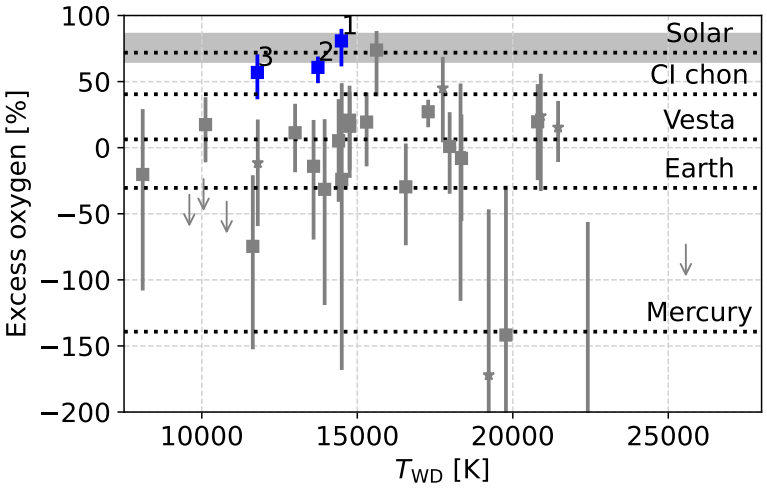

Fig. 6.5 Oxygen excesses of white dwarfs in our sample (star; hydrogen-dominated, square; helium-dominated), compared with Solar System bodies (Mercury: Hauck et al. 2013; Nittler et al. 2018, Earth: McDonough 2003, Vesta: Steenstra et al. 2016, CI chondrites & Solar photosphere Lodders 2003, FGK stars (grey band; Brewer et al. 2016)). The three blue points signal white dwarfs with significant ($\geq 2\sigma$) oxygen excesses in the default, state-corrected calculation (see Section 6.4.2). These labelled systems are 1: WD1425+540, 2: GALEXJ2339, and 3: WD1232+563.

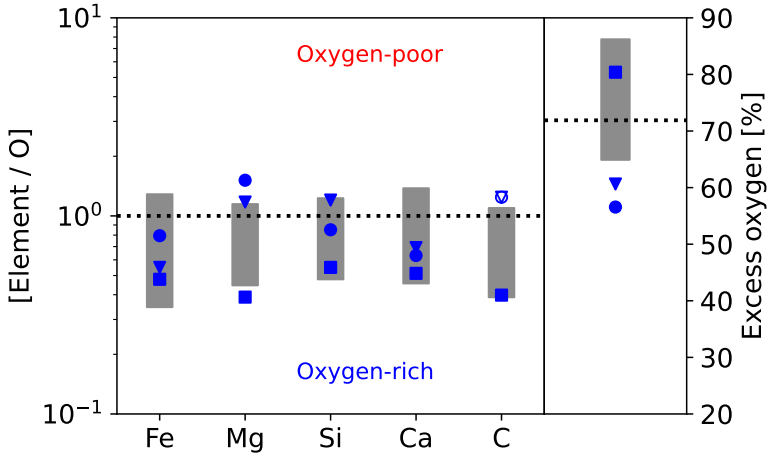

Fig. 6.6 Comparison of oxygen-rich pollutants ($\geq 2\sigma$, blue) to a sample of nearby FGK stars (grey band, Brewer et al. 2016), plotted relative to oxygen, relative to the Solar ratio. Filled markers represent measured abundances (square; WD1425+540, triangle; GALEXJ2339, circle; WD1232+563), while open markers are any non-measured abundances, inferred by `PyllutedWD`.

during the star's post-main sequence evolution. In the models of Malamud & Perets (2017a), complete water retention is only expected if the pollutant originates beyond $\sim$100 AU, which would require it to be analogous to an Oort cloud comet. If the comet originates from a closer orbit, with less ice, asynchronous accretion could explain the high level of oxygen excess, as it is just within the expected temperature range for asynchronous accretion to be noticeable. In the near future, the discovery and analysis of hot white dwarfs with hydrogen-dominated atmospheres will provide opportunities to find more clear-cut examples of asynchronous ice-refractory accretion. We discuss the system SDSS J0914+1914 as an interesting case study in Section 6.5.2.

6.4.5 Comparison with previous estimates of oxygen excesses

Table 6.2 shows all 9 white dwarfs with previously suggested oxygen excesses. Our procedure for calculating the oxygen excesses of white dwarfs is generally more conservative than that in previous works, and no new oxygen-rich systems were identified. For just three systems with previously suggested oxygen excesses, we find an excess with $\geq 2\sigma$ significance. The inferred oxygen excesses for GALEXJ2339 and WD1225+540 are nearly identical to those reported by Klein et al. (2021) and Xu et al. (2019). For WD1425+540, we find a substantially higher oxygen excess than reported by Xu et al. (2017), but this is due to a different definition of the oxygen excess in their work. When the same definition is used, their methodology yields an oxygen excess of 84% in steady-state, which is in line with our new analysis.

For an additional five systems, our analysis infers a potential oxygen excess, but only at $< 2\sigma$. These white dwarfs are unlikely to be accreting dry material, but there is insufficient evidence for wet accretion at this statistical level. The case of GD61 is right on this threshold, with an inferred significance of 1.9σ. For this system, we identify a lower median excess than reported by Farihi et al. (2013) due to longer relative diffusion timescales of oxygen in the updated models of Koester et al. (2020). In addition, we find a $\sim 25\%$ probability of GD61 being in a declining state. This option was ruled out by Farihi et al. (2013) based on the presence of circumstellar material (Farihi et al., 2011), although a declining state can be consistent with an infrared excess if the system is just accreting at a lower rate than before. Together with the abundance uncertainties, this pushes the significance of the oxygen excess in our computation just below 2σ. A similar argument applies to our results for GD378 (Klein et al., 2021), SDSSJ1242+5226 (Raddi et al., 2015), SDSSJ2047-1259 (Hoskin et al., 2020), and WD1536+520 (Farihi et al., 2016). If the accretion state is not constrained with a very high degree of certainty, as is seldom the case for white dwarfs with helium-dominated atmospheres, the possibility of a declining state will often suppress the significance of an oxygen excess below 2σ.

Finally, our inferred oxygen excess for SDSSJ0956+5912 (-21^{+51}_{-87}%, taking the abundances from the Gran Telescopio Canarias reported by Hollands et al. (2022)) differs substantially from the estimates by Hollands et al. (2022), who reported a value of $\sim 45\%$ with the same abundances. In this case, our Bayesian analysis with `PyllutedWD` confidently infers the accretion to be in a late declining state, at more than two diffusion timescales after accretion. However, Blouin (2020) showed that with the updated constitutive physics in their model, the diffusion timescale of magnesium in old white dwarfs with helium-dominated atmospheres could be shorter than currently modelled, potentially biasing the analysis of this system to a declining state. We further discuss the challenges of confidently inferring accretion states in Section 6.5.4.

6.5 Discussion

6.5.1 Interpretation of dry/wet photospheric abundances

The predicted rapid sublimative erosion of ices around warm ($\gtrsim 10,000$ K) white dwarfs implies that the material accreting from a single comet may initially appear highly volatile-rich, and become dry as accretion continues. In light of this possibility, we advise a cautious approach to the interpretation of volatile abundances of warm white dwarfs. While the detection of an oxygen excess always points to the presence of ices, the inferred quantity might not match the pollutant's bulk composition. Additionally, abundances that seem to suggest the accretion of a dry asteroid, might in fact correspond to the late accretion stage of a wet comet. The effects of asynchronous ice-refractory accretion are most important for the hottest white dwarfs, especially for those with hydrogen-dominated atmospheres, where downward diffusion of heavy elements does not average over different accretion stages. For the hottest stars, the initial wet accretion phase is expected to be short, with much longer-lasting dry accretion. At no point during the accretion process is it guaranteed that the abundances of a white dwarf atmosphere match the bulk composition of an accreting comet. For white dwarfs with helium-dominated atmospheres, the same argument applies, but only down to $\sim 15,000$ K, when the timescale for the downward diffusion of heavy elements exceeds 1 Myr, and the wet and dry accretion stages likely become indistinguishable.

6.5.2 Observational tests for asynchronous volatile-refractory accretion

The proposed scenario of asynchronous ice-rock accretion makes two observational predictions, and can either be corroborated or ruled out by future data. The first prediction is that there exists an anti-correlation between white dwarf temperature and the inferred fraction

of wet pollutants. While we find that there are currently not enough white dwarfs with determined oxygen abundances to investigate this trend, upcoming large-scale spectroscopic surveys (4MOST/WEAVE/DESI/SDSS-V) will provide an opportunity to significantly expand the size of this sample in a uniform manner. White dwarfs with hydrogen-dominated envelopes are most useful for this purpose, as they are almost certainly in a steady-state accretion phase, which is typically necessary for the oxygen excess to be well-constrained. However, we also emphasize the requirement for sufficiently small errors on atmospheric abundances of O, Si, Mg, and Fe, as current limits are insufficient for significant statistical results. A second difficulty for the verification of this prediction is the same trend has previously been predicted based on the hypothesized inside-out scattering of planetesimals from the surrounding planetary system (Jura & Young, 2014; Malamud & Perets, 2016). Due to this similar prediction from dynamic models, the detection of such a trend will never provide definite evidence in favour of asynchronous accretion. Recent evidence seems to argue against the inside-out depopulation of planetesimals, however, as the implied decline of the inward scattering rate over time (Li et al., 2022) has not been observed (Blouin & Xu, 2022).

Pure ice accretion onto SDSS J0914+1914?

Secondly, the process of asynchronous ice-rock accretion could be proven by the identification of hot white dwarfs with super-Solar volatile abundance ratios. Out of the three systems in our white dwarf sample identified to be oxygen-rich, none clearly falls within this category. However, there is one example of a white dwarf, SDSS J091405.30+191412.2 (Gänsicke et al., 2019), where only oxygen and sulphur were detected, and so virtually all the accreting oxygen appears to be in the form of ices. Interestingly, SDSS J0914+1914 is extremely warm for a polluted white dwarf ($T_{\rm eff} = 27,750 \pm 310$ K) and has a hydrogen-dominated atmosphere. At such a high temperature, the sublimative erosion and accretion of ices is expected to dramatically outpace the accretion of minerals, and the short diffusion timescale allows for a clear compositional separation of wet and dry accretion phases (See Fig. 6.3).

In the work by Gänsicke et al. (2019), the extreme inferred composition of the accreting material was suggested to match the deep layers of an evaporating ice giant planet. In this scenario, EUV photons from the star ionize hydrogen from the planetary envelope (Bourrier & Lecavelier des Etangs, 2013; Owen, 2019), triggering a hydrodynamic outflow of hydrogen that takes with it significant amounts of H_2O and H_2S. To distinguish both scenarios, the compositional differences of ice giants and comets can be compared. Most strikingly, only ice giants are massive enough to bind substantial amounts of gaseous hydrogen and helium from their natal environments (Bodenheimer & Pollack, 1986; Mizuno, 1980; Pollack et al., 1996).

In the cases of Uranus and Neptune, their bulk gaseous hydrogen content has been modelled at 10% and 5%, respectively (Podolak et al., 1995), although both numbers are subject to uncertainty (Helled et al., 2020; Podolak et al., 2022; Vazan et al., 2022). Compared to these estimates, the disc around SDSS J0914+1914 is depleted in hydrogen by more than an order of magnitude, explained by Gänsicke et al. (2019) as the result of radiation pressure. In Appendix C.4, we verify that radiation pressure can indeed push out neutral hydrogen atoms, but we show that the other rock-forming elements are equally affected. In addition, the pressure felt by hydrogen atoms is strongly dependent on the degree of red/blue shifting, complicating the picture significantly.

Helium atoms are unaffected by radiation pressure, however, and their abundance is more suitable to distinguish the two accretion scenarios. The chemical inertness of helium makes it extremely depleted in comets, at least by a factor 10^4 in comet Austin (Stern et al., 1992). In contrast, helium is abundant in all layers of ice giants, which are too small for helium to phase-separate (Guillot et al., 2022; Mankovich & Fortney, 2020; Miguel et al., 2022), predicting an approximately solar ratio of He/H, similar to that observed in their outer layers (Conrath et al., 1987, 1991). Following the model by Moses et al. (2020), the ratio of $\log(\mathrm{He}/\mathrm{O})$ in Uranus and Neptune drops from virtually zero in their outer layers to 0.5 and -0.22 in their deep interiors, respectively. The current upper limit for SDSS J0914+1914 was determined by Gänsicke et al. (2019) at $\log(\mathrm{He}/\mathrm{O}) < 1.05$, which is not strict enough to distinguish between both scenarios. In the future, a detection of helium at or near the current upper limit can confirm an ice giant scenario, while a tighter constraint on the star's helium abundance below $\log(\mathrm{He}/\mathrm{O}) \lesssim -1$ would rule it out, favouring a scenario of asynchronous accretion of volatiles and refractories.

6.5.3 Uncertainties in volatile/refractory accretion timescales

The importance of asynchronous volatile-refractory accretion can be quantified by the accretion timescale ratio of ices relative to rocks. Currently, both timescales are subject to significant uncertainties. In our calculation of sublimative erosion, we assume that the sublimation occurs in a highly eccentric disc following a tidal disruption. If the accretion process occurs in a tighter, circular disc, the sublimation timescale becomes substantially shorter. Secondly, the interiors of cometary fragments likely consist of a complex matrix of different minerals and ices, with some porosity depending on its interior pressure (Durham et al. 2005; Leliwa-Kopystyński & Kossacki 2000; Yasui & Arakawa 2009), rather than a single species. When a fragment is insufficiently permeable, vapour could remain trapped inside, shielded by an outer dust layer, making volatile escape take a different form (Fulle et al., 2019, 2020; Gundlach et al., 2020). Modelling of such processes remains contingent

on various uncertain thermal and permeability coefficients, even in current state-of-the-art models (Davidsson, 2021; Malamud et al., 2022). Additionally, in the geometry of an eccentric tidal disc, the environment can become radially opaque, in which case the radiative flux received by fragments depends largely on the vertical structure of the disc. Finally, a portion of a comet's volatiles may also be lost prior to its tidal disruption, during the preceding tidal evolution (Malamud & Perets (2016, 2017a,b), Pham et al, in prep.). Such a scenario of asynchronous accretion can also lead to pure volatile accretion, albeit at lower accretion rates.

On the refractory side of the comparison, the accretion timescale of rocky material is also not very well constrained. It was inferred to be between $10^4 - 10^6$ yr by Girven et al. (2012), based on the difference in pollution rates between white dwarfs with hydrogen and helium-dominated atmospheres. This estimate was later adjusted upwards to $10^5 - 10^7$ yr by Cunningham et al. (2021) using updated diffusion timescales. However, bursts of rapid accretion of rocky material might be required to explain the occasional measurement of extremely highly polluted atmospheres (Farihi et al., 2012). If rocky accretion timescales are indeed on this shorter side of the estimations, asynchronous ice-rock accretion only operates if tidal disruptions produce icy fragments smaller than 100 m, which could still be reasonable given the relatively weak material strength of ice (Davidsson, 1999; Greenberg et al., 1995; Gundlach & Blum, 2016).

Vapour accretion after sublimative erosion

Besides uncertainties relating to sublimative erosion itself, the accretion of eccentric gas onto white dwarfs has not been studied in detail. Trevascus et al. (2021) showed that gas released by a body on a moderately eccentric trajectory can remain on a similar orbit for several orbital periods due to aerodynamic coupling, but it is not clear if this generalizes to the highly eccentric ($e \sim 0.999$) orbits expected after a tidal disruption. It is unlikely that the vapour promptly circularizes via shocks induced by orbit crossings analogous to stellar disruption around black holes (Rees, 1988), as the gravitational field is much weaker than this analogous case. When circularization does occur, energy released by the process will heat the gas to a highly ionized state. At this point, its effective viscosity is likely increased by the magneto-rotational instability, and most of the gas can viscously accrete within tens of years (Rafikov, 2011b). In the recently published paper by Okuya et al. (2023), the accretion of silicate grains and water vapour onto a white dwarf were modelled together for the first time. In their work, the water vapour, released at the Roche radius, accretes slowly onto the white dwarf over the span of a Myr. However, it is not clear that this same timescale will apply for the highly eccentric discs expected to form after a tidal disruption event.

6.5.4 Challenges in accurately constraining the accretion state

To confidently infer the oxygen excess of pollutants, or more broadly their composition, the accretion state of the system must be well-constrained. In this work, we use the Bayesian code `PyllutedWD` (Buchan et al., 2022) for this purpose (see Fig. C.3 for the posterior distributions). Our approach has the advantage of yielding a likelihood distribution of possible accretion states, constrained by all available elements, but is still limited in three ways. First, it assumes a physical model for the formation of a pollutant (described by Harrison et al. 2021a, see also Rogers et al. 2022b) that could be over-simplified. Second, if the true diffusion timescales of particular elements differ from the modelled values (in our case by Koester et al. 2020), the Bayesian model will be biased towards a particular accretion state. The uncertainty of accretion timescales is a known issue for cool white dwarfs with helium-dominated atmospheres (Blouin, 2020; Heinonen et al., 2020). Similarly, because the errors on the diffusion timescales of elements are due to systematics, and therefore largely unknown, the true distribution of consistent accretion states is likely to be broader than our modelled values.

More generally, because the accretion states of white dwarfs with helium-dominated atmospheres are difficult to constrain in practice, accounting for the relevant uncertainties almost always produces a broad range of possible pollutant compositions. In our analysis, this means that no systems can currently be claimed to have swallowed oxygen-rich pollutants with 3σ significance. For only three systems, the abundances are such that we infer an oxygen excess at $\geq 2\sigma$. To improve the constraints on accretion states, it helps if the abundances and upper limits of as many elements as possible are reported (see Buchan et al. 2022; Harrison et al. 2021a), but significant uncertainties are likely to remain. In light of this, it might be that white dwarfs with hydrogen-dominated atmospheres are most suitable for statistically strong claims about the compositions of their pollutants, and that future work should focus on building a sizeable sample of polluted white dwarfs with this atmospheric type. However, in the current sample, the abundance errors on the white dwarfs with hydrogen-dominated atmospheres are also prohibitively large for strong statistical statements about their water content, showing that reduced uncertainties are required across the board to allow the presence of water to be statistically proven.

6.6 Summary and conclusions

The presence of water ice in planetesimals may be necessary to form habitable planets in the otherwise dry inner zones of planetary systems. Polluted white dwarfs provide a unique opportunity to assess this water content in systems around other stars (Farihi et al., 2013,

2016; Hollands et al., 2022; Hoskin et al., 2020; Klein et al., 2021; Raddi et al., 2015; Xu et al., 2019, 2017), but the analysis is made complex by details of the accretion process. In this work, we study the pollution of white dwarfs with cometary material, and investigate the scenario suggested by Malamud & Perets (2016), where icy fragments potentially sublimate and accrete prior to the pollutant's rocky components. We find that the timescale for sublimative erosion is indeed short, less than 1 Myr when the stellar temperature exceeds $10,000$ K (Eq. 6.4c). Based on this result, we suggest that the accretion of a single comet might begin with a volatile-rich phase, followed by the accretion of dry dust (Figs. 6.3, 6.4). The proposed scenario of asynchronous ice-rock accretion makes two testable predictions:

1. There is an anti-correlation between white dwarf temperature and the inferred fraction of wet pollutants. This trend should continue down to $t_{\rm acc} = t_{\rm sub}$ ($\sim 10,000$ K) for white dwarfs with hydrogen-dominated atmospheres, and down to $t_{\rm acc} = t_{\rm sink}$ for those with helium-dominated atmospheres ($\sim 15,000$ K).

2. Some hot white dwarfs will be found with volatile abundances that far exceed the plausible range for comets. These systems can be explained as examples where accretion is caught in the early phase of sublimative erosion.

To test these predictions, we collate and analyse a sample of white dwarfs from the literature. We find that due to large combined uncertainties on abundances and accretion states, only three systems show significant (2σ) evidence of water, an insufficient number to investigate the first prediction. Incidentally, the scenario of asynchronous accretion might explain the extremely volatile composition of material accreting onto SDSS J0914+1914, where only oxygen and sulphur were observed. To distinguish this scenario from the accretion of an ice giant, proposed by Gänsicke et al. (2019), a stricter constraint on the helium abundance is required.

Given our results, we advise a cautious approach to the interpretation of volatile abundances of warm ($> 10,000$ K) white dwarfs. While the identification of an oxygen excess points to the presence of water in the accreting material, the inferred value does not necessarily match the bulk composition of the comet. Similarly, a pollutant that appears to be dry, might in fact be volatile-rich if it is observed in the later stages of its accretion. Finally, we show the importance of interpreting pollutant compositions in a statistical manner, and highlight the difficulty of making statistically strong statements given the large uncertainties on abundances and accretion states. For stars with helium-dominated atmospheres, accounting for uncertainties in their accretion state alone (build-up/steady-state/declining) often already produces a broad range of possible pollutant compositions. In this work, uncertainties on abundances and accretion states limit the significance of most inferred oxygen excesses

below 2σ. In light of this, we emphasize the need for reduced uncertainties on atmospheric abundances, and encourage observational efforts to focus on expanding the sample of polluted white dwarfs with hydrogen-dominated atmospheres, whose accretion states are typically well-constrained.

Chapter 7

Conclusions

"I mean to say, Krestyan Ivanovich, that I go my own way, a particular way. I'm my own particular man and, as it seems to me, I don't depend on anybody. I also go for walks, Krestyan Ivanovich."

- Fyodor Dostoevsky, The Double, 1846

In this thesis, I have contributed to the literature on the formation and destruction of planets and planetesimals, by suggesting new ideas with supporting calculations. The work presented in this thesis tries to answer three questions, ordered chronologically according to a planet's lifetime. The first question that I investigate, is whether the spin distribution of planetesimals can be explained by their formation in a gravitational collapse. The second topic deals with the growth of planets by pebble accretion. Specifically, I try to find out how much envelope opacity is generated by the accretion of pebbles as a planet grows, and how that effects the formation of planets. In the final chapters, I move from the formation of planets to their destruction, and try to answer how planetary material can accrete onto white dwarfs, and what consequences the accretion process has for the ratios of heavy elements in the white dwarf atmosphere.

7.1 Formation of planetesimals and their spins

In chapter 2 of this thesis, I have studied a process that can cause the spins and orbits of objects to become aligned via the exchange between orbital and rotational angular momentum during a gravitational collapse. The formation of planetesimals provides a natural application for this theory, because they likely form via a collapse while in orbit around a central star. The

collapse itself can be triggered by a range of different mechanisms, including the streaming instability (Johansen et al., 2007; Schäfer et al., 2017; Youdin & Goodman, 2005).

I have found that the direction of spin-up during a gravitational collapse is typically in the prograde direction, and that this can be explained via a simple geometric argument: particles in a collapsing cloud that are at different distances from the central star orbit with different angular velocities, and thus shear away from one another over time. During the collapse, even a minimal amount of shear causes the centre-of-mass of the cloud to move slightly closer to the central star. Since the planetesimal ultimately forms at the centre-of-mass (excluding any material ejection), it will form on a slight interior orbit relative to the cloud from which it originates. Because this new orbit contains less orbital angular momentum, and because the total amount of angular momentum is conserved, the planetesimal should form with an increased rotational angular momentum: a prograde spin. Using simple N-body simulations, I have confirmed that this process indeed happens, and I have simulated different cloud sizes and orbits to identify the main trends, which also follow from simple analytical arguments. I find that the spin-up develops quadratically over time during the collapse ($\delta L_{\rm rot}/L_{\rm H} \propto t^2$), before slowing down when the collapse completes ($t \sim t_{\rm ff}$). The total amount of spin angular momentum gained during a collapse depends strongly on the size of the cloud relative to the hill radius, scaling as $\delta L_{\rm rot}/L_{\rm H} \propto t_{\rm ff}^2 \propto (R_{\rm cl}/R_{\rm H})^5$. This means that the process of prograde spin-up is only important for clouds that are comparable to their Hill radius prior to their collapse.

The mechanism as described above is most naturally applicable to the formation of planetesimals, and evidence of strong spin alignment is indeed seen in the trans-Neptunian binaries (Grundy et al., 2019). The link between the spins of these objects and their formation in gravitational collapses was previously also made by Nesvorný et al. (2021, 2019), who performed more detailed numerical simulations, but did not discuss the underlying mechanism. The fundamental idea presented in this thesis, that the spins of planetesimals might differ from that of the clouds from which they form, is not entirely new either, and was previously discussed by Safronov (1972) in his classic book on planet formation. However, lacking computational resources, his arguments relied entirely on the conservation of angular momentum and energy, and he was unable to deduce the direction of spin angular momentum change. Aided substantially by computer simulations, I was able to formulate a physical mechanism that explains both the magnitude and direction of the spin-up.

7.1.1 Future work

In my thesis, I have described the physical mechanism that could be responsible for the prograde spins of objects that form via gravitational collapse using simple analytical cal-

culations and N-body simulations. As I see it, this work could be extended in three main directions. First, the analytical basis for the theory could be greatly improved by generalizing the calculations to apply to any cloud with an arbitrary shape, to differently shaped external potentials, and by more self-consistently combining the collapse of the cloud with the shear it experiences. Second, the application to the formation of planetesimals could be explored in more detail by performing more sophisticated numerical simulations. Such simulations were previously performed by Nesvorný et al. (2021, 2019) for the streaming instability, but did not track the spin of collapsing clouds over time to explicitly investigate prograde spin-up. Alternatively, the formation of planetesimals could be simulated with other scenarios than the streaming instability, with a different set of initial conditions. Third, it would be fascinating to further investigate the applications of prograde spin-up to the formation of objects beyond just planetesimals. Potential applications could include the formation of stars in clusters, molecular clouds subject to the galactic potential, and the formation of galaxies themselves. Each of these situations is sufficiently different that they would necessitate individual investigations. It is likely, however, that current codes can be repurposed to track the spins of objects during their formation via collapse. A follow-up project to investigate prograde spin-up in the context of galaxy formation is currently underway.

7.2 Planetary growth and opacity due to pebble accretion

In chapter 3, I move to the growth stage of planets, where they are accreting both planetesimals and small pebbles from the surrounding disc. In addition to these solids, a planet also begins to gravitationally bind gas from the surrounding disc. The amount of gas that a planet of a certain mass can bind, depends on the cooling rate of the envelope, as cooler gas contracts, allowing for more nebular gas to flow in. Since the cooling rate of a planet is set by the opacity of its envelope, it is crucial to constrain this opacity during planetary growth.

In this work, I study how the accretion of solids can change the opacity of an envelope. The simple opacity model that I designed for this purpose is an extension of previous works by Mordasini (2014) and Ormel (2014), and contains two populations of solids. The larger solids represent the accretion of pebbles onto the planet, and their sizes are set by a combination of erosion, fragmentation, and the sweep-up of small dust grains, which form the second population in the model. I have formulated simple analytical expressions for the expected opacity in different physical regimes, where the size of pebbles is either mass-limited (pebbles grow with increased accretion rates) or fragmentation-limited (pebbles stay the same size). I then applied this model to a large parameter space of planetary masses, accretion rates, and distances to the central star to elucidate trends in the opacity.

I find that pebbles are expected to drastically change their size during the accretion process onto a planet. In some cases, pebbles with mm-cm entry sizes can be eroded down to a few microns in an outer planetary envelope, where they are accelerated by the planet's gravity. This can produce high opacities in a planet's outer envelope. In the deeper envelope, pebbles can stick together and grow, reducing the opacity substantially. A key parameter in setting the pebble opacity is the pebble accretion rate. At lower accretion rates, any additional accretion is compensated by growth to larger sizes, maintaining an equal pebble surface area in the envelope, and opacities generally remain low. However, when the accretion rate exceeds a certain rate (around 10^{-5} $M_{\oplus}/yr$), the maximum pebble size is reached due to the fragmentation barrier, and excess accretion can significantly increase the opacity. For small planets with high pebble accretion rates, the envelope can become fully convective. The results from our model show that the opacity within a planetary envelope can vary by several orders of magnitude, and that parameterizing opacity with a single value, as is often done, is usually a poor approximation.

7.2.1 Future work

Future work on opacity models could be taken in different directions. One possibility is to further develop detailed numerical models, such as those constructed by Movshovitz & Podolak (2008) and Movshovitz et al. (2010), which contain grains of many different sizes. The main challenge for such models is to be numerically efficient, such that they can be run at many different times in a planet's evolution. In this thesis, I have shown that different accretion rates and planetary masses result in extreme variations of the opacity from solids, and that an opacity calculation at one given mass should not be extrapolated to the entire formation channel of a planet. Alternatively, analytical models like the one constructed in this thesis could also be improved, or aided by new data on collision experiments to refine the regimes of sticking, bouncing, fragmenting, or eroding collisions. Perhaps most importantly, however, is that detailed opacity models begin to be incorporated into population synthesis models, and other models of planetary evolution. These formation models are one of the main ways in which our current understanding of planet formation is tested, by checking whether they can reproduce the population of observed planets or individual systems. However, they often use the convenient assumption of a high envelope opacity to limit the amount of gas accretion, which we show is usually a poor approximation. By integrating planet formation calculations with physical opacity models, we can better test our current understanding of the planet formation process.

7.3 Accretion of planetary material onto white dwarfs

In chapters 4 -6, I study the destruction of planets and planetesimals, and their eventual accretion onto white dwarfs. This area of research is developing quickly, as increasing numbers of polluted white dwarfs with heavy elements in their spectra are found. As a population, around half of white dwarfs are polluted with one or more elements (Koester et al., 2014; Zuckerman et al., 2003, 2010). So far, most studies have focused on interpreting the ratios of these elements to infer the composition of the accreting material (e.g., Buchan et al., 2022; Harrison et al., 2021a, 2018; Hollands et al., 2018; Putirka & Xu, 2021; Swan et al., 2019a). However, the processes via which the material accretes onto a white dwarf remain quite poorly understood. In my work presented in this thesis, I try to formulate a likely pathway for this accretion process, and then link it to observables such as the infrared excess and the accreted composition.

I find that accretion likely begins with the tidal disruption of an asteroid, and the formation of a highly eccentric disc. The largest fragments in this disc are likely km-sized, a size that is determined by the material strength of the fragments and by how deep within the star's Roche radius they are scattered. Only small (sub-cm) fragments are susceptible to PR drag, while larger fragments likely remain on their released orbit for long periods of time unless they are disrupted. If most of the asteroid's mass is still contained in these larger fragments, the accretion process is likely limited by the timescale on which they are collisionally ground down into dust. I find that there are multiple processes that can trigger the required high-velocity collisions for this to occur, including orbital perturbations by the Yarkovski effect (Veras et al., 2015a,b; Veras & Scheeres, 2020), and differential precession by general relativity (Debes et al., 2012; Veras et al., 2014a). I model the collision rate induced by differential precession, assuming a simple model where collisions are fully catastrophic. Small dust grains that are produced in the collisions accrete via drag forces, and produce an infrared excess if accretion is sufficiently slow. I find that optically thin PR drag alone can produce a substantial infrared excess when the accretion rate exceeds 10^7 g/s. However, surveys in reality rarely find substantial infrared excesses. To reconcile this, I suggest that an infrared excess can be avoided by more rapid dust circularization, for instance via enhanced drag due to the presence of gas near the disc's pericentre.

If an asteroid is differentiated into a metallic core and a rocky mantle, the tidal disruption that precedes accretion will spread the core and mantle fragments over different orbits. Therefore, any accretion process where the accretion time of a fragment depends on its orbit will cause the two components (core and mantle) to accrete onto the white dwarf in a proportion that is not constant over time. I coin this idea that different elements accrete over different timescales *asynchronous accretion*, and it has consequences for the observational

interpretation of white dwarf abundances. Due to asynchronous accretion, the elemental ratios observed in a white dwarf atmosphere may not match the bulk composition of an asteroid that is currently accreting onto the white dwarf, especially if the sinking timescale of the elements is short relative to the accretion timescale, as is the case for white dwarfs with hydrogen-dominated atmospheres. In the core-mantle differentiated scenario, I also find that mantle fragments are ejected during the tidal disruption with greater numbers than the core fragments, causing the circumstellar disc to be enriched in core material by up to 20%.

Finally, I also consider the accretion of comets onto white dwarfs, which can contain both icy and rocky fragments. If comets accrete onto hot white dwarfs with effective temperatures in excess of around 10.000 K, the ices in their fragments can rapidly sublimate after the tidal disruption due to the intense thermal radiation received at the pericentre of their orbits. Because the rocky components are not affected by radiation in the same manner, this can cause the ices in the comet to accrete before the rocky components, providing a second potential scenario of asynchronous accretion. This scenario has clear observational predictions, that can be used to validate it, or rule out this scenario. First, there should be an anti-correlation between white dwarf temperature and the fraction of pollutants inferred to contain water ice. Second, some hot white dwarfs should be found to have swallowed impactors that contain almost exclusively ice, as they are caught in the early accretion stage during which rapid sublimation takes place. I compiled and analysed a sample containing all white dwarfs with oxygen detections, but found that only three systems show any indication of water ice, too few to perform any statistical analysis. This is an interesting finding in itself, however, as far more systems were previously suggested to be water-rich. Our results show the importance of interpreting pollutant compositions in a statistical manner, and highlight the difficulty of making statistically strong statements given the large uncertainties on abundances and accretion states.

7.3.1 Future work

The study of the white dwarf accretion processes remains a young field, and much is still left to be done. In the first place, it is important to further improve the link between accretion scenarios and their observational outcomes, to turn the current speculation of the dominant accretion processes into verifiable science. One important aspect that I have focused on in this thesis is the infrared excess generated by circumstellar discs. In my work, I calculated the infrared excess of the highly eccentric discs expected from current accretion theory, provided that they are optically thin. Other works tend to take a contrasting empirical approach, where the infrared excess of a particular system is fitted with a circular disc and a variable inner and outer radius. Recently, Ballering et al. (2022) extended these models to also have a flexible

opening angle and dust mass, and added radiative transfer to the calculation. Much could be gained by performing such a calculation again, but then with physically motivated, highly eccentric discs, rather than a circular structure.

For the other two observables, the detection of gas and transits, we are currently still far away from a self-consistent accretion scenario. While it is often suggested that collisions and sublimation can produce gas during the accretion process, no model has yet been constructed that combines the production and evolution of this gas. Some progress was recently made by Okuya et al. (2023), who modelled the evolution of a gas disc and a dust disc, but this was done under the assumption that both components already start on circular orbits in a fully formed state. The conclusion of these authors was that the gas must contain a different composition from the dust in order to overlap sufficiently to produce a substantial drag force. It would be very instructive to see whether the conclusions change when the assumption of circular orbits is relaxed, to the expected, highly eccentric initial disc. For the detection of transits, it is similarly true that no model has yet computed the feasible evolution of a planetesimal fragment to the close-in, slightly eccentric orbits at which they are sometimes observed.

In the final part of my thesis, I have discussed the possibility that the asynchronous accretion of various elements in a planetesimal or comet can cause the relative abundances of these elements to vary over time during the accretion of a single object. Future work on this topic is required in two directions. First, from a theoretical perspective, the models developed in this thesis can be much improved when the main accretion scenarios are better constrained. For the ice-refractory accretion models in chapter 6, it is particularly important for a self-consistent gas-solid accretion model to be developed. Second, as the sample of known polluted white dwarfs continues to expand, population statistics can be used in the future to verify or falsify the predictions from asynchronous accretion models. This is perhaps easiest for the accretion of refractory and volatile elements, which would predict the rare occurrence of extremely volatile accretion events if accretion occurs asynchronously, which is otherwise hard to explain. A large-scale observational campaign with Hubble to increase the sample of polluted white dwarfs with oxygen abundances is currently underway, motivated in part by the work presented in this thesis (Rogers et al., 2022a).

Appendix A

Prograde spin-up appendices

A.1 Rebound settings and convergence

In this appendix, we describe the settings of our REBOUND runs used to model cloud collapse in the final stage of the streaming instability. First, we spread the particles evenly across the clouds to ensure that their density is uniform. To do so, we employ a Voronoi (Voronoi, 1908) algorithm with Lloyd iterations (Lloyd, 1982) until a high level of uniformity is achieved.

As the clouds contract, particles begin to collide. We model these collisions with an inflated particle approach to reduce the number of numerical particles (N_n) from the number of physical particles (N_p). In this approach, the radius of the numerical particles (s_n) is blown up to maintain total cross-section: $s_\mathrm{n} = s_\mathrm{p}\left(N_\mathrm{p}/N_\mathrm{n}\right)^{1/2}$. An interesting convenience that follows from the larger particles, as pointed out by Rein et al. (2010), is that the use of a gravitational softening parameter becomes redundant. We note that the inflated particle approach is only valid if the initial volume filling factor of the particles is well below the size of the cloud prior to collapse, in our simulations typically set to the Hill radius. Because the Hill radius is proportional to the orbital separation, the filling factor of a cloud with otherwise identical parameters ($N_\mathrm{n}, s_\mathrm{p}$) is reduced when it is positioned further from the star. In order to ensure that the cloud collapse behaves in the same manner at every semimajor axis, we instead fix the initial volume filling factor at $f = 10^{-3}$ in every simulation. This stylized approach is not suitable for resolving the physical system that forms from a collapse, as was modelled by Nesvorný et al. (2021); Robinson et al. (2020), but it is suitable for gauging the total amount of spin-up during the collapse. It allows for the use of far fewer numerical particles while maintaining convergence in this result. We show this in Fig. A.1, where the obtained rotation is indeed not dependent on the chosen number of numerical particles nor

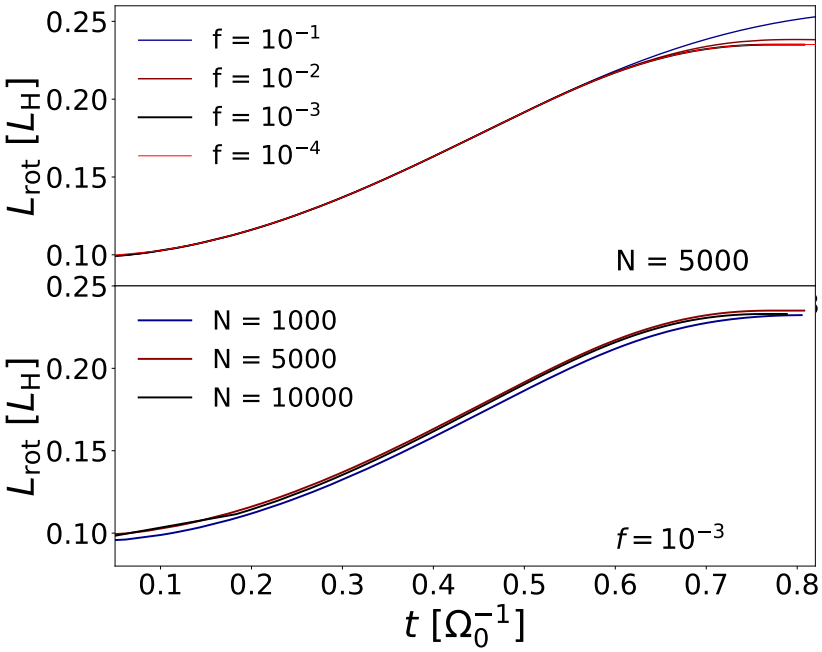

Fig. A.1 Dependence of the prograde spin-up over time on numerical parameters. Top: variation of the filling factor of the simulation box between $10^{-4} \leq f \leq 10^{-1}$. The runs correspond to $N_n = 5000$ numerical particles and are run at 5 AU. Bottom: variation of the number of numerical particles $10^3 \leq N_n \leq 10^4$, computed with a filling factor of $f = 10^{-3}$. The magnitude of prograde spin-up is found to be insensitive to these numerical parameters.

on the choice of filling factor. The coefficient of restitution in our model is taken to be zero, a choice that was not found to influence the results.

For the integration procedure of the N-body simulation, we use the default REBOUND module IAS15 (Everhart, 1985). IAS15 is a highly accurate, 15th-order, non-symplectic integrator that is optimized for integrations that include close encounters. The step-size in IAS15 is set dynamically, and includes predictive loops to reduce run-time. The precision is set with an accuracy parameter, for which we take the default value of 10^{-9}. At this level, the integration is typically accurate down to machine precision (Rein & Spiegel, 2015), and improved accuracy cannot be achieved with a smaller time-step or different integration procedure. Experimentation with the less accurate Gragg-Bulirsch-Stoer integration method in REBOUND was not found to significantly improve runtime of our simulations, and so we favoured IAS15 for its higher precision, especially in the resolving of collisions.

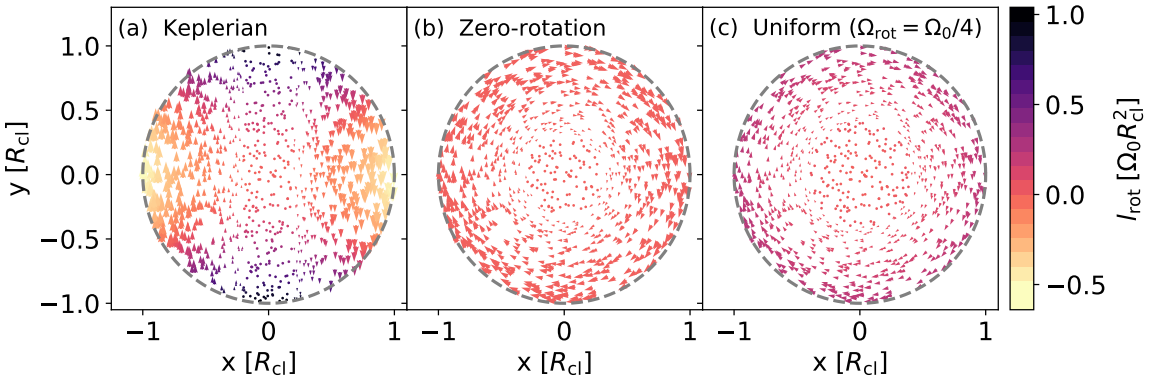

Fig. A.2 Quiver plot of initial velocities in the co-moving frame for three setups used in this paper. While our simulations use spherical clouds, this plot shows their cross sections at z=0. The arrow sizes correspond to the magnitude of the particle velocities and the colors correspond to the rotational contribution (from Eq. A.2c). The left panel (a) indicates the Keplerian setup (A.3), which yields a total prograde rotation equal to $L_{\rm rot} \simeq 0.1 M_{\rm cl} \omega_0 R_{\rm cl}^2$. The middle panel (b) corresponds to the zero-rotation initial condition (Eq. A.4), while the right panel (c) corresponds to uniform rotation with the same initial rotational angular momentum as the Keplerian setup.

A.2 Angular momentum transformation between local rotating and inertial frames

In local simulations such as the co-moving frame with/without shearing sheet approximation, particle positions and velocities are determined in a frame that is both rotating and translated relative to the star. In order to calculate the rotation vector of a cloud from these quantities, it is necessary to transform the vectors correctly to an inertial frame with the origin located on the studied object. The results of such a transformation for circular orbits are given in 3D without derivation by Nesvorný et al. (2019) and in 1D by Dones & Tremaine (1993a); Giuli (1968). As far as we are aware, only a limited 1D justification is shown by Lissauer & Kary (1991). Because we could not find a complete 3D derivation of the required transformation anywhere, we provide it here.

Let the first, co-moving frame with Cartesian coordinates (x, y, z) be centred at a (vector) distance $\mathbf{r_0}$ of a central object, in a frame that is rotating around the central object with the rotation vector $\boldsymbol{\omega_0} = \omega_0 \hat{z}$. Let the second frame with Cartesian coordinates (x', y', z') share its origin with the first frame, but be stationary (inertial). In order to transform a vector from the first to the second frame, the following operations are required. First, the frame is translated such that the origin coincides with the centre of the orbit: $\mathbf{r} \rightarrow \mathbf{r} + \mathbf{r_0}$. Then the frame is rotated around the origin with $-\omega_0$, such that the frame becomes inertial: $\mathbf{v} \rightarrow \mathbf{v} + \boldsymbol{\omega_0} \times \mathbf{r}$.

Finally, the frame is translated back, such that the origin is again located at the centre of the cloud: $\mathbf{r}+\mathbf{r_0} \rightarrow \mathbf{r}$. Together, these transformations lead to the following distance and velocity vectors in the stationary frame:

$$\mathbf{r}' = \mathbf{r} \tag{A.1a}$$

$$\mathbf{v}' = \mathbf{v} + \boldsymbol{\omega_0} \times (\mathbf{r}+\mathbf{r_0}). \tag{A.1b}$$

The rotation of a particle is given by its velocity relative to the cloud's centre-of-mass. If the centre-of-mass remains located on $\mathbf{r_0}$, it corresponds to $\mathbf{v}'_{\rm cm} = \boldsymbol{\omega_0} \times \mathbf{r_0}$ and the specific rotational angular momentum of a particle is given by:

$$\mathbf{l}'_{\rm rot} = \mathbf{r}' \times (\mathbf{v}' - \mathbf{v}'_{\rm cm}) \tag{A.2a}$$

$$= \mathbf{r} \times (\mathbf{v} + \boldsymbol{\omega_0} \times \mathbf{r}) \tag{A.2b}$$

$$= \begin{pmatrix} yv_{\rm x} - zv_{\rm y} - \omega_0 xz \\ zv_{\rm x} - xv_{\rm z} - \omega_0 yz \\ xv_{\rm y} - yv_{\rm x} + \omega_0(x^2+y^2) \end{pmatrix}. \tag{A.2c}$$

This final equation can trivially be generalized to any direction of $\boldsymbol{\omega_0}$ by using non-zero xy-components in Eq. A.2b. We note that there is, however, a potential issue with this calculation in a co-moving frame. If the centre-of-mass of the cloud shifts inward by a significant distance, the transformation no longer uses the right reference point for the rotation, as the object forms on an orbit slightly interior to the initial centre-of-mass. The magnitude of this error grows with $\delta R/r_0 \propto (R_{\rm cl}\omega_0 t/r_0)^2$ (see Eq. 2.9b) and is not quantitatively important in the calculations performed in this work.

A.3 Initial rotational condition of spherical clouds

In this section, we explain the setups used to investigate prograde spin-up. We refer to the first setup we use as Keplerian, meaning that all particles in the cloud begin with velocities in the stationary frame (whose axes directions at $t = 0$ coincide with a corotating frame) equal to:

$$\mathbf{v}'_{\rm Keplerian}(t=0) = \boldsymbol{\omega} \times \mathbf{r}. \tag{A.3}$$

We show these velocities translated to a co-moving frame in panel (a) of Fig. A.2. In this frame, the velocity differences are mainly visible as shear ($v_{\rm y} \simeq -\frac{3}{2}\omega_0 x$) on the x-axis. From Eq. A.2c, it is easy to see that the rotational contribution of particles on the x-axis becomes retrograde due to this shear, ranging from 0 to $-0.5\omega_0 R_{\rm cl}^2$. On the y-axis, however, the shear

is negligible and absolute velocity differences are minimal. Nevertheless, the curvature of the orbit (captured in the term $\omega_0(x^2+y^2)$) provides significant directional differences in velocity, which lead to prograde rotational contributions ranging from 0 to $\omega_0 R_{\rm cl}^2$. When integrated over the complete sphere, the net initial rotational condition of the Keplerian setup is around $L_{\rm rot} \simeq 0.1 M_{\rm cl}\omega_0 R_{\rm cl}^2$.

We refer to the second setup used in this work as the zero-rotation condition. In this setup, we set all the velocities equal to

$$\mathbf{v}'_{\rm zero-rotation}(t=0) = \boldsymbol{\omega_0} \times \mathbf{r_0}, \tag{A.4}$$

such that all particles begin with the same velocity as a particle that is located at the sphere's centre-of-mass and orbits in a circular motion. Without velocity differences, the particles in the cloud have no initial rotation. However, this is not immediately visibly apparent in the corotating frame (panel (b) of Fig. A.2), where the velocities are transformed (Eq. A.1b). Even though the particles provide no physical rotational angular momentum, their rotation visibly appears to start in a retrograde condition in this frame with a rotational period equal to the orbital period.

Finally, the third setup we use in this paper is one with a uniform cloud rotation rate ($\omega_{\rm rot}$) where the initial velocities are set equal to:

$$\mathbf{v}'_{\rm uniform}(t=0) = \boldsymbol{\omega_0} \times \mathbf{r_0} + \boldsymbol{\omega}_{\rm rot} \times (\mathbf{r} - \mathbf{r_0}). \tag{A.5}$$

The initial rotational condition in this setup trivially follows as $L_{\rm rot} = I_{\rm cl}\omega_{\rm rot} = 0.4 M_{\rm cl}\omega_{\rm rot} R_{\rm cl}^2$. In Fig. A.2, we plot the velocities in a corotating frame for the case where $\omega_{\rm rot} = \omega_0/4$ and the initial rotational angular momentum is identical to the Keplerian setup. In the special case where $\omega_{\rm rot} = \omega_0$ is chosen, all the particles appear stationary in the co-moving frame.

A.4 Collapse of a spherical cloud in a co-moving frame

In Fig. A.3, we repeat the collapse of an initially non-rotating spherical cloud in orbit (same calculation as Fig. 2.5), visualized instead in the commonly used corotating frame - rather than a stationary one. In this frame, the curvature of the orbital motion that is naturally present in a stationary frame is instead introduced by the Coriolis acceleration. In the first panel, the non-rotating cloud visually appears to have a retrograde rotation, which is a consequence of the non-inertiality of the frame (see also Fig. A.2(b)). As the cloud shears out and contracts, it again first attains a barlike shape. When the particles are pulled toward the centre-of-mass, they wrap around it in a prograde fashion. Finally, the collapse finishes

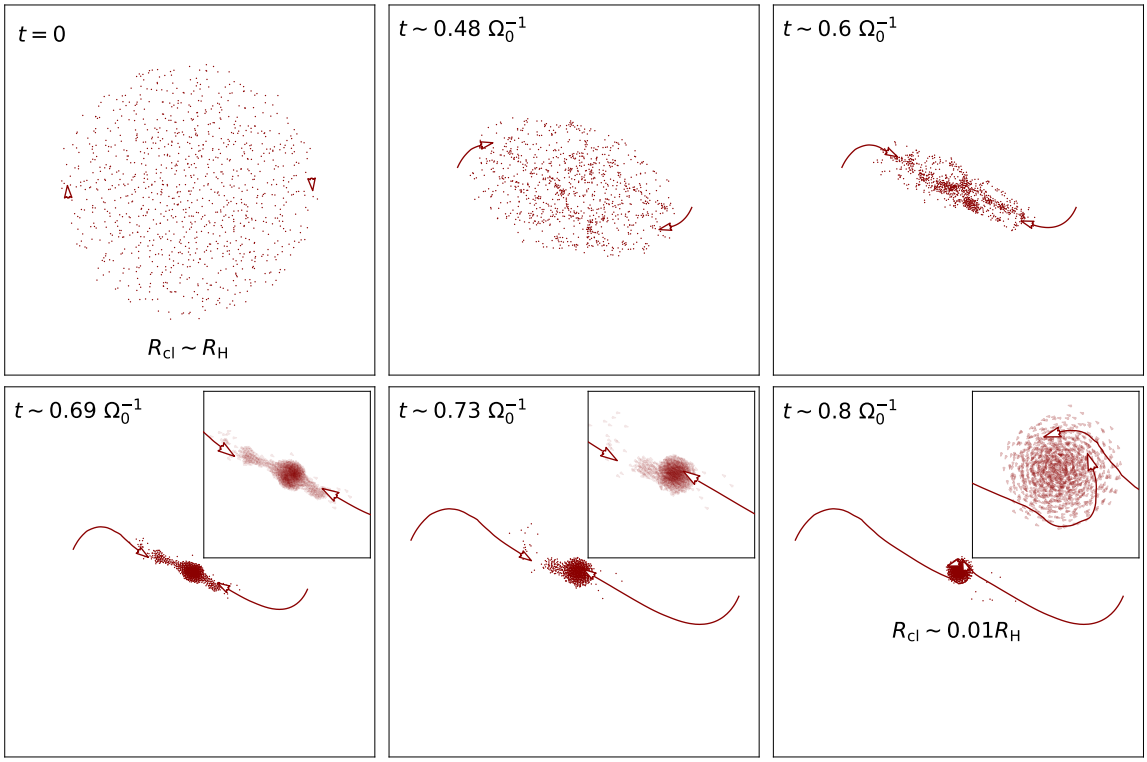

Fig. A.3 Overview of the collapse of a uniform cloud in orbit around a central mass (same as Fig. 2.5), shown in a co-moving frame. The spherical cloud is initiated with size $R_{\rm H}$ and without any rotation. The central mass is located left from the cloud. The velocity directions (magnitudes not to scale) and trajectory of the particles are highlighted for an interior and exterior particle that both wrap around the centre-of-mass in a prograde fashion.

and a spherical object with prograde rotation has formed. The physical shape and multiplicity of the system that forms, depends on the numerical parameters assumed, such as the filling factor and number of numerical particles. Importantly, however, the rotational direction and its magnitude remain unaffected by these numerical parameters.

Appendix B

Opacity appendices

B.1 Expression of the critical metal mass with a non-isothermal radiative layer

In this Appendix, we slightly modify the analytical structure model of Brouwers & Ormel (2020) to derive an expression for the critical metal mass that is more appropriate to study the effects of envelope opacity. The original model consists of an outer radiative region, followed by an intermediate convective region with solar composition and a polluted interior convective region that consists primarily of silicate vapour. Because that model was built with a grain-free envelope in mind, the radiative region was assumed to be isothermal. This ceases to be a good approximation when the opacity from solids is included, and the radiative temperature gradient becomes important.

Fortunately, it is straightforward to modify the model to be applicable to a scenario with higher envelope opacities. We shift the temperature boundary of the intermediate convective region from $T_{\rm disk}$ to $T_{\rm rcb}$ and recalculate the thermodynamic structure of the intermediate layer. This amounts to a single variable change in Eqs. 9a-9c of Brouwers & Ormel (2020):

$$r'_{\rm B} = \frac{\gamma_{\rm xy}-1}{\gamma_{\rm xy}} r_{\rm B} \quad \text{to} \quad r'_{\rm B} = \frac{\gamma_{\rm xy}-1}{\gamma_{\rm xy}} \frac{T_{\rm disk}}{T_{\rm rcb}} r_{\rm B} \tag{B.1}$$

which in effect lowers the density of the intermediate region and increases its temperature. The relation between the opacity and density at the RCB then becomes:

$$\kappa_{\rm rcb} = \frac{64\pi\bar{\sigma} T_{\rm rcb}^4 r'_{\rm B}}{3\rho_{\rm rcb} L}. \tag{B.2}$$

The corresponding structure equations of the polluted region remain unchanged. The only modification we have to make is at the outer boundary of the polluted region, where the density changes from

$$\rho_{\rm vap} = \left(\frac{T_{\rm vap}}{T_{\rm disk}}\right)^{\frac{1}{\gamma_{\rm xy}-1}} \frac{\mu_{\rm g}}{\mu_{\rm xy}} \rho_{\rm rcb} \quad \text{to} \quad \rho_{\rm vap} = \left(\frac{T_{\rm vap}}{T_{\rm rcb}}\right)^{\frac{1}{\gamma_{\rm xy}-1}} \frac{\mu_{\rm g}}{\mu_{\rm xy}} \rho_{\rm rcb}. \tag{B.3}$$

In our model for a polluted envelope, most of the mass is contained in the inner regions. In order to derive the critical metal mass, we substitute the modified variables into Eq. 22b of Brouwers & Ormel (2020) and follow the same steps as in Sect. 4.2 of that work. In practice, this comes down to substituting $T_{\rm rcb}$ for $T_{\rm d}$ in their Eq. 27. The critical metal mass is approximated to occur at the crossover mass where $M_{\rm xy} = M_{\rm z}$, which yields:

$$M_{\rm z,crit} \approx 5.5\ {\rm M}_\oplus \left(\frac{\kappa_{\rm rcb}}{0.01\ {\rm g\ cm^{-2}}}\right)^{\frac{1}{6}} \left(\frac{d}{\rm AU}\right)^{\frac{7}{108}} \left(\frac{T_{\rm vap}}{2500\ {\rm K}}\right)^{\frac{8}{27}} \left(\frac{\dot{M}_{\rm peb}}{10^{-6}\ {\rm M}_\oplus\ {\rm yr^{-1}}}\right)^{\frac{1}{6}} \left(\frac{M_{\rm c}}{\rm M_\oplus}\right)^{\frac{1}{2}} \left(\frac{T_{\rm rcb}}{T_{\rm disk}}\right)^{-\frac{126}{972}}. \tag{B.4}$$

The only difference in the final expression is the appearance of an inverse scaling with $T_{\rm rcb}/T_{\rm disk}$. This is due to a combination of two opposing effects. The first effect is that a higher RCB temperature leads to a lower RCB density at the same pressure and, therefore, results in an increased critical mass. The second trend is that a higher RCB temperature moves the location of the RCB inward to a higher pressure and an increased density at the same opacity, leading to a reduced critical mass. In combination, these two trends yield a slight inverse scaling in the final expression.

B.2 Variation of the limiting velocity

The most important free parameter in our model is the limiting velocity (Eq. 3.13), which represents the upper limit to the terminal velocity of pebbles during their sedimentation. It combines the velocity limits from erosion (Eq. 3.9a) and fragmentation. In the main text, we assumed a limiting velocity of 2.4 m/s, corresponding to the onset of erosion by micron-sized dust grains (Schräpler et al., 2018). Because smaller dust grains are more effective at removing mass, the erosion velocity scales inversely with grain size. In fig. B.1, we vary the limiting velocity between 0.4-40 m/s, which corresponds to erosion from grain sizes between 0.05-100 μm.

Fig. B.1 illustrates that the value of the critical velocity has important consequences for the opacity. If the limiting velocity is reduced below our default value of 2.4 m/s, the pebbles are velocity-limited to smaller sizes and the opacity can significantly increase. Due to this, a broader range of envelopes become fully convective when they experience a given pebble accretion rate. The opposite trend is also true when the limiting velocity is increased. A higher velocity limit means that pebbles are more often limited by growth, which in turn means that higher accretion rates are required to keep envelopes of the same mass convective. Within an envelope whose sedimenting pebbles are already limited by growth, a further increase of the limiting velocity has no effect.

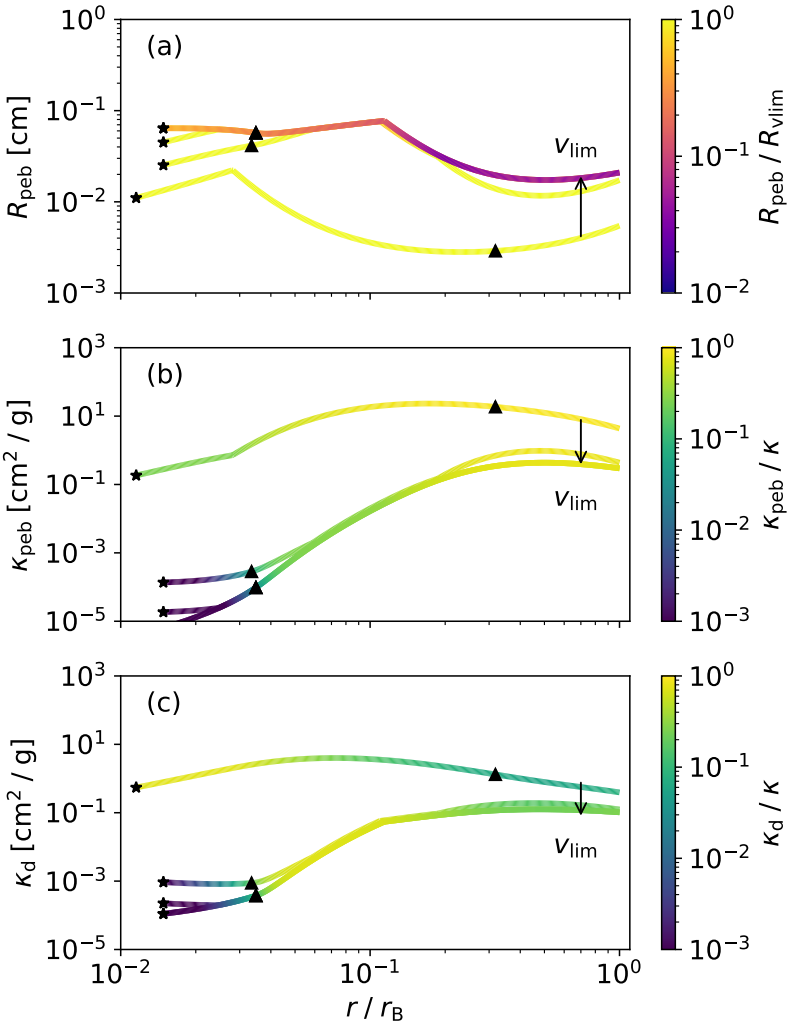

Fig. B.1 Pebble growth tracks (a), their resulting pebble opacity (b), and produced dust opacity (c) for a standard set of model runs at 5 AU (see Table 3.1). This figure is the same as Fig. 3.4, but now the mass is fixed at the default 5 $M_\oplus$ and the limiting velocity (Eq. 3.13) is varied a logarithmically between $0.4 - 40$ m/s.

Appendix C

White dwarf appendices

C.1 Neglection of asteroid rotation on tidal disc geometry

The predicted asynchronicity between the accretion of core and mantle fragments due to collisions or scattering is caused by their spreading to distinct orbital zones after a tidal disruption. In our calculation of the fragment orbits (Eq. 4.6b), we neglected the effect of self-gravity and the rotation of the disrupted object. In this appendix, we validate that these contributions are indeed negligible in the context of white dwarf pollution by asteroids. To account for the energy of rotation ($\varepsilon_{\mathrm{rot,i}}$) and self-gravity ($u_{\mathrm{SG,i}}$), we modify the total fragment energy (ε_{i}) in Eq. 5 of Brouwers et al. (2022):

$$\varepsilon_{\mathrm{i}} = u_{\star\mathrm{G,i}} + u_{\mathrm{SG,i}} + \varepsilon_{\mathrm{k,i}} + \varepsilon_{\mathrm{rot,i}} \tag{C.1a}$$

$$= -\frac{GM_{\mathrm{WD}}}{r_{\mathrm{i}}} - \frac{GM\left(<R_{\mathrm{i}}\right)}{R_{\mathrm{i}}} + \frac{1}{2}\left| GM_{\mathrm{WD}}\left(\frac{2}{r_{\mathrm{B}}} - \frac{1}{a_0}\right)\hat{\theta} + \boldsymbol{\omega}_{\mathrm{rot}}^{\mathbf{2}} \times {\mathbf{R}_{\mathrm{i}}}^{2}\right| \tag{C.1b}$$

where $\boldsymbol{\omega}_{\mathrm{rot}}$ is the rotation vector of the disrupted object and $\mathbf{R}_{\mathrm{i}}$ is the vector distance of a fragment to the object's centre. To investigate at what size the two new terms begin to dominate differences between fragment orbits, we evaluate the transition size $R_{\mathrm{transition}}$ where their radial derivatives along a line through the star and the disrupting object's centre are equal:

$$\frac{d}{dR_{\mathrm{i}}}\left(u_{\star\mathrm{G,i}} + \varepsilon_{\mathrm{k,i}}\right) = \frac{d}{dR_{\mathrm{i}}}\left(u_{\mathrm{SG,i}} + \varepsilon_{\mathrm{rot,i}}\right), \tag{C.2}$$

where $\mathbf{R}_{\mathrm{i}} = (r_{\mathrm{i}} - r_{\mathrm{b}})\hat{\mathbf{r}}$ because we consider a radial line. The transition size is smallest if the object's rotation is equal to the critical rate $\omega_{\mathrm{crit}} = \sqrt{4\pi G\rho/3}$ (Pravec & Harris, 2000), in

which case it evaluates to:

$$R_{\text{transition}} = \frac{3M_{\text{WD}}}{4\pi\rho r_{\text{B}}^2} \qquad \text{if } \omega_{\text{rot}} = \omega_{\text{crit}}\hat{\mathbf{z}} \tag{C.3a}$$

$$= 1.2 \cdot 10^5 \text{ km} \left(\frac{\rho}{5 \text{ g/cm}^3}\right)^{-1} \left(\frac{r_{\text{B}}}{\text{R}_\odot}\right)^{-1} \left(\frac{M_{\text{WD}}}{0.6 \text{ M}_\odot}\right), \tag{C.3b}$$

which corresponds to a size in between Uranus and Jupiter, far larger than the asteroids and minor planets considered in this work. Therefore, we conclude that rotation and self-gravity do not affect the general shape of the tidal disc. Since $\text{R}_\oplus \ll R_{\text{transition}}$, this is consistent with the SPH simulations by Malamud & Perets (2020a,b), where Earth-mass planets were shown to tidally disrupt into tidal discs with distinct core and mantle fragment zones.

C.2 Filling timescale of a tidal disc

When an asteroid tidally disrupts, its fragments are initially clustered around the same true anomaly, and some time is required to spread them out into a fully formed tidal disc. The validity of the accretion models discussed in Section 5.3 depends on the requirement that the fragments completely spread out to fill a disc before other accretion processes (scattering, collisions, sublimative erosion) become important. In this appendix, we provide a short derivation of this spreading timescale. Our derivation is most comparable to calculations by Nixon et al. (2020) and follows similar arguments to those presented by Veras et al. (2014a), although our derivation is applicable to both dispersive and non-dispersive disruptions.

We begin by specifying the semi-major axis of (a_{inner}) and outer (a_{outer}) fragments from Eq. 4.6b. The fragments break off in a range of distances from the central star between $r_{\text{B}} - R_{\text{ast}}$ and $r_{\text{B}} + R_{\text{ast}}$, which yields:

$$a_{\text{inner}} = a_{\text{ast}} \left(1 + \frac{2a_{\text{ast}}R_{\text{ast}}}{r_{\text{B}}\left(r_{\text{B}} - R_{\text{ast}}\right)}\right)^{-1}, \tag{C.4a}$$

$$a_{\text{outer}} = a_{\text{ast}} \left(1 - \frac{2a_{\text{ast}}R_{\text{ast}}}{r_{\text{B}}\left(r_{\text{B}} + R_{\text{ast}}\right)}\right)^{-1}. \tag{C.4b}$$

The total orbital width (Δa) of the tidal disc that forms is thus:

$$\Delta a = a_{\text{outer}} - a_{\text{inner}} \tag{C.5a}$$

$$\simeq \frac{4a_{\text{ast}}^2 R_{\text{ast}}}{r_{\text{B}}^2}, \tag{C.5b}$$

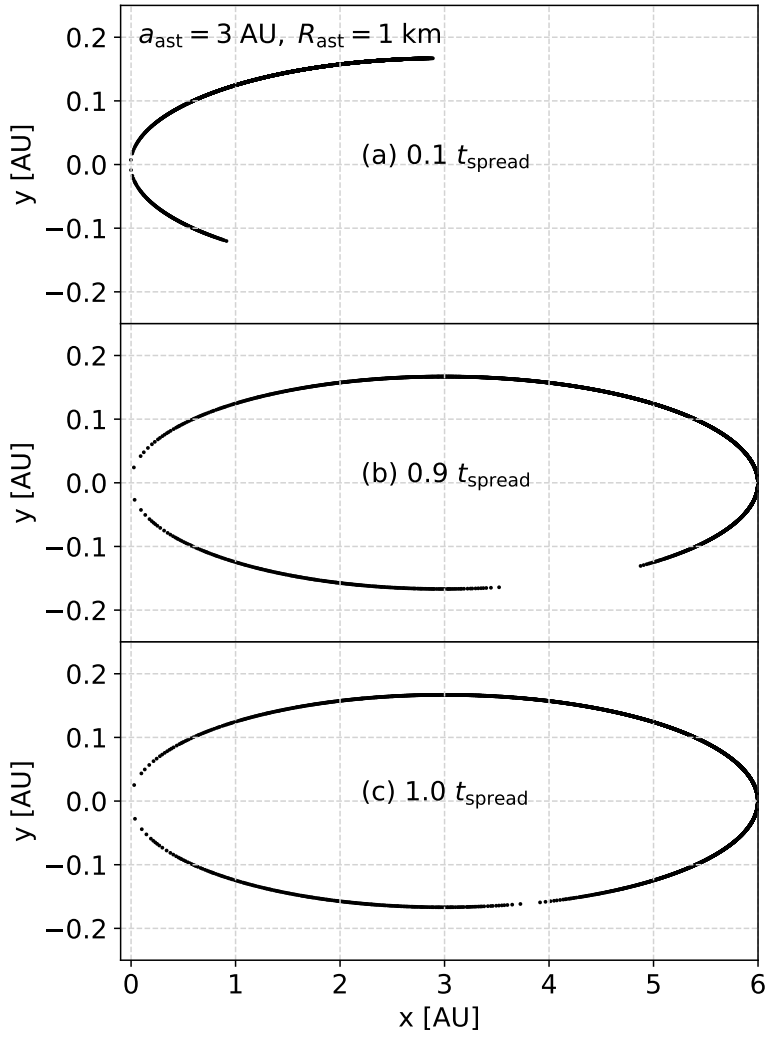

Fig. C.1 Snapshots indicating the spreading of fragments in a tidal disc after the disruption of a small asteroid ($a_{ast} = 3$ AU, $R_{ast} = 1$ km). The inner and outer fragments re-align after nearly precisely one spreading timescale, as defined by Eq. C.7b.

where we used a Maclaurin expansion around $R_{\rm ast}/r_{\rm B} \ll 1$, which is always valid for disruptions around white dwarfs. Next, the derivative of the orbital time $P = 2\pi\sqrt{a/GM_{\rm WD}}$ can be used to specify the corresponding spread in orbital periods ΔP:

$$\Delta P = \frac{dP}{da}\Delta a \tag{C.6a}$$

$$= 3\pi\sqrt{\frac{a_{\rm ast}}{GM_{\rm WD}}}\Delta a. \tag{C.6b}$$

The spreading timescale $t_{\rm spread}$ can be defined as the time required for and outer particle to return to the same true anomaly. The number of orbits required is $N_{\rm spread} = P/\Delta P$, so the spreading timescale can be written as:

$$t_{\rm spread} = \frac{P^2}{\Delta P} \tag{C.7a}$$

$$= \frac{\pi r_{\rm B}^2}{3R_{\rm ast}}\sqrt{\frac{a_{\rm ast}}{GM_{\rm WD}}} \tag{C.7b}$$

$$= 120\ {\rm yr}\left(\frac{a_{\rm ast}}{3\ {\rm AU}}\right)^{\frac{1}{2}}\left(\frac{R_{\rm ast}}{\rm km}\right)^{-1}\left(\frac{r_{\rm B}}{\rm R_\odot}\right)^{2}\left(\frac{M_{\rm WD}}{0.6\ {\rm M_\odot}}\right)^{-\frac{1}{2}}, \tag{C.7c}$$

which is much shorter than typical accretion timescales, but might be comparable to the initial accretion phase. In Fig. C.1, we validate Eq. C.7b with a visual comparison to the position of fragments in a tidal disc at three snapshots in time. The orbital elements of the fragments are given by Eq. 4.6b and their true anomalies are exactly specified as a function of time by Kepler's laws. The filling of the tidal disc agrees well with Eq. C.7b, and outer fragments re-align after nearly exactly one spreading timescale.

C.3 Neglection of heat diffusion during fragment sublimation

In this appendix, we validate the assumption in Section 6.2 that inward heat transport can be neglected in the energy balance of sublimating icy fragments around a white dwarf. The key variable to calculate is the time (δt) that a fragment spends inside the sublimation zone where $T > T_{\rm sub}$ around the star. We begin with an estimation of the distance ($d_{\rm sub}$) for the onset of sublimation, which follows from the equilibrium temperature:

$$d_{\rm sub} = \frac{R_{\rm WD}\sqrt{1-A}}{2}\left(\frac{T_{\rm WD}}{T_{\rm sub}}\right)^2. \tag{C.8}$$

The edge of the sublimation zone has the following eccentric anomaly ($E_{\rm sub}$) and mean anomaly ($M_{\rm sub}$):

$$1 - e\cos\left(E_{\rm sub}\right) = d_{\rm sub}/a \tag{C.9a}$$

$$M_{\rm sub} = E_{\rm sub} - e\sin\left(E_{\rm sub}\right). \tag{C.9b}$$

The time spent in the sublimation zone is given by $\delta t = 2M_{\rm sub}/\bar{\omega}$ with $\bar{\omega} = \sqrt{GM_{\rm WD}/a^3}$. The equations above do not have a general closed form solution, and we instead perform an asymptotic expansion, using the following substitutions:

$$e = 1 - \varepsilon\ ,\ E_{\rm sub} = \delta^{1/2} x_{\rm sub}\ ,\ \lambda = \delta/\varepsilon, \tag{C.10}$$

where ε, δ are both small numbers and $x_{\rm sub}, \lambda$ are order unity. With these substitutions, Eqs. C.9a and C.9b reduce to the following leading order terms in ε:

$$x_{\rm sub} = \sqrt{\frac{2}{\lambda}}\left(\frac{d_{\rm sub}}{a\varepsilon} - 1\right)^{1/2}, \tag{C.11a}$$

$$M_{\rm sub} = \varepsilon^{3/2}\lambda^{1/2} x_{\rm sub}\left(1 + \frac{\lambda x_{\rm sub}^2}{6}\right). \tag{C.11b}$$

Together, the factors λ cancel out, and we find the time spent in the sublimation zone:

$$\delta t_{\rm sub} = \frac{\sqrt{2}\,(1-e)^{3/2}}{3\bar{\omega}}\sqrt{\frac{d_{\rm sub}}{r_{\rm B}} - 1}\left(\frac{d_{\rm sub}}{r_{\rm B}} + 2\right) \tag{C.12}$$

$$= \begin{cases} \frac{\sqrt{2}(1-e)^{3/2}}{\bar{\omega}}\left(\frac{d_{\rm sub}}{r_{\rm B}} - 1\right)^{1/2} & \text{if } \mathrm{d_{sub}} \sim \mathrm{r_B} \\ \frac{\sqrt{2}}{3\bar{\omega}}\left(\frac{d_{\rm sub}}{a}\right)^{\frac{3}{2}} & \text{if } \mathrm{d_{sub}} \gg \mathrm{r_B}, \end{cases} \tag{C.13}$$

where $r_{\rm B} = a(1-e)$. The time spent inside the sublimation zone does not depend on the semi-major axis of the fragment, which cancels out in Eq. C.12.

During the time $\delta t_{\rm sub}$ that the fragment spends inside the sublimation zone, a portion of the heat will conduct inward and penetrate to deeper layers, as described by the spherical heat diffusion equation. A typical estimate of this distance is defined by the so-called skin depth (e.g., Huebner et al., 2006):

$$\delta R_{\rm skin} = \sqrt{\frac{K_{\rm th}\delta t_{\rm sub}}{\pi\rho C_{\rm p}}}. \tag{C.14}$$

In the most interesting scenario of rapid sublimation ($d_{\rm sub} \gg r_{\rm B}$), the skin depth during sublimation is:

$$\delta R_{\rm skin} \simeq 6\ {\rm cm} \left(\frac{T_{\rm WD}}{10^4\ {\rm K}}\right)^{\frac{3}{2}} \left(\frac{T_{\rm sub}}{300\ {\rm K}}\right)^{-\frac{3}{2}} \left(\frac{R_{\rm WD}}{{\rm R}_\oplus}\right)^{\frac{3}{4}} \left(\frac{M_{\rm WD}}{0.6\ {\rm M}_\odot}\right)^{-\frac{1}{4}} \left(\frac{\rho_{\rm frag}}{1\ {\rm g/cm^3}}\right)^{-\frac{1}{2}} \left(\frac{C_{\rm p}}{2\cdot 10^7\ [{\rm cgs}]}\right)^{-\frac{1}{2}} \left(\frac{K_{\rm th}}{2\cdot 10^5\ [{\rm cgs}]}\right)^{\frac{1}{2}} \left(\frac{1-A}{1}\right)^{\frac{3}{8}}, \tag{C.15}$$

where $K_{\rm th}, C_{\rm p}$ are the fragment's average thermal conductivity and heat capacity, normalized to those of crystalline ice at 300 K (Klinger, 1975, 1980). While in the sublimation zone, however, the fragment's radius also shrinks a distance $\delta R_{\rm sub}$ during its pericentre passage. This can be estimated from Eq. 6.3b as:

$$\delta R_{\rm sub} = -\frac{d\bar{R}_{\rm frag}}{dt} P_{\rm frag} \tag{C.16a}$$

$$= \frac{(1-A)\pi\sigma_{\rm sb} T_{\rm WD}^4 R_{\rm WD}^2}{2H_{\rm sub}\rho_{\rm frag}\sqrt{GM_{\rm WD}a_{\rm frag}(1-e_{\rm frag}^2)}} \tag{C.16b}$$

$$\simeq 4\ {\rm cm} \left(\frac{T_{\rm WD}}{10^4\ {\rm K}}\right)^4 \left(\frac{R_{\rm WD}}{{\rm R}_\oplus}\right)^2 \left(\frac{1-A}{1}\right) \left(\frac{r_{\rm B}}{{\rm R}_\odot}\right)^{-\frac{1}{2}} \left(\frac{\rho_{\rm frag}}{1\ {\rm g/cm^3}}\right)^{-1} \left(\frac{H_{\rm sub}}{2.7\cdot 10^{10}\ {\rm erg/g}}\right)^{-1} \left(\frac{M_{\rm WD}}{0.6\ {\rm M}_\odot}\right)^{-\frac{1}{2}}. \tag{C.16c}$$

Since the two values are typically comparable, and because the sublimation of ice is far more energetically expensive than heating it to the sublimation temperature, heat conduction is not expected to alter the picture described in the main text. In fact, the thermal conductivity can be *several orders of magnitude* lower than the quoted value if the fragment is an aggregate of porous pebbles (Gundlach & Blum, 2012; Gundlach et al., 2020), in which case conduction becomes entirely negligible. The opposite is true for rocky fragments, which lose almost no mass by sublimative erosion unless the star exceeds 30,000 K (see Fig. 6.2), causing conduction to become comparatively more important. However, in this case where sublimative erosion is already prevented by re-radiation, a further reduction via inward heat transport only emphasizes this result.

C.4 Radiation pressure around SDSS J0914+1914

The disc around SDSS J0914+1914 is notably depleted in hydrogen relative to oxygen ($\log({\rm H/O}) = -0.29 \pm 0.3$), by about 3 orders of magnitude compared to the lower tropo-

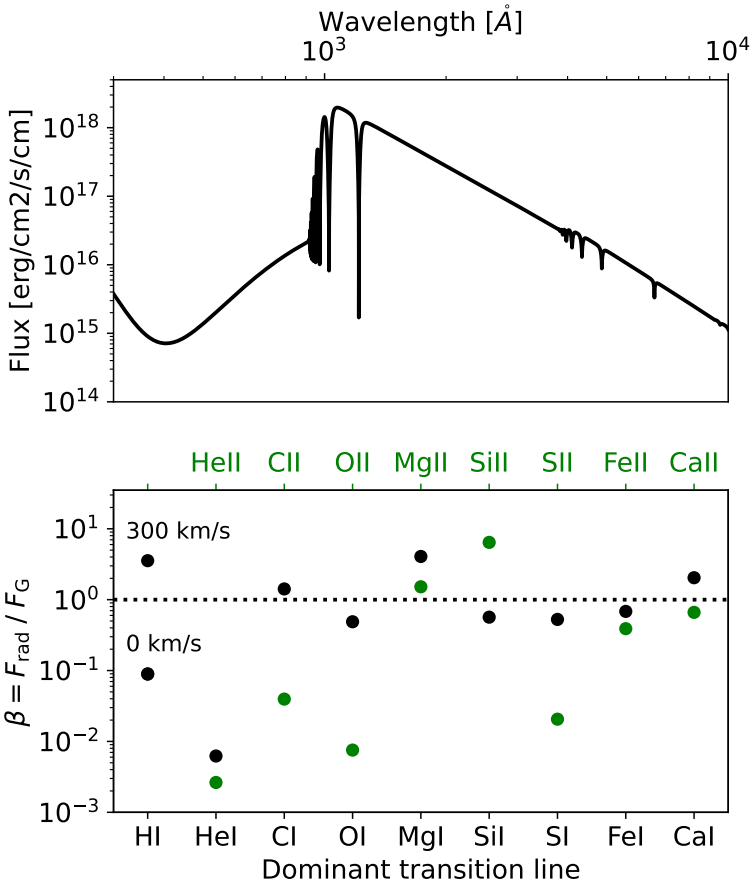

Fig. C.2 Top: model spectrum of WD J0914+191, generated with the model of Koester et al. (2020). Bottom: force ratio of the radiation pressure on atoms and ions around SDSS J0914+1914, relative to gravity. The radiation pressures are calculated at the strongest line for a given state, as compiled by Verner et al. (1994). Neutral hydrogen can experience intense radiation pressure relative to stellar gravity ($\beta \gg 1$), but the radiation pressures on C, Ca, and Mg atoms also exceed unity. Only helium feels a negligible radiation pressure relative to the gravitational force of the star.

spheres of Uranus and Neptune (Moses et al., 2020), and by a factor 3 when compared to the ices of comet 67P/Churyumov-Gerasimenko (Rubin et al., 2019). According to Gänsicke et al. (2019), hydrogen depletion is likely due to the blow-out of hydrogen by the radiation pressure from the white dwarf.

To gauge the importance of radiation pressure on the orbits of hydrogen, helium and other elements around SDSS J0914+1914, we follow the calculations by Shestakova (2015) and Cherenkov et al. (2018). Unlike dust, single atoms interact most strongly with light at wavelengths corresponding to narrow transition lines. For atoms with no velocity relative to the illuminating source, their radiation pressure can be approximated as:

$$F_{\rm rad} = \frac{\pi e^2}{m_{\rm e} c^2} f_{\rm line} I_\nu, \tag{C.17}$$

where $e, m_{\rm e}$ are the electron charge and mass, $f_{\rm line}$ is the oscillator strength of the line and I_ν is the directional radiative energy flux at frequency ν. To gauge whether there is enough radiative interaction to unbind an atom, the ratio of radiative and gravitational forces $\beta = F_{\rm rad}/F_{\rm G}$ are typically compared, with $\beta > 1$ causing ejection. The total radiation pressure of a gas parcel depends on the excitation and ionization states of its atoms, given by the Boltzmann and Saha equations, which requires a good thermodynamic model of the circumstellar disc to include. Given that this geometry is poorly constrained, we simplify the calculation here, and calculate the radiation pressure at the strongest lines for a given ionization level, with wavelengths and oscillator strengths compiled by Verner et al. (1994). The stellar flux is computed with a model spectrum from Koester et al. (2020), which is plotted in the top panel of Fig. C.2.

The importance of radiation pressure relative to gravitation is plotted in Fig. C.2. For neutral hydrogen, we find that the radiation pressure is minimal in the centre of the Ly-α line, but that it overwhelms gravity at typical orthogonal speeds of 300 km/s. Unshielded hydrogen atoms will accelerate away from the star until they are ionized, at which point the radiative force all but disappears (Bourrier & Lecavelier des Etangs, 2013). The fraction of hydrogen that remains bound to the white dwarf is determined by the relative rates of ionization and acceleration and by the self-shielding of the gas. Furthermore, we find that the neutral states of C, N, Ca, Mg, and Fe are also characterized by values of β near or exceeding unity. In contrast, helium is almost entirely unaffected, with $\beta \ll 1$. We conclude, therefore, that the radiation pressure from the star is unlikely to be the cause of the depleted helium around SDSS J0914+1914, which reinforces the proposition that a stricter upper limit or a detection of helium in the photosphere can distinguish between accretion from an ice giant and the scenario where volatiles and refractories accrete asynchronously.

C.5 Posterior distributions of accretion state and excess oxygen

Fig. C.3 indicates the posterior distribution of the accretion states for all white dwarfs contained in our sample, ordered by their diffusion timescales (short-long). The accretion states of white dwarfs with hydrogen-dominated atmospheres are well-constrained, as their short diffusion times make anything except steady-state accretion unlikely. White dwarfs with helium-dominated atmospheres require the abundances of many elements to be known to constrain the accretion state. In general, older stars with longer diffusion timescales are more likely to be in a post-accretion (declining) state. In a few cases, for instance WD1232+563, the ratios of photospheric abundances imply that an early accretion state (build-up) is likely, where the white dwarf has been accreting for less than three diffusion timescales.

Fig. C.4 shows the corresponding posterior distribution of the oxygen excesses for the white dwarfs in our sample. For most white dwarfs with reported oxygen abundances or upper limits, the relative abundances and/or the accretion state are too poorly constrained to pinpoint the oxygen excess with any certainty. In three cases, however, oxygen excesses are found with greater than 2σ significance. No systems were found to be reduced in oxygen with the same statistical threshold.

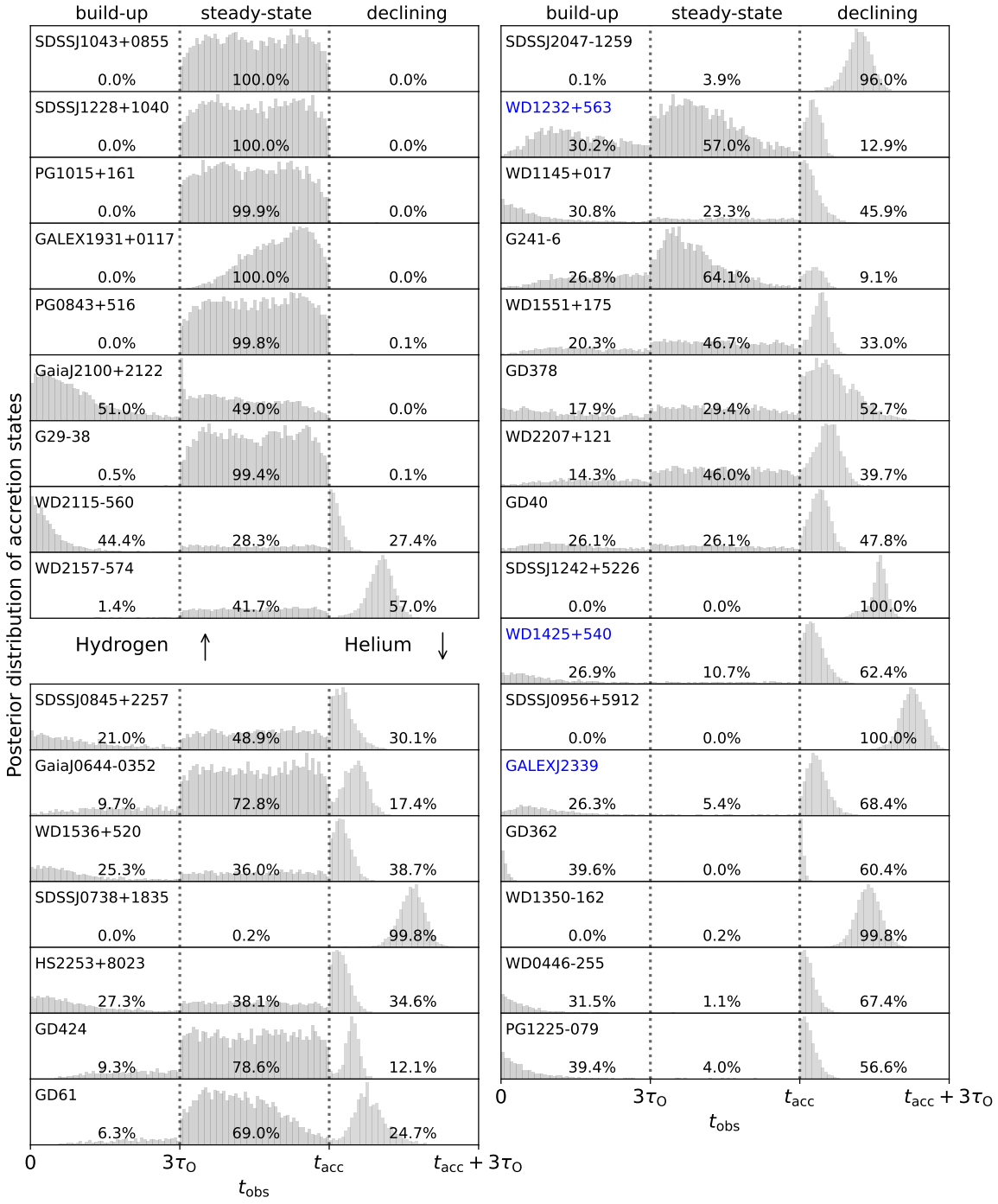

Fig. C.3 Posterior distribution of the accretion states in our runs with `PyllutedWD`, ordered by their diffusion timescales (short-long). The histograms for the build-up and declining states share the same scaling on their x-axis from 0 to 3 oxygen diffusion timescales. The histograms of steady-state accretion in the middle panels have a custom x-scale, depending on the modelled length of the accretion event ($t_{\rm acc}$). The blue labels indicate systems with a significant oxygen excess above 2σ.

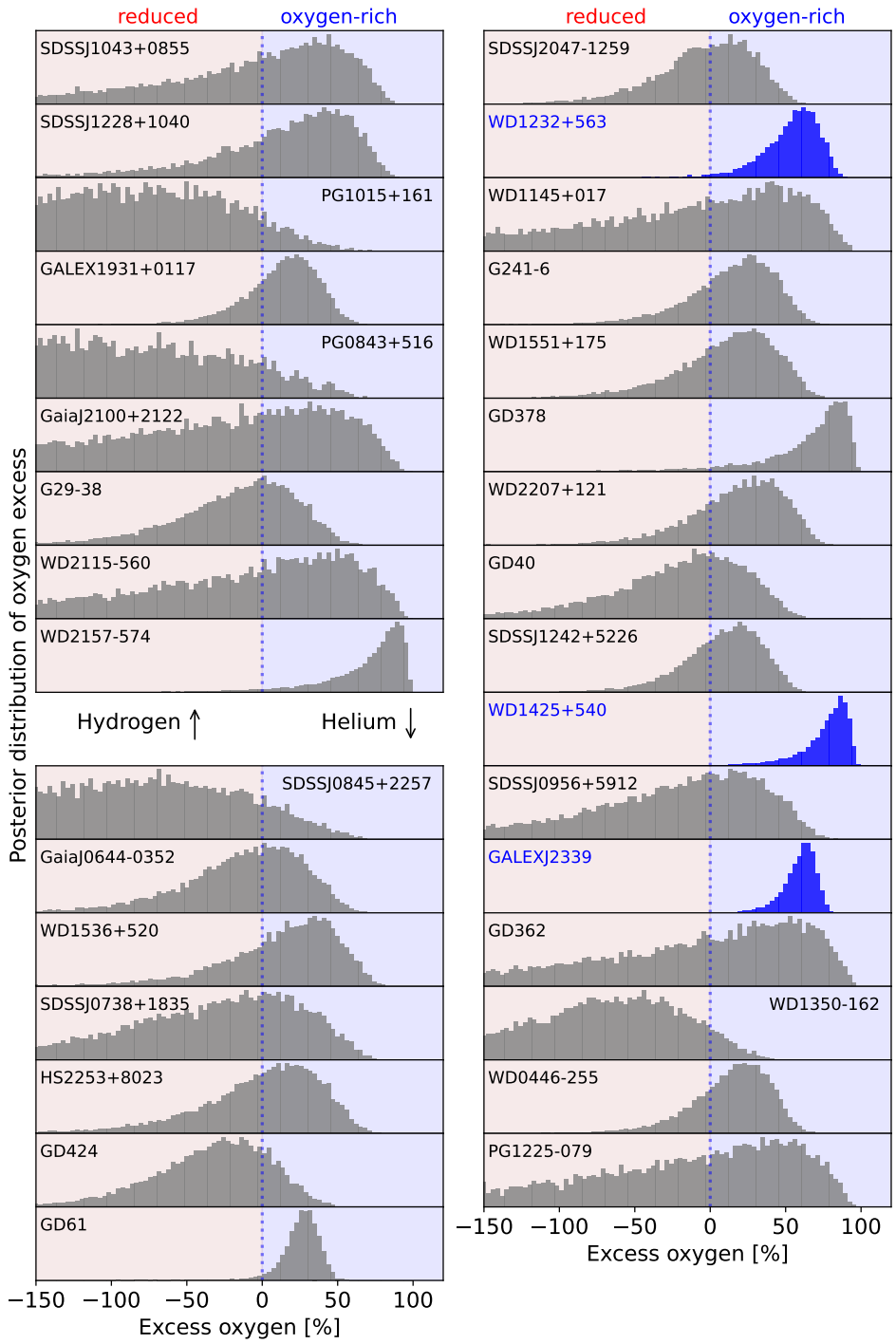

Fig. C.4 Posterior distribution of the oxygen excess in our runs with `PyllutedWD`, ordered by their diffusion timescales (short-long). The blue histograms and labels indicate systems with a significant (2σ) oxygen excess. No systems were found to be reduced in oxygen with the same threshold for significance.

C.6 White dwarf sample used in chapter 5

Table C.1 Properties and abundances of white dwarfs in the sample for chapter 5, ordered by type and effective temperature

System	Type	$T_{\rm eff}$ [K]	Mass [$M_\odot$]	$\log(g/{\rm ms}^{-2})$	log(Fe/Hx)	log(Mg/Hx)	log(Si/Hx)	log(Ca/Hx)
GaiaJ2100+2122$^{(hh,\overline{dd})}$	H	25565.0	0.693	8.1	-4.96±0.1	-5.08±0.1	-5.13±0.12	-6.23±0.13
GaiaJ2100+2122$^{(hh,\overline{dd})}$	H	25565.0	0.693	8.1	-4.96±0.2	-5.12±0.2	-5.12±0.2	-6.23±0.2
PG0843+516$^{(f,\overline{u})}$	H	22412.0	0.577	7.902	-3.84±0.18	-4.82±0.2	-4.59±0.12	-6.26±0.2
GALEX1931+0117$^{(q,\overline{d})}$	H	21457.0	0.573	7.9	-4.43±0.09	-4.42±0.06	-4.24±0.07	-6.11±0.05
SDSSJ1228+1040$^{(j,\overline{e})}$	H	20900.0	0.73	8.15	-5.2±0.3	-5.2±0.2	-5.2±0.2	-5.94±0.2
PG1015+161$^{(e,\overline{u})}$	H	19226.0	0.642	8.04	-4.92±0.2	-5.6±0.2	-5.42±0.21	-6.4±0.2
SDSSJ1043+0855$^{(j,\overline{i})}$	H	18320.0	0.65	8.05	-6.15±0.3	-5.11±0.2	-5.33±0.5	-5.96±0.2
WD0611-6931$^{(hh,\overline{dd})}$	H	17750.0	0.702	8.14	-3.77±0.1	-4.67±0.1	-4.6±0.21	-6.19±0.1
HE0106-3253$^{(d,a,\overline{u})}$	H	17350.0	0.62	8.12	-4.7±0.06	-5.57±0.2	-5.48±0.05	-5.93±0.11
GD56$^{(b,\overline{u})}$	H	15270.0	0.67	8.09	-5.44±0.2	-5.55±0.2	-5.69±0.2	-6.86±0.2
WD1145+288$^{(d,l,\overline{u})}$	H	12140.0	0.685	8.14	-5.43±0.2	-6.0±0.2	<-4.7	-6.88±0.08
G29-38$^{(q,\overline{m})}$	H	11800.0	0.85	8.4	-5.9±0.1	-5.77±0.13	-5.6±0.17	-6.58±0.12
WD2105-820$^{(aa,\overline{v})}$	H	10890.0	0.86	8.41	-6.0±0.2	-6.0±0.2	<-5.5	-8.2±0.1
GaiaJ1814-7355$^{(hh,\overline{dd})}$	H	10190.0	0.58	7.996	-6.06±0.19	-6.14±0.08	-	-7.22±0.15
WDJ1814-7354$^{(dd,\overline{z})}$	H	10090.0	0.59	8.0	-6.06±0.19	-6.14±0.08	<-6.0	-7.22±0.15
WD2115-560$^{(aa,\overline{v})}$	H	9600.0	0.58	7.97	-6.4±0.1	-6.4±0.1	-6.2±0.1	-7.4±0.1
WD1257+278$^{(u,b,\tilde{i})}$	H	8609.0	0.73	8.24	-7.47±0.09	-7.49±0.08	-	-8.38±0.06
WD0354+463$^{(u,b,\tilde{i})}$	H	8240.0	0.57	7.96	-7.13±0.11	-6.7±0.05	-	-8.2±0.03
NLTT25792$^{(t,u,\tilde{i})}$	H	7903.0	0.618	8.04	-7.16±0.04	-7.24±0.05	-	-8.07±0.06
G166-58$^{(b,\overline{u})}$	H	7390.0	0.58	7.99	-8.22±0.13	-8.06±0.05	<-8.2	-9.33±0.08
WD1455+298$^{(u,\tilde{i})}$	H	7383.0	0.589	7.97	-8.4±0.08	-8.03±0.06	-	-9.51±0.03
G74-7$^{(u,\tilde{i})}$	H	7306.0	0.572	8.06	-8.03±0.09	-7.79±0.06	-	-9.05±0.04
WD2157-574$^{(aa,\overline{v})}$	H	7010.0	0.63	8.06	-7.3±0.1	-7.0±0.1	-7.0±0.1	-8.1±0.1
NLTT 6390$^{(t,\overline{h})}$	H	6040.0	0.53	7.9	-8.57±0.11	-8.66±0.2	-	-10.0±0.04
NLTT 1675$^{(t,\overline{h})}$	H	6020.0	0.61	8.04	-8.63±0.13	-8.56±0.12	-	-9.53±0.03
NLTT43806$^{(e,\overline{c})}$	H	5838.0	0.704	8.186	-7.8±0.17	-7.1±0.13	-7.2±0.14	-7.9±0.19
NLTT 19686$^{(y,\overline{p})}$	H	5230.0	0.54	7.93	-8.93±0.14	-8.2±0.3	-	-8.7±0.04
WD1536+520$^{(o,\overline{s})}$	He	20800.0	0.58	7.96	-4.5±0.15	-4.06±0.15	-4.32±0.15	-5.28±0.15
SDSSJ0845+2257$^{(v,\overline{n})}$	He	19780.0	0.679	8.18	-4.6±0.2	-4.7±0.15	-4.8±0.3	-5.95±0.1
GaiaJ0644-0352$^{(hh,\overline{dd})}$	He	18350.0	0.704	8.18	-6.46±0.1	-5.74±0.1	-5.98±0.1	-6.77±0.1
GaiaJ0644-0352$^{(hh,\overline{dd})}$	He	18350.0	0.704	8.18	-6.46±0.16	-5.75±0.15	-5.98±0.1	-6.74±0.18
SDSSJ2047-1259$^{(bb,cc,\overline{y})}$	He	17970.0	0.617	8.04	-6.4±0.2	-5.6±0.1	-5.6±0.1	-6.9±0.1
GD61$^{(c,\overline{k})}$	He	17280.0	0.71	8.2	-7.6±0.07	-6.69±0.05	-6.82±0.04	-7.9±0.06
GD424$^{(bb,\overline{x})}$	He	16560.0	0.77	8.25	-5.53±0.12	-5.15±0.04	-5.29±0.04	-6.15±0.05
GD378$^{(ee,\overline{bb})}$	He	15620.0	0.551	7.93	-7.51±0.36	-7.44±0.2	-7.49±0.12	-8.7±0.76
G241-6$^{(p,n,\overline{j})}$	He	15300.0	0.71	8.0	-6.82±0.14	-6.26±0.1	-6.62±0.2	-7.3±0.2
WD1551+175$^{(d,o,n,\overline{u})}$	He	14756.0	0.57	8.02	-6.6±0.1	-6.29±0.05	-6.33±0.1	-6.93±0.07
WD2207+121$^{(m,\overline{u})}$	He	14752.0	0.57	7.97	-6.46±0.13	-6.15±0.1	-6.17±0.11	-7.4±0.08
WD1145+017$^{(k,\overline{w})}$	He	14500.0	0.656	8.11	-5.61±0.2	-5.91±0.2	-5.89±0.2	-7.0±0.2
WD1425+540$^{(n,\overline{r})}$	He	14490.0	0.56	7.95	-8.15±0.14	-8.16±0.2	-8.03±0.31	-9.26±0.1
HS2253+8023$^{(ee,\overline{b})}$	He	14400.0	0.84	8.4	-6.17±0.17	-6.1±0.14	-6.27±0.13	-6.99±0.11
SDSSJ0738+1835$^{(i,\overline{g})}$	He	13950.0	0.841	8.4	-4.98±0.09	-4.68±0.07	-4.9±0.16	-6.23±0.15
GALEXJ2339$^{(ee,\overline{bb})}$	He	13735.0	0.548	7.93	-6.99±0.3	-6.58±0.14	-6.59±0.08	-8.03±0.75
GD40$^{(m,\overline{j})}$	He	13594.0	0.6	8.02	-6.47±0.12	-6.2±0.16	-6.44±0.3	-6.9±0.2
SDSSJ1242+5226$^{(w,\overline{o})}$	He	13000.0	0.59	8.0	-5.9±0.15	-5.26±0.15	-5.3±0.06	-6.53±0.1
WD1232+563$^{(m,\overline{u})}$	He	11787.0	0.77	8.3	-6.45±0.11	-6.09±0.05	-6.36±0.13	-7.69±0.05

Table C.1 – continued on next page

WD1350-162$^{(aa,\overline{v})}$	He	11640.0	0.6	8.02	-7.1±0.1	-6.8±0.1	-7.3±0.2	-8.7±0.1
PG1225-079$^{(g,\overline{f,l})}$	He	10800.0	0.58	8.0	-7.42±0.07	-7.5±0.2	-7.45±0.1	-8.06±0.03
WD0446-255$^{(aa,\overline{v})}$	He	10120.0	0.58	8.0	-6.9±0.1	-6.6±0.1	-6.5±0.1	-7.4±0.1
GD362$^{(r,s,\overline{a})}$	He	10057.0	0.551	7.95	-5.65±0.1	-5.98±0.25	-5.84±0.3	-6.24±0.1
WD0449-259$^{(aa,\overline{v})}$	He	9850.0	0.61	8.04	-7.9±0.2	-8.3±0.4	<-7.3	-9.1±0.1
WD2216-657$^{(aa,\overline{v})}$	He	9120.0	0.61	8.05	-8.0±0.2	-7.1±0.1	<-7.0	-9.0±0.1
SDSSJ0956+5912$^{(z,\overline{q})}$	He	8843.0	0.683	8.168	-6.2±0.1	-5.2±0.1	-	-7.1±0.1
SDSSJ1340+2702$^{(z,\overline{q})}$	He	8413.0	0.6	8.0	-5.6±0.1	-5.1±0.1	-	-7.0±0.1
WD0122-227$^{(aa,\overline{v})}$	He	8380.0	0.61	8.06	-8.5±0.2	-8.5±0.4	<-7.6	-10.1±0.1
SDSSJ0956+5912$^{(ff,\overline{cc})}$	He	8100.0	0.59	8.02	-6.9±0.1	-5.5±0.1	-5.7±0.2	-7.3±0.05
SDSSJ0046+2717$^{(z,\overline{q})}$	He	8053.0	0.879	8.465	-6.3±0.3	-5.4±0.2	-	-7.2±0.2
SDSSJ1038-0036$^{(z,\overline{q})}$	He	7996.0	0.6	8.0	-6.9±0.1	-6.3±0.1	-	-7.4±0.1
SDSSJ1158+4712$^{(z,\overline{q})}$	He	7840.0	0.6	8.0	-6.9±0.2	-6.7±0.1	-	-8.3±0.1
SDSSJ0744+2701$^{(z,\overline{q})}$	He	7829.0	0.676	8.16	-7.0±0.2	-6.7±0.2	-	-7.8±0.2
SDSSJ1041+3432$^{(z,\overline{q})}$	He	7728.0	0.769	8.301	-6.8±0.2	-6.8±0.2	-	-8.0±0.2
SDSSJ1308+0957$^{(z,\overline{q})}$	He	7692.0	0.6	8.0	-6.9±0.3	-7.0±0.2	-	-8.1±0.2
SDSSJ1356+0236$^{(z,\overline{q})}$	He	7662.0	0.595	8.028	-6.7±0.2	-6.3±0.1	-	-8.0±0.1
SDSSJ0816+2330$^{(z,\overline{q})}$	He	7642.0	0.6	8.0	-6.5±0.3	-6.0±0.3	-	-7.6±0.3
SDSSJ1234+5208$^{(z,\overline{q})}$	He	7627.0	0.637	8.098	-6.3±0.1	-5.7±0.1	-	-7.5±0.1
SDSSJ1038-0036$^{(ff,\overline{cc})}$	He	7560.0	0.61	8.06	-7.4±0.1	-6.6±0.1	-6.4±0.2	-7.6±0.05
SDSSJ0946+2024$^{(z,\overline{q})}$	He	7540.0	0.6	8.0	-6.9±0.2	-6.5±0.2	-	-8.0±0.2
SDSSJ2319+3018$^{(z,\overline{q})}$	He	7478.0	0.6	8.0	-7.3±0.3	-7.2±0.3	-	-8.5±0.3
SDSSJ0252+0054$^{(z,\overline{q})}$	He	7478.0	0.596	8.031	-7.2±0.2	-7.1±0.2	-	-8.5±0.2
SDSSJ1319+3641$^{(z,\overline{q})}$	He	7464.0	0.763	8.294	-7.4±0.3	-7.2±0.2	-	-8.6±0.3
SDSSJ1150+4928$^{(z,\overline{q})}$	He	7417.0	0.694	8.189	-7.9±0.5	-7.5±0.5	-	-9.1±0.3
SDSSJ1320+0204$^{(z,\overline{q})}$	He	7356.0	0.6	8.0	-7.1±0.3	-7.0±0.3	-	-8.3±0.3
SDSSJ1507+4034$^{(z,\overline{q})}$	He	7304.0	0.6	8.0	-6.8±0.2	-6.3±0.1	-	-8.0±0.2
SDSSJ1144+3720$^{(z,\overline{q})}$	He	7280.0	0.446	7.768	-7.6±0.4	-7.0±0.2	-	-8.5±0.2
SDSSJ0901+0752$^{(z,\overline{q})}$	He	7263.0	0.57	7.989	-6.1±0.2	-5.8±0.2	-	-7.1±0.2
SDSSJ0902+1004$^{(z,\overline{q})}$	He	7250.0	0.6	8.0	-8.19±0.22	-7.29±0.24	-	-8.25±0.22
SDSSJ0143+0113$^{(z,\overline{q})}$	He	7229.0	0.687	8.178	-7.0±0.1	-6.6±0.1	-	-8.2±0.1
SDSSJ2352+3344$^{(z,\overline{q})}$	He	7200.0	0.6	8.0	-7.1±0.3	-6.9±0.2	-	-8.3±0.2
SDSSJ1612+3534$^{(z,\overline{q})}$	He	7181.0	0.6	8.0	-7.3±0.5	-7.3±0.3	-	-8.5±0.5
SDSSJ1058+3143$^{(z,\overline{q})}$	He	7173.0	0.675	8.159	-7.7±0.2	-7.4±0.2	-	-9.0±0.1
SDSSJ1149+0519$^{(z,\overline{q})}$	He	7173.0	0.525	7.914	-7.5±0.2	-7.3±0.1	-	-8.2±0.1
SDSSJ0842+1406$^{(z,\overline{q})}$	He	7075.0	0.567	7.985	-7.4±0.1	-7.2±0.1	-	-8.4±0.1
SDSSJ1443+5833$^{(z,\overline{q})}$	He	7061.0	0.6	8.0	-7.3±0.2	-7.1±0.1	-	-8.5±0.2
SDSSJ1405+1549$^{(z,\overline{q})}$	He	7055.0	0.621	8.073	-7.3±0.1	-6.9±0.1	-	-8.5±0.1
SDSSJ1445+0913$^{(z,\overline{q})}$	He	7035.0	0.6	8.0	-6.6±0.2	-6.2±0.1	-	-7.7±0.2
SDSSJ0806+3055$^{(z,\overline{q})}$	He	7017.0	0.6	8.0	-7.0±0.3	-6.8±0.2	-	-7.9±0.3
SDSSJ0117+0021$^{(z,\overline{q})}$	He	6994.0	0.608	8.052	-7.6±0.1	-7.2±0.1	-	-8.8±0.1
SDSSJ2238+0213$^{(z,\overline{q})}$	He	6986.0	0.6	8.0	-7.5±0.2	-7.4±0.2	-	-8.6±0.2
SDSSJ0447+1124$^{(z,\overline{q})}$	He	6966.0	0.492	7.858	-7.7±0.3	-7.3±0.3	-	-9.0±0.3
SDSSJ1443+3014$^{(z,\overline{q})}$	He	6955.0	0.6	8.0	-7.1±0.2	-6.5±0.2	-	-8.1±0.3
SDSSJ0150+1354$^{(z,\overline{q})}$	He	6953.0	0.741	8.262	-6.8±0.2	-6.0±0.1	-	-7.7±0.2
SDSSJ0010-0430$^{(z,\overline{q})}$	He	6903.0	0.651	8.122	-7.0±0.1	-6.7±0.1	-	-8.5±0.1
SDSSJ0818+1247$^{(z,\overline{q})}$	He	6895.0	0.6	8.0	-7.8±0.4	-7.2±0.3	-	-9.0±0.3
SDSSJ1112+0700$^{(z,\overline{q})}$	He	6891.0	0.497	7.867	-8.5±0.5	-7.6±0.3	-	-9.7±0.2
SDSSJ1554+1735$^{(z,\overline{q})}$	He	6847.0	0.721	8.231	-7.6±0.1	-7.1±0.1	-	-8.4±0.1
SDSSJ0806+4058$^{(z,\overline{q})}$	He	6808.0	0.6	8.0	-7.49±0.08	-7.38±0.12	-	-8.49±0.08
SDSSJ1134+1542$^{(z,\overline{q})}$	He	6806.0	0.6	8.0	-7.3±0.4	-6.9±0.1	-	-8.5±0.1
SDSSJ1549+2633$^{(z,\overline{q})}$	He	6794.0	0.614	8.063	-8.0±0.2	-7.9±0.1	-	-9.6±0.2
SDSSJ0252-0401$^{(z,\overline{q})}$	He	6773.0	0.53	7.924	-8.0±0.2	-6.8±0.1	-	-8.9±0.1
SDSSJ1017+2419$^{(z,\overline{q})}$	He	6772.0	0.84	8.409	-7.3±0.2	-6.7±0.2	-	-8.4±0.2

Table C.1 – continued on next page

SDSSJ0148-0112$^{(z,\bar{q})}$	He	6760.0	0.6	8.0	-7.9±0.5	-7.3±0.3	-	-9.0±0.2
SDSSJ0144+0305$^{(z,\bar{q})}$	He	6753.0	0.6	8.0	-7.2±0.3	-7.1±0.3	-	-8.3±0.3
SDSSJ0908+4119$^{(z,\bar{q})}$	He	6746.0	0.6	8.0	-7.1±0.3	-6.8±0.2	-	-8.7±0.3
SDSSJ1626+3303$^{(z,\bar{q})}$	He	6715.0	0.6	8.0	-7.5±0.3	-7.1±0.1	-	-8.6±0.2
SDSSJ1329+1301$^{(z,\bar{q})}$	He	6706.0	0.381	7.636	-8.0±0.3	-7.4±0.1	-	-8.9±0.2
SDSSJ1158+1845$^{(z,\bar{q})}$	He	6696.0	0.6	8.04	-7.4±0.2	-6.4±0.1	-	-8.6±0.2
SDSSJ1220+0929$^{(z,\bar{q})}$	He	6677.0	0.6	8.0	-7.4±0.1	-6.8±0.1	-	-8.4±0.1
SDSSJ0929+4247$^{(z,\bar{q})}$	He	6676.0	0.489	7.853	-7.1±0.2	-6.5±0.2	-	-8.3±0.2
SDSSJ0937+5228$^{(z,\bar{q})}$	He	6660.0	0.585	8.015	-7.4±0.2	-6.9±0.1	-	-8.4±0.1
SDSSJ1624+3310$^{(z,\bar{q})}$	He	6654.0	0.6	8.0	-8.0±0.4	-7.2±0.1	-	-9.2±0.3
SDSSJ1500+2315$^{(z,\bar{q})}$	He	6630.0	0.6	8.0	-7.0±0.4	-6.6±0.2	-	-8.2±0.4
SDSSJ0843+5614$^{(z,\bar{q})}$	He	6624.0	0.761	8.292	-7.5±0.2	-6.9±0.2	-	-8.7±0.2
SDSSJ0744+4408$^{(z,\bar{q})}$	He	6612.0	0.6	8.0	-7.5±0.2	-7.4±0.2	-	-8.6±0.2
SDSSJ1211+2326$^{(z,\bar{q})}$	He	6609.0	1.005	8.663	-6.9±0.2	-6.7±0.1	-	-8.3±0.2
SDSSJ1157+6138$^{(z,\bar{q})}$	He	6607.0	0.6	8.0	-8.2±0.5	-7.6±0.5	-	-9.3±0.3
SDSSJ0234-0510$^{(z,\bar{q})}$	He	6601.0	0.6	8.0	-7.3±0.2	-6.9±0.2	-	-8.5±0.2
SDSSJ1546+3009$^{(z,\bar{q})}$	He	6600.0	0.6	8.0	-7.19±0.12	-7.19±0.15	-	-8.4±0.12
SDSSJ1428+4403$^{(z,\bar{q})}$	He	6574.0	0.614	8.064	-8.9±0.2	-7.9±0.1	-	-9.5±0.1
SDSSJ0906+1141$^{(z,\bar{q})}$	He	6556.0	0.6	8.0	-7.3±0.2	-6.9±0.2	-	-8.5±0.2
SDSSJ1610+4006$^{(z,\bar{q})}$	He	6552.0	0.6	8.0	-7.2±0.2	-7.3±0.1	-	-8.7±0.3
SDSSJ0053+3115$^{(z,\bar{q})}$	He	6548.0	0.6	8.0	-7.6±0.5	-7.6±0.5	-	-8.8±0.5
SDSSJ1347+1415$^{(z,\bar{q})}$	He	6520.0	0.696	8.194	-7.3±0.2	-7.1±0.1	-	-8.6±0.2
SDSSJ1421+1843$^{(z,\bar{q})}$	He	6517.0	0.562	7.978	-7.3±0.2	-6.7±0.1	-	-8.5±0.1
SDSSJ2333+1058$^{(z,\bar{q})}$	He	6515.0	0.6	8.0	-7.6±0.4	-7.0±0.2	-	-8.7±0.3
SDSSJ2235-0056$^{(z,\bar{q})}$	He	6514.0	0.758	8.288	-7.2±0.2	-7.1±0.1	-	-8.4±0.2
SDSSJ1540+5352$^{(z,\bar{q})}$	He	6500.0	0.6	8.0	-7.5±0.3	-6.8±0.1	-	-8.7±0.3
SDSSJ1218+0023$^{(z,\bar{q})}$	He	6500.0	0.776	8.314	-8.5±0.3	-7.8±0.2	-	-9.2±0.2
SDSSJ1616+3303$^{(z,\bar{q})}$	He	6491.0	0.569	7.991	-7.1±0.2	-6.7±0.1	-	-8.2±0.1
SDSSJ1303+4055$^{(z,\bar{q})}$	He	6481.0	0.618	8.071	-7.9±0.3	-7.2±0.2	-	-8.7±0.3
SDSSJ0002+3209$^{(z,\bar{q})}$	He	6466.0	0.737	8.257	-7.9±0.2	-7.4±0.2	-	-9.1±0.2
SDSSJ1339+2643$^{(z,\bar{q})}$	He	6452.0	0.622	8.077	-8.4±0.2	-7.6±0.1	-	-9.0±0.2
SDSSJ0830-0319$^{(z,\bar{q})}$	He	6424.0	0.428	7.736	-8.2±0.1	-8.2±0.1	-	-9.4±0.1
SDSSJ1604+1830$^{(z,\bar{q})}$	He	6421.0	0.636	8.1	-8.5±0.3	-8.4±0.2	-	-9.6±0.1
SDSSJ1254+3551$^{(z,\bar{q})}$	He	6417.0	0.597	8.036	-8.1±0.2	-7.6±0.2	-	-9.7±0.2
SDSSJ1038+0432$^{(z,\bar{q})}$	He	6363.0	0.6	8.0	-7.0±0.2	-6.6±0.2	-	-7.6±0.3
SDSSJ1430-0151$^{(z,\bar{q})}$	He	6344.0	0.621	8.076	-6.4±0.1	-6.0±0.1	-	-7.6±0.1
SDSSJ2330+2805$^{(z,\bar{q})}$	He	6344.0	0.6	8.0	-8.1±0.4	-7.5±0.2	-	-9.3±0.2
SDSSJ1024+4531$^{(z,\bar{q})}$	He	6339.0	0.803	8.356	-7.6±0.2	-7.3±0.2	-	-8.4±0.2
SDSSJ0933+6334$^{(z,\bar{q})}$	He	6337.0	0.6	8.0	-7.0±0.3	-7.0±0.3	-	-8.6±0.3
SDSSJ1448+1047$^{(z,\bar{q})}$	He	6331.0	0.682	8.173	-7.8±0.2	-7.5±0.1	-	-9.1±0.2
SDSSJ0939+4136$^{(z,\bar{q})}$	He	6321.0	0.848	8.422	-6.6±0.2	-6.8±0.2	-	-8.1±0.2
SDSSJ1102+2827$^{(z,\bar{q})}$	He	6320.0	0.6	8.0	-6.7±0.4	-6.2±0.2	-	-7.8±0.4
SDSSJ1230+3143$^{(z,\bar{q})}$	He	6310.0	0.398	7.676	-8.3±0.3	-8.1±0.3	-	-9.6±0.3
SDSSJ0047+1628$^{(z,\bar{q})}$	He	6300.0	0.6	8.0	-6.7±0.2	-6.8±0.2	-	-8.0±0.2
SDSSJ0851+1543$^{(z,\bar{q})}$	He	6284.0	0.649	8.12	-8.2±0.2	-7.4±0.2	-	-8.6±0.1
SDSSJ1404+3620$^{(z,\bar{q})}$	He	6284.0	0.709	8.216	-8.3±0.2	-7.3±0.1	-	-8.7±0.1
SDSSJ0948+3008$^{(z,\bar{q})}$	He	6284.0	0.228	7.21	-8.1±0.2	-7.9±0.2	-	-9.1±0.2
SDSSJ1014+2827$^{(z,\bar{q})}$	He	6269.0	0.6	8.0	-6.5±0.3	-6.4±0.2	-	-7.9±0.3
SDSSJ1257-0310$^{(z,\bar{q})}$	He	6269.0	0.6	8.0	-7.4±0.2	-7.1±0.1	-	-8.6±0.1
SDSSJ0201+2015$^{(z,\bar{q})}$	He	6250.0	0.63	8.091	-8.0±0.2	-7.3±0.2	-	-9.0±0.2
SDSSJ0108-0537$^{(z,\bar{q})}$	He	6250.0	0.241	7.256	-7.9±0.3	-8.2±0.3	-	-8.5±0.3
SDSSJ1549+1906$^{(z,\bar{q})}$	He	6246.0	0.6	8.0	-7.3±0.3	-7.0±0.1	-	-8.7±0.2
SDSSJ0116+2050$^{(z,\bar{q})}$	He	6245.0	0.6	8.0	-7.6±0.1	-7.4±0.1	-	-8.8±0.1
SDSSJ2238-0113$^{(z,\bar{q})}$	He	6228.0	0.6	8.0	-8.0±0.2	-7.6±0.2	-	-9.4±0.2

Table C.1 – continued on next page

SDSSJ1019+3535$^{(z,\overline{q})}$	He	6224.0	0.6	8.0	-7.9±0.4	-7.0±0.4	-	-8.8±0.4
SDSSJ1158+5448$^{(z,\overline{q})}$	He	6213.0	0.6	8.0	-7.8±0.4	-7.3±0.2	-	-9.0±0.3
SDSSJ0114+3505$^{(z,\overline{q})}$	He	6209.0	0.6	8.0	-7.1±0.1	-7.0±0.1	-	-8.4±0.1
SDSSJ1543+2024$^{(z,\overline{q})}$	He	6206.0	0.6	8.0	-7.6±0.4	-7.1±0.2	-	-8.7±0.2
SDSSJ1524+4049$^{(z,\overline{q})}$	He	6203.0	0.701	8.203	-7.5±0.2	-7.1±0.1	-	-8.4±0.1
SDSSJ1314+3748$^{(z,\overline{q})}$	He	6201.0	0.819	8.379	-7.1±0.4	-6.9±0.2	-	-8.2±0.4
SDSSJ1534+1242$^{(z,\overline{q})}$	He	6197.0	0.6	8.0	-6.7±0.3	-6.9±0.2	-	-7.9±0.3
SDSSJ1356+2416$^{(z,\overline{q})}$	He	6173.0	0.58	8.01	-8.2±0.2	-7.3±0.2	-	-9.1±0.2
SDSSJ1336+3547$^{(z,\overline{q})}$	He	6172.0	0.609	8.057	-7.9±0.1	-7.1±0.1	-	-8.9±0.1
SDSSJ1005+2244$^{(z,\overline{q})}$	He	6165.0	0.6	8.0	-7.8±0.5	-7.9±0.5	-	-9.1±0.4
SDSSJ2340+0817$^{(z,\overline{q})}$	He	6151.0	0.661	8.141	-7.2±0.3	-7.4±0.3	-	-8.7±0.2
SDSSJ1033+1809$^{(z,\overline{q})}$	He	6147.0	0.743	8.267	-7.6±0.3	-7.7±0.3	-	-8.6±0.3
SDSSJ2109-0039$^{(z,\overline{q})}$	He	6132.0	0.572	7.997	-7.6±0.4	-7.7±0.4	-	-8.8±0.5
SDSSJ1542+4650$^{(z,\overline{q})}$	He	6130.0	0.744	8.269	-6.9±0.1	-6.5±0.1	-	-8.1±0.2
SDSSJ2357+2348$^{(z,\overline{q})}$	He	6117.0	0.6	8.0	-7.8±0.3	-7.3±0.1	-	-9.2±0.1
SDSSJ0158-0942$^{(z,\overline{q})}$	He	6115.0	0.567	7.99	-8.8±0.5	-8.7±0.5	-	-9.9±0.2
SDSSJ1024+1014$^{(z,\overline{q})}$	He	6105.0	0.6	8.0	-6.6±0.3	-6.1±0.3	-	-7.7±0.3
SDSSJ0044+0418$^{(z,\overline{q})}$	He	6104.0	0.711	8.22	-8.4±0.2	-8.3±0.3	-	-9.8±0.1
SDSSJ1330+3029$^{(z,\overline{q})}$	He	6100.0	0.6	8.0	-7.3±0.06	-7.15±0.1	-	-8.4±0.06
SDSSJ0013+1109$^{(z,\overline{q})}$	He	6090.0	0.6	8.0	-8.0±0.5	-7.5±0.4	-	-9.2±0.4
SDSSJ1017+3447$^{(z,\overline{q})}$	He	6089.0	0.576	8.004	-8.6±0.5	-8.6±0.5	-	-9.8±0.5
SDSSJ0208-0542$^{(z,\overline{q})}$	He	6085.0	0.6	8.0	-7.1±0.3	-7.2±0.3	-	-8.2±0.3
SDSSJ1245+0822$^{(z,\overline{q})}$	He	6074.0	0.6	8.0	-7.6±0.2	-7.0±0.2	-	-8.3±0.2
SDSSJ2340+0124$^{(z,\overline{q})}$	He	6072.0	0.574	8.0	-8.0±0.2	-7.2±0.1	-	-8.8±0.1
SDSSJ1043+3516$^{(z,\overline{q})}$	He	6069.0	0.657	8.135	-7.6±0.1	-7.5±0.1	-	-9.3±0.1
SDSSJ1545+5236$^{(z,\overline{q})}$	He	6068.0	0.639	8.107	-8.0±0.2	-7.5±0.1	-	-8.9±0.1
SDSSJ2352+1922$^{(z,\overline{q})}$	He	6067.0	0.6	8.0	-7.2±0.3	-6.8±0.1	-	-8.3±0.2
SDSSJ1132+3323$^{(z,\overline{q})}$	He	6062.0	0.6	8.0	-7.1±0.2	-6.8±0.2	-	-8.3±0.2
SDSSJ0925+3130$^{(z,\overline{q})}$	He	6050.0	0.6	8.0	-7.6±0.2	-7.4±0.2	-	-8.6±0.2
SDSSJ0800+2242$^{(z,\overline{q})}$	He	6049.0	0.6	8.0	-8.7±0.5	-8.7±0.5	-	-9.9±0.3
SDSSJ0838+2322$^{(z,\overline{q})}$	He	6048.0	0.727	8.244	-8.7±0.5	-8.6±0.5	-	-9.8±0.2
SDSSJ1158+5942$^{(z,\overline{q})}$	He	6046.0	0.587	8.022	-8.4±0.3	-7.7±0.2	-	-8.9±0.3
SDSSJ2157+1206$^{(z,\overline{q})}$	He	6042.0	0.531	7.93	-8.1±0.1	-7.6±0.1	-	-9.1±0.1
SDSSJ0939+5019$^{(z,\overline{q})}$	He	6030.0	0.536	7.939	-7.0±0.2	-6.7±0.2	-	-8.4±0.2
SDSSJ2225+2338$^{(z,\overline{q})}$	He	6029.0	0.535	7.937	-8.4±0.1	-7.7±0.1	-	-9.3±0.1
SDSSJ0144+1920$^{(z,\overline{q})}$	He	6024.0	0.5	7.877	-7.6±0.2	-7.3±0.2	-	-8.7±0.2
SDSSJ1040+2407$^{(z,\overline{q})}$	He	6023.0	0.686	8.181	-7.2±0.2	-6.8±0.1	-	-8.1±0.2
SDSSJ0721+3928$^{(z,\overline{q})}$	He	6022.0	0.296	7.433	-8.4±0.2	-7.7±0.2	-	-9.3±0.2
SDSSJ1229+0743$^{(z,\overline{q})}$	He	6014.0	0.204	7.133	-7.3±0.2	-7.3±0.2	-	-8.9±0.2
SDSSJ0135+1302$^{(z,\overline{q})}$	He	6013.0	0.633	8.097	-8.1±0.3	-7.9±0.2	-	-9.2±0.1
SDSSJ1217+1157$^{(z,\overline{q})}$	He	6012.0	0.285	7.401	-8.7±0.3	-7.8±0.2	-	-9.6±0.2
SDSSJ0913+4127$^{(z,\overline{q})}$	He	6010.0	0.6	8.0	-7.4±0.5	-7.3±0.3	-	-8.6±0.3
SDSSJ1308+0258$^{(z,\overline{q})}$	He	6003.0	0.6	8.0	-7.8±0.2	-7.9±0.2	-	-9.3±0.2
SDSSJ1205+3536$^{(z,\overline{q})}$	He	6000.0	0.684	8.178	-7.6±0.1	-7.2±0.1	-	-8.9±0.1
SDSSJ1345+1153$^{(z,\overline{q})}$	He	6000.0	0.689	8.19	-6.9±0.2	-7.0±0.1	-	-8.1±0.1
SDSSJ1627+4646$^{(z,\overline{q})}$	He	6000.0	0.45	7.785	-8.3±0.5	-7.9±0.3	-	-9.4±0.5
SDSSJ0741+3146$^{(z,\overline{q})}$	He	5974.0	0.701	8.205	-7.5±0.2	-7.6±0.2	-	-9.0±0.2
SDSSJ0842+1536$^{(z,\overline{q})}$	He	5966.0	0.823	8.385	-8.6±0.2	-8.5±0.2	-	-9.8±0.4
SDSSJ1535+1247$^{(z,\overline{q})}$	He	5950.0	0.682	8.175	-7.5±0.1	-7.0±0.1	-	-8.6±0.1
SDSSJ1401+3659$^{(z,\overline{q})}$	He	5931.0	0.557	7.973	-9.2±0.3	-8.1±0.3	-	-10.1±0.1
SDSSJ0823+0546$^{(gg,\overline{aa})}$	He	5920.0	0.6	7.945	-7.35±0.1	-7.85±0.1	-	-9.8±0.1
SDSSJ1405+2542$^{(z,\overline{q})}$	He	5890.0	0.6	8.0	-8.4±0.5	-7.8±0.3	-	-9.5±0.4
SDSSJ0004+0819$^{(z,\overline{q})}$	He	5843.0	0.6	8.0	-7.6±0.4	-7.2±0.2	-	-8.8±0.2
SDSSJ1105+0228$^{(z,\overline{q})}$	He	5842.0	0.6	8.0	-8.0±0.4	-7.6±0.2	-	-9.1±0.4

Table C.1 – continued on next page

SDSSJ2110+0512$^{(z,\overline{q})}$	He	5828.0	0.6	8.0	-8.3±0.5	-7.7±0.5	-	-9.4±0.5
SDSSJ1706+2541$^{(z,\overline{q})}$	He	5813.0	0.6	8.0	-9.0±0.5	-8.9±0.5	-	-10.1±0.3
SDSSJ0019+2209$^{(z,\overline{q})}$	He	5797.0	0.365	7.608	-8.5±0.2	-8.4±0.2	-	-9.7±0.2
SDSSJ0006+0520$^{(z,\overline{q})}$	He	5783.0	0.478	7.839	-9.6±0.3	-8.6±0.5	-	-9.8±0.2
SDSSJ0908+5136$^{(z,\overline{q})}$	He	5779.0	0.447	7.78	-9.0±0.3	-8.9±0.3	-	-10.1±0.3
SDSSJ2343-0010$^{(z,\overline{q})}$	He	5778.0	0.309	7.475	-8.5±0.5	-7.9±0.3	-	-9.6±0.3
SDSSJ1103+4144$^{(z,\overline{q})}$	He	5728.0	0.327	7.521	-8.3±0.2	-7.7±0.2	-	-9.4±0.1
SDSSJ1102+0214$^{(z,\overline{q})}$	He	5699.0	0.658	8.137	-8.6±0.4	-8.0±0.5	-	-9.8±0.1
SDSSJ1259+4729$^{(z,\overline{q})}$	He	5682.0	0.454	7.795	-8.7±0.5	-8.6±0.5	-	-9.8±0.4
SDSSJ1535+1247$^{(ff,\overline{cc})}$	He	5680.0	0.61	8.06	-7.6±0.1	-6.9±0.1	-6.5±0.3	-8.5±0.05
SDSSJ2231+0906$^{(z,\overline{q})}$	He	5679.0	0.567	7.992	-9.0±0.2	-8.1±0.5	-	-9.9±0.1
SDSSJ1259+3112$^{(z,\overline{q})}$	He	5664.0	0.589	8.027	-8.6±0.4	-8.6±0.4	-	-9.8±0.3
SDSSJ1351+2645$^{(z,\overline{q})}$	He	5640.0	0.421	7.73	-7.8±0.3	-7.9±0.2	-	-8.5±0.2
SDSSJ1429+3841$^{(z,\overline{q})}$	He	5636.0	0.375	7.634	-9.2±0.5	-9.1±0.5	-	-10.3±0.2
SDSSJ2230+1905$^{(z,\overline{q})}$	He	5631.0	0.6	8.0	-7.1±0.2	-6.8±0.2	-	-8.5±0.3
SDSSJ1055+3725$^{(z,\overline{q})}$	He	5614.0	0.361	7.605	-8.2±0.5	-8.2±0.2	-	-8.4±0.3
SDSSJ1006+1752$^{(z,\overline{q})}$	He	5605.0	0.731	8.251	-8.3±0.5	-8.3±0.5	-	-9.5±0.5
SDSSJ1321-0237$^{(z,\overline{q})}$	He	5592.0	0.6	8.0	-7.3±0.3	-6.9±0.2	-	-8.7±0.3
SDSSJ0126+2534$^{(z,\overline{q})}$	He	5588.0	0.87	8.456	-8.3±0.5	-8.3±0.5	-	-9.5±0.3
SDSSJ0758+1013$^{(z,\overline{q})}$	He	5585.0	0.6	8.0	-7.1±0.2	-7.0±0.2	-	-8.5±0.2
SDSSJ2328+0830$^{(z,\overline{q})}$	He	5566.0	0.6	8.0	-7.8±0.4	-7.3±0.1	-	-9.0±0.3
SDSSJ0512-0505$^{(gg,\overline{aa})}$	He	5560.0	0.803	8.05	-7.75±0.1	-7.65±0.1	-	-8.9±0.1
SDSSJ1502+3744$^{(z,\overline{q})}$	He	5525.0	0.624	8.084	-8.9±0.5	-8.8±0.5	-	-10.1±0.2
SDSSJ1342+1813$^{(z,\overline{q})}$	He	5524.0	0.6	8.0	-7.9±0.5	-7.8±0.5	-	-9.0±0.5
SDSSJ1537+3608$^{(z,\overline{q})}$	He	5519.0	0.6	8.0	-8.6±0.5	-8.6±0.5	-	-9.8±0.3
SDSSJ1019+2045$^{(z,\overline{q})}$	He	5515.0	0.6	8.0	-8.2±0.5	-8.2±0.5	-	-9.4±0.4
SDSSJ1411+3410$^{(z,\overline{q})}$	He	5500.0	0.807	8.363	-7.1±0.5	-6.6±0.2	-	-8.3±0.4
SDSSJ0924+4301$^{(z,\overline{q})}$	He	5500.0	0.6	8.0	-9.0±0.5	-9.0±0.5	-	-10.2±0.4
SDSSJ0916+2540$^{(z,\overline{q})}$	He	5497.0	0.612	8.066	-7.2±0.2	-6.5±0.2	-	-7.5±0.2
SDSSJ1032+1338$^{(z,\overline{q})}$	He	5479.0	0.6	8.0	-8.1±0.3	-7.3±0.3	-	-9.1±0.3
SDSSJ1641+1856$^{(z,\overline{q})}$	He	5470.0	0.536	7.941	-9.9±0.3	-9.2±0.5	-	-10.4±0.2
SDSSJ2123+0016$^{(z,\overline{q})}$	He	5463.0	0.675	8.166	-8.4±0.4	-8.3±0.5	-	-9.6±0.2
SDSSJ1238+2149$^{(z,\overline{q})}$	He	5437.0	0.632	8.097	-7.9±0.3	-7.3±0.2	-	-8.9±0.3
SDSSJ1257+3238$^{(z,\overline{q})}$	He	5376.0	0.6	8.0	-7.6±0.4	-7.2±0.2	-	-8.8±0.2
SDSSJ1158+0454$^{(z,\overline{q})}$	He	5344.0	0.566	7.991	-7.5±0.3	-7.0±0.1	-	-8.5±0.2
SDSSJ1144+1218$^{(z,\overline{q})}$	He	5320.0	0.577	8.009	-8.3±0.2	-7.8±0.2	-	-9.3±0.1
SDSSJ0052+1846$^{(z,\overline{q})}$	He	5305.0	0.6	8.0	-7.5±0.3	-7.1±0.2	-	-9.0±0.3
SDSSJ1649+2238$^{(z,\overline{q})}$	He	5261.0	0.634	8.101	-7.4±0.2	-6.7±0.2	-	-8.4±0.2
SDSSJ0913+2627$^{(z,\overline{q})}$	He	5252.0	0.6	8.161	-8.5±0.4	-8.5±0.5	-	-9.7±0.3
SDSSJ0739+3112$^{(z,\overline{q})}$	He	5221.0	0.6	8.0	-8.0±0.5	-7.9±0.5	-	-9.2±0.4
SDSSJ1518+0506$^{(z,\overline{q})}$	He	5187.0	0.672	8.161	-8.7±0.3	-8.3±0.3	-	-9.3±0.2
SDSSJ1046+1329$^{(z,\overline{q})}$	He	5177.0	0.507	7.895	-8.2±0.5	-8.1±0.5	-	-9.3±0.3
SDSSJ1350+1058$^{(z,\overline{q})}$	He	5176.0	0.902	8.505	-8.3±0.5	-8.3±0.5	-	-9.5±0.3
SDSSJ0807+4930$^{(z,\overline{q})}$	He	5172.0	0.574	8.005	-7.2±0.2	-6.8±0.2	-	-8.3±0.2
SDSSJ1316+1918$^{(z,\overline{q})}$	He	5160.0	0.375	7.639	-9.2±0.5	-9.1±0.5	-	-10.3±0.4
SDSSJ2304+2415$^{(z,\overline{q})}$	He	5102.0	0.53	7.935	-8.9±0.2	-7.3±0.2	-	-9.2±0.2
SDSSJ0056+2453$^{(z,\overline{q})}$	He	5061.0	0.6	8.0	-9.1±0.5	-9.0±0.5	-	-10.2±0.5
SDSSJ0736+4118$^{(z,\overline{q})}$	He	5010.0	0.711	8.222	-7.3±0.3	-7.3±0.3	-	-8.5±0.3
SDSSJ1147+5429$^{(z,\overline{q})}$	He	5000.0	0.6	8.0	-8.3±0.5	-8.3±0.5	-	-9.5±0.5
SDSSJ1224+2838$^{(z,\overline{q})}$	He	4991.0	0.576	8.01	-9.1±0.5	-9.0±0.5	-	-10.2±0.1
SDSSJ0744+4649$^{(z,\overline{q})}$	He	4861.0	0.602	8.052	-7.6±0.2	-7.6±0.2	-	-8.3±0.1
SDSSJ0852+3402$^{(z,\overline{q})}$	He	4806.0	0.425	7.743	-8.9±0.5	-8.9±0.5	-	-10.1±0.3
SDSSJ1152+5101$^{(z,\overline{q})}$	He	4790.0	0.6	8.0	-9.2±0.5	-9.1±0.5	-	-10.4±0.3
LHS2534$^{(gg,\overline{cc})}$	He	4780.0	0.55	7.97	-9.06±0.08	-8.62±0.06	-	-10.08±0.11

Table C.1 – continued on next page

SDSSJ0744+1640[z,q̄]	He	4703.0	0.515	7.91	-9.1±0.5	-9.1±0.5	-	-10.3±0.3
SDSSJ1226+2936[z,q̄]	He	4680.0	0.6	8.0	-8.93±0.33	-8.63±0.34	-	-10.04±0.33
SDSSJ1636+1619[z,q̄]	He	4410.0	0.669	8.096	-8.3±1.0	-8.3±1.0	-	-9.5±0.1

References stellar properties:[a]Zuckerman et al. (2007) [b]Klein et al. (2011) [c]Zuckerman et al. (2011) [d]Vennes et al. (2011) [e]Gänsicke et al. (2012) [f]Klein et al. (2011) [g]Dufour et al. (2012) [h]Kawka & Vennes (2012) [i]Vennes & Kawka (2013) [j]Jura & Xu (2012) [k]Farihi et al. (2013) [l]Xu et al. (2013) [m]Xu et al. (2014) [n]Wilson et al. (2015) [o]Raddi et al. (2015) [p]Kawka & Vennes (2016) [q]Hollands et al. (2017) [r]Xu et al. (2017) [s]Farihi et al. (2016) [t]Melis & Dufour (2017) [u]Xu et al. (2019) [v]Swan et al. (2019a) [w]Fortin-Archambault et al. (2020) [x]Izquierdo et al. (2021) [y]Hoskin et al. (2020) [z]González Egea et al. (2021) [aa]Harrison et al. (2021a) [bb]Klein et al. (2021) [cc]Hollands et al. (2021) [dd]Rogers et al. (2022b)
References abundances:[ā]Farihi et al. (2010) [b̄]Gianninas et al. (2011) [c̄]Farihi et al. (2011) [d̄]Xu et al. (2019) [ē]Kilic et al. (2020) [f̄]Koester et al. (2014) [ḡ]Klein et al. (2011) [ī]Dufour et al. (2012) [j̄]Tremblay et al. (2011) [k̄]Fortin-Archambault et al. (2020) [l̄]Kleinman et al. (2013) [m̄]Coutu et al. (2019) [n̄]Bergeron et al. (2011) [ō]Farihi et al. (2016) [p̄]Jura & Xu (2012) [q̄]Xu et al. (2014) [r̄]Leggett et al. (2018) [s̄]Becklin et al. (2005) [t̄]Kawka & Vennes (2012) [ū]Vennes & Kawka (2013) [v̄]Wilson et al. (2015) [w̄]Raddi et al. (2015) [x̄]Blouin et al. (2019) [ȳ]Kawka & Vennes (2016) [z̄]Hollands et al. (2017) [āā]Swan et al. (2019a) [b̄b̄]Izquierdo et al. (2021) [c̄c̄]Hoskin et al. (2020) [d̄d̄]González Egea et al. (2021) [ēē]Klein et al. (2021) [f̄f̄]Hollands et al. (2021) [ḡḡ]Harrison et al. (2021a) [h̄h̄]Rogers et al. (2022b)

Table C.2 Properties of white dwarfs used in our sample for chapter 6, ordered by their oxygen diffusion timescales (short to long)

System	Type	$T_{\rm eff}$ [K]	Mass [$M_\odot$]	$\log(g/{\rm ms}^{-2})$
SDSSJ1228+1040[d]	H	20900	0.73	8.15
PG1015+161[s]	H	19226	0.642	8.04
GALEX1931+0117[h]	H	21457	0.573	7.9
PG0843+516[h]	H	22412	0.577	7.902
GaiaJ2100+2122[w]	H	25565	0.693	8.1
G29-38[g]	H	11800	0.85	8.4
WD2115-560[p]	H	9600	0.58	7.97
WD2157-574[p]	H	7010	0.63	8.06
SDSSJ0845+2257[l]	He	19780	0.679	8.18
GaiaJ0644-0352[w]	He	18350	0.704	8.18
WD1536+520[m]	He	20800	0.58	7.96
SDSSJ0738+1835[f]	He	13950	0.841	8.4
HS2253+8023[c]	He	14400	0.84	8.4
GD424[r]	He	16560	0.77	8.25
GD61[a]	He	17280	0.71	8.2
SDSSJ2047-1259[t]	He	17970	0.617	8.04
WD1232+563[p]	He	11787	0.77	8.3
WD1145+017[u]	He	14500	0.656	8.11
G241-6[b,e]	He	15300	0.71	8.0
WD1551+175[b,q]	He	14756	0.57	8.02
GD378[d]	He	15620	0.551	7.93
WD2207+121[p]	He	14752	0.57	7.97
GD40[p]	He	13594	0.6	8.02
SDSSJ1242+5226[k]	He	13000	0.59	8.0
WD1425+540[b]	He	14490	0.56	7.95
SDSSJ0956+5912[v]	He	8100	0.59	8.02
GALEXJ2339[d]	He	13735	0.548	7.93
GD362[n]	He	10057	0.551	7.95
WD1350-162[p]	He	11640	0.6	8.02
WD0446-255[p]	He	10120	0.58	8.0
PG1225-079[d]	He	10800	0.58	8.0

References:[a]Farihi et al. (2011) [b]Bergeron et al. (2011) [c]Klein et al. (2011) [d]Tremblay et al. (2011) [e]Jura & Xu (2012) [f]Dufour et al. (2012) [g]Xu et al. (2014) [h]Koester et al. (2014) [i]Wilson et al. (2015) [j]Raddi et al. (2015) [k]Raddi et al. (2015) [l]Wilson et al. (2015) [m]Farihi et al. (2016) [n]Leggett et al. (2018) [o]Swan et al. (2019a) [p]Coutu et al. (2019) [q]Xu et al. (2019) [r]Izquierdo et al. (2021) [s]Kilic et al. (2020) [t]Hoskin et al. (2020) [u]Fortin-Archambault et al. (2020) [v]Hollands et al. (2022)

C.7 White dwarf sample used in chapter 6

Table C.3 Abundances of white dwarfs used in our sample for chapter 6.

System	log(Al/Hx)	log(Ti/Hx)	log(Ca/Hx)	log(Ni/Hx)	log(Fe/Hx)	log(Cr/Hx)	log(Mg/Hx)	log(Si/Hx)	log(Na/Hx)	log(O/Hx)	log(C/Hx)	log(N/Hx)
GD424[r]	-6.3±0.1	-7.78±0.09	-6.15±0.05	-6.93±0.1	-5.53±0.12	-7.19±0.07	-5.15±0.04	-5.29±0.04	<-6.5	-4.59±0.12	-	-
GALEXJ2339[u]	<-7.7	-9.58±0.4	-8.03±0.75	<-8.0	-6.99±0.3	-8.73±0.26	-6.58±0.14	-6.59±0.08	<-8.0	-5.52±0.05	-	-
GD378[u]	<-7.7	-10.13±0.46	-8.7±0.76	<-8.3	-7.51±0.36	-9.72±0.68	-7.44±0.2	-7.49±0.12	<-7.2	-6.04±0.31	-7.35±0.24	<-7.3
WD0446-255[p]	-7.3±0.3	-8.8±0.1	-7.4±0.1	-8.2±0.1	-6.9±0.1	-8.5±0.1	-6.6±0.1	-6.5±0.1	-7.9±0.1	-5.8±0.1	-	-
PG0843+516[q]	-6.5±0.2	-	-	-6.3±0.3	-4.6±0.2	-5.8±0.3	-5.0±0.2	-5.2±0.2	-	-5.0±0.3	-	-
GALEX1931+0117[c]	<-5.85	<-7.0	-5.83±0.1	<-5.6	-4.1±0.1	-5.92±0.14	-4.1±0.1	-4.35±0.11	-	-3.68±0.1	<-4.85	-
SDSSJ2047-1259[s]	<-6.5	-	-6.9±0.1	-7.4±0.1	-6.4±0.2	-	-5.6±0.1	-5.6±0.1	-	-4.8±0.1	-6.1±0.1	<-7.0
WD1551+175[q]	-6.99±0.15	-8.68±0.11	-6.93±0.07	<-7.5	-6.6±0.1	-8.25±0.07	-6.29±0.05	-6.33±0.1	-	-5.48±0.15	-	-
PG1015+161[q]	-	-	-6.45±0.2	-	-5.5±0.3	<-5.8	-5.3±0.2	-6.4±0.2	-	-5.5±0.2	<-8.0	-
GD40[e]	-7.35±0.12	-8.61±0.2	-6.9±0.2	-7.84±0.26	-6.47±0.12	-8.31±0.16	-6.2±0.16	-6.44±0.3	-	-5.62±0.1	-7.8±0.2	<-8.8
G241-6[e]	<-7.7	-8.97±0.1	-7.3±0.2	-8.15±0.4	-6.82±0.14	-8.46±0.1	-6.26±0.1	-6.62±0.2	-	-5.64±0.11	<-8.5	<-8.9
GD61[h]	<-7.8	<-8.6	-7.9±0.06	<-8.8	-7.6±0.07	<-8.0	-6.69±0.05	-6.82±0.04	<-6.8	-5.95±0.04	<-9.1	<-8.0
HS2253+8023[d]	<-6.7	-8.74±0.19	-6.99±0.11	-7.31±0.22	-6.17±0.17	-8.01±0.18	-6.1±0.14	-6.27±0.13	<-6.8	-5.37±0.13	-	-
SDSSJ0738+1835[g]	-6.39±0.11	-7.95±0.11	-6.23±0.15	-6.31±0.1	-4.98±0.09	-6.76±0.12	-4.68±0.07	-4.9±0.16	-6.36±0.16	-3.81±0.19	-	-
SDSSJ1228+1040[f]	-5.75±0.2	-	-5.94±0.2	<-6.5	-5.2±0.3	<-6.0	-5.2±0.2	-5.2±0.2	-	-4.55±0.2	-7.5±0.2	-
G29-38[j]	<-6.1	-7.9±0.16	-6.58±0.12	<-7.3	-5.9±0.1	-7.51±0.12	-5.77±0.13	-5.6±0.17	<-6.7	-5.0±0.12	-6.9±0.12	<-5.7
SDSSJ1242+5226[k]	<-6.5	-8.2±0.2	-6.53±0.1	<-7.3	-5.9±0.15	-7.5±0.2	-5.26±0.15	-5.3±0.06	-7.2±0.2	-4.3±0.1	<-4.7	<-5.0
SDSSJ0845+2257[l]	-5.7±0.15	<-7.15	-5.95±0.1	-5.65±0.3	-4.6±0.2	-6.4±0.3	-4.7±0.15	-4.8±0.3	-	-4.25±0.2	-4.9±0.2	<-6.3
WD1536+520[m]	-5.38±0.15	-6.84±0.15	-5.28±0.15	-	-4.5±0.15	-5.93±0.15	-4.06±0.15	-4.32±0.15	-	-3.4±0.15	<-4.2	-
SDSSJ1043+0855[n]	-7.06±0.3	<-7.0	-5.96±0.2	-7.38±0.3	-6.15±0.3	<-6.5	-5.11±0.2	-5.33±0.5	-	-4.9±0.2	-6.15±0.3	-
WD1425+540[o]	-	-	-9.26±0.1	-9.67±0.2	-8.15±0.14	-	-8.16±0.2	-8.03±0.31	-	-6.62±0.23	-7.29±0.17	-8.09±0.1
WD1232+563[q]	<-7.5	-8.96±0.11	-7.69±0.05	<-7.3	-6.45±0.11	-8.16±0.07	-6.09±0.05	-6.36±0.13	-	-5.14±0.15	-	-
WD2207+121[q]	-7.08±0.15	-8.84±0.14	-7.4±0.08	-7.55±0.2	-6.46±0.13	-8.16±0.19	-6.15±0.1	-6.17±0.11	-	-5.32±0.15	-	-
WD1145+017[t]	-6.89±0.2	-8.57±0.2	-7.0±0.2	-7.02±0.3	-5.61±0.2	-7.92±0.4	-5.91±0.2	-5.89±0.2	-	-5.12±0.35	-7.5±0.4	<-7.0
WD1350-162[p]	-	-10.0±0.1	-8.7±0.1	-	-7.1±0.1	-9.0±0.2	-6.8±0.1	-7.3±0.2	-	-6.2±0.1	-	-
SDSSJ0956+5912[v]	-6.5±0.1	-8.9±0.2	-7.3±0.05	-	-6.9±0.1	-	-5.5±0.1	-5.7±0.2	-6.8±0.2	-4.6±0.2	<-4.1	-
WD2157-574[p]	-8.1±0.1	-	-8.1±0.1	-8.8±0.1	-7.3±0.1	-	-7.0±0.1	-7.0±0.1	-	<-3.8	<-3.6	<-3.0
GD362[a]	-6.4±0.2	-7.95±0.1	-6.24±0.1	-7.07±0.15	-5.65±0.1	-7.41±0.1	-5.98±0.25	-5.84±0.3	-7.79±0.2	<-5.14	<-5.64	<-4.14
WD2115-560[p]	-7.6±0.1	-	-7.4±0.1	-	-6.4±0.1	-	-6.4±0.1	-6.2±0.1	-	<-5.0	<-4.3	<-4.0
PG1225-079[]	<-7.84	-9.45±0.23	-8.06±0.19	-8.76±0.18	-7.42±0.23	-9.27±0.23	-7.5±0.2	-7.45±0.1	<-8.26	<-5.54	-7.8±0.1	-
GaiaJ2100+2122[w]	<-6.28	<-6.69	-6.23±0.13	<-5.11	-4.96±0.1	<-5.78	-5.08±0.1	-5.13±0.12	<-5.18	<-4.1	-	-
GaiaJ0644-0352[w]	-6.76±0.1	-8.37±0.12	-6.74±0.18	<-7.21	-6.46±0.16	-7.81±0.13	-5.75±0.15	-5.98±0.1	<-5.65	-5.19±0.14	-	-

References:[a]Zuckerman et al. (2007) [b]Melis et al. (2011) [c]Vennes et al. (2011) [d]Klein et al. (2011) [e]Jura & Xu (2012) [f]Gänsicke et al. (2012) [g]Dufour et al. (2012) [h]Farihi et al. (2013) [i]Xu et al. (2013) [j]Xu et al. (2014) [k]Raddi et al. (2015) [l]Wilson et al. (2015) [m]Farihi et al. (2016) [n]Melis & Dufour (2017) [o]Xu et al. (2017) [p]Swan et al. (2019a) [q]Xu et al. (2019) [r]Izquierdo et al. (2021) [s]Hoskin et al. (2020) [t]Fortin-Archambault et al. (2020) [u]Klein et al. (2021) [v]Hollands et al. (2022) [x]Koester et al. (2014) [y]Wilson et al. (2016)

References

Adibekyan, V., Dorn, C., Sousa, S. G., et al. 2021, Science, 374, 330

Airy, G. B. 1846, MNRAS, 7, 121

Albarède, F. 2009, Nature, 461, 1227

Ali-Dib, M., Cumming, A., & Lin, D. N. C. 2020, MNRAS, 494, 2440

Alibert, Y. 2017, A&A, 606, A69

Alibert, Y., Venturini, J., Helled, R., et al. 2018, Nature Astronomy, 2, 873

ALMA Partnership, Brogan, C. L., Pérez, L. M., et al. 2015, ApJ, 808, L3

Althaus, L. G., Córsico, A. H., Isern, J., & García-Berro, E. 2010, A&A Rev., 18, 471

Antoniadou, K. I. & Veras, D. 2016, MNRAS, 463, 4108

Asphaug, E. & Benz, W. 1994, Nature, 370, 120

Ataiee, S., Baruteau, C., Alibert, Y., & Benz, W. 2018, A&A, 615, A110

Bae, J., Isella, A., Zhu, Z., et al. 2022, arXiv e-prints, arXiv:2210.13314

Ballering, N. P., Levens, C. I., Su, K. Y. L., & Cleeves, L. I. 2022, ApJ, 939, 108

Ballesteros-Paredes, J., Klessen, R. S., Mac Low, M. M., & Vazquez-Semadeni, E. 2007, in Protostars and Planets V, ed. B. Reipurth, D. Jewitt, & K. Keil, 63

Batalha, N. M., Rowe, J. F., Bryson, S. T., et al. 2013, ApJS, 204, 24

Bear, E. & Soker, N. 2011, MNRAS, 414, 1788

Bear, E. & Soker, N. 2013, New Astronomy, 19, 56

Bear, E. & Soker, N. 2015, Monthly Notices of the Royal Astronomical Society, 450, 4233

Becklin, E. E., Farihi, J., Jura, M., et al. 2005, ApJ, 632, L119

Beckmann, W. & Lacmann, R. 1982, Journal of Crystal Growth, 58, 433

Bell, K. R. & Lin, D. N. C. 1994, ApJ, 427, 987

Belloche, A. 2013, in EAS Publications Series, Vol. 62, EAS Publications Series, ed. P. Hennebelle & C. Charbonnel, 25–66

Benacquista, M. 2013, Stellar Structure and Evolution (Springer), 47–63

Benecchi, S. D., Noll, K. S., Grundy, W. M., et al. 2009, Icarus, 200, 292

Benecchi, S. D., Noll, K. S., Stephens, D. C., Grundy, W. M., & Rawlins, J. 2011, Icarus, 213, 693

Benisty, M., Dominik, C., Follette, K., et al. 2022, arXiv e-prints, arXiv:2203.09991

Benz, W. & Asphaug, E. 1999, Icarus, 142, 5

Bergeron, P., Wesemael, F., Dufour, P., et al. 2011, ApJ, 737, 28

Bernardinelli, P. H., Bernstein, G. M., Montet, B. T., et al. 2021, ApJ, 921, L37

Binzel, R. P., Rivkin, A. S., Stuart, J. S., et al. 2004, Icarus, 170, 259

Birnstiel, T., Ricci, L., Trotta, F., et al. 2010, A&A, 516, L14

Bitsch, B., Johansen, A., Lambrechts, M., & Morbidelli, A. 2015, A&A, 575, A28

Bitsch, B., Morbidelli, A., Johansen, A., et al. 2018, A&A, 612, A30

Bitsch, B. & Savvidou, S. 2021, arXiv e-prints, arXiv:2101.03818

Blitz, L. & Rosolowsky, E. 2005, in Astrophysics and Space Science Library, Vol. 327, The Initial Mass Function 50 Years Later, ed. E. Corbelli, F. Palla, & H. Zinnecker, 287

Blouin, S. 2020, MNRAS, 496, 1881

Blouin, S., Dufour, P., Thibeault, C., & Allard, N. F. 2019, ApJ, 878, 63

Blouin, S. & Xu, S. 2022, MNRAS, 510, 1059

Blum, J. 2018, Space Sci. Rev., 214, 52

Bodenheimer, P. & Pollack, J. B. 1986, Icarus, 67, 391

Bodenheimer, P., Stevenson, D. J., Lissauer, J. J., & D'Angelo, G. 2018, ApJ, 868, 138

Bonsor, A., Carter, P. J., Hollands, M., et al. 2020, MNRAS, 492, 2683

Bonsor, A., Farihi, J., Wyatt, M. C., & van Lieshout, R. 2017, MNRAS, 468, 154

Bonsor, A., Mustill, A. J., & Wyatt, M. C. 2011, MNRAS, 414, 930

Bonsor, A. & Wyatt, M. 2010, MNRAS, 409, 1631

Borucki, W. J., Koch, D., Basri, G., et al. 2010, Science, 327, 977

Borucki, W. J., Koch, D. G., Basri, G., et al. 2011, ApJ, 736, 19

Boss, A. P. 1998, ApJ, 503, 923

Boss, A. P. 2021, ApJ, 911, 146

Bottke, William F., J., Vokrouhlický, D., Rubincam, D. P., & Nesvorný, D. 2006, Annual Review of Earth and Planetary Sciences, 34, 157

Bottke, W. F., Durda, D. D., Nesvorný, D., et al. 2005a, Icarus, 175, 111

Bottke, W. F., Durda, D. D., Nesvorný, D., et al. 2005b, Icarus, 179, 63

Bourrier, V. & Lecavelier des Etangs, A. 2013, A&A, 557, A124

Braine, J., Hughes, A., Rosolowsky, E., et al. 2020, A&A, 633, A17

Braine, J., Rosolowsky, E., Gratier, P., Corbelli, E., & Schuster, K. F. 2018, A&A, 612, A51

Brewer, J. M., Fischer, D. A., Valenti, J. A., & Piskunov, N. 2016, ApJS, 225, 32

Brouwers, M. G., Bonsor, A., & Malamud, U. 2022, MNRAS, 509, 2404

Brouwers, M. G. & Ormel, C. W. 2020, A&A, 634, A15

Brouwers, M. G., Ormel, C. W., Bonsor, A., & Vazan, A. 2021, A&A, 653, A103

Brouwers, M. G., Vazan, A., & Ormel, C. W. 2018, A&A, 611, A65

Brown, J. C., Veras, D., & Gänsicke, B. T. 2017, MNRAS, 468, 1575

Bryan, M. L., Chiang, E., Bowler, B. P., et al. 2020, AJ, 159, 181

Bryan, M. L., Chiang, E., Morley, C. V., Mace, G. N., & Bowler, B. P. 2021, AJ, 162, 217

Bryan, M. L., Knutson, H. A., Lee, E. J., et al. 2019, AJ, 157, 52

Buchan, A. M., Bonsor, A., Shorttle, O., et al. 2022, MNRAS, 510, 3512

Budaj, J., Maliuk, A., & Hubeny, I. 2022, A&A, 660, A72

Burns, J. A. 1975, Icarus, 25, 545

Burns, J. A., Lamy, P. L., & Soter, S. 1979, Icarus, 40, 1

Cai, M. X., Tan, J. C., & Portegies Zwart, S. 2022, MNRAS, 510, 5486

Cameron, A. G. W. 1978, Moon and Planets, 18, 5

Canup, R. M. 2012, Science, 338, 1052

Carbognani, A. 2017, Planet. Space Sci., 147, 1

Carrasco-González, C., Sierra, A., Flock, M., et al. 2019, ApJ, 883, 71

Carrera, D., Simon, J. B., Li, R., Kretke, K. A., & Klahr, H. 2021, AJ, 161, 96

Caselli, P., Benson, P. J., Myers, P. C., & Tafalla, M. 2002, ApJ, 572, 238

Chachan, Y., Lee, E. J., & Knutson, H. A. 2021, arXiv e-prints, arXiv:2101.10333

Chambers, J. E. 2014, Icarus, 233, 83

Chatterjee, S. & Tan, J. C. 2014, ApJ, 780, 53

Chen, Y.-X., Li, Y.-P., Li, H., & Lin, D. N. C. 2020, ApJ, 896, 135

Cherenkov, A. A., Bisikalo, D. V., & Kosovichev, A. G. 2018, MNRAS, 475, 605

Chiang, E., Kite, E., Kalas, P., Graham, J. R., & Clampin, M. 2009, ApJ, 693, 734

Chiang, E. I. & Goldreich, P. 1997, ApJ, 490, 368

Cimerman, N. P., Kuiper, R., & Ormel, C. W. 2017, MNRAS, 471, 4662

Clausius, R. 1850, Annalen der Physik, 155, 368

Conrath, B., Gautier, D., Hanel, R., Lindal, G., & Marten, A. 1987, J. Geophys. Res., 92, 15003

Conrath, B. J., Gautier, D., Lindal, G. F., Samuelson, R. E., & Shaffer, W. A. 1991, Journal of Geophysical Research Supplement, 96, 18907

Corsaro, E., Lee, Y.-N., García, R. A., et al. 2017, Nature Astronomy, 1, 0064

Coutu, S., Dufour, P., Bergeron, P., et al. 2019, ApJ, 885, 74

Cridland, A. J., Rosotti, G. P., Tabone, B., et al. 2022, A&A, 662, A90

Cunningham, T., Tremblay, P.-E., Bauer, E. B., et al. 2021, MNRAS, 503, 1646

Cunningham, T., Tremblay, P.-E., Freytag, B., Ludwig, H.-G., & Koester, D. 2019, MNRAS, 488, 2503

Cunningham, T., Wheatley, P. J., Tremblay, P.-E., et al. 2022, Nature, 602, 219

Dauphas, N. & Chaussidon, M. 2011, Annual Review of Earth and Planetary Sciences, 39, 351

Davidsson, B. J. 2001, Icarus, 149, 375

Davidsson, B. J. R. 1999, Icarus, 142, 525

Davidsson, B. J. R. 2021, MNRAS, 505, 5654

Davis, D. R., Weidenschilling, S. J., Farinella, P., Paolicchi, P., & Binzel, R. P. 1989, in Asteroids II, ed. R. P. Binzel, T. Gehrels, & M. S. Matthews, 805–826

Debes, J. H. & Sigurdsson, S. 2002, ApJ, 572, 556

Debes, J. H., Walsh, K. J., & Stark, C. 2012, ApJ, 747, 148

Debras, F. & Chabrier, G. 2019, ApJ, 872, 100

Debras, F., Chabrier, G., & Stevenson, D. J. 2021, ApJ

Degewij, J. & Gehrels, T. 1976, in Bulletin of the American Astronomical Society, Vol. 8, 459

Deng, H., Mayer, L., & Meru, F. 2017, ApJ, 847, 43

Dennihy, E., Clemens, J. C., Dunlap, B. H., et al. 2018, ApJ, 854, 40

Dennihy, E., Debes, J. H., & Clemens, C. J. 2017, in Astronomical Society of the Pacific Conference Series, Vol. 509, 20th European White Dwarf Workshop, ed. P. E. Tremblay, B. Gaensicke, & T. Marsh, 113

Dittmann, A. J. 2021, MNRAS, 508, 1842

Dobrovolskis, A. R. 1982, Icarus, 52, 136

Dobrovolskis, A. R. 1990, Icarus, 88, 24

Dohnanyi, J. S. 1969, J. Geophys. Res., 74, 2531

Dominik, C. & Tielens, A. G. G. M. 1997, ApJ, 480, 647

Dones, L. & Tremaine, S. 1993a, Icarus, 103, 67

Dones, L. & Tremaine, S. 1993b, Science, 259, 350

Dong, S. & Zhu, Z. 2013, ApJ, 778, 53

Doyle, A. E., Klein, B., Zuckerman, B., Schlichting, H. E., & Young, E. D. 2020, IAU Symposium, 357, 28

Doyle, A. E., Young, E. D., Klein, B., Zuckerman, B., & Schlichting, H. E. 2019, Science, 366, 356

Drazkowska, J., Bitsch, B., Lambrechts, M., et al. 2022, arXiv e-prints, arXiv:2203.09759

Drazkowska, J., Stammler, S. M., & Birnstiel, T. 2021, arXiv e-prints, arXiv:2101.01728

Drążkowska, J. & Alibert, Y. 2017, A&A, 608, A92

Dufour, P., Kilic, M., Fontaine, G., et al. 2012, ApJ, 749, 6

Dullemond, C. P., Birnstiel, T., Huang, J., et al. 2018, ApJ, 869, L46

Duncan, M., Quinn, T., & Tremaine, S. 1989, Icarus, 82, 402

Duncan, M. J. & Lissauer, J. J. 1998, Icarus, 134, 303

Durda, D. D., Greenberg, R., & Jedicke, R. 1998, Icarus, 135, 431

Durham, W. B., McKinnon, W. B., & Stern, L. A. 2005, Geophys. Res. Lett., 32, L18202

Duvvuri, G. M., Redfield, S., & Veras, D. 2020, ApJ, 893, 166

Eriksson, L. E. J., Johansen, A., & Liu, B. 2020, A&A, 635, A110

Estrada, P. R., Cuzzi, J. N., & Umurhan, O. M. 2022, ApJ, 936, 42

Evans, Neal J., I., Dunham, M. M., Jørgensen, J. K., et al. 2009, ApJS, 181, 321

Evans, J. 1998, The history and practice of ancient astronomy (Oxford University Press), 296

Everhart, E. 1985, 115, 185

Farihi, J. 2016, New A Rev., 71, 9

Farihi, J., Barstow, M. A., Redfield, S., Dufour, P., & Hambly, N. C. 2010, MNRAS, 404, 2123

Farihi, J., Brinkworth, C. S., Gänsicke, B. T., et al. 2011, ApJ, 728, L8

Farihi, J., Gänsicke, B. T., & Koester, D. 2013, Science, 342, 218

Farihi, J., Gänsicke, B. T., Wyatt, M. C., et al. 2012, MNRAS, 424, 464

Farihi, J., Hermes, J. J., Marsh, T. R., et al. 2022, MNRAS, 511, 1647

Farihi, J., Koester, D., Zuckerman, B., et al. 2016, MNRAS, 463, 3186

Farihi, J., van Lieshout, R., Cauley, P. W., et al. 2018, MNRAS, 481, 2601

Farihi, J., Wyatt, M. C., Greaves, J. S., et al. 2014, MNRAS, 444, 1821

Farihi, J., Zuckerman, B., & Becklin, E. E. 2008, ApJ, 674, 431

Ferguson, F. T., Nuth, J. A., & Johnson, N. M. 2004, Journal of Chemical & Engineering Data, 49, 497

Fernandes, R. B., Mulders, G. D., Pascucci, I., Mordasini, C., & Emsenhuber, A. 2019, ApJ, 874, 81

Fischer, D. A. & Valenti, J. 2005, ApJ, 622, 1102

Fleck, R. C., J. & Clark, F. O. 1981, ApJ, 245, 898

Fortin-Archambault, M., Dufour, P., & Xu, S. 2020, ApJ, 888, 47

Fraser, W. C. 2009, ApJ, 706, 119

Fraser, W. C., Bannister, M. T., Pike, R. E., et al. 2017, Nature Astronomy, 1, 0088

Freedman, R. S., Lustig-Yaeger, J., Fortney, J. J., et al. 2014, ApJS, 214, 25

Freedman, R. S., Marley, M. S., & Lodders, K. 2008, ApJS, 174, 504

Fulle, M., Blum, J., & Rotundi, A. 2019, ApJ, 879, L8

Fulle, M., Blum, J., Rotundi, A., et al. 2020, MNRAS, 493, 4039

Fulton, B. J. & Petigura, E. A. 2018, AJ, 156, 264

Fulton, B. J., Petigura, E. A., Howard, A. W., et al. 2017, AJ, 154, 109

Fulton, B. J., Rosenthal, L. J., Hirsch, L. A., et al. 2021, ApJS, 255, 14

Galle, J. G. 1846, MNRAS, 7, 153

Gänsicke, B. T., Koester, D., Farihi, J., et al. 2012, MNRAS, 424, 333

Gänsicke, B. T., Koester, D., Marsh, T. R., Rebassa-Mansergas, A., & Southworth, J. 2008, MNRAS, 391, L103

Gänsicke, B. T., Marsh, T. R., & Southworth, J. 2007, MNRAS, 380, L35

Gänsicke, B. T., Marsh, T. R., Southworth, J., & Rebassa-Mansergas, A. 2006, Science, 314, 1908

Gänsicke, B. T., Schreiber, M. R., Toloza, O., et al. 2019, Nature, 576, 61

Gentile Fusillo, N. P., Gänsicke, B. T., Farihi, J., et al. 2017, MNRAS, 468, 971

Gianninas, A., Bergeron, P., & Ruiz, M. T. 2011, ApJ, 743, 138

Ginzburg, S., Schlichting, H. E., & Sari, R. 2016, ApJ, 825, 29

Ginzburg, S., Schlichting, H. E., & Sari, R. 2018, MNRAS, 476, 759

Girven, J., Brinkworth, C. S., Farihi, J., et al. 2012, ApJ, 749, 154

Giuli, R. T. 1968, Icarus, 8, 301

Goldreich, P. & Peale, S. J. 1968, ARA&A, 6, 287

Goldreich, P. & Ward, W. R. 1973, ApJ, 183, 1051

González Egea, E., Raddi, R., Koester, D., et al. 2021, MNRAS, 501, 3916

Greenberg, J. M., Mizutani, H., & Yamamoto, T. 1995, A&A, 295, L35

Grishin, E. & Veras, D. 2019, MNRAS, 489, 168

Grundy, W. M., Noll, K. S., Roe, H. G., et al. 2019, Icarus, 334, 62

Guidry, J. A., Vanderbosch, Z. P., Hermes, J. J., et al. 2021, ApJ, 912, 125

Guilera, O. M., Sándor, Z., Ronco, M. P., Venturini, J., & Miller Bertolami, M. M. 2020, arXiv e-prints, arXiv:2005.10868

Guillot, T., Fletcher, L. N., Helled, R., et al. 2022, arXiv e-prints, arXiv:2205.04100

Gundlach, B. & Blum, J. 2012, Icarus, 219, 618

Gundlach, B. & Blum, J. 2015, ApJ, 798, 34

Gundlach, B. & Blum, J. 2016, Astronomy & Astrophysics, 589, A111

Gundlach, B., Fulle, M., & Blum, J. 2020, MNRAS, 493, 3690

Gundlach, B., Skorov, Y. V., & Blum, J. 2011, Icarus, 213, 710

Gupta, A., Nicholson, L., & Schlichting, H. E. 2022, MNRAS, 516, 4585

Gupta, A. & Schlichting, H. E. 2018, arXiv e-prints, arXiv:1811.03202

Güttler, C., Blum, J., Zsom, A., Ormel, C. W., & Dullemond, C. P. 2010, A&A, 513, A56

Hall, C., Forgan, D., & Rice, K. 2017, MNRAS, 470, 2517

Harrison, J. H. D., Bonsor, A., Kama, M., et al. 2021a, MNRAS, 504, 2853

Harrison, J. H. D., Bonsor, A., & Madhusudhan, N. 2018, MNRAS, 479, 3814

Harrison, J. H. D., Shorttle, O., & Bonsor, A. 2021b, Earth and Planetary Science Letters, 554, 116694

Hauck, S. A., Margot, J.-L., Solomon, S. C., et al. 2013, Journal of Geophysical Research (Planets), 118, 1204

Haugbølle, T., Weber, P., Wielandt, D. P., et al. 2019, AJ, 158, 55

Hayashi, C. 1981, Progress of Theoretical Physics Supplement, 70, 35

Heinonen, R. A., Saumon, D., Daligault, J., et al. 2020, arXiv e-prints, arXiv:2005.05891

Helled, R. & Bodenheimer, P. 2014, ApJ, 789, 69

Helled, R., Nettelmann, N., & Guillot, T. 2020, Space Sci. Rev., 216, 38

Heras, A. M., Rauer, H., Aerts, C., et al. 2020, in European Planetary Science Congress, EPSC2020–396

Hevey, P. J. & Sanders, I. S. 2006, Meteoritics & Planetary Science, 41, 95

Ho, C. S. K. & Van Eylen, V. 2023, MNRAS, 519, 4056

Hogg, M. A., Cutter, R., & Wynn, G. A. 2021, MNRAS, 500, 2986

Hollands, M. A., Gänsicke, B. T., & Koester, D. 2018, MNRAS, 477, 93

Hollands, M. A., Koester, D., Alekseev, V., Herbert, E. L., & Gänsicke, B. T. 2017, MNRAS, 467, 4970

Hollands, M. A., Tremblay, P. E., Gänsicke, B. T., & Koester, D. 2022, MNRAS, 511, 71

Hollands, M. A., Tremblay, P.-E., Gänsicke, B. T., Koester, D., & Gentile-Fusillo, N. P. 2021, Nature Astronomy, 5, 451

Hoskin, M. J., Toloza, O., Gänsicke, B. T., et al. 2020, MNRAS, 499, 171

Howard, A. W., Marcy, G. W., Bryson, S. T., et al. 2012, ApJS, 201, 15

Howell, S. B., Sobeck, C., Haas, M., et al. 2014, PASP, 126, 398

Hoyle, F. 1951, in Problems of Cosmical Aerodynamics, 195

Hsu, D. C., Ford, E. B., Ragozzine, D., & Ashby, K. 2019, AJ, 158, 109

Hsu, D. C., Ford, E. B., & Terrien, R. 2020, MNRAS, 498, 2249

Hu, X., Tan, J. C., Zhu, Z., et al. 2018, ApJ, 857, 20

Hu, X., Zhu, Z., Tan, J. C., & Chatterjee, S. 2016, ApJ, 816, 19

Huebner, W. F., Benkhoff, J., Capria, M.-T., et al. 2006, Heat and Gas Diffusion in Comet Nuclei (International Space Science Institute), 84

Hull, C. L. H., Yang, H., Li, Z.-Y., et al. 2018, ApJ, 860, 82

Iaroslavitz, E. & Podolak, M. 2007, Icarus, 187, 600

Ikoma, M. & Hori, Y. 2012, ApJ, 753, 66

Izquierdo, P., Rodríguez-Gil, P., Gänsicke, B. T., et al. 2018, MNRAS, 481, 703

Izquierdo, P., Toloza, O., Gänsicke, B. T., et al. 2021, MNRAS, 501, 4276

Jackson, R. J., Deliyannis, C. P., & Jeffries, R. D. 2018, MNRAS, 476, 3245

Jackson, R. J. & Jeffries, R. D. 2010, MNRAS, 402, 1380

Jeffreson, S. M. R., Kruijssen, J. M. D., Keller, B. W., Chevance, M., & Glover, S. C. O. 2020, MNRAS, 498, 385

Jennings, R. M. & Chiang, E. 2021, MNRAS, 507, 5187

Jin, S. & Mordasini, C. 2018, ApJ, 853, 163

Johansen, A., Blum, J., Tanaka, H., et al. 2014, in Protostars and Planets VI, ed. H. Beuther, R. S. Klessen, C. P. Dullemond, & T. Henning, 547–570

Johansen, A. & Lacerda, P. 2010, MNRAS, 404, 475

Johansen, A. & Nordlund, Å. 2020, arXiv e-prints, arXiv:2009.07837

Johansen, A., Oishi, J. S., Mac Low, M.-M., et al. 2007, Nature, 448, 1022

Johansen, A., Youdin, A., & Mac Low, M.-M. 2009, ApJ, 704, L75

Jung, Y. K., Zang, W., Han, C., et al. 2022, AJ, 164, 262

Jura, M. 2003, ApJ, 584, L91

Jura, M., Farihi, J., Zuckerman, B., & Becklin, E. E. 2007, AJ, 133, 1927

Jura, M. & Xu, S. 2012, AJ, 143, 6

Jura, M., Xu, S., & Young, E. D. 2013, ApJ, 775, L41

Jura, M. & Young, E. D. 2014, Annual Review of Earth and Planetary Sciences, 42, 45

Kama, M., Trapman, L., Fedele, D., et al. 2020, A&A, 634, A88

Kataoka, A., Muto, T., Momose, M., Tsukagoshi, T., & Dullemond, C. P. 2016, ApJ, 820, 54

Kawka, A. & Vennes, S. 2012, A&A, 538, A13

Kawka, A. & Vennes, S. 2016, MNRAS, 458, 325

Kenyon, S. J. & Bromley, B. C. 2017a, ApJ, 844, 116

Kenyon, S. J. & Bromley, B. C. 2017b, ApJ, 850, 50

Kilic, M., Bergeron, P., Kosakowski, A., et al. 2020, ApJ, 898, 84

Klahr, H. & Schreiber, A. 2020, ApJ, 901, 54

Klein, B., Jura, M., Koester, D., & Zuckerman, B. 2011, ApJ, 741, 64

Klein, B., Jura, M., Koester, D., Zuckerman, B., & Melis, C. 2010, ApJ, 709, 950

Klein, B. L., Doyle, A. E., Zuckerman, B., et al. 2021, ApJ, 914, 61

Kleinman, S. J., Kepler, S. O., Koester, D., et al. 2013, ApJS, 204, 5

Klinger, J. 1975, Journal of Glaciology, 14, 517

Klinger, J. 1980, Science, 209, 271

Knudsen, M. 1909, Annalen der Physik, 333, 999

Koch-Westenholz, U. 1995, Mesopotamian Astrology (Museum Tusculanum Press), 37

Koester, D. 2009, A&A, 498, 517

Koester, D., Gänsicke, B. T., & Farihi, J. 2014, A&A, 566, A34

Koester, D., Kepler, S. O., & Irwin, A. W. 2020, A&A, 635, A103

Kossacki, K. J., Markiewicz, W. J., Skorov, Y., & Kömle, N. I. 1999, Planet. Space Sci., 47, 1521

Krapp, L., Benítez-Llambay, P., Gressel, O., & Pessah, M. E. 2019, ApJ, 878, L30

Krijt, S., Ormel, C. W., Dominik, C., & Tielens, A. G. G. M. 2015, A&A, 574, A83

Krijt, S., Ormel, C. W., Dominik, C., & Tielens, A. G. G. M. 2016, A&A, 586, A20

Kuiper, G. P. 1951, Proceedings of the National Academy of Science, 37, 1

Kurokawa, H. & Tanigawa, T. 2018, MNRAS, 479, 635

Lambrechts, M. & Johansen, A. 2012, A&A, 544, A32

Lambrechts, M., Johansen, A., & Morbidelli, A. 2014, A&A, 572, A35

Lambrechts, M. & Lega, E. 2017, A&A, 606, A146

Langmuir, I. 1913, Physical Review, 2, 329

Larson, R. B. 1981, MNRAS, 194, 809

Lauer, T. R., Faber, S. M., Gebhardt, K., et al. 2005, AJ, 129, 2138

Ledoux, P. 1947, ApJ, 105, 305

Lee, E. J. & Chiang, E. 2015, ApJ, 811, 41

Lee, E. J. & Chiang, E. 2016, ApJ, 817, 90

Lee, E. J. & Connors, N. J. 2021, ApJ, 908, 32

Lee, E. J., Karalis, A., & Thorngren, D. P. 2022, ApJ, 941, 186

Lee, E. J., Murray, N., & Rahman, M. 2012, ApJ, 752, 146

Lee, Y., Stark, A. A., Kim, H.-G., & Moon, D.-S. 2001, ApJS, 136, 137

Lee, Y.-N. & Hennebelle, P. 2016a, A&A, 591, A30

Lee, Y.-N. & Hennebelle, P. 2016b, A&A, 591, A31

Leggett, S. K., Bergeron, P., Subasavage, J. P., et al. 2018, ApJS, 239, 26

Leliwa-Kopystyński, J. & Kossacki, K. J. 2000, Planet. Space Sci., 48, 727

Lesur, G., Ercolano, B., Flock, M., et al. 2022, arXiv e-prints, arXiv:2203.09821

Li, D., Mustill, A. J., & Davies, M. B. 2021, MNRAS, 508, 5671

Li, D., Mustill, A. J., & Davies, M. B. 2022, ApJ, 924, 61

Li, R., Youdin, A., & Simon, J. 2019, arXiv e-prints, arXiv:1906.09261

Lichtenberg, T., Golabek, G. J., Gerya, T. V., & Meyer, M. R. 2016, Icarus, 274, 350

Lin, C. C., Mestel, L., & Shu, F. H. 1965, ApJ, 142, 1431

Lissauer, J. J. & Kary, D. M. 1991, Icarus, 94, 126

Lissauer, J. J. & Safronov, V. S. 1991, Icarus, 93, 288

Lissauer, J. J. & Stewart, G. R. 1993, in Protostars and Planets III, ed. E. H. Levy & J. I. Lunine, 1061

Liu, B. & Ji, J. 2020, Research in Astronomy and Astrophysics, 20, 164

Liu, B., Lambrechts, M., Johansen, A., & Liu, F. 2019, A&A, 632, A7

Liu, B. & Ormel, C. W. 2018, A&A, 615, A138

Lloyd, S. 1982, IEEE Transactions on Information Theory, 28, 129

Lodato, G., Dipierro, G., Ragusa, E., et al. 2019, MNRAS, 486, 453

Lodders, K. 2003, ApJ, 591, 1220

Löhne, T., Krivov, A. V., & Rodmann, J. 2008, The Astrophysical Journal, 673, 1123

Lopez, E. D. & Fortney, J. J. 2013, ApJ, 776, 2

Love, S. G. & Brownlee, D. E. 1991, Icarus, 89, 26

Lozovsky, M., Helled, R., Rosenberg, E. D., & Bodenheimer, P. 2017, ApJ, 836, 227

Luque, R. & Pallé, E. 2022, Science, 377, 1211

Lyra, W., Johansen, A., Cañas, M. H., & Yang, C.-C. 2023, arXiv e-prints, arXiv:2301.03825

Machida, M. N., Kokubo, E., Inutsuka, S.-i., & Matsumoto, T. 2008, Astrophysical Journal, 685, 1220

Madigan, A.-M., Halle, A., Moody, M., et al. 2018, ApJ, 853, 141

Malamud, U., Grishin, E., & Brouwers, M. 2021, MNRAS, 501, 3806

Malamud, U., Landeck, W. A., Bischoff, D., et al. 2022, arXiv e-prints, arXiv:2206.00012

Malamud, U. & Perets, H. B. 2016, ApJ, 832, 160

Malamud, U. & Perets, H. B. 2017a, ApJ, 842, 67

Malamud, U. & Perets, H. B. 2017b, ApJ, 849, 8

Malamud, U. & Perets, H. B. 2020a, MNRAS, 128

Malamud, U. & Perets, H. B. 2020b, MNRAS, 129

Maldonado, R. F., Villaver, E., Mustill, A. J., Chavez, M., & Bertone, E. 2020, MNRAS, 499, 1854

Maldonado, R. F., Villaver, E., Mustill, A. J., Chávez, M., & Bertone, E. 2021, MNRAS, 501, L43

Mankovich, C. R. & Fortney, J. J. 2020, ApJ, 889, 51

Mann, A. W., Johnson, M. C., Vanderburg, A., et al. 2020, AJ, 160, 179

Manser, C. J., Gänsicke, B. T., Eggl, S., et al. 2019, Science, 364, 66

Manser, C. J., Gänsicke, B. T., Gentile Fusillo, N. P., et al. 2020, MNRAS, 493, 2127

Manser, C. J., Gänsicke, B. T., Koester, D., Marsh, T. R., & Southworth, J. 2016a, MNRAS, 462, 1461

Manser, C. J., Gänsicke, B. T., Marsh, T. R., et al. 2016b, MNRAS, 455, 4467

Mao, S. & Paczynski, B. 1991, ApJ, 374, L37

Marois, C., Macintosh, B., Barman, T., et al. 2008, Science, 322, 1348

Marsset, M., Fraser, W. C., Bannister, M. T., et al. 2020, Planetary Science Journal, 1, 16

Mayor, M., Marmier, M., Lovis, C., et al. 2011, arXiv e-prints, arXiv:1109.2497

Mayor, M. & Queloz, D. 1995, Nature, 378, 355

McAuliffe, J. P. & Christou, A. A. 2006, Icarus, 180, 8

McDonald, C. H. & Veras, D. 2021, MNRAS, 506, 4031

McDonough, W. F. 2003, Treatise on Geochemistry, 2, 568

McKee, C. F. & Ostriker, E. C. 2007, ARA&A, 45, 565

Medeiros, H., Lazzaro, D., & Kodama, T. 2018, Planet. Space Sci., 160, 77

Melis, C. & Dufour, P. 2017, ApJ, 834, 1

Melis, C., Farihi, J., Dufour, P., et al. 2011, ApJ, 732, 90

Mestel, L. 1952, MNRAS, 112, 583

Mestel, L. 1966, MNRAS, 131, 307

Miguel, Y., Bazot, M., Guillot, T., et al. 2022, A&A, 662, A18

Miner, E. D. 1990, Uranus: The Planet, Rings and Satellites (Ellis Horwood Ltd), 0–30

Mizuno, H. 1980, Progress of Theoretical Physics, 64, 544

Mohanty, S., Jankovic, M. R., Tan, J. C., & Owen, J. E. 2018, ApJ, 861, 144

Moldenhauer, T., Kuiper, R., Kley, W., & Ormel, C. 2020, in European Planetary Science Congress, EPSC2020–390

Morbidelli, A., Bottke, W. F., Nesvorný, D., & Levison, H. F. 2009, Icarus, 204, 558

Morbidelli, A., Chambers, J., Lunine, J. I., et al. 2000, Meteoritics & Planetary Science, 35, 1309

Morbidelli, A., Lambrechts, M., Jacobson, S., & Bitsch, B. 2015, Icarus, 258, 418

Morbidelli, A. & Nesvorny, D. 2012, A&A, 546, A18

Mordasini, C. 2014, A&A, 572, A118

Mordasini, C., Mollière, P., Dittkrist, K.-M., Jin, S., & Alibert, Y. 2015, International Journal of Astrobiology, 14, 201

Morgan, J. W. & Anders, E. 1980, Proceedings of the National Academy of Science, 77, 6973

Moses, J. I., Cavalié, T., Fletcher, L. N., & Roman, M. T. 2020, Philosophical Transactions of the Royal Society of London Series A, 378, 20190477

Movshovitz, N., Bodenheimer, P., Podolak, M., & Lissauer, J. J. 2010, Icarus, 209, 616

Movshovitz, N. & Podolak, M. 2008, Icarus, 194, 368

Mulders, G. D. 2018, in Handbook of Exoplanets, ed. H. J. Deeg & J. A. Belmonte (Springer), 153

Mulders, G. D., Mordasini, C., Pascucci, I., et al. 2019, ApJ, 887, 157

Müller, S., Helled, R., & Cumming, A. 2020, A&A, 638, A121

Musiolik, G. & Wurm, G. 2019, ApJ, 873, 58

Mustill, A. J. & Villaver, E. 2012, ApJ, 761, 121

Mustill, A. J., Villaver, E., Veras, D., Gänsicke, B. T., & Bonsor, A. 2018, MNRAS, 476, 3939

Nagahara, H., Kushiro, I., & Mysen, B. O. 1994, Geochim. Cosmochim. Acta, 58, 1951

Nauenberg, M. 1972, ApJ, 175, 417

Nayakshin, S. 2010, MNRAS, 408, 2381

Nesvorný, D., Li, R., Simon, J. B., et al. 2021, planetary science journal, 2, 27

Nesvorný, D., Li, R., Youdin, A. N., Simon, J. B., & Grundy, W. M. 2019, Nature Astronomy, 3, 808

Nesvorný, D., Youdin, A. N., & Richardson, D. C. 2010, AJ, 140, 785

Nittler, L. R., Chabot, N. L., Grove, T. L., & Peplowski, P. N. 2018, in Mercury. The View after MESSENGER, ed. S. C. Solomon, L. R. Nittler, & B. J. Anderson (Cambridge University Press), 30–51

Nixon, C. J., Pringle, J. E., Coughlin, E. R., Swan, A., & Farihi, J. 2020, arXiv e-prints, arXiv:2006.07639

Noll, K. S., Grundy, W. M., Chiang, E. I., Margot, J. L., & Kern, S. D. 2008, Binaries in the Kuiper Belt (University of Arizona Press), 345

O'Connor, C. E. & Lai, D. 2020, MNRAS, 498, 4005

Offner, S. S. R., Moe, M., Kratter, K. M., et al. 2022, arXiv e-prints, arXiv:2203.10066

Ogihara, M., Kunitomo, M., & Hori, Y. 2020, ApJ, 899, 91

Ohashi, S., Kataoka, A., van der Marel, N., et al. 2020, ApJ, 900, 81

Okuya, A., Ida, S., Hyodo, R., & Okuzumi, S. 2023, MNRAS, 519, 1657

Okuzumi, S., Tanaka, H., Kobayashi, H., & Wada, K. 2012, ApJ, 752, 106

Ormel, C. W. 2014, ApJ, 789, L18

Ormel, C. W. & Cuzzi, J. N. 2007, A&A, 466, 413

Ormel, C. W. & Klahr, H. H. 2010, A&A, 520, A43

Ormel, C. W. & Liu, B. 2018, A&A, 615, A178

Ormel, C. W., Shi, J.-M., & Kuiper, R. 2015, MNRAS, 447, 3512

Ormel, C. W., Vazan, A., & Brouwers, M. G. 2021, A&A, 647, A175

Owen, J. E. 2019, Annual Review of Earth and Planetary Sciences, 47, 67

Owen, J. E. & Wu, Y. 2017, ApJ, 847, 29

Paardekooper, S.-J., McNally, C. P., & Lovascio, F. 2020, MNRAS, 499, 4223

Paardekooper, S.-J., McNally, C. P., & Lovascio, F. 2021, MNRAS, 502, 1579

Paardekooper, S. J. & Mellema, G. 2004, A&A, 425, L9

Paardekooper, S. J. & Mellema, G. 2006, A&A, 453, 1129

Palme, H. & O'Neill, H. S. C. 2003, Treatise on Geochemistry, 2, 568

Pan, M. & Sari, R. 2005, Icarus, 173, 342

Pascucci, I., Mulders, G. D., Gould, A., & Fernandes, R. 2018, ApJ, 856, L28

Peebles, P. J. E. 1969, ApJ, 155, 393

Persson, B. N. J. & Biele, J. 2021, arXiv e-prints, arXiv:2110.15258

Pfalzner, S., Dehghani, S., & Michel, A. 2022, ApJ, 939, L10

Pinhas, A., Madhusudhan, N., & Clarke, C. 2016, MNRAS, 463, 4516

Pinilla, P., Klarmann, L., Birnstiel, T., et al. 2016, A&A, 585, A35

Pinilla, P. & Youdin, A. 2017, in Astrophysics and Space Science Library, Vol. 445, Formation, Evolution, and Dynamics of Young Solar Systems, ed. M. Pessah & O. Gressel, 91

Pirogov, L., Zinchenko, I., Caselli, P., Johansson, L. E. B., & Myers, P. C. 2003, A&A, 405, 639

Planes, M. B., Millán, E. N., Urbassek, H. M., & Bringa, E. M. 2017, A&A, 607, A19

Podolak, J. I., Malamud, U., & Podolak, M. 2022, Icarus, 382, 115017

Podolak, M. 2003, Icarus, 165, 428

Podolak, M., Pollack, J. B., & Reynolds, R. T. 1988, Icarus, 73, 163

Podolak, M., Weizman, A., & Marley, M. 1995, Planet. Space Sci., 43, 1517

Pohl, L. & Britt, D. T. 2020, Meteoritics and Planetary Science, 55, 962

Pollack, J. B., Hubickyj, O., Bodenheimer, P., et al. 1996, Icarus, 124, 62

Popovas, A., Nordlund, Å., & Ramsey, J. P. 2019, MNRAS, 482, L107

Popovas, A., Nordlund, Å., Ramsey, J. P., & Ormel, C. W. 2018, MNRAS, 479, 5136

Pravec, P. & Harris, A. W. 2000, Icarus, 148, 12

Pravec, P., Harris, A. W., Vokrouhlický, D., et al. 2008, Icarus, 197, 497

Putirka, K. D. & Xu, S. 2021, Nature Communications, 12, 6168

Quillen, A. C. & Faber, P. 2006, MNRAS, 373, 1245

Raddi, R., Gänsicke, B. T., Koester, D., et al. 2015, MNRAS, 450, 2083

Rafikov, R. R. 2011a, ApJ, 732, L3

Rafikov, R. R. 2011b, MNRAS, 416, L55

Rafikov, R. R. 2018, The Astrophysical Journal, 861, 35

Rafikov, R. R. & Garmilla, J. A. 2012, ApJ, 760, 123

Ragozzine, D. & Wolf, A. S. 2009, ApJ, 698, 1778

Rappaport, S., Gary, B. L., Kaye, T., et al. 2016, MNRAS, 458, 3904

Rauer, H., Catala, C., Aerts, C., et al. 2014, Experimental Astronomy, 38, 249

Raymond, S. N., O'Brien, D. P., Morbidelli, A., & Kaib, N. A. 2009, Icarus, 203, 644

Reach, W. T., Kuchner, M. J., von Hippel, T., et al. 2005, ApJ, 635, L161

Rees, M. J. 1988, Nature, 333, 523

Rein, H., Lesur, G., & Leinhardt, Z. M. 2010, A&A, 511, A69

Rein, H. & Liu, S. F. 2012, A&A, 537, A128

Rein, H. & Spiegel, D. S. 2015, MNRAS, 446, 1424

Renaud, F., Bournaud, F., Emsellem, E., et al. 2013, MNRAS, 436, 1836

Rey-Raposo, R., Dobbs, C., & Duarte-Cabral, A. 2015, MNRAS, 446, L46

Rey-Raposo, R. & Read, J. I. 2018, MNRAS, 481, L16

Ricker, G. R., Winn, J. N., Vanderspek, R., et al. 2015, Journal of Astronomical Telescopes, Instruments, and Systems, 1, 014003

Robinson, J. E., Fraser, W. C., Fitzsimmons, A., & Lacerda, P. 2020, A&A, 643, A55

Rocchetto, M., Farihi, J., Gänsicke, B. T., & Bergfors, C. 2015, MNRAS, 449, 574

Rogers, J. G., Gupta, A., Owen, J. E., & Schlichting, H. E. 2021, MNRAS, 508, 5886

Rogers, L., Bonsor, A., Brouwers, M. G., et al. 2022a, How diverse is the bulk composition of exoplanetary material?, HST Proposal. Cycle 30, ID. #17185

Rogers, L. K., Bonsor, A., Xu, S., et al. 2022b, MNRAS

Rogers, L. K., Xu, S., Bonsor, A., et al. 2020, MNRAS, 494, 2861

Rossow, W. B. 1978, Icarus, 36, 1

Rubin, M., Altwegg, K., Balsiger, H., et al. 2019, MNRAS, 489, 594

Rubincam, D. P. 2000, Icarus, 148, 2

Rucska, J. J. & Wadsley, J. W. 2021, MNRAS, 500, 520

Sabotta, S., Schlecker, M., Chaturvedi, P., et al. 2021, A&A, 653, A114

Sachs, A. 1974, Philosophical Transactions of the Royal Society of London. Series A, Mathematical and Physical Sciences, 276, 43

Safronov, V. S. 1962, Problems of Cosmogeny, 8, 177

Safronov, V. S. 1966, Soviet Ast., 9, 987

Safronov, V. S. 1969, Evoliutsiia doplanetnogo oblaka. (Academy of the sciences of the USSR)

Safronov, V. S. 1972, Evolution of the protoplanetary cloud and formation of the earth and planets. (Keter Publishing House)

Salaris, M., Althaus, L. G., & García-Berro, E. 2013, A&A, 555, A96

Santerne, A., Moutou, C., Tsantaki, M., et al. 2016, A&A, 587, A64

Sato, T., Okuzumi, S., & Ida, S. 2016, A&A, 589, A15

Savvidou, S., Bitsch, B., & Lambrechts, M. 2020, A&A, 640, A63

Schäfer, C., Speith, R., & Kley, W. 2007, A&A, 470, 733

Schäfer, U., Yang, C.-C., & Johansen, A. 2017, A&A, 597, A69

Scheeres, D. J., Britt, D., Carry, B., & Holsapple, K. A. 2015, Asteroid Interiors and Morphology (University of Arizona Press), 745–766

Schoonenberg, D., Liu, B., Ormel, C. W., & Dorn, C. 2019, A&A, 627, A149

Schoonenberg, D. & Ormel, C. W. 2017, A&A, 602, A21

Schräpler, R., Blum, J., Krijt, S., & Raabe, J.-H. 2018, ApJ, 853, 74

Seizinger, A., Krijt, S., & Kley, W. 2013, A&A, 560, A45

Shestakova, L. I. 2015, Solar System Research, 49, 139

Shmidt, O. I. 1957, Chetyre lektsii O treorii proiskhozhdeniia Zemli. (Izdatel'stvo AN SSSR)

Siebert, J., Sossi, P. A., Blanchard, I., et al. 2018, Earth and Planetary Science Letters, 485, 130

Simon, J. B., Armitage, P. J., Li, R., & Youdin, A. N. 2016, ApJ, 822, 55

Simon, J. B., Armitage, P. J., Youdin, A. N., & Li, R. 2017, ApJ, 847, L12

Smallwood, J. L., Martin, R. G., Livio, M., & Lubow, S. H. 2018, MNRAS, 480, 57

Stadel, J. G. 2001, PhD thesis, UNIVERSITY OF WASHINGTON

Stark, A. A. & Lee, Y. 2005, ApJ, 619, L159

Steckloff, J. K., Debes, J., Steele, A., et al. 2021, ApJ, 913, L31

Steele, A., Debes, J., Xu, S., Yeh, S., & Dufour, P. 2021, The Astrophysical Journal, 911, 25

Steenstra, E. S., Knibbe, J. S., Rai, N., & van Westrenen, W. 2016, Geochim. Cosmochim. Acta, 177, 48

Steinberg, E. & Sari, R. 2015, AJ, 149, 124

Stern, S. A., Green, J. C., Cash, W., & Cook, T. A. 1992, Icarus, 95, 157

Stevenson, D. J. 1982, Planet. Space Sci., 30, 755

Stone, J. M., Gardiner, T. A., Teuben, P., Hawley, J. F., & Simon, J. B. 2008, ApJS, 178, 137

Swan, A., Farihi, J., Koester, D., et al. 2019a, MNRAS, 490, 202

Swan, A., Farihi, J., & Wilson, T. G. 2019b, MNRAS, 484, L109

Swan, A., Farihi, J., Wilson, T. G., & Parsons, S. G. 2020, arXiv e-prints, arXiv:2006.05999

Swan, A., Kenyon, S. J., Farihi, J., et al. 2021, arXiv e-prints, arXiv:2106.09025

Tanaka, H., Inaba, S., & Nakazawa, K. 1996, Icarus, 123, 450

Tazzari, M., Clarke, C. J., Testi, L., et al. 2020a, arXiv e-prints, arXiv:2010.02249

Tazzari, M., Testi, L., Natta, A., et al. 2020b, arXiv e-prints, arXiv:2010.02248

Tobin, J. J., Sheehan, P. D., Megeath, S. T., et al. 2020, ApJ, 890, 130

Tokunaga, A. T., Becklin, E. E., & Zuckerman, B. 1990, ApJ, 358, L21

Tremaine, S. 1995, AJ, 110, 628

Tremblay, P. E., Bergeron, P., & Gianninas, A. 2011, ApJ, 730, 128

Trevascus, D., Price, D. J., Nealon, R., et al. 2021, MNRAS, 505, L21

Trierweiler, I. L., Doyle, A. E., Melis, C., Walsh, K. J., & Young, E. D. 2022, ApJ, 936, 30

Turner, S. G. D. & Wyatt, M. C. 2020, MNRAS, 491, 4672

Tychoniec, Ł., Manara, C. F., Rosotti, G. P., et al. 2020, A&A, 640, A19

Valletta, C. & Helled, R. 2019, ApJ, 871, 127

Valletta, C. & Helled, R. 2020, ApJ, 900, 133

Van Eylen, V., Agentoft, C., Lundkvist, M. S., et al. 2018, MNRAS, 479, 4786

van Lieshout, R., Min, M., & Dominik, C. 2014, A&A, 572, A76

Van Lieshout, R., Min, M., & Dominik, C. 2014, A&A, 572, A76

Vanderbosch, Z., Hermes, J. J., Dennihy, E., et al. 2020, ApJ, 897, 171

Vanderbosch, Z. P., Rappaport, S., Guidry, J. A., et al. 2021, ApJ, 917, 41

Vanderburg, A., Johnson, J. A., Rappaport, S., et al. 2015, Nature, 526, 546

Vazan, A., Sari, R., & Kessel, R. 2020, arXiv e-prints, arXiv:2011.00602

Vazan, A., Sari, R., & Kessel, R. 2022, ApJ, 926, 150

Venkatraman Krishnan, V., Bailes, M., van Straten, W., et al. 2020, Science, 367, 577

Vennes, S. & Kawka, A. 2013, ApJ, 779, 70

Vennes, S., Kawka, A., & Németh, P. 2011, MNRAS, 413, 2545

Venturini, J., Alibert, Y., & Benz, W. 2016, A&A, 596, A90

Venturini, J., Alibert, Y., Benz, W., & Ikoma, M. 2015, A&A, 576, A114

Veras, D. 2016, Royal Society Open Science, 3, 150571

Veras, D. 2021, Planetary Systems Around White Dwarfs (Oxford University Press), 1

Veras, D., Carter, P. J., Leinhardt, Z. M., & Gänsicke, B. T. 2017, MNRAS, 465, 1008

Veras, D., Eggl, S., & Gänsicke, B. T. 2015a, MNRAS, 451, 2814

Veras, D., Georgakarakos, N., Mustill, A. J., et al. 2021, MNRAS, 506, 1148

Veras, D., Higuchi, A., & Ida, S. 2019, MNRAS, 485, 708

Veras, D., Leinhardt, Z. M., Bonsor, A., & Gänsicke, B. T. 2014a, MNRAS, 445, 2244

Veras, D., Leinhardt, Z. M., Eggl, S., & Gänsicke, B. T. 2015b, MNRAS, 451, 3453

Veras, D., Mustill, A. J., Gänsicke, B. T., et al. 2016, MNRAS, 458, 3942

Veras, D. & Scheeres, D. J. 2020, MNRAS, 492, 2437

Veras, D., Shannon, A., & Gänsicke, B. T. 2014b, MNRAS, 445, 4175

Veras, D. & Tout, C. A. 2012, MNRAS, 422, 1648

Veras, D., Wyatt, M. C., Mustill, A. J., Bonsor, A., & Eldridge, J. J. 2011, MNRAS, 417, 2104

Verner, D. A., Barthel, P. D., & Tytler, D. 1994, A&AS, 108, 287

Villaver, E. & Livio, M. 2009, ApJ, 705, L81

Villaver, E., Livio, M., Mustill, A. J., & Siess, L. 2014, ApJ, 794, 3

Visser, R. G., Ormel, C. W., Dominik, C., & Ida, S. 2020, Icarus, 335, 113380

Voronoi, G. 1908, Journal für die reine und angewandte Mathematik (Crelles Journal), 1908, 198

Wahl, S. M., Hubbard, W. B., Militzer, B., et al. 2017, Geophys. Res. Lett., 44, 4649

Weber, P., Benítez-Llambay, P., Gressel, O., Krapp, L., & Pessah, M. E. 2018, ApJ, 854, 153

Weidenschilling, S. J. 1977a, MNRAS, 180, 57

Weidenschilling, S. J. 1977b, Ap&SS, 51, 153

Wernke, H. N. & Madigan, A.-M. 2019, ApJ, 880, 42

Wetherill, G. W. 1985, Science, 228, 877

Wilson, D. J., Gänsicke, B. T., Farihi, J., & Koester, D. 2016, MNRAS, 459, 3282

Wilson, D. J., Gänsicke, B. T., Koester, D., et al. 2015, MNRAS, 451, 3237

Wilson, T. G., Farihi, J., Gänsicke, B. T., & Swan, A. 2019, MNRAS, 487, 133

Wisdom, J. 1980, AJ, 85, 1122

Wittenmyer, R. A., Wang, S., Horner, J., et al. 2020, MNRAS, 492, 377

Wolszczan, A. & Frail, D. A. 1992, Nature, 355, 145

Workman, R. K. & Hart, S. R. 2005, Earth and Planetary Science Letters, 231, 53

Wright, D. 1987, Quarterly Journal of the Royal Astronomical Society, 28, 79

Wurm, G., Paraskov, G., & Krauss, O. 2005, Icarus, 178, 253

Wyatt, M. C., Bonsor, A., Jackson, A. P., Marino, S., & Shannon, A. 2017, MNRAS, 464, 3385

Wyatt, M. C., Clarke, C. J., & Booth, M. 2011, Celestial Mechanics and Dynamical Astronomy, 111, 1

Wyatt, M. C., Farihi, J., Pringle, J. E., & Bonsor, A. 2014, MNRAS, 439, 3371

Wyatt, M. C., Smith, R., Greaves, J., et al. 2007, the Astrophysical Journal, 658, 569

Xu, S., Dufour, P., Klein, B., et al. 2019, AJ, 158, 242

Xu, S., Jura, M., Klein, B., Koester, D., & Zuckerman, B. 2013, ApJ, 766, 132

Xu, S., Jura, M., Koester, D., Klein, B., & Zuckerman, B. 2014, ApJ, 783, 79

Xu, S., Su, K. Y. L., Rogers, L. K., et al. 2018, ApJ, 866, 108

Xu, S., Zuckerman, B., Dufour, P., et al. 2017, ApJ, 836, L7

Yang, H., Zang, W., Gould, A., et al. 2022, MNRAS, 516, 1894

Yang, J.-Y., Xie, J.-W., & Zhou, J.-L. 2020, AJ, 159, 164

Yasui, M. & Arakawa, M. 2009, Journal of Geophysical Research (Planets), 114, E09004

Youdin, A. N. & Goodman, J. 2005, ApJ, 620, 459

Youdin, A. N. & Shu, F. H. 2002, ApJ, 580, 494

Zhang, Y., Liu, S.-F., & Lin, D. N. C. 2021, ApJ, 915, 91

Zhou, G., Wirth, C. P., Huang, C. X., et al. 2022, AJ, 163, 289

Zhu, W., Petrovich, C., Wu, Y., Dong, S., & Xie, J. 2018, ApJ, 860, 101

Zhu, Z. 2019, MNRAS, 483, 4221

Zhu, Z. & Yang, C.-C. 2021, MNRAS, 501, 467

Zuckerman, B. & Becklin, E. E. 1987, Nature, 330, 138

Zuckerman, B., Koester, D., Dufour, P., et al. 2011, ApJ, 739, 101

Zuckerman, B., Koester, D., Melis, C., Hansen, B. M., & Jura, M. 2007, ApJ, 671, 872

Zuckerman, B., Koester, D., Reid, I. N., & Hünsch, M. 2003, ApJ, 596, 477

Zuckerman, B., Melis, C., Klein, B., Koester, D., & Jura, M. 2010, ApJ, 722, 725